UNIVERSITY OF CALIFORNIA, SAN DIEGO

Development of multiscale modeling methods for clinical decision making in single ventricle heart patients

A dissertation submitted in partial satisfaction of the
requirements for the degree
Doctor of Philosophy

in

Engineering Sciences with a Specialization in Computational Science

by

Mahdi Esmaily-Moghadam

Committee in charge:

Professor Alison Lesley Marsden, Chair
Professor Jurijs Bazilevs
Professor Juan Carlos Del Alamo
Professor Philip E. Gill
Professor Beth J. Printz
Professor Sutanu Sarkar

2014

The dissertation of Mahdi Esmaily-Moghadam is approved, and it is acceptable in quality and form for publication on microfilm and electronically:

_____

_____

_____

_____

_____

_____
Chair

University of California, San Diego

2014

DEDICATION

To those seeking the truth with honesty and rationality.

EPIGRAPH

I do not feel obliged to believe that the same God
who has endowed us with senses, reason, and intellect
has intended us to forgo their use and by some other
means to give us knowledge which we can attain by them.
—Galileo Galilei

What are we calling "I"? ...
It is true enough to say that, in physical terms,
you are little more than an eddy in great river of life.
—Sam Harris

TABLE OF CONTENTS

LIST OF FIGURES

LIST OF TABLES

LIST OF ABBREVIATIONS

AA	Ascending aorta
ABG	Assisted bi-directional Glenn
BC	Boundary condition
BGLN	Bi-directional Glenn
CFD	Computational fluid dynamics
CS	Central shunt
FE	Finite element
FSI	Fluid-structure interaction
LHS	Left-hand-side
LPN	Lumped parameter network
LS	Linear solver
MBTS	Modified Blalock-Taussig shunt
nsd	Number of spatial dimensions
OD	Oxygen delivery
OSI	Oscillatory shear index
PA	Pulmonary artery
PC	Pre-conditioner
PDA	Patent ductus arteriosus
PDE	Partial differential equations
PVR	Pulmonary vascular resistance
RT	Residence time
SPS	Systemic-to-pulmonary shunt
WSS	Wall shear stress
WSSG	Wall shear stress gradient

ACKNOWLEDGEMENTS

I would like to express my ultimate gratitude toward professor Alison Marsden for her guidance in the last five years. She had a huge positive impact on my academic career. Undoubtedly, I acquired a wide range of skills, which goes beyond my academic life, by working under her supervision and I would be always grateful for that.

I thank my family, specifically my sister for her kindness, my father for his unconditional support, and my mother for her love. I am very grateful to Ashkan Jafarpour for being an indispensable friend in the last five years. I also thank my lab mates Weiguang Yang, Sethuraman Sankaran, Dibyendu Sengupta, and Matthew Bockman for helping me to get started in the first year and Ethan Kung, Christopher Long, and Abhay Ramachandra for all the help that I received from them.

I specifically thank Yuri Bazilevs and Tain-Yen Hsia for providing the numerical and clinical impetus for the present work. I acknowledge the use of software from the Simvascular open source project through Simbios (http://simtk.org), as well as the expertise of Nathan Wilson. I gratefully acknowledge Hyun Jin Kim for her help regarding the Lagrange method coding and implementation. I also acknowledge Jeffrey A. Feinstein, Vishal Nigam, and Adam Dorfman for their valuable assistance regarding stage-one objective function and design parameters selection, and Jane Burns and Andrew Kahn for the Kawasaki disease simulations, and Bari Murtuza for his clinical insight. I also thank Giancarlo Pennati, Francesco Migliavacca, and Irene Vignon-Clementel for sharing their expertise in the LPN modeling.

I gratefully acknowledge funding resources of this work that was mainly provided by a Leducq Foundation Network of Excellent grant and partially by a Burroughs Wellcome Fund Career Award at the Scientific Interface and a Kaplan Fellowship. I also acknowledge other funding resources, INRIA associated team grant, NIH grant RHL102596A, the NSF CAREER Awards OCI 1150184, 1055091, and OCI-105509 as well as the computational resources that were provided by the national XSEDE program.

Chapter 2, in full, is a reprint of the material as it appears in A modular numerical method for implicit 0D/3D coupling in cardiovascular finite element simulations in *Journal of Computational Physics*, 224, 63-79, 2013. Authors are M. Esmaily-Moghadam, I. Vignon-Clementel, R. Figliola, and A. Marsden. The dissertation author was the primary investigator and author of this paper.

Chapter 3, in full, is a reprint of the material as it appears in A comparison of outlet boundary treatments for prevention of backflow divergence with relevance to blood flow simulations in *Computational Mechanics*, 48(3), 277-291, 2011. Authors are M. Esmaily-Moghadam, Y. Bazilevs, I. Vignon-Clementel, and A. Marsden. The dissertation author was the primary investigator and author of this paper.

Chapter 4, in full, is a reprint of the material as it appears in A new preconditioning technique for implicitly coupled multidomain simulations with applications to hemodynamics, *Computational Mechanics*, 2013, DOI: 10.1007/s00466-013-0868-1. Authors are M. Esmaily-Moghadam, Y. Bazilevs, and A. Marsden. The dissertation author was the primary investigator and author of this paper.

Chapter 5, in full, is a reprint of the material as it appears in Efficient and Highly Scalable Parallel Algorithms for Iterative Linear Solvers in *Parallel Computing*. Authors are M. Esmaily-Moghadam, Y. Bazilevs, and A. Marsden. The dissertation author was the primary investigator and author of this paper.

Chapter 6, in full, is a reprint of the material as it appears in A non-discrete method for computation of residence time in fluid mechanics simulations in *Physics of Fluids*, 2013, DOI: 10.1063/1.4819142. Authors are M. Esmaily-Moghadam, T-Y. Hsia, and A. Marsden. The dissertation author was the primary investigator and author of this paper.

Chapter 7, in full, is a reprint of the material as it appears in Optimization of shunt placement for the Norwood surgery using multi-domain modeling in *Journal of Biomechanical Engineering*, 134(5), 051002, 2012. Authors are M. Esmaily-Moghadam, F. Migliavacca, I. Vignon-Clementel, T-Y. Hsia, and A. Marsden. The dissertation author was the primary investigator and author of this paper.

Chapter 8, in full, is a reprint of the material as it appears in Simulations re-

veal adverse hemodynamics in patients with multiple systemic to pulmonary shunts in *Journal of Biomechanical Engineering*. Authors are M. Esmaily-Moghadam, B. Murtuza, T-Y. Hsia, and A. Marsden. The dissertation author was the primary investigator and author of this paper.

Chapter 9, in full, is a reprint of the material as it appears in The Assisted Bidirectional Glenn: simulations of a novel surgical approach for first stage single ventricle heart patients in *The Journal of Thoracic and Cardiovascular Surgery*. Authors are M. Esmaily-Moghadam, T-Y. Hsia, and A. Marsden. The dissertation author was the primary investigator and author of this paper.

VITA

2014	Ph. D. in Engineering Sciences, University of California, San Diego
2009	M. S. in Mechanical Engineering, Sharif University of Technology, Tehran, Iran
2007	B. S. in Mechanical Engineering, Sharif University of Technology, Tehran, Iran

PUBLICATIONS

D. Sengupta, E. Kung, **M. Esmaily-Moghadam**, A.M. Kahn, O. Shirinsky, G.A. Lyskina, J.C. Burns, A.L. Marsden, Thrombotic risk stratification using computational modeling in patients with coronary artery aneurysms following Kawasaki disease, *Biomechanics and Modeling in Mechanobiology* , 2014, DOI: 10.1007/s10237-014-0570-z.

C.C. Long, **M. Esmaily-Moghadam**, A.L. Marsden, Y. Bazilevs, Computation of Residence Time in the Simulation of Pulsatile Ventricular Assist Devices, *Computational Mechanics*, 2013, DOI: 10.1007/s00466-013-0931-y.

G. Arbia, C. Corsini, **M. Esmaily-Moghadam**, A.L. Marsden, F. Migliavacca, T-Y. Hsia, G. Pennati, I.E. Vignon-Clementel, Numerical blood flow simulation in surgical corrections: what do we need for an accurate analysis?, *Journal of Surgical Research*, 2013, DOI: 10.1016/j.jss.2013.07.037.

J. Lee, **M. Esmaily-Moghadam**, E. Kung, H. Cao, T. Beebe, L. Fang, Y. Miller, C-L. Lien, N. C. Chi, A.L. Marsden, T.K. Hsiai, Moving Domain Computational Fluid Dynamics to Interface with an Embryonic Model of Cardiac Morphogenesis, *PLoS ONE*, 8(8), e72924, 2013.

M. Esmaily-Moghadam, T-Y. Hsia, A. Marsden, A non-discrete method for computation of residence time in fluid mechanics simulations, *Physics of Fluids*, 2013, DOI: 10.1063/1.4819142.

M. Esmaily-Moghadam, Y. Bazilevs, A. Marsden, A new preconditioning technique for implicitly coupled multidomain simulations with applications to hemodynamics, *Computational Mechanics*, 2013, DOI: 10.1007/s00466-013-0868-1.

D.A. Steinman, et al., Variability of CFD solutions for pressure and flow in a giant aneurysm: The SBC2012 CFD challenge, *Journal of Biomechanical Engineering*, 135(2), 021016, 2013.

M. Esmaily-Moghadam, I. Vignon-Clementel, R. Figliola, A. Marsden, A modular numerical method for implicit 0D/3D coupling in cardiovascular finite element simulations, *Journal of Computational Physics*, 224, 63-79, 2013.

M. Esmaily-Moghadam, F. Migliavacca, I. Vignon-Clementel, T-Y. Hsia, A. Marsden, Optimization of shunt placement for the Norwood surgery using multi-domain modeling, *Journal of Biomechanical Engineering*, 134(5), 051002, 2012.

S. Sankaran, **M. Esmaily-Moghadam**, J. Guccione, A. Kahn, E. Tseng, A. Marsden, Patient-specific multiscale modeling of blood flow for coronary artery bypass graft surgery, *Annals of Biomedical Engineering*, 40(10), 2228-2242, 2012.

M. Esmaily-Moghadam, Y. Bazilevs, I. Vignon-Clementel, A. Marsden, A comparison of outlet boundary treatments for prevention of backflow divergence with relevance to blood flow simulations, *Computational Mechanics*, 48(3), 277-291, 2011.

M. Esmaily-Moghadam, M.B. Shafii, Rotary Magnetohydrodynamic Micropump Based on Slug Trapping Valve, *Journal of Microelectromechanical Systems*, 20(1), 260-269, 2011.

M. Esmaily-Moghadam, M.B. Shafii, E.A. Dehkordi, Hydromagnetic Micropump and Flow Controller. Part A: Experiments with nickel particles added to water, *Experimental Thermal and Fluid Science*, 33(6), 1021-1028, 2009.

M. B. Shafii, E.A. Dehkordi, **M. Esmaily-Moghadam**, E. E. Koochesfahani, Using nucleators to control freckles in unidirectional solidification, *Experimental Thermal and Fluid Science*, 33(8), 1209-1215, 2009.

M. Esmaily-Moghadam, M.B. Shafii, Hydromagnetic Micropump and Flow Controller, *Sharif Mechanical Engineering Newsletter*, 34, 52-56, 2008 (In Persian).

M. Esmaily-Moghadam, Y. Bazilevs, A. Marsden, Efficient and Highly Scalable Parallel Algorithms for Iterative Linear Solvers, *Parallel Computing* (in review).

B. Murtuza, **M. Esmaily-Moghadam**, F. Migliavacca, G. Christov, J. Marek, M. Kostolny, V.T Tsang, M.R. de Leval, A. Marsden, T-Y. Hsia, Neonatal Systemic-to-Pulmonary Shunts with Concomitant Patent Ductus Arteriosus: A Clinical and Computational Modeling Study, *The Journal of Thoracic and Cardiovascular Surgery* (in review).

M. Esmaily-Moghadam, B. Murtuza, T-Y. Hsia, A. Marsden, Simulations reveal adverse hemodynamics in patients with multiple systemic to pulmonary shunts, *Journal of Biomechanical Engineering* (in review).

M. Esmaily-Moghadam, T-Y. Hsia, A. Marsden, The Assisted Bidirectional Glenn: simulations of a novel surgical approach for first stage single ventricle heart patients, *The Journal of Thoracic and Cardiovascular Surgery* (to be submitted).

M. Esmaily-Moghadam, Y. Bazilevs, A. Marsden, A bi-partitioned iterative algorithm for solving linear systems obtained from incompressible flow problems (under preparation).

ABSTRACT OF THE DISSERTATION

Development of multiscale modeling methods for clinical decision making in single ventricle heart patients

by

Mahdi Esmaily-Moghadam

Doctor of Philosophy in Engineering Sciences with a Specialization in Computational Science

University of California, San Diego, 2014

Professor Alison Lesley Marsden, Chair

Infants with single ventricle physiology generally undergo three palliative surgeries starting with stage-one, in which a systemic-to-pulmonary connection is established via a shunt. Mortality is the highest among stage-one patients (up to 23%) due to sub-optimal oxygen delivery, ventricle volume overload, myocardial ischemia, and high risk of shunt blockage. The clinical objective of the present study is to simulate the stage-one circulation, analyze possible surgical options, optimize current surgical methods, and explore a novel alternative surgical option.

Simulating the stage-one circulation in single ventricle repair requires a set of numerical tools that are developed in the first part of this dissertation. First, an

implicit and modular multidomain framework with excellent stability and convergence properties is introduced that allows multiscale simulation of the circulatory system. Second, a stabilized formulation is presented for treating backflow at Neumann boundaries that is inexpensive, stable, simple, and minimally intrusive, and offers a promising alternative to previous methods. Third, an efficient preconditioner for coupled boundary conditions and an efficient iterative algorithm for solving system of equations governing incompressible flows are introduced. Fourth, a scalable parallel data structure is introduced for performing algebraic operations in iterative solvers efficiently. Fifth, an Eulerian formulation is proposed for calculating residence time that lacks mesh dependency and avoids the high computational cost of Lagrangian particle-based approaches. These tools are applicable to other cardiac mechanics and CFD simulations as well.

In second part of this dissertation, single ventricle physiology is studied using the tools presented in the first part. First, a multiscale model of single ventricle physiology is simulated and the shunt geometry is optimized to maximize oxygen delivery and improve performance. Second, surgical scenarios single and multiple systemic-to-pulmonary connections are compared, revealing higher thrombotic risk and lower oxygen delivery in the presence of multiple connections. Third, a novel stage one palliative surgery, which provides an alternative source of blood flow in case of shunt blockage and may ultimately reduce the number of open chest surgeries from three to two, is proposed and tested using multiscale modeling. Results reveal the proposed surgical method, the Assisted Bidirectional Glenn, can deliver more oxygen at a reduced heart load with only a modest increase in venous return pressure.

Chapter 1

Introduction

Neonates with pulmonary atresia or severe pulmonary stenosis in association with balanced or unbalanced ventricles, represent a heterogeneous group of patients that often require initial surgical palliation by means of a systemic-to-pulmonary artery shunt (SPS) [2]. The Norwood procedure, performed in 2.4 out of 10,000 live births diagnosed with hypoplastic left heart syndrome and other single ventricle conditions, requires insertion of a SPS [3, 4]. These conditions are generally fatal without surgical treatment following closure of the patent ductus arteriosus, a natural systemic-to-pulmonary connection present in neonates which closes automatically after few days.

Depending on the size of the single ventricle, single ventricle patients and some patients diagnosed with pulmonary atresia or severe pulmonary stenosis undergo three palliative open-heart surgeries to unload the heart, improve oxygenation, and provide a growing and reliable source of pulmonary blood flow. The first stage of these surgeries is called a Norwood procedure (or variant thereof) [5, 6]. In this procedure, performed within the first few days of life, single functional ventricle is dedicated to provide systemic perfusion, and the pulmonary blood flow is derived from a SPS between the brachiocephalic artery and the pulmonary artery (PA), the so-called modified Blalock-Taussig shunt (MBTS) (Figure 1.1-a). The purpose of shunt insertion, connecting the systemic vessels and the PA, is to provide a source of pulmonary blood flow and ensure sufficient oxygenation. Following shunt insertion, the systemic and pulmonary circulations are arranged in parallel,

such that blood travels through the aorta to both the body and lungs, and returns to the right atrium through the pulmonary and systemic venous systems. In this configuration, the heart carries a higher volume load since it must drive the systemic and pulmonary circulations in parallel, and aortic saturation is compromised due to mixing of oxygenated pulmonary and deoxygenated systemic venous blood [7].

In the subsequent surgeries, the SPS is removed and the upper- and lower-body venous return is rerouted to the lungs; hence blood is pumped to the systemic and pulmonary arteries in series rather than in parallel. In the second stage, the hemi-Fontan or bi-directional Glenn (BGLN) surgery, the SPS is taken down and the superior vena cava is connected to the PA, partially unloading the heart (Figure 1.1-b). Although systemic saturation is improved [8] compared to the first stage, the lower body and pulmonary venous returns still mix and systemic saturation remains sub-optimal. In the final palliative surgery, the Fontan, the inferior vena cava is also anastomosed to the PA and the right side of the heart is completely bypassed, creating an in-series circulation [9] (Figure 1.1-c). Although most Fontan patients achieve near-normal systematic saturation, many still suffer from morbidities including thrombosis, arrhythmias, exercise intolerance, and cardiac failure [10, 11]. Despite significant improvements in surgical and management methods for the single ventricle pathway, significant morbidity and mortality remain at all three stages. The stage-one surgery, the focus of this dissertation, presents the highest risk, with mortality rates as high as 23% [12].

The clinical objective of this dissertation is to identify important factors with significant effect on the physiological condition of stage-one single ventricle patients, gain insight into the hemodynamic conditions in this unusual anatomic arrangement, investigate the possibility of improving current surgical methods by performing optimization, and investigate alternative surgical options for these patients. Considering this wide range of goals and the ethical constraints imposed on clinical studies, we adopt a simulation framework. Simulations provide a means to augment the surgeons' expertise and decision-making by providing a quantitative assessment tool to test different surgical configurations. Achieving the clinical ob-

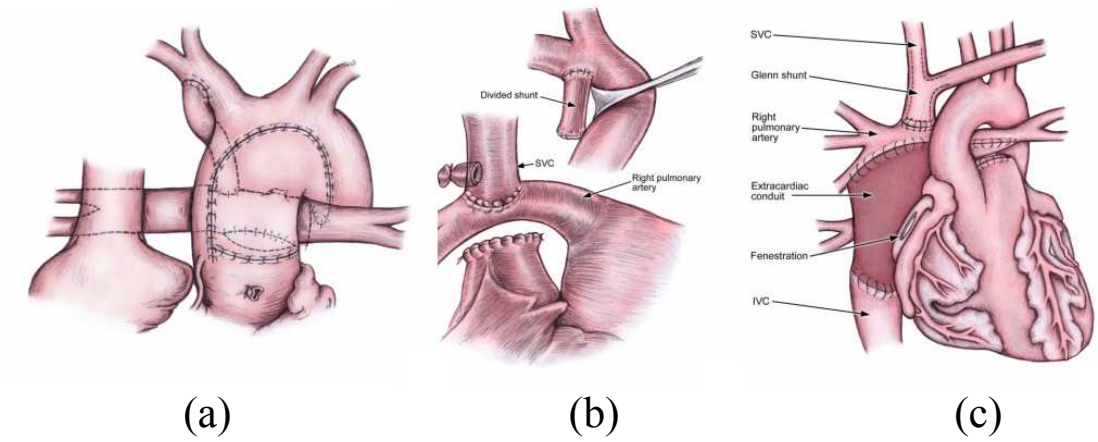

Figure 1.1: Three stages of single ventricle palliation: (a) insertion of a SPS between systemic and pulmonary circulation (Norwood), (b) removal of the shunt and connection of superior vena-cava to the PA (BGLN), (c) connection of inferior vena-cava to the PA (Fontan).

jectives of this study relies on developing a set of numerical tools in the context of cardiovascular blood flow simulation. Development of these tools is a major objective of this study.

Considering the parallel circulation in the stage-one circulation, the single ventricle must provide both systemic and pulmonary blood flow while maintaining a delicate balance that provides sufficient blood supply to both the pulmonary arteries and systemic circulation. Too much pulmonary blood flow can lead to heart failure, and too little may result in unacceptable cyanosis or inadequate oxygenation [13, 14, 15]. Previous modeling and clinical studies have shown a direct link between shunt diameter and flow distribution between the systemic and pulmonary circulations, as well as cardiac output [16]. Therefore, the outcome of stage-one surgery directly depends on the surgical intervention as well as overall circulatory and physiological conditions. This presents a multiscale problem, in which the accurate prediction of surgical outcomes requires capturing the dynamic interplay between local hemodynamics and circulatory physiology, as well as large-scale to small-scale vessels.

Due to the involvement of a vast range of length scales, complex geometry, and circulatory dynamics, accurate modeling and numerical stability remain

significant challenges in the study of cardiovascular flow. While small vessels and capillaries contribute the majority of total vascular resistance in each organ, and generally determine the direction of the flow in large vessels, most flow features of clinical interest develop inside large vessels, and thus both domains are required for an accurate representation of cardiovascular flow dynamics. Computational Fluid Dynamics (CFD) simulations have been used extensively to model blood flow in large vessels (e.g. [17, 18, 19, 20]). Although these studies provide useful spatial and temporal information in the large vessels, their accuracy largely relies on the accuracy of the downstream circulation model imposed through the boundary conditions (BC). Due to computational cost and lack of image resolution for reconstruction, it is currently impossible to include entire complex vascular networks in 3D patient specific models. Thus, to incorporate all relevant scales into a unified model, a multidomain approach must be utilized, where the temporal and spatial flow behavior is predicted for large vessels in the 3D domain, and the contribution of the numerous small vessels is predicted by a computationally efficient lower order lumped parameter network (LPN).

It is well understood that in addition to the effect of the small scale capillaries, the overall shunt resistance is an important parameter influencing the balance between systemic and pulmonary perfusion in stage-one patients. Initial CFD simulations [21, 1, 22] and in vitro studies [23, 24] assessed local hemodynamics and estimated the relation between shunt geometry and resistance. To gain understanding about global parameters such as total oxygen delivery (OD), cardiac output, and pulmonary and systemic flow rates, a multidomain model was previously introduced [25, 26]. These studies showed that the increase of shunt diameter decreases the equivalent resistance of the entire circulation, which in turn increases the cardiac output. Therefore, to obtain a more realistic representation of the stage-one circulatory system, which incorporates effects of both small and large vessels as well as the heart in a closed loop model, we adopt a the multidomain approach in the present study. The necessary formulation of multidomain approach for coupling an arbitrary LPN to a finite element (FE) Navier-Stokes solver is presented in Chapter 2. As described in this chapter, the use of elabo-

rate closed-loop LPN models of the heart and the circulatory system as BCs for CFD simulations can provide valuable global dynamic information, particularly for patient specific simulations.

Simulation divergence due to backflow is a common, but often undiscussed, problem in three-dimensional simulations of blood flow in the large vessels. In particular, the multidomain framework described in Chapter 2 usually requires Neumann BCs on both inflows and outflows, making it vulnerable to bulk or partial backflow. Because backflow is a naturally occurring physiologic phenomenon, careful treatment is necessary to realistically model backflow without artificially altering the local flow dynamics [27, 28, 29]. To address this issue, we quantitatively compare three available methods in Chapter 3 for treatment of outlets to prevent backflow divergence in FE Navier-Stokes solvers. The methods examined are: 1) adding a stabilization term to the boundary nodes formulation [30], 2) constraining the velocity to be normal to the outlet, and 3) using Lagrange multipliers to constrain the velocity profile at all or some of the outlets [27]. Detailed comparisons are made to evaluate robustness, stability characteristics, impact on local and global flow physics, computational cost, implementation effort, and ease-of-use.

Performing optimization, as was one objective of the present study, requires running multiple multidomain simulations in a reasonable time frame [31, 32]. In these simulations a large portion of computational resources is dedicated to solving a system of linear equations. The conventional methods for solving this system are, however, not very effective where physiological models with high aspect ratio or coupled BCs are concerned. BCs in these applications are critical for obtaining accurate and physiologically realistic solutions, and pose numerical challenges due to the coupling between flow and pressure [33]. In Chapter 4, we will show that implicit time integration methods, which have favorable stability characteristics, lead to an ill-conditioned problem, deteriorating the performance of traditional iterative linear equation solvers. Hence, we present a novel and efficient pre-conditioner in this chapter that exploits the strong coupling between flow and pressure and significantly reduces simulation cost. This pre-conditioner is integrated into a novel and efficient iterative method designed for incompressible flow problems.

A second avenue for performing multidomain simulations in a more reasonable time frame is by adopting parallel processing [34, 35, 36]. Achieving linear speedup in CFD simulations relies on designing proper parallel algorithms with efficient communication. Hence, in Chapter 5, a parallel data structure that gives optimized memory layout for problems involving iterative solution of sparse linear systems is developed, and its efficient implementation is presented. This parallel data structure is designed to reduce communication overhead and improve parallel scalability by allowing overlap between inter-processor communications and local computations when performing matrix-vector products, reducing the computational cost of vector inner products, and simplifying the implementation of parallel iterative linear solver algorithms.

Predicting the risk of thrombosis in stage-one patients, as well as many other clinical applications, is of critical importance [37, 38]. Cardiovascular simulations provide a promising means to predict risk of thrombosis in grafts, devices, and surgical anatomies in adult and pediatric patients. Although the pathways for platelet activation and clot formation are not yet fully understood, recent findings suggest that thrombosis risk is increased in regions of flow recirculation and high residence time (RT). Current approaches for calculating RT are typically based tracking positions of a finite number of Lagrangian particles that are released into the flow field [39, 40, 41, 42, 43]. However, special care must be taken to achieve temporal and spatial convergence, often requiring repeated simulations [39, 40]. In Chapter 6, we introduce a non-discrete method in which RT is calculated in an Eulerian framework using the advection-diffusion equation. The presented approach avoids multiple drawbacks associated with the conventional method and can be incorporated in the FE framework as an extra post-processing step.

The numerical tools developed in Chapters 2 to 6 are used in a clinical setting to study stage-one single ventricle surgery in Chapters 7 to 9. In Chapter 7, an idealized MBTS anatomy is parameterized and coupled to a closed-loop LPN of the Norwood surgical anatomy using the multidomain approach. Note that capturing global changes in cardiac output and OD resulting from changes in local geometry and physiology is contingent on using a closed-loop LPN model in these

patients. Then, the multidomain simulations are integrated into a fully automated derivative-free optimization algorithm to obtain optimal MBTS geometries with variable parameters of shunt diameter, anastomosis location and angles. Considering the major clinical complications associated with the stage-one surgery, which are mainly related to insufficient OD, and also the utility of our simulation framework, three objective functions 1) systemic, 2) coronary and 3) combined systemic and coronary OD are maximized.

In some clinical scenarios, patients receive two systemic-to-pulmonary connections, either by leaving the ductus arteriosus open, or by adding an additional central shunt in conjunction with the MBTS [44, 45]. This practice has been motivated by the thinking that an additional source of pulmonary blood flow could beneficially increase pulmonary flow and provide the security of an alternate pathway in case of thrombosis [14]. However, there have been clinical reports of premature shunt occlusion when more than one shunt is employed, leading to speculation that multiple shunts may in fact lead to unfavorable hemodynamics and increased mortality. In Chapter 8, we investigate the hypothesis that multiple shunts may lead to undesirable flow competition, resulting in increased RT and elevated risk of thrombosis, as well as pulmonary over-circulation. CFD-based multidomain simulations were performed to compare a range of shunt configurations and systematically quantify flow competition, pulmonary circulation, and other clinically relevant parameters. In total, 23 cases were evaluated by systematically changing the patent ductus arteriosus or central shunt diameter, pulmonary vascular resistance (PVR), and MBTS position and compared by quantifying OD to the systemic and coronary beds, wall shear stress (WSS), WSS gradient, oscillatory shear index, and RT in the PA and MBTS.

While there are several variations of stage-one surgery, all lead to a delicate physiological condition with a high rate of mortality, as compared to subsequent stages [7]. Single ventricle is overloaded, oxygen saturation is suboptimal, there is a significant risk of pulmonary circulation blockage by thrombus formation in the MBTS, and myocardial ischemia is common due to the diastolic coronary blood flow steal and low oxygen saturation [13, 14, 15]. To mitigate these drawbacks,

we introduce a novel surgical method, the Assisted bidirectional Glenn (ABG), for stage one single ventricle repair in Chapter 9. To compare this new surgical approach to the classical surgical options, idealized 3D anatomical models of the MBTS, BGLN, and ABG are constructed and simulated using our multidomain framework. To model pre-stage one and two conditions, two levels of PVR are simulated. These are to examine and compare oxygen saturation level, OD, heart load, superior vena-cava pressure, and pulmonary flow rate between ABG, MBTS, and BGLN surgeries. Finally, we draw conclusions and discuss future directions.

In the following chapters, regular italicized font is used for scalars, and bold italicized font for vectors, tensors, and matrices. Roman subscripts are used to construct new variable names and italic superscripts are used as indices. This is to distinguish between variable sets and construction of new variable names. For example, $u^{a,i}$ represent velocity at node a and direction i. It can also be written as $\boldsymbol{u}^a$ and $\boldsymbol{u}(\boldsymbol{x}, t)$ to denote a vector at node a or a vector field as a function of $\boldsymbol{x}$ and t. To distinguish between velocity in the solid and fluid domains, we may use $\boldsymbol{u}_{\mathrm{s}}$ and $\boldsymbol{u}_{\mathrm{f}}$, respectively.

Chapter 2

A Modular Coupling Framework for Cardiovascular Simulations

Implementation of BCs in cardiovascular simulations poses numerical challenges due to the complex dynamic behavior of the circulatory system. Multidomain simulations have been recently adopted for studying circulatory system behavior. This type of simulation involves coupling of two domains to incorporate various scales of the circulatory system in a single model. Large vessels are generally included in a high-order 3D CFD domain and the rest of the circulation, i.e. the heart and vessels that are not included in the 3D domain, are often modeled in a reduced order domain. 0D models are often used as a reduced order domain, by combining resistor, capacitor, inductor, and diode elements in a LPN [46]. The temporal behavior of the 0D model is represented by a set of ODE's, derived from the analogous electrical circuit representation of the LPN components. The coupling between the 3D domain and the reduced order model must ensure conservation of mass, which imposes constraints on flow rates, and continuity of pressure or normal stress. However, it is known that this can lead to the imposition of defective BCs [47] and problems of well-posedness [47, 48].

In general, coupling between the 3D domain and a lower order 1D or 0D model can be done using either a monolithic or a partitioned approach. In a monolithic approach, the complete coupled system is solved simultaneously, either by analytic implementation of the lower order model, or by numerical integration.

A simple 0D model with a known analytical solution can be directly implemented inside the 3D solver as a *hard coded* BC, with a monolithic implementation of the Dirichlet-to-Neumann operator [49]. Monolithic implementation of open-loop coupled BCs, such as resistance, Windkessel (RCR), impedance, or simple heart models, in which the relation between the pressure (normal stress) and the flow rate of this boundary is precisely known, has been demonstrated for up to second order ODEs, including coronary artery models [29, 50, 51]. However from a practical point of view, any modification to these hard-coded BCs requires detailed end-user knowledge of the 3D solver and intrusive implementation. A modular, and easily modifiable system for coupling an arbitrary LPN network to a 3D solver is therefore desirable, as it increases applicability to a variety of disease applications, and does not require end-user modification of the 3D solver. Similarly, when the 0D network is more complex, leading to higher order or nonlinear networks of ODEs or coupling of multiple outlets the *Dirichlet-to-Neumann* operator must be computed numerically if there is no analytical solution for the ODE system. The monolithic coupling approach has been compared in detail to its explicit-in-time counterpart, in the context of fractional step methods [52]. The monolithic solution of such a 3D-0D coupled system requires a significant change in the 3D solver, and may lead to an ill-conditioned numerical system, unless proper care is taken for its preconditioning [53, 54].

An alternative to the fully coupled monolithic schemes is the partitioned approach, which has been the focus of much work in the last decade. In the partitioned approach, having a separate solver for the 0D domain enables us to relate flow rates and pressures at the coupled boundaries for any arbitrary closed-loop, high order, nonlinear LPN, with a wide range of components such as diodes and nonlinear resistors. Such an approach facilitates the use of existing solvers and allows for the use of different numerical schemes in the 0D and 3D domains. With the partitioned approach, coupling in time between the 3D and the reduced (0D or 1D) domains can be either explicit, at one extreme, or implicit at the other. This choice may be motivated by the time-step requirement of the Navier-Stokes solver, which must be sufficiently small to use an explicit method [55], or by issues

of numerical stability.

Several recent studies have used a partitioned approach with implicit staggered schemes. In most of these studies a backward Euler scheme is used for the time discretization of the 3D model and an implicit discretization is used for the reduced model. Gauss-Seidel schemes with a number of sub-iterations between the higher dimensional domain and the reduced model domain have been proposed [47]. However, for realistic flow values, this approach has been found to require too many sub-relaxation steps [53]. More recently, some partitioned strategies have used a general heterogeneous coupling approach in which average quantities are passed at the interface [56, 57]. A proof of concept was demonstrated on multiple 3D domains representing a bifurcating carotid artery [57]. In the coupling method proposed in [56], two nonlinear iteration loops were required. These studies also advocated use of Newton methods to achieve convergence. In another previous study, a cycle by cycle open-loop simulation was used, and the outlet BCs were corrected to re-balance outlet flow rates [58]. Despite this recent work, the effectiveness of an iterative implicit coupled approach with complex closed-loop LPNs, in which simultaneous temporal data in the LPN is required, has not been previously established. As noted in [55], these systems may suffer from ill-conditioning, and special care must be taken to ensure numerical stability.

In this chapter, a time-implicit approach is proposed to couple the Navier-Stokes equations solved in the 3D domain, to complex closed-loop 0D models. This overcomes current limitations related to numerical instability and restrictive time step choices. The contributions of the coupling to both the tangent matrix and the residual vector are evaluated with an independent code. The *Dirichlet-to-Neumann operator* is thus numerically, rather than analytically, determined. With proper communication protocols between the two domains, this approach provides much higher flexibility for modeling the entire circulatory system, with no requirement for modification or intrusion into the 3D solver, once the coupling framework has been implemented. Hence this method incorporates attractive features of both monolithic and partitioned approaches. The adopted time discretization scheme is second order accurate or higher, and allows both domains to be marched in

time simultaneously using a predictor-corrector algorithm. This facilitate use of a implicit integration scheme in the 0D domain. We also aim to overcome previous restrictions that required use of only Neumann BCs in the 3D domain, by expanding our formulation to include Dirichlet coupling. This offers greater flexibility in choosing LPN components, yet maintains the well-posedness of the problem. Based on the selected component at the 3D-0D interface, which is dictated by the physiological relevance of the LPN, a Dirichlet or Neumann BC can be used. In previous approaches, to couple a heart model to the 3D domain, a combination of Dirichlet and Neumann BCs with an augmented Lagrangian constraint was used. While this approach allows one to prescribe a physiologic flow profile during systole, it requires appropriate numerics to perform the switching, and is associated with increased implementation complexity, and higher computational cost [50, 59]. Here, the coupling is applied as a Dirichlet condition, with a chosen velocity profile. The coupling term in this case is not strictly a part of the variational formulation, since it is an essential BC that changes at each nonlinear iteration of the 3D solver, according to the 0D numerical solution.

Neumann boundaries are vulnerable to numerical instabilities caused by backflow, which is inevitable and physiologic for many cardiovascular applications such as the ascending aorta (AA). Considering these challenges, as detailed in Chapter 3, we incorporate a new relatively non-intrusive and robust method that relies on a stabilized formulation in the presence of inward flow, therefore expanding the practicality of Neumann boundaries to a wider range of problems. Therefore with the introduced coupling method, based on user preference, a Neumann or Dirichlet BC can be used to couple the lumped heart model to the 3D domain.

This chapter is organized as follows: we first describe the FE formulation of the 3D solver and then introduce the essential multidomain formulation for coupling any arbitrary 0D domain to a 3D FE discretized domain. Two possible methods for coupling 0D and 3D domains, i.e. using modified classical Neumann and Dirichlet BCs, and important considerations related to both of these methods are discussed. To the best of our knowledge, this represents the first study of heterogeneous multidomain coupling, in which these two variations are discussed

and compared. Therefore, we make a detailed comparison of the pros and cons of these methods, in which we contrast the effects of increasing LPN contribution to the tangent matrix. The stability, accuracy, and cost of the numerical method presented here are established through multiple case studies.

In what follows, we solve a coupled problem in which the Navier-Stokes equations of blood flow in a 3D domain are numerically coupled to a system of ODE's in a 0D domain. Both systems are solved numerically, with appropriate information exchange in each time step at the coupled boundaries. We first describe the numerical methods used for each domain and then describe the coupling algorithm.

2.1 3D solver formulation

Throughout this study, the fluid is considered to be incompressible and Newtonian and walls are assumed to be rigid, unless otherwise stated. Starting with the Navier-Stokes equations, the momentum and continuity equations can be written as,

$$\rho\dot{\boldsymbol{u}} + \rho\boldsymbol{u}\cdot\nabla\boldsymbol{u} - \nabla\cdot\boldsymbol{T} - \boldsymbol{f} = 0,$$

$$\nabla\cdot\boldsymbol{u} = 0, \tag{2.1}$$

$$\boldsymbol{T} = -p\boldsymbol{I} + \mu(\nabla\boldsymbol{u} + \nabla\boldsymbol{u}^T), \tag{2.2}$$

$$\boldsymbol{u} = \boldsymbol{g},\ \boldsymbol{x}\in\Gamma_{\mathrm{g}} \tag{2.3}$$

$$\boldsymbol{T}\cdot\boldsymbol{n} = \boldsymbol{h},\ \boldsymbol{x}\in\Gamma_{\mathrm{h}} \tag{2.4}$$

where ρ, μ, t, $\boldsymbol{x}$, $\boldsymbol{h}$, $\boldsymbol{g}$, $\dot{\boldsymbol{u}} = \dot{\boldsymbol{u}}(\boldsymbol{x},t)$, $\boldsymbol{u} = \boldsymbol{u}(\boldsymbol{x},t)$, $p = p(\boldsymbol{x},t)$, $\boldsymbol{f} = \boldsymbol{f}(\boldsymbol{x},t)$, and $\boldsymbol{T}$ are the density, viscosity, time, position vector, Neumann boundary traction, Dirichlet boundary imposed velocity, velocity time derivative taken with respect to a fixed spatial location, velocity vector, pressure, body forces vector, and stress tensor, respectively. Since shear rate is on the order of 100 s^{-1} throughout this study, blood is assumed to behave as a Newtonian fluid [60]. Unless stated otherwise, density and viscosity are set to be 1060 $\mathrm{kg/m}^3$ and 0.004 Pa·s based on blood rheological properties.

In Equations (2.3) and (2.4), the Neumann and Dirichlet boundaries are denoted by Γ_{h} and Γ_{g}, respectively. As shown in Figure 2.1, these boundaries can be split to coupled and uncoupled domains, $\Gamma_{\mathrm{h}} = \Gamma_{\mathrm{h_c}} \cup \Gamma_{\mathrm{h_u}}$ and $\Gamma_{\mathrm{g}} = \Gamma_{\mathrm{g_c}} \cup \Gamma_{\mathrm{g_u}}$. Note that for the coupled boundaries, $\boldsymbol{g} = \boldsymbol{g}(\boldsymbol{u}, p; \boldsymbol{x}, t)$ and $\boldsymbol{h} = \boldsymbol{h}(\boldsymbol{u}, p; \boldsymbol{x}, t)$ are computed based on the 0D domain behavior, whereas for the uncoupled boundaries $\boldsymbol{g} = \boldsymbol{g}(\boldsymbol{x}, t)$ and $\boldsymbol{h} = \boldsymbol{h}(\boldsymbol{x}, t)$ are prescribed values.

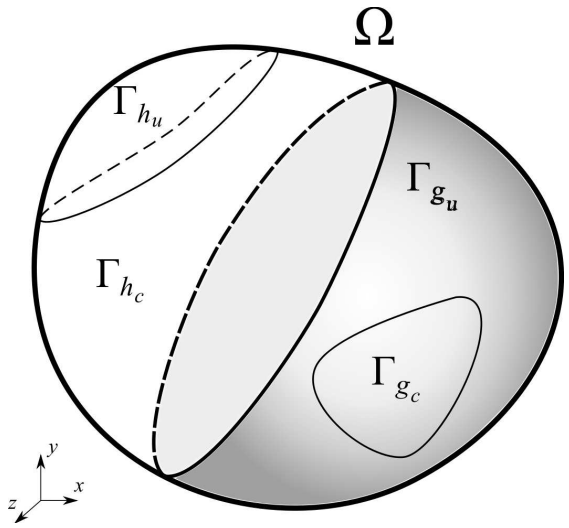

Figure 2.1: Schematic of the Neumann, $\Gamma_{\mathrm{h}} = \Gamma_{\mathrm{h_c}} \cup \Gamma_{\mathrm{h_u}}$, and Dirichlet, $\Gamma_{\mathrm{g}} = \Gamma_{\mathrm{g_c}} \cup \Gamma_{\mathrm{g_u}}$, boundaries, each divided into coupled and uncoupled boundaries. Ω is the entire 3D computational domain and $\Gamma_{\mathrm{h}} \cup \Gamma_{\mathrm{g}} = \partial\Omega$.

The equivalent weak form of Equations (2.1) to (2.4) is:

$$B_{\mathrm{G}}(\boldsymbol{w}, q; \boldsymbol{u}, p) = \int_{\Omega} \boldsymbol{w} \cdot (\rho \dot{\boldsymbol{u}} + \rho \boldsymbol{u} \cdot \nabla \boldsymbol{u} - \boldsymbol{f}) \mathrm{d}\Omega$$

$$+ \int_{\Omega} \nabla \boldsymbol{w} : \boldsymbol{T} \mathrm{d}\Omega + \int_{\Omega} \mathrm{q} \nabla \cdot \boldsymbol{u} \mathrm{d}\Omega - \int_{\Gamma_{\mathrm{h}}} \boldsymbol{w} \cdot \boldsymbol{h} \mathrm{d}\Gamma, \tag{2.5}$$

where $\boldsymbol{w}$ and q are velocity and pressure test functions, respectively, and

$$\boldsymbol{\mathcal{S}}_{\mathrm{h}} = \left\{ \boldsymbol{u} | \boldsymbol{u}(\boldsymbol{x}, t) \in (H^1)^{\mathrm{nsd}} \times [0, T],\ \boldsymbol{u} = \boldsymbol{g} \text{ on } \Gamma_{\mathrm{g}} \right\},$$

$$\boldsymbol{\mathcal{W}}_{\mathrm{h}} = \left\{ \boldsymbol{w} | \boldsymbol{w}(\boldsymbol{x}) \in (H^1)^{\mathrm{nsd}},\ \boldsymbol{w} = \boldsymbol{0} \text{ on } \Gamma_{\mathrm{g}} \right\},$$

$$\mathcal{Q}_{\mathrm{h}} = \left\{ q | q(\boldsymbol{x}) \in L^2 \right\},$$

$$\mathcal{P}_{\mathrm{h}} = \left\{ p | p(\boldsymbol{x}, t) \in L^2 \times [0, T] \right\}, \tag{2.6}$$

are the discrete solution and weight spaces defined on the computational domain, $\Omega \in \mathbb{R}^{\mathrm{nsd}}$. Equation (2.5) is obtained by applying the Galerkin method to the strong form of the Navier-Stokes equations. Since it convenient to use one discretized space, equal-order interpolation functions are generally used for pressure and velocity. However, Equation (2.5) with equal-order functions does not meet the so called Babuska-Brezzi condition and is unstable in the presented form [61, 62]. In the discrete setting, we make use of a stabilized formulation (see, e.g., [63, 64, 65, 66]), which allows equal-order velocity and pressure interpolation, and addresses the convective instability associated with Galerkin's method by setting

$$\begin{aligned} B\left(\boldsymbol{w}, q; \boldsymbol{u}, p\right) = B_{\mathrm{G}} + \sum_{e \in \boldsymbol{I}_{\mathrm{e}}} \int_{\Omega^e} \rho \nabla \boldsymbol{w} : \left(\bar{\tau} \boldsymbol{u}_{\mathrm{p}} \otimes \left(\boldsymbol{u}_{\mathrm{p}} \cdot \nabla \boldsymbol{u} \right) - \boldsymbol{u} \otimes \boldsymbol{u}_{\mathrm{p}} + \tau_{\mathrm{C}} \nabla \cdot \boldsymbol{u} \boldsymbol{I} \right) \mathrm{d}\Omega \\ + \sum_{e \in \boldsymbol{I}_{\mathrm{e}}} \int_{\Omega^e} \left[\rho \boldsymbol{w} \cdot \left(\boldsymbol{u}_{\mathrm{p}} \cdot \nabla \boldsymbol{u} \right) - \boldsymbol{u}_{\mathrm{p}} \cdot \nabla q \right] \mathrm{d}\Omega = 0, \end{aligned} \tag{2.7}$$

in which $\boldsymbol{I}_{\mathrm{e}}$ is the index set of elements, each with interior Ω^e, and

$$\begin{aligned} \boldsymbol{u}_{\mathrm{p}} &= -\tau_{\mathrm{M}} \left(\dot{\boldsymbol{u}} + \boldsymbol{u} \cdot \nabla \boldsymbol{u} + \frac{1}{\rho} \nabla p - \frac{\mu}{\rho} \nabla^2 \boldsymbol{u} \right), \\ \tau_{\mathrm{M}} &= \left[\left(\frac{2 c_1}{\Delta t} \right)^2 + \boldsymbol{u} \cdot \boldsymbol{\xi} \boldsymbol{u} + c_2 \left(\frac{\mu}{\rho} \right)^2 \boldsymbol{\xi} : \boldsymbol{\xi} \right]^{-\frac{1}{2}}, \\ \bar{\tau} &= \left(\boldsymbol{u}_{\mathrm{p}} \cdot \boldsymbol{\xi} \boldsymbol{u}_{\mathrm{p}} \right)^{-\frac{1}{2}}, \\ \tau_{\mathrm{C}} &= \left[\mathrm{tr}\left(\boldsymbol{\xi} \right) \tau_{\mathrm{M}} \right]^{-1}, \end{aligned} \tag{2.8}$$

in which c_1 and c_2 are constants of this model, set to 1 and 3, respectively, $\boldsymbol{\xi}$ is an nsd $\times$ nsd covariant matrix, obtained from a mapping between the physical and parent domains which is inversely proportional to the square of mesh size, and Δt is the time step size. The second, third, and fifth terms inside the integral in Equation (2.7) are stream-wise upwind Petrov-Galerkin (SUPG) terms, which are essential for achieving a stable scheme, and are common between different stabilized formulations. As we will see later, the last term generates a Laplacian operator acting on the pressure field and directly relates the continuity equation to the pressure.

To solve the stabilized weak form at time t^n, variables are interpolated in space using

$$\begin{aligned}
\boldsymbol{w}(\boldsymbol{x}) &= \sum_{a\in\boldsymbol{I}_\mathrm{a}} N^a(\boldsymbol{x})\boldsymbol{w}^a,\\
q(\boldsymbol{x}) &= \sum_{a\in I_\mathrm{a}} N^a(\boldsymbol{x})q^a,\\
\boldsymbol{u}(\boldsymbol{x}, t=t^n) = \boldsymbol{u}^n(\boldsymbol{x}) &= \sum_{a\in\boldsymbol{I}_\mathrm{a}} N^a(\boldsymbol{x})\boldsymbol{u}^{a,n},\\
p(\boldsymbol{x}, t=t^n) = p^n(\boldsymbol{x}) &= \sum_{a\in I_\mathrm{a}} N^a(\boldsymbol{x})p^{a,n},
\end{aligned} \tag{2.9}$$

in which $\boldsymbol{I}_\mathrm{a}$, N^a, $\boldsymbol{w}^a$, q^a, $\boldsymbol{u}^a$, and p^a are the index set of mesh nodal points, interpolation functions corresponding to node a, velocity and pressure weights and solution at nodal point a, respectively. Substituting Equation (2.9) in (2.7), the result must hold for any $\boldsymbol{w}^a$ and q^a, hence

$$\begin{aligned}
\boldsymbol{R}^a_\mathrm{m}\left(\dot{\boldsymbol{u}}, \boldsymbol{u}, p\right) &= \sum_{e\in\boldsymbol{I}_\mathrm{e}} \int_{\Omega^e} \rho N^a \left(\dot{\boldsymbol{u}} + (\boldsymbol{u}+\boldsymbol{u}_\mathrm{p})\cdot\nabla\boldsymbol{u}\right)\mathrm{d}\Omega\\
&+ \sum_{e\in\boldsymbol{I}_\mathrm{e}} \int_{\Omega^e} (\nabla N^a)^\mathrm{T}\left(-p\boldsymbol{I} + \mu\nabla\boldsymbol{u}^\mathrm{s} + \rho\bar{\tau}\boldsymbol{u}_\mathrm{p}\otimes(\boldsymbol{u}_\mathrm{p}\cdot\nabla\boldsymbol{u}) - \rho\boldsymbol{u}\otimes\boldsymbol{u}_\mathrm{p} + \rho\tau_\mathrm{C}\nabla\cdot\boldsymbol{u}\boldsymbol{I}\right)\mathrm{d}\Omega\\
&- \int_{\Gamma_\mathrm{h}} N^a\boldsymbol{h}\mathrm{d}\Gamma = \boldsymbol{0},\\
R^a_\mathrm{c}\left(\boldsymbol{u}, p\right) &= \int_\Omega \left[N^a\nabla\cdot\boldsymbol{u} - (\nabla N^a)^\mathrm{T}\boldsymbol{u}_\mathrm{p}\right]\mathrm{d}\Omega = 0,
\end{aligned} \tag{2.10}$$

in which $\boldsymbol{R}^a_\mathrm{m}$ and R^a_c are the momentum and continuity residuals at node a, respectively. Due to the nonlinear terms, Equation (2.10) is solved iteratively using the Newton-Raphson method for linearization. To relate $\dot{\boldsymbol{u}}$ to $\boldsymbol{u}$ and to time-integrate Equation (2.10), the second order generalized-α method is adopted, which works as follows [67].

1. Predict the solution at time step $n+1$, given the solution at time step n, i.e. $\left\{\dot{\boldsymbol{u}}^{a,n},\ \boldsymbol{u}^{a,n},\ p^{a,n}\right\}_{a\in\boldsymbol{I}_\mathrm{a}}$

$$\begin{aligned}
\left\{\dot{\boldsymbol{u}}^{a,n+1}\right\}_{a\in\boldsymbol{I}_\mathrm{a}} &= \frac{\gamma-1}{\gamma}\left\{\dot{\boldsymbol{u}}^{a,n}\right\}_{a\in\boldsymbol{I}_\mathrm{a}},\\
\left\{\boldsymbol{u}^{a,n+1}\right\}_{a\in\boldsymbol{I}_\mathrm{a}} &= \left\{\boldsymbol{u}^{a,n}\right\}_{a\in\boldsymbol{I}_\mathrm{a}},
\end{aligned}$$

$$\left\{p^{a,n+1}\right\}_{a\in\boldsymbol{I}_{\mathrm{a}}} = \left\{p^{a,n}\right\}_{a\in\boldsymbol{I}_{\mathrm{a}}}. \tag{2.11}$$

in which

$$\begin{aligned}\gamma &= 0.5 + \alpha_{\mathrm{m}} - \alpha_{\mathrm{f}},\\ \alpha_{\mathrm{m}} &= \frac{1}{1+\rho_\infty},\\ \alpha_{\mathrm{f}} &= \frac{3-\rho_\infty}{2(1+\rho_\infty)},\end{aligned} \tag{2.12}$$

and ρ_∞ are the generalized-α method coefficients. An initial condition is used to initialize the simulation when $n = 1$. In this study, a zero-valued initial condition is used for all the simulations in the 3D domain.

2. Calculate acceleration and velocity at $n+\alpha_{\mathrm{m}}$ and $n+\alpha_{\mathrm{f}}$, respectively

$$\begin{aligned}\left\{\dot{\boldsymbol{u}}^{a,n+\alpha_{\mathrm{m}}}\right\}_{a\in\boldsymbol{I}_{\mathrm{a}}} &= (1-\alpha_{\mathrm{m}})\left\{\dot{\boldsymbol{u}}^{a,n}\right\}_{a\in\boldsymbol{I}_{\mathrm{a}}} + \alpha_{\mathrm{m}}\left\{\dot{\boldsymbol{u}}^{a,n+1}\right\}_{a\in\boldsymbol{I}_{\mathrm{a}}},\\ \left\{\boldsymbol{u}^{a,n+\alpha_{\mathrm{f}}}\right\}_{a\in\boldsymbol{I}_{\mathrm{a}}} &= (1-\alpha_{\mathrm{f}})\left\{\boldsymbol{u}^{a,n}\right\}_{a\in\boldsymbol{I}_{\mathrm{a}}} + \alpha_{\mathrm{f}}\left\{\boldsymbol{u}^{a,n+1}\right\}_{a\in\boldsymbol{I}_{\mathrm{a}}}.\end{aligned} \tag{2.13}$$

3. Perform a Newton-Raphson iteration on Equation (2.10), using $\dot{\boldsymbol{u}}^{n+\alpha_{\mathrm{m}}}$, $\boldsymbol{u}^{n+\alpha_{\mathrm{f}}}$ and p^{n+1} (obtained from Equations (2.9) and (2.13)) as the current point. Hence, a linear system of equations is formed by differentiating the right-hand-side vector, i.e. $\boldsymbol{R}_{\mathrm{m}} = \{\boldsymbol{R}^a_{\mathrm{m}}\}_{a\in\boldsymbol{I}_{\mathrm{a}}}$ and $\boldsymbol{R}_{\mathrm{c}} = \{R^a_{\mathrm{c}}\}_{a\in\boldsymbol{I}_{\mathrm{a}}}$, with respect to the solutions $\boldsymbol{y}_{\mathrm{u}}$ and $\boldsymbol{y}_{\mathrm{p}}$.

$$\begin{aligned}\boldsymbol{K}\boldsymbol{y}_{\mathrm{u}} + \boldsymbol{G}\boldsymbol{y}_{\mathrm{p}} &= -\boldsymbol{R}_{\mathrm{m}}\left(\dot{\boldsymbol{u}}^{n+\alpha_{\mathrm{m}}}, \boldsymbol{u}^{n+\alpha_{\mathrm{f}}}, p^{n+1}\right),\\ \boldsymbol{D}\boldsymbol{y}_{\mathrm{u}} + \boldsymbol{L}\boldsymbol{y}_{\mathrm{p}} &= -\boldsymbol{R}_{\mathrm{c}}\left(\boldsymbol{u}^{n+\alpha_{\mathrm{f}}}, p^{n+1}\right),\end{aligned} \tag{2.14}$$

in which $\boldsymbol{K}$, $\boldsymbol{G}$, $\boldsymbol{D}$, and $\boldsymbol{L}$ are blocks of the left-hand-side (LHS) matrix, defined at row a and column b as

$$\begin{aligned}\boldsymbol{K}^{ab} &\approx \frac{\partial \boldsymbol{R}^a_{\mathrm{m}}}{\partial \boldsymbol{y}^b_{\mathrm{u}}},\\ \boldsymbol{G}^{ab} &\approx \frac{\partial \boldsymbol{R}^a_{\mathrm{m}}}{\partial y^b_{\mathrm{p}}},\\ \boldsymbol{D}^{ab} &\approx \frac{\partial R^a_{\mathrm{c}}}{\partial \boldsymbol{y}^b_{\mathrm{u}}},\end{aligned}$$

$$L^{ab} \approx \frac{\partial R_{\mathrm{c}}^a}{\partial y_{\mathrm{p}}^b}. \tag{2.15}$$

Note that $\boldsymbol{y}_{\mathrm{u}}$ and $\boldsymbol{y}_{\mathrm{p}}$, which are the correction to velocity and pressure, respectively, are defined such that $\boldsymbol{G} \approx -\boldsymbol{D}^T$.

4. Correct the predicted values at time step $n+1$ based on the solution of (2.14).

$$\begin{aligned}
\dot{\boldsymbol{u}}^{a,n+1} &\leftarrow \dot{\boldsymbol{u}}^{a,n+1} + \boldsymbol{y}_{\mathrm{u}}^a \quad \forall\, a \in \boldsymbol{I}_{\mathrm{a}}, \\
\boldsymbol{u}^{a,n+1} &\leftarrow \boldsymbol{u}^{a,n+1} + \gamma \Delta t \boldsymbol{y}_{\mathrm{u}}^a \quad \forall\, a \in \boldsymbol{I}_{\mathrm{a}}, \\
p^{a,n+1} &\leftarrow p^{a,n+1} + \alpha_{\mathrm{f}} \gamma \Delta t y_{\mathrm{p}}^a \quad \forall\, a \in \boldsymbol{I}_{\mathrm{a}}.
\end{aligned} \tag{2.16}$$

To perform another iteration, go back to step 2, otherwise go back to step 1 and increase n by one.

Defining $\tilde{\alpha}_{\mathrm{f}} \equiv \gamma \Delta t \alpha_{\mathrm{f}}$, from Equations (2.9), (2.13), and (2.16)

$$\begin{aligned}
\frac{\partial \dot{\boldsymbol{u}}^{n+\alpha_{\mathrm{m}}}}{\partial \boldsymbol{y}_{\mathrm{u}}^a} &= \alpha_{\mathrm{m}} N^a, \\
\frac{\partial \boldsymbol{u}^{n+\alpha_{\mathrm{f}}}}{\partial \boldsymbol{y}_{\mathrm{u}}^a} &= \alpha_{\mathrm{f}} \gamma \Delta t N^a = \tilde{\alpha}_{\mathrm{f}} N^a, \\
\frac{\partial p^{n+1}}{\partial \boldsymbol{y}_{\mathrm{p}}^a} &= \tilde{\alpha}_{\mathrm{f}} N^a.
\end{aligned} \tag{2.17}$$

Hence, the LHS matrix blocks are calculated from Equations (2.10), (2.15), and (2.17) as follows.

$$\begin{aligned}
\boldsymbol{K}^{ab} = \sum_{e \in \boldsymbol{I}_{\mathrm{e}}} \int_{\Omega^e} \big[& \rho \alpha_{\mathrm{m}} N^a N^b \boldsymbol{I} + \rho \tilde{\alpha}_{\mathrm{f}} N^a \left(\boldsymbol{u} + \boldsymbol{u}_{\mathrm{p}} \right) \cdot \nabla N^b \boldsymbol{I} \\
& + \mu \tilde{\alpha}_{\mathrm{f}} \left(\nabla N^a \cdot \nabla N^b \boldsymbol{I} + \nabla N^b \otimes \nabla N^a \right) + \rho \tilde{\alpha}_{\mathrm{f}} \bar{\tau} \boldsymbol{u}_{\mathrm{p}} \cdot \nabla N^a \boldsymbol{u}_{\mathrm{p}} \cdot \nabla N^b \boldsymbol{I} \\
& + \rho \tau_{\mathrm{M}} \boldsymbol{u} \cdot \nabla N^a \left(\alpha_{\mathrm{m}} N^b + \tilde{\alpha}_{\mathrm{f}} \boldsymbol{u} \cdot \nabla N^b \right) \boldsymbol{I} + \rho \tilde{\alpha}_{\mathrm{f}} \tau_{\mathrm{C}} \nabla N^a \otimes \nabla N^b \big] \, \mathrm{d}\Omega \\
\boldsymbol{G}^{ab} = \sum_{e \in \boldsymbol{I}_{\mathrm{e}}} \int_{\Omega^e} & \left[-\tilde{\alpha}_{\mathrm{f}} \nabla N^a N^b + \tilde{\alpha}_{\mathrm{f}} \tau_{\mathrm{M}} \boldsymbol{u} \cdot \nabla N^a \nabla N^b \right] \mathrm{d}\Omega, \\
\boldsymbol{D}^{ab} = \sum_{e \in \boldsymbol{I}_{\mathrm{e}}} \int_{\Omega^e} & \left[\tilde{\alpha}_{\mathrm{f}} N^a \nabla N^b + \tau_{\mathrm{M}} \nabla N^a \left(\alpha_{\mathrm{m}} N^b + \tilde{\alpha}_{\mathrm{f}} \boldsymbol{u} \cdot \nabla N^b \right) \right] \mathrm{d}\Omega, \\
L^{ab} = \sum_{e \in \boldsymbol{I}_{\mathrm{e}}} \int_{\Omega^e} & \left[\frac{\tilde{\alpha}_{\mathrm{f}} \tau_{\mathrm{M}}}{\rho} \nabla N^a \cdot \nabla N^b \right] \mathrm{d}\Omega,
\end{aligned} \tag{2.18}$$

Remarks:

1. Advective velocities, e.g. $\tilde{\boldsymbol{u}}$ in $\tilde{\boldsymbol{u}} \cdot \nabla \boldsymbol{u}$ are assumed constant while differentiating Equations (2.10) with respect to velocity. In practice, this generally improves the convergence rate when doing Newton-Raphson iterations. We also note that derivatives of stabilization time constants, i.e. τ_{M}, τ_{C}, and $\bar{\tau}$, are neglected.

2. Since Galerkin's terms compared to stabilization terms and acceleration and advection terms compared to viscosity terms (specifically in high Reynolds number flows) are generally bigger, $\boldsymbol{K}^{ab}$ is a diagonally dominated matrix. Note that in Equation (2.18), the acceleration, advection, and part of the viscosity and stabilization terms are added diagonally to $\boldsymbol{K}^{ab}$. Although, $\boldsymbol{K}^{ab}$ for $a \neq b$ is not added diagonally to $\boldsymbol{K}$, as shown in Chapter 4, fewer iterations are required to solve a system with $\boldsymbol{K}$ on the LHS compared to a system formed by all four blocks that are shown in Equation (2.14).

3. In Equation (2.16), y_{p}^{a} is the change in $p^{a,n+1}$ divided by $\alpha_{\mathrm{f}}\gamma\Delta t$. As a result, Galerkin's terms in $\boldsymbol{G}^{ab}$ and $\boldsymbol{D}^{ab}$ produce a structure such that $\boldsymbol{G} \approx -\boldsymbol{D}^{T}$ and for a symmetric matrix $\boldsymbol{M}$, $\boldsymbol{DMG}$ is nearly symmetric. Note the terms in $\boldsymbol{G}^{ab}$ and $\boldsymbol{D}^{ab}$ that are proportional to τ_{M} are not antisymmetric, however those terms are smaller and can be neglected in the formulation without significantly affecting the convergence rate.

4. The structure of $\boldsymbol{L}$ is identical to a LHS matrix calculated for Laplace's equation. The symmetric structure of this elliptic operator will be exploited in Chapter 4.

As we will detail Chapter 4, the system shown in Equation (2.14) is solved with a combination of a conjugate gradient method and a preconditioned Generalized Minimum Residual (GMRES) method. The spectral radius of infinite time step (ρ_{∞} in Equation (2.12)) is set to 0.2 for all studies. For more details about the FE discretization and linearization of the Navier-Stokes equations see [67].

2.2 Strongly coupled multidomain formulation

For each LPN, we use a circuit analogy in which current and voltage are analogous to flow and pressure, and resistors, capacitors, diodes, and inductors represent the resistance to flow, distensibility of the vessels, valves, and flow inertia, respectively [46]. Each LPN is described by a set of ODE's.

The multidomain approach presented here should seamlessly integrate the 3D domain, where spatial and time dependent data are computed, with the 0D domain, where only time dependent data are desired. Since the uncoupled Neumann and Dirichlet boundaries are prescribed in time and space, the velocity and pressure field in the 3D domain can be solved via Equation (2.7) once the coupled boundaries $\boldsymbol{h}, \forall \boldsymbol{x} \in \Gamma_{\mathrm{h_c}}$ and $\boldsymbol{g}, \forall \boldsymbol{x} \in \Gamma_{\mathrm{g_c}}$ are known.

Let us define the coupled Neumann and Dirichlet boundary indices as $\eta_{\mathrm{h}} = \{1, 2, ..., n_{\mathrm{h}}\}$ and $\eta_{\mathrm{g}} = \{1, 2, ..., n_{\mathrm{g}}\}$, where n_{h} and n_{g} are the number of coupled Neumann and Dirichlet boundaries, respectively. The flow rate and spatially averaged pressure of the coupled boundaries are defined as,

$$Q^i(t) = \int_{\Gamma^i} \boldsymbol{u} \cdot \boldsymbol{n} \mathrm{d}\Gamma, \tag{2.19}$$

$$\mathcal{P}^i(t) = \frac{\int_{\Gamma^i} p \mathrm{d}\Gamma}{\int_{\Gamma^i} \mathrm{d}\Gamma}, \tag{2.20}$$

where $\Gamma^i \subset \Gamma_{\mathrm{h_c}} \cup \Gamma_{\mathrm{g_c}}, i \in \eta_{\mathrm{h}} \cup \eta_{\mathrm{g}}$ is the boundary of the surface i. Based on these values, $\boldsymbol{h}$ and $\boldsymbol{g}$ for the coupled surfaces are defined as,

$$\boldsymbol{h}(\boldsymbol{u}, p; \boldsymbol{x}, t) = -\mathcal{P}^i \boldsymbol{n},\ \boldsymbol{x} \in \Gamma^i,\ i \in \eta_{\mathrm{h}} \tag{2.21}$$

$$\boldsymbol{g}(\boldsymbol{u}, p; \boldsymbol{x}, t) = \frac{\phi(\boldsymbol{x}, t)}{\int_{\Gamma^i} \phi \mathrm{d}\Gamma} Q^i \boldsymbol{n},\ \boldsymbol{x} \in \Gamma^i,\ i \in \eta_{\mathrm{g}} \tag{2.22}$$

where, $\phi(\boldsymbol{x}, t)$ is the prescribed velocity profile. For cases in which we have fully developed axial flow at the coupled surface, and the cross section is not necessarily circular, this function can be approximately replaced by the solution of Poisson's equation with a constant source term and zero Dirichlet BC at the wall. For a Newtonian, steady and unidirectional flow, Equation (2.1) reduces to [68],

$$\nabla^2 \boldsymbol{u} = \frac{1}{\mu} \nabla p, \tag{2.23}$$

where $\boldsymbol{u}$ is non-zero only in the axial direction (i.e. along the vessel centerline) and pressure gradient is constant for that direction. Replacing $\boldsymbol{u} \cdot \boldsymbol{n}$ with ϕ, Equation (2.23) is a Poisson equation with constant source term, which must be zero at the walls due to the no-slip BC.

Some 0D models, such as resistance and Windkessel [29] models, are simple enough that the relation between the boundary traction and surface flow rate, can be explicitly derived (Figure 2.2). For these types of BCs $\mathcal{P}^i$ is a function of the flow rate of the same surface only, i.e. $\mathcal{P}^i = \mathcal{P}^i(Q^i),\ i \in \eta_{\mathrm{h}}$. For example, a resistance BC is imposed by $\mathcal{P}^i = RQ^i$.

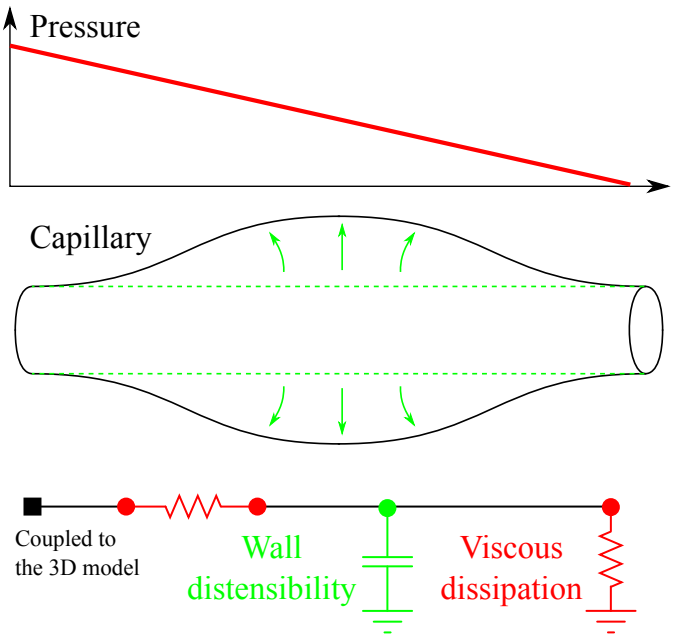

Figure 2.2: Schematic of a RCR (Windkessel) circuit for modeling capillaries. The wall distensibility is modeled by including a capacitor, which stores blood as pressure increases. Pressure drop due to the viscous dissipation is modeled using two resistors.

In general an explicit function does not exist or must be solved numerically for $\mathcal{P}^i,\ i \in \eta_{\mathrm{h}}$ and $Q^i,\ i \in \eta_{\mathrm{g}}$. That relationship can be a nonlinear function of $Q^j,\ j \in \eta_{\mathrm{h}}$ and $\mathcal{P}^k,\ k \in \eta_{\mathrm{g}}$ represented by a system of ordinary differential equations. Hence, a multidomain approach is used, in which the following system of ordinary differential equations is solved to represent the circulation outside of

the 3D domain,

$$\dot{\boldsymbol{\mathcal{X}}} = \tilde{\boldsymbol{A}}\boldsymbol{\mathcal{X}} + \tilde{\boldsymbol{b}}(Q^i, \mathcal{P}^j, t),\ i \in \eta_{\mathrm{h}},\ j \in \eta_{\mathrm{g}}, \tag{2.24}$$

and to find $\mathcal{P}^i,\ i \in \eta_{\mathrm{h}}$ and $Q^i,\ i \in \eta_{\mathrm{g}}$ for the coupled boundaries,

$$\mathcal{P}^i = \mathcal{P}^i(Q^j, \mathcal{P}^k, \mathcal{X}^l, t),\ i, j \in \eta_{\mathrm{h}},\ k \in \eta_{\mathrm{g}},\ l \in \eta_{\mathcal{X}}, \tag{2.25}$$

$$Q^i = Q^i(Q^j, \mathcal{P}^k, \mathcal{X}^l, t),\ j \in \eta_{\mathrm{h}},\ i, k \in \eta_{\mathrm{g}},\ l \in \eta_{\mathcal{X}}, \tag{2.26}$$

where, $\mathcal{X}^i$ are the unknowns in the 0D domain and $\eta_{\mathcal{X}}$ is their corresponding index set. Generally unknowns in the 0D domain are selected such that, $\{Q^i, \mathcal{P}^j\} \subset \boldsymbol{\mathcal{X}}$ for $i \in \eta_{\mathrm{g}},\ j \in \eta_{\mathrm{h}}$.

The data passed between the two domains is shown schematically in Figure 2.3. The first type of coupling occurs when a flow rate is passed from the 3D to the 0D domain, and a pressure is passed from the 0D to the 3D domain to impose the traction via Equations (2.7) and (2.21). This type of coupling will be referred to as *Neumann coupling*. We note that due to the coupling this BC is not strictly a classic Neumann condition. The second type of coupling occurs when a pressure is passed from the 3D to the 0D domain and a flow rate is passed back to the 3D domain to impose a spatial velocity profile via Equation (2.22). This type of coupling will be referred to as *Dirichlet coupling*. In some situations, we may have all of one type (either Dirichlet or Neumann) or we may have a mix of two types of boundaries in the same model. In our formulation these data are exchanged between the two domains at each Newton iteration of the nonlinear Navier-Stokes solver to ensure convergence of both domains simultaneously.

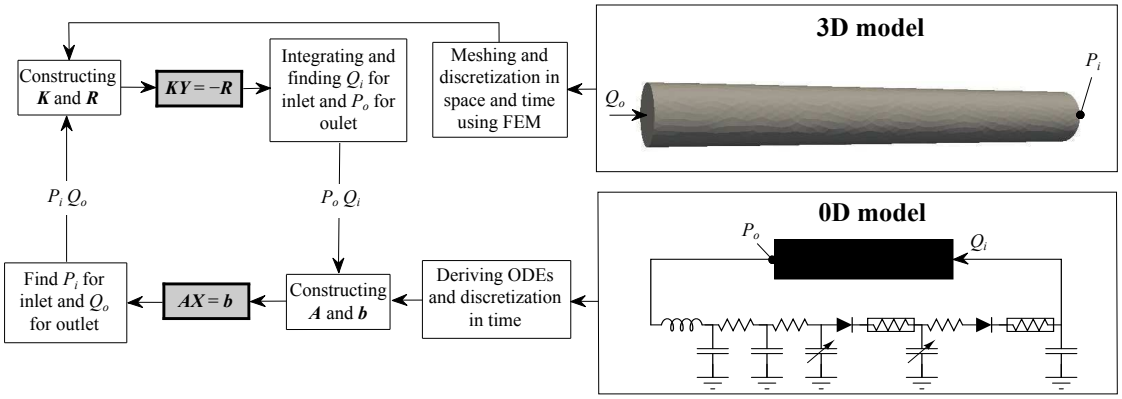

Figure 2.3: Schematic of strongly coupled iterative multidomain solver. In the 0D domain ODE's, discretized in time, can be solved by receiving the flow rate of coupled Neumann surfaces and pressure of coupled Dirichlet surfaces from the 3D domain. The 3D domain, discretized in space and time, requires the pressure of coupled Neumann surfaces and flow rate of coupled Dirichlet surfaces from the 0D domain to solve the linearized N-S equations. In this schematic, $\boldsymbol{A\mathcal{X}} = \boldsymbol{b}$, and $\boldsymbol{KY} = -\boldsymbol{R}$ are the linearized system of equations solved in the 0D and 3D domains, respectively.

In the discrete setting the linearized version of Equation (2.24) is solved for time advancement in the 0D domain. This can be represented by,

$$\boldsymbol{A\mathcal{X}}^{\tilde{n}+1} = \boldsymbol{b}(\boldsymbol{\mathcal{X}}^{\tilde{n}}, Q_i^m, \mathcal{P}_j^m, t),\ i \in \eta_{\mathrm{h}},\ j \in \eta_{\mathrm{g}},\ m \in \{n, n+1\}. \tag{2.27}$$

where $\tilde{n}$ and n denote the time steps in the 0D and 3D domains, respectively. This system of ODE's representing the LPN is advanced in time with a 4th order Runge-Kutta method. Since the integration of Equation (2.27) is cheap relative to the 3D domain time-advancement, the time between n and $n+1$ is split into 1000 0D-domain sub-time steps to increase accuracy and prevent potential sources of instability emanating from the 0D domain.

At the start of the simulation, the 0D and 3D domains are initialized with $\boldsymbol{\mathcal{X}}^1$ and $\{\boldsymbol{u}^1, \boldsymbol{p}^1\}$, respectively. In the generalized-α method, the solution at n is fixed and the solution at $n+1$ is corrected after each nonlinear Newton-Raphson iteration [67]. In each time step, from n to $n+1$ in the 3D domain, the following steps are performed:

1. Set $k = 0$ and predict unknowns at time step $n + 1$ in the 3D domain based on the solution at time step n, using Equation (2.11).

2. Use Equations (2.19) and (2.20) to compute the flow rate, $\{Q^{i,n}, Q^{i,n+1}\}\ \forall i \in \eta_{\mathrm{h}}$, and pressure of the coupled boundaries, $\{\mathcal{P}^{i,n}, \mathcal{P}^{i,n+1}\}\ \forall i \in \eta_{\mathrm{g}}$, and pass them to the 0D domain.

3. After receiving the flow and pressure data at time steps n and $n + 1$ in the 0D domain and retrieving $\boldsymbol{\mathcal{X}}^n$ as the starting point of integration, integrate the ODE's up to time step $n + 1$ using Equation (2.27).

4. After receiving $\mathcal{P}^{i,n+1}\ \forall i \in \eta_{\mathrm{h}}$ and $Q^{i,n+1}\ \forall i \in \eta_{\mathrm{g}}$ from the 0D domain, calculate the traction at the coupled Neumann boundaries and the nodal velocities at the coupled Dirichlet boundaries by using Equations (2.21) and (2.22), respectively.

5. Use Equations (2.10) and (2.18) to construct the residual vector and tangent matrix and solve the linearized Navier-Stokes equations to find $\boldsymbol{y}_{\mathrm{u}}$ and $\boldsymbol{y}_{\mathrm{p}}$.

6. Correct the velocity and pressure in the 3D domain, using Equation (2.16).

7. Set $k \leftarrow k + 1$ and go back to the second step if the residual is not small enough, $\|\boldsymbol{R}_{\mathrm{m}}\|^2 + \|\boldsymbol{R}_{\mathrm{c}}\|^2 > \epsilon^2$, or the number of iterations has not exceed the maximum specified value, $k > k_{max}$.

8. Before going to the next 3D-domain time step, calculate $\boldsymbol{\mathcal{X}}^{n+1}$ based on the corrected flow rate and pressure. Then set $n \leftarrow n + 1$ and go back to the first step.

Compared to the method implemented in [55], the coupling in our approach is implicit in time (Figure 2.4). This framework therefore offers the flexibility to use either an implicit or explicit time-integration method in the 0D domain.

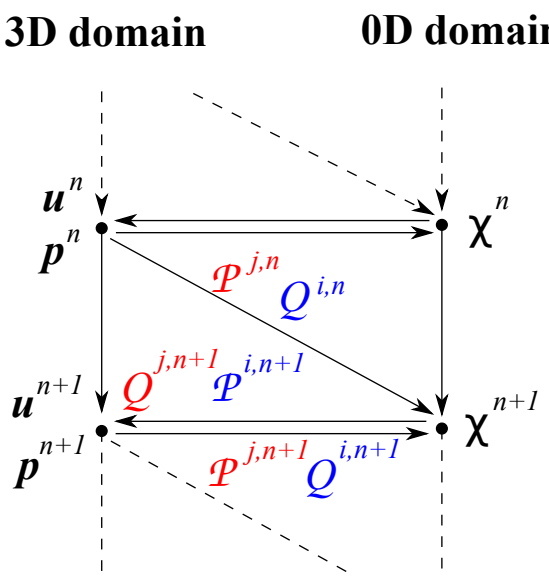

Figure 2.4: Schematic of time marching in both 3D and 0D domains. The 0D domain sends corrected $\mathcal{P}^{i,n+1}$ and $Q^{j,n+1}$ to the 3D domain and receives $Q^{i,n}$ and $\mathcal{P}^{j,n}$ and the corrected $Q^{i,n+1}$ and $\mathcal{P}^{j,n+1}$ values from the 3D domain. In this figure $i \in \eta_{\mathrm{h}}$ and $j \in \eta_{\mathrm{g}}$.

2.2.1 Remarks on coupling the Neumann boundaries

In the case of a coupled Neumann boundary, the pressure is passed from the 0D to the 3D domain, and flow rates are passed from the 3D to the 0D domain. If the circuit element directly connected to the coupled boundary is a capacitor, then using the presented numerical scheme it is essential to assign a Neumann boundary to avoid instabilities (see Appendix A). In this case, the flow rate is a natural forcing term in the system of ODEs, whereas pressure is a state variable. This type of BC, in contrast to the Dirichlet BC, does not require a pre-specified spatial velocity profile. For the coupled Neumann boundaries, the pressures can be assembled into the discretized residual vector using,

$$\boldsymbol{R}^a_{\mathrm{m}} \leftarrow \boldsymbol{R}^a_{\mathrm{m}} + \int_{\Gamma^i} N^a \mathcal{P}^{i,n+1} \boldsymbol{n} \mathrm{d}\Gamma, \ \mathrm{i} \in \eta_{\mathrm{h}}, \tag{2.28}$$

where $N^a(\boldsymbol{x})$ is the shape function for node a.

For the coupled Neumann boundaries, the same Newton approach is used to solve the nonlinear formulation as without the coupling. Hence, the algorithm

contains only one nonlinear iteration loop involving the 3D solver. Since the added term to the momentum residual vector in Equation (2.28) depends on the velocity, the contribution of the 0D domain can be added to the tangent matrix to obtain a robust implicit scheme. For an implicit coupling, the contribution of the coupled surface terms in the tangent matrix in Equation (2.14) is

$$\boldsymbol{K}^{ab} \leftarrow \boldsymbol{K}^{ab} + \frac{\partial \boldsymbol{R}^{a}_{\mathrm{m}}}{\partial \boldsymbol{y}^{b}_{\mathrm{u}}}. \tag{2.29}$$

Using Equations (2.19) and (2.29), and the fact that $\mathcal{P}^{i,n+1}$ is constant over Γ^i,

$$\begin{aligned}\boldsymbol{K}^{ab} &\leftarrow \boldsymbol{K}^{ab} + \left(\frac{\partial \boldsymbol{R}^{a}_{\mathrm{m}}}{\partial Q^{l,n+1}} \otimes \frac{\partial Q^{l,n+1}}{\partial \boldsymbol{u}^{c,n+1}}\right) \frac{\partial \boldsymbol{u}^{c,n+1}}{\partial \boldsymbol{y}^{b,n+1}_{\mathrm{m}}} \\ &= \boldsymbol{K}^{ab} + \gamma \Delta t M_{kl} \int_{\Gamma_k} N^a \boldsymbol{n} \mathrm{d}\Gamma \otimes \int_{\Gamma_l} \mathrm{N}^{\mathrm{b}} \boldsymbol{n} \mathrm{d}\Gamma,\end{aligned} \tag{2.30}$$

where M^{ij} is an $n_{\mathrm{h}} \times n_{\mathrm{h}}$ matrix

$$M^{ij} = \frac{\partial \mathcal{P}^{i,n+1}}{\partial Q^{j,n+1}},\ i,j \in \eta_{\mathrm{h}}. \tag{2.31}$$

Generally, this matrix is not available analytically. Therefore, it must be calculated numerically row-by-row, in this case using a finite difference method. This is done by passing $Q^{j,n+1} + \epsilon,\ j \in \eta_{\mathrm{h}}$ to the 0D domain, solving for the resulting pressure, and then dividing the change in $\mathcal{P}^{i,n+1},\ i \in \eta_{\mathrm{h}}$ by ϵ. This Jacobian-like matrix is,

$$M^{ij} = \frac{\mathcal{P}^{i,n+1}(Q^{j,n+1} + \epsilon; Q^{j,n}) - \mathcal{P}^{i,n+1}(Q^{j,n+1}; Q^{j,n})}{\epsilon}. \tag{2.32}$$

In the above expression, ϵ can be selected as,

$$\epsilon = \max\{\epsilon_{\mathrm{abs}}, \epsilon_{\mathrm{rel}} \left|Q^{j,n+1}\right|\}, \tag{2.33}$$

where ϵ_{abs} depends on the machine precision and ϵ_{rel} is chosen based on the accuracy requirements. Because of the low computational cost of solving the 0D domain equations, it is worth noting that this step requires essentially no additional computational time.

Generally, the off diagonal entries of M^{ij}, which can be physically interpreted as the effect of changing the flow rate at face j on the pressure at face i, are negligible compared to the diagonal terms. Neglecting the off diagonal entries

improves the sparsity of the tangent matrix, which can be exploited in the linear solver (LS). This is the choice that was implemented in this work. This matrix is computed only once for a linear LPN.

To explore this choice further, in this chapter, we will compare three cases with increasing levels of contribution to the tangent matrix within each Newton iteration. We refer to the case in which we update the matrix at each iteration as the *implicit* method. We refer to the case of partial update, i.e. when the matrix is computed just once at the start of the simulation, as the *semi-implicit* method. We refer to the case of no update, i.e. when no contribution is added to the tangent matrix, as the *explicit* method. In subsequent chapters, we adopt the semi-implicit method for coupling. Here we explore the trade-offs in cost and stability among these three methods.

The method described here for the coupled Neumann boundaries can result in numerical instability due to backflow at the coupled faces of the model. This is a well-known problem in cardiovascular simulation, but one that is often overlooked. This problem results when flow is entering the domain without explicit prescription of a velocity profile. In many situations, accurately capturing backflow is essential to reproducing the correct physiological behavior. For example a heart model coupled with the AA as a Neumann boundary will result in flow entering the domain during systole without a prescribed velocity profile since the flow normally reverses direction during this phase of the cardiac cycle. Except in very simple geometries, if the Neumann boundaries are not treated with care, the solution will diverge rapidly. This issue has been addressed in previous work by enforcing a velocity profile using Lagrange constraints, by enforcing normal velocity at the outflow face, or by extending the outlets unrealistically using long cylindrical sections. As elaborated in Chapter 3, a stable, accurate and non-intrusive method for addressing this issue is to add an advective stabilization term to the weak form of the Navier-Stokes equations [27, 69, 59, 30]. The added term in Equation (3.1) is an outward traction, opposite the direction of backflow, which pushes the flow in the direction of the outward normal. Because the added traction is defined to be zero when the flow is directed outward, the added term is only active in the

presence of flow reversal at the boundary.

2.2.2 Remarks on coupling the Dirichlet boundaries

The Dirichlet type of BC requires prescription of spatial velocity profile information, which is scaled by the flow rate (received from the 0D domain) via Equation (2.22). The pressure and velocity solutions inside the 3D domain depend on the chosen velocity profile, $\phi(\boldsymbol{x}, t)$, which is typically either a Poiseuille or Womersley profile. Sensitivity of the solution to the chosen profile, however, is problem-specific and varies depending on the interaction between the BCs and geometry in the 3D domain.

If the circuit element in the LPN adjacent to the coupled boundary is an inductor, it is essential to assign a Dirichlet BC to obtain a stable solution, as outlined in Appendix A. In this case, pressure is a natural forcing term in the system of ODEs that represents the 0D domain, whereas flow is a state variable. The Dirichlet BC is updated at the beginning of each nonlinear iteration, using the same procedure as for the Neumann boundaries. In this case, no contribution to the tangent matrix is necessary and coupling is time-implicit. The nodal velocities at $n+1$ are computed using Equation (2.22) after receiving flow rates at the coupled Dirichlet surfaces from the 0D domain. Nodal acceleration is then corrected according to the time discretization scheme,

$$\dot{\boldsymbol{u}}^{a,n+1} = \frac{\gamma - 1}{\gamma}\dot{\boldsymbol{u}}^{a,n} + \frac{1}{\gamma \Delta t}(\boldsymbol{u}^{a,n+1} - \boldsymbol{u}^{a,n}),\ a \in \Gamma_{\mathrm{g_c}}. \tag{2.34}$$

If all the coupled boundaries are Dirichlet and there are no Neumann boundaries, an additional constraint is needed in the 3D domain formulation to prevent pressure drift, namely

$$\int_{\Omega} p \mathrm{d}\Omega = 0, \quad \text{if } \Gamma = \Gamma_{\mathrm{g}}. \tag{2.35}$$

In this case, the boundary pressures that are sent to the 0D domain are only pressure differences. All relative pressures received in the 0D domain must be added to the mean pressure in the 3D domain, $\bar{\mathcal{P}}$, to obtain the correct absolute coupling pressure. For this additional mean pressure unknown, the following additional

conservation of mass equation must be enforced in the 0D domain,

$$\sum_{i=1}^{n_{\mathrm{g}}} Q^i = 0. \tag{2.36}$$

To relate equation (2.36) to $\bar{\mathcal{P}}$, the governing equation for the inductors adjacent to the coupled boundaries in the 0D domain can be used as

$$L^i \frac{\mathrm{dQ^i}}{\mathrm{dt}} = L^i f^i = \bar{\mathcal{P}} + \mathcal{P}^i - \mathcal{P}^i_{\mathrm{d}},\ i \in \eta_{\mathrm{g}}, \tag{2.37}$$

where, as shown in Figure 2.5, L^i, f^i, and $\mathcal{P}^i_{\mathrm{d}}$ are the inductance, time derivative of the coupled surface flow rate, and distal pressure, respectively. Dividing Equation (2.37) by L^i and using Equation (2.36), one can show

$$\bar{\mathcal{P}} = (\sum_{i=1}^{n_{\mathrm{g}}} \frac{1}{L^i})^{-1} \sum_{j=1}^{n_{\mathrm{g}}} \frac{\mathcal{P}^j_{\mathrm{d}} - \mathcal{P}^j}{L^j}. \tag{2.38}$$

Denoting $\tilde{f}^i$ as the time derivative of the flow rate at the coupled surfaces computed in the 0D domain, based on a coupling pressure of $\bar{\mathcal{P}} = 0$,

$$L^i \tilde{f}^i = \mathcal{P}^i - \mathcal{P}^i_{\mathrm{d}},\ i \in \eta_{\mathrm{g}}, \tag{2.39}$$

and using Equation (2.37) one can show

$$f^i = \tilde{f}^i - (L^i \sum_{j=1}^{n_{\mathrm{g}}} \frac{1}{L^j})^{-1} \sum_{k=1}^{n_{\mathrm{g}}} \tilde{f}^k,\ i \in \eta_{\mathrm{g}}. \tag{2.40}$$

Since $\tilde{f}^i$ is found from Equation (2.39) with no knowledge of $\bar{\mathcal{P}}$, using Equation (2.40), the correct f^i to be imposed in the 3D domain can be calculated with the above expression.

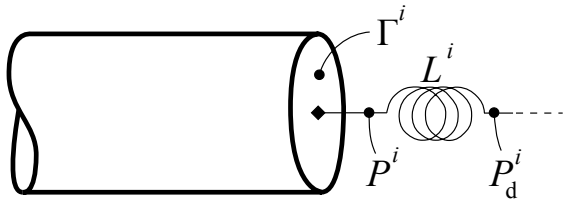

Figure 2.5: Schematic of a Dirichlet boundary, Γ^i, coupled via an inductor to the 0D domain. Coupled surface pressure and distal pressure are denoted by $\mathcal{P}^i$ and $\mathcal{P}^i_{\mathrm{d}}$, respectively.

2.3 Model construction and simulation methods

To create the geometric models throughout this study, a customized in-house version of the open source Simvascular package was used [70]. Models for idealized geometries, e.g. cylinder and single ventricle models, were analytically defined and constructed by lofting together circles. For the patient-specific models, starting from the X-ray computed tomography (CT scan), the geometry of each artery is identified and segmented [20]. By lofting these segments through the centerline of the vessels, the solid model is created. The 3D models are meshed with tetrahedral elements using the commercial package MeshSim©(Simmetrix, Clifton Park, NY).

Two finite-element solver codes are used throughout this study. In Chapters 2, 3, and 7, a customized version of Phasta [71] (open sourced as part of the Simvascular project at simtk.org) is used for simulations. Experimental validation of this solver in the context of cardiovascular flow simulations is discussed in [72]. In Chapters 4, 5, 6, 8, and 9, a separate in-house code, called the multi-physics finite element solver (MUPFES), is used for solving the fluid flow equations as well as fluid-structure interaction and advection-diffusion problems [73]. This code is verified using test cases presented in [74], among others, and is used in other studies such as [75, 76, 77].

2.4 Multidomain framework test results

We demonstrate the coupled formulation using three representative cardiovascular problems. The first is a verification exercise in a simple cylinder, the second is a simple closed-loop model with one inlet and one outlet, and the third is a model of a surgery for single ventricle heart patients with a closed-loop complex network and multiple outlets. Both Dirichlet and Neumann methods are demonstrated and compared. The time step size for the 3D solver is set to 5×10^{-4} s. Nonlinear iterations are performed until the average second norm of the residual vector is less than 5×10^{-4} or the number of iterations exceeds 45.

2.4.1 Verification using a Windkessel model

A cylinder with an unsteady prescribed Dirichlet BC at the inlet, and a Windkessel (RCR) model at the outlet, is considered for verification purposes. The model is shown in Figure 2.6, and is meshed with 331,636 tetrahedral elements. In this model R_{p}, C, R_{d}, and $Q(t)$ are the proximal resistance, capacitance, distal resistance, and time dependent inflow, respectively.

Figure 2.6: Windkessel model coupled to a cylinder with an uncoupled Dirichlet inlet BC. The cylinder diameter and length are 4.0 and 30.0 cm, respectively.

Prescribing inlet flow rate as $Q = Q_0 \left(\sin(\frac{t^*}{2})\right)^2$, the pressure at the outlet can be determined analytically as,

$$\frac{P_{ex}}{R_{\mathrm{d}} Q_0} = \left(\frac{R_{\mathrm{p}}}{R_{\mathrm{d}}} + \frac{1}{2}\right) \sin(\frac{t^*}{2})^{\,2} + \frac{1}{4}\left(1 - e^{-t^*} - \sin(t^*)\right), \tag{2.41}$$

where $t^* = \frac{t}{R_{\mathrm{d}} C}$ is the non-dimensional time.

In this simple case, a numerical solution of the 0D model is not necessary since the circuit equation can be solved analytically. For verification purposes, we compare three quantities: 1) the analytical ODE solution (Equation (2.41)), 2) the hard-coded RCR coupling (pure monolithic approach [29]), and 3) the numerically coupled solution, using the methods described in this chapter. There is only one ODE that is time-integrated in the 0D domain to obtain the pressure of the capacitor. In Figure 2.7, the analytical solution from Equation (2.41) is compared to the coupled 3D-0D simulation results. This simulation is carried out for 1 sec with $Q_0 = 10$, $R_{\mathrm{p}} = 0.1$, $R_{\mathrm{d}} = 1.0$, $C = \frac{1}{4\pi}$ in cgs units. The 3D domain time step size is 1 ms and since 1000 time steps per each 3D domain time step is performed, and each Runge-Kutta time step is 1 μs.

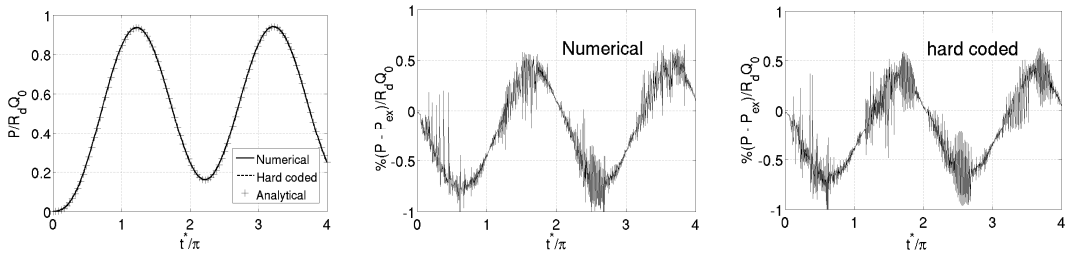

(a) (b) (c)

Figure 2.7: Cylinder with periodic inflow BC coupled to the Windkessel model shown in Figure 2.6, (a) Analytical (+), numerical coupled (solid line) and monolithic or hard coded (dash line) outlet pressures, (b) Normalized error of numerical solution in percent, (c) Normalized error of hard coded solution in percent.

Comparing the analytical and numerical results in Figure 2.7, the error is less than 1% at all times. The norm of the error, i.e. $100 \left\| \frac{P-P_{\text{ex}}}{R_{\text{d}}Q_0} \right\|$, for the hard coded and numerical results is 0.42% and 0.46%, respectively. The total simulation time, keeping everything else fixed, was 48 min and 44 min for the monolithic (i.e. hard-coded) and partitioned (i.e. numerically coupled) simulations, respectively.

Considering the small time step size used in the 0D domain, the error due to the 0D integration is negligible. Hence, the small error in Figure 2.7 is due to the difference between flow rate at the inlet and outlet of the 3D model. From this figure, the error is proportional to the time derivative of the flow rate. The norm of the mass conservation error, i.e. the difference between the inlet and outlet flow rates is $100 \left\| \frac{Q_{\text{i}}-Q_{\text{o}}}{Q_0} \right\|$, equal to 0.024%.

2.4.2 Closed-loop cylinder model

In this second example both the inlet and outlet of the cylinder are coupled Neumann boundaries. The heart model along with the other blocks of the LPN is shown in Figure 2.8. Flow is initiated in the 3D model by the pressure difference produced by the heart model in the LPN. As described in [16] the following relation is assumed between atrial volume, V_a, electrical activation, $A_{\text{a}}(t)$, and atrial pressure, P_{a},

$$P_{\text{a}} = A_{\text{a}}E_{\text{a}}(V_{\text{a}} - V_{\text{a}_{\text{u}}}) + P_{\text{a}_0}(e^{K_{\text{a}}(V_{\text{a}}-V_{\text{a}_{\text{u}}})} - 1) \tag{2.42}$$

Table 2.1: Figure 2.8 parameters values. $\hat{R}$ are non-linear resistances modeling the heart valves.

Block	Parameter	Value	Unit
Artery	R	0.05	mmHg s/ml
	C	0.02	ml/mmHg
	L	0.004	mmHg s^2/ml
Capillary	R	5.00	mmHg s/ml
	C	0.20	ml/mmHg
Vein	R	0.09	mmHg s/ml
	C	1.00	ml/mmHg
Atrium	$\hat{R}$	4×10^{-4}	mmHg s^2/ml^2
	E_{a}	7.35	mmHg/ml
	$V_{\mathrm{a_u}}$	1.0	ml
	$P_{\mathrm{a_0}}$	0.17	mmHg
	K_{a}	0.484	1/ml
Ventricle	R	0.09	mmHg s/ml
	$E_{\mathrm{v_1}}$	18.5	mmHg/ml
	$E_{\mathrm{v_2}}$	-0.042	mmHg/ml^2
	$V_{\mathrm{v_u}}$	4.0	ml
	$P_{\mathrm{v_0}}$	0.9	mmHg
	K_{v}	0.062	1/ml
Aorta	$\hat{R}$	4×10^{-5}	mmHg s^2/ml^2
	C	0.1	ml/mmHg

$A_{\mathrm{a}}(t)$ is modeled with a sinusoidal function which is non-zero during atrial contraction and E_{a}, $P_{\mathrm{a_0}}$, K_{a}, and $V_{\mathrm{a_u}}$ are constants of this model. The same model is used for the ventricle, except the first term in Equation (2.42) that models systole, is replaced with a parabolic function,

$$P_{\mathrm{v}} = A_{\mathrm{v}}[E_{\mathrm{v_1}}(V_{\mathrm{v}} - V_{\mathrm{v_u}}) + E_{\mathrm{v_2}}(V_{\mathrm{v}} - V_{\mathrm{v_u}})^2] + P_{\mathrm{v_0}}(e^{K_{\mathrm{v}}(V_{\mathrm{v}} - V_{\mathrm{v_u}})} - 1). \tag{2.43}$$

Equations (2.42) and (2.43) relate the pressures and volumes of heart chambers. Nonlinear resistances are incorporated into the heart model to account for the pressure drop caused by turbulence in the aortic and tricuspid valves. The parameter values of the heart model and the rest of LPN are shown in Table 2.1.

The 0D/3D coupled system was solved using 331,636 elements in the 3D domain, for 2.4 seconds (3 cardiac cycles), with a time step size of 2.4 ms. The pressures at certain points in the LPN, including the coupled surfaces, are shown

in Figure 2.8. The interaction between the aortic capacitor in the 0D domain with the fluid inertia in the 3D domain causes aortic pressure oscillations. As expected, this pressure oscillation is damped following the resistive element representing the capillaries. In Figure 2.9 a snapshot of pressure and velocity contours is shown for this simulation at $t = 1.1T$.

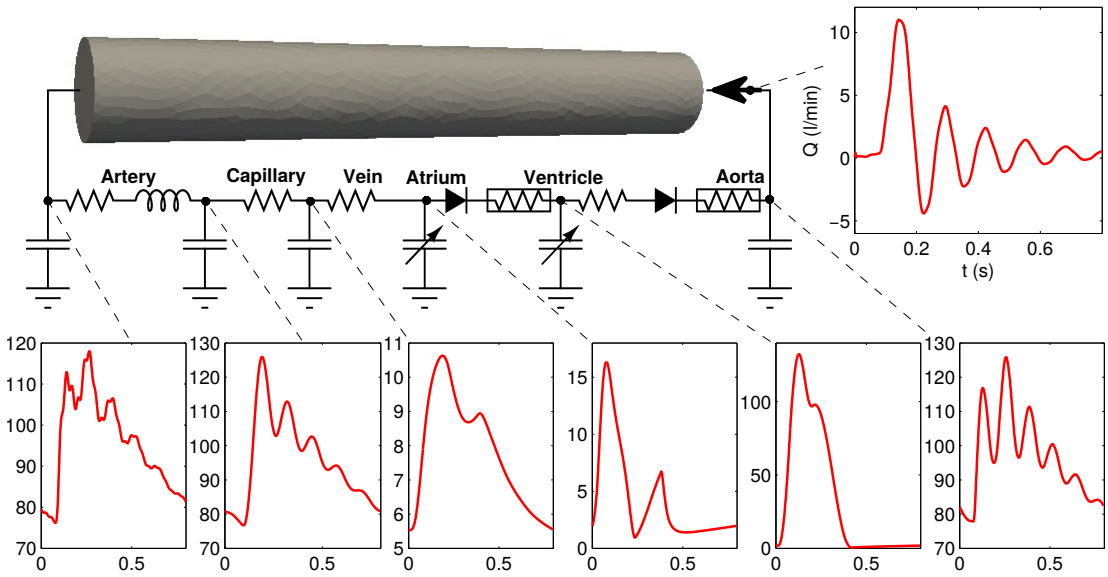

Figure 2.8: LPN for the coupled cylinder case. This hypothetical model includes 6 blocks for the systemic artery, capillaries, veins, atrium, ventricle, and aorta. The pressure of certain points in mmHg versus time is plotted. The flow rate at the inlet of the cylinder is also plotted.

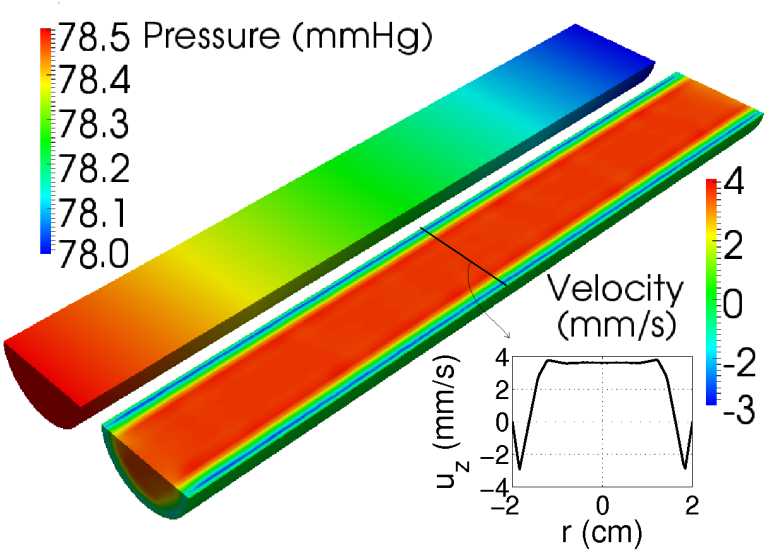

Figure 2.9: Contours of pressure and velocity along the cylinder axis of the LPN shown in Figure 2.8 during flow acceleration ($t = 1.1T$). The velocity profile for the coupled Neumann boundaries is not imposed, but is a part of the solution. We confirm that the velocity has developed into a Womersley profile with forward flow at the center and backward flow at regions close to the cylinder wall, typical of high Womersley numbers (here 28.8).

The results in Figure 2.8 correspond to the last cycle of a three cycle simulation. The pressure-volume loop of the heart chambers for all the three cycles is shown in Figure 2.10. As shown in this figure, the difference between the second and third cycles is less than the first and second cycles. In this case, due to the accurate initialization of the unknowns in the 0D domain, a few cycles are sufficient to obtain a periodic solution.

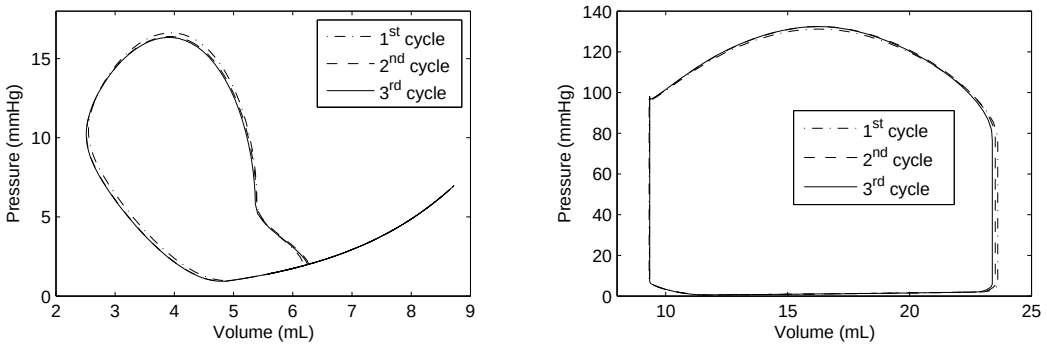

(a) (b)

Figure 2.10: Atrium (a) and ventricle (b) pressure-volume loops for the LPN shown in Figure 2.8. Convergence of the heart model with number of simulated cardiac cycles is shown in this figure.

2.4.3 Comparison of the Neumann and Dirichlet coupled boundary approaches

To compare the use of Neumann and Dirichlet coupling methods in terms of stability, accuracy, mesh sensitivity, and computational cost, we consider the coupled model shown in Figure 2.8. For the coupled Neumann BCs, we use the model as shown. For the Dirichlet case, to obtain a stable algorithm, we modify the model to include inductors at both the inlet and outlet of the cylinder. For this case, Equation (2.40) is used to account for the average pressure from the 3D domain in the 0D domain.

As shown in Tables 2.2 and 2.3, the effect of time step size and mesh size are studied and compared for the coupled Neumann and Dirichlet models. For the Neumann cases, the stability of simulations without backflow treatment (i.e. $\beta = 0$) and the effect of including $\boldsymbol{M}$ (Equation (2.31)) in the formulation (i.e. I/SI/E) is studied further. Here, the explicit method (E) neglects the contribution of $\boldsymbol{M}$ in the LHS matrix, the semi-implicit method (SI) evaluates $\boldsymbol{M}$ only once at the beginning of the simulation, and the implicit method (I) updates $\boldsymbol{M}$ at each iteration in each time step. A simulation with 331,636 elements, a time step of 0.1 ms, and $\beta = 0.2$ of each corresponding case serves as the reference case in these

tables. The results are not reported for the unstable cases.

Table 2.2: The effect of time step size, left hand side contribution ($\boldsymbol{M}$ in Equation (2.31)), stabilization coefficient, and mesh size on the stability and accuracy of the coupled Neumann boundary case. Results of the diverged cases are shown by a dash. Δt: 3D solver time step size in millisecond, I/SI/E: Implicit/Semi-Implicit/Explicit, nEl: Number of elements, β: backflow stabilization coefficient, nIt: Average number of nonlinear iteration needed to reduce second norm of residual to less than 10^{-3}, $\mathrm{t_{sim}}$: Total simulation time in a parallel 8× 2.8 GHz processors machine in minutes. $err = 100\frac{\|Q-Q_{\mathrm{ref}}\|_2}{\|Q_{\mathrm{ref}}\|_2}$: Normalized aortic flow rate error, as compared to the reference case in percent.

Case	Δt	I/SI/E	β	nEl	nIt	$\mathrm{t_{sim}}$	err
N1	1.6	I	0.2	24450	9.1	19.5	7.81
N2	1.6	SI	0.2	24450	9.1	16.3	7.81
N3	1.6	E	0.2	24450	10.2	18.2	7.81
N4	6.4	I	0.2	24450	30.6	16.1	9.83
N5	6.4	SI	0.2	24450	30.1	13.4	9.83
N6	6.4	E	0.2	24450	-	-	-
N7	0.4	SI	0.2	24450	6.3	45.6	8.20
N8	0.4	SI	0.2	109547	5.0	158.4	2.26
N9	0.4	SI	0.2	331636	4.6	438.5	1.10
N10	6.4	SI	0.0	24450	31.3	14.1	20.2
N11	0.4	SI	0.0	24450	-	-	-
N12	0.4	SI	0.0	331636	-	-	-

Table 2.3: The effect of time step size and mesh size on the stability and accuracy of the coupled Dirichlet boundary case. See Table 2.2 for abbreviations.

Case	Δt	nEl	nIt	$\mathrm{t_{sim}}$	err
D1	32	24450	8.0	0.73	12.6
D2	6.4	24450	6.2	2.68	3.80
D3	1.6	24450	6.0	10.5	3.27
D4	0.4	24450	6.0	42.7	3.47
D5	0.4	109547	4.6	146	0.61
D6	0.4	331636	4.0	389	0.16

The results of these two tables suggest:

1. The accuracy of the coupled Neumann case is independent of the contribution of $\boldsymbol{M}$ to the tangent matrix as expected.

2. The stability and convergence rate of the coupled Neumann case is improved by switching from the explicit to the semi-implicit. But there is no further improvement gained from switching to an implicit method. This indicates that the time-accumulated contribution of the nonlinear 0D components in a cardiac cycle is negligible compared to the linear components.

3. Using a semi-implicit method can reduce computational cost by improving convergence. However due to the excessive cost of evaluating $\boldsymbol{M}$ at each iteration, the implicit method is not cost effective.

4. In contrast to the coupled Dirichlet case, the time step size should be limited for the coupled Neumann case to avoid instabilities due to backflow.

5. The stabilized boundary formulation is essential for stability of the Neumann boundaries, especially for smaller time step or mesh sizes.

6. Fewer elements are required to obtain a mesh independent solution for the coupled Dirichlet case as compared to the coupled Neumann case.

7. The coupled Dirichlet case has better convergence rates at larger time step sizes, which is consistent with its lower computational cost.

Combining these observations, we conclude that the Dirichlet BC is the least costly approach, but has the drawback of requiring additional information or assumptions about the velocity profile at the coupled surfaces.

2.4.4 Single ventricle multidomain model

In the third example, the first stage surgical anatomy of a hypoplastic left heart syndrome patient, described in Chapter 1, is modeled using a multidomain approach. The LPN along with the MBTS anatomy is shown in Figure 2.11. In this LPN, there is only one functional ventricle and it is used to pump blood to the aorta. A shunt is inserted between the brachiocephalic artery and the PA to supply blood to the lungs. The diameter of the shunt, which should be chosen properly to maintain the ratio of systemic to the pulmonary blood flow at an optimal value, is

3.5 mm in this case study. The AA, RPA, RCCA, and RCA diameters are 10, 5, 3, and 2.5 mm, respectively. To account for the effect of intra-myocardial pressure on the coronary perfusion, the distal end of the capacitor between CB and CA2 is connected to the ventricular pressure. With in the current framework, other LPNs can also be used to model coronary circulation [78].

The 3D model is meshed with tetrahedral elements. For the interior, four mesh sizes of 1.0, 0.8, 0.625, and 0.5 mm are selected, that produce approximately 130K, 210K, 400K, and 700K tetrahedral elements, respectively. The mesh size for the coronary artery wall is 40% of the interior mesh size and the mesh size for the rest of the walls is 80% of the interior mesh size. After simulating five cardiac cycles, the differences between the cardiac output with the first three meshes and the last mesh (most refined one) are 2.91%, 0.793%, and 0.524%, respectively. Based on these results, an interior mesh size of 0.625 mm is chosen for this study, which produced a mesh with approximately 400K elements. This example follows previous work of Migliavacca et al, and the parameters in the 0D domain are tuned based on physiological data obtained from a typical set of patients (see Appendix B for LPN values) [16].

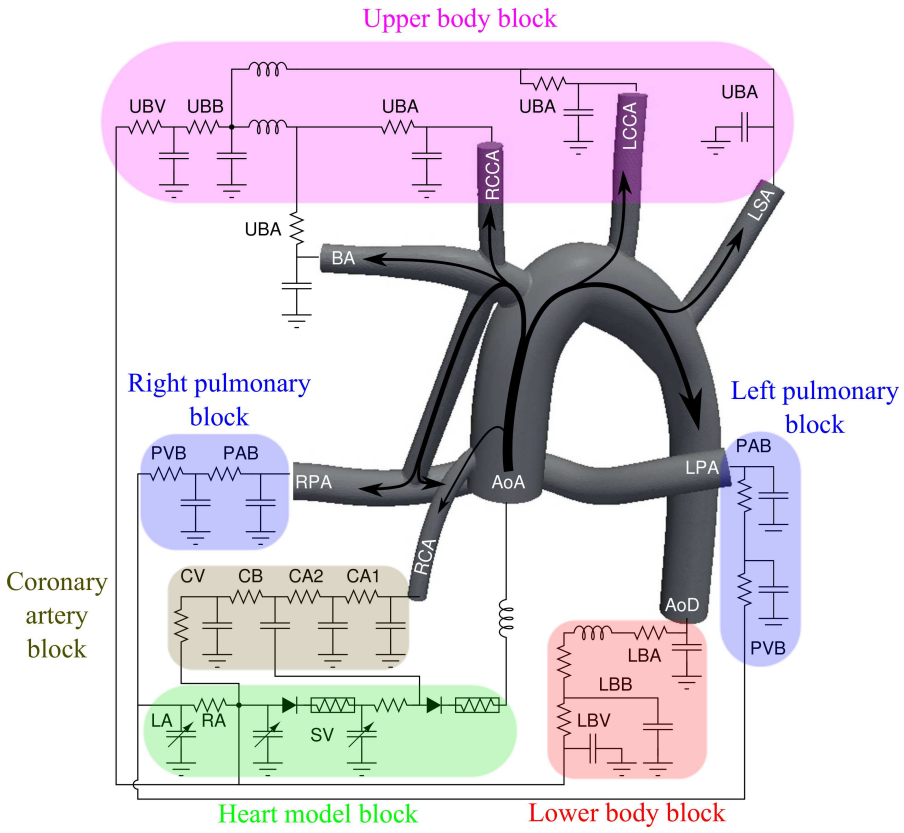

Figure 2.11: The LPN coupled to the geometry with MBTS anatomy. This LPN contains blocks for the upper body arteries (UBA), upper body capillary bed (UBB), upper body veins (UBV), PA bed (PAB), pulmonary vein bed (PVB), lower body arteries (LBA), lower body capillary bed (LBB), lower body veins (LBV), two coronary artery (CA1, CA2), coronary capillary bed (CB), coronary veins (CV), left atrium (LA), right atrium (RA), and single ventricle (SV). The AA, descending aorta (AoD), brachiocephalic artery (BA), right common carotid artery (RCCA), left common carotid artery (LCCA), left subclavian artery (LSA), left PA (LPA), right PA (RPA), right coronary artery (RCA) are shown in the 3D model. Note the left coronary artery, which is omitted here to make the schematic less crowded, is connected to an LPN block identical to that of the right coronary artery. Also note, the inertance connected to the AA is replaced by a capacitor if Neumann BC is imposed at the AA.

Since all coupled boundaries, including AA, are adjacent to capacitors, we use coupled Neumann BCs with a semi-implicit approach for all coupled surfaces. This model is meshed with 400,936 elements. Since all coupled boundaries of the MBTS model exhibit significant backflow during part of the cardiac cycle, these

simulations require backflow stabilization, and we set $\beta = 0.2$.

The resulting pressure and flow rate of the coupled surfaces are shown in Figure 2.12. As expected, the results predict a lower pressure for the pulmonary branches compared to the systemic side. In contrast to the other branches, the coronary flow waveform has a second peak in diastole. There is significant backflow in the brachiocephalic and right common carotid arteries due to the shunt flow, which reduces the diastolic pressure in these branches.

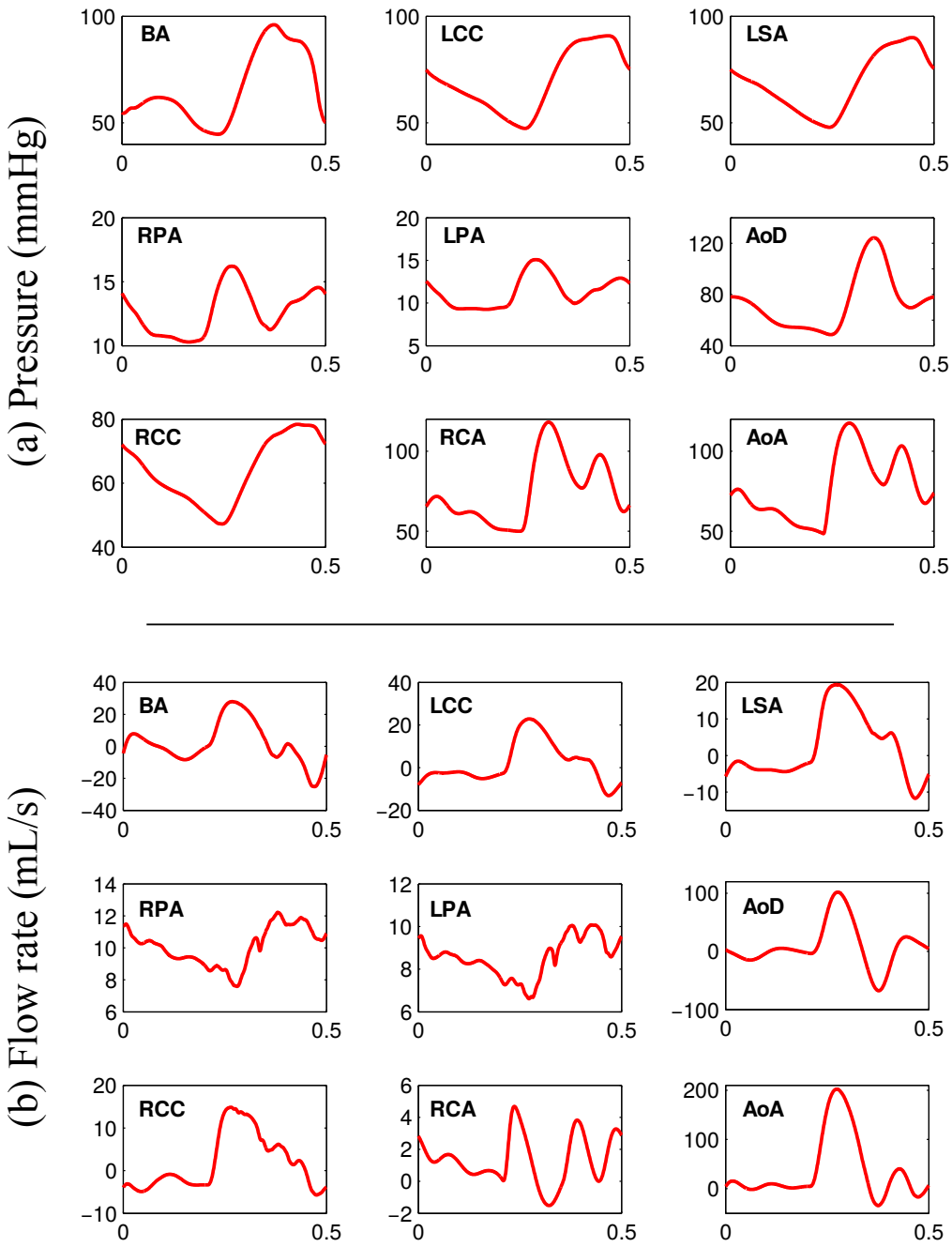

Figure 2.12: Pressure (a) and flow rate (b) plots for the LPN shown in Figure 2.11 for the coupled surfaces. Pressure plots are in mmHg versus time in seconds. Flow rate plots are in mL/s versus time in seconds.

To see the interaction of the two domains, the ventricular pressure-volume loop of three simulations with 3.0, 3.5, and 4.0 mm shunt (using the LPN and

model shown in Figure 2.11) is shown in Figure 2.13. The 4.0 mm shunt diverts more blood to the pulmonary bed, which has a lower resistance compared to the systemic bed. Therefore, this geometry has lowest total resistance seen by the heart, which leads to the largest stroke volume, and hence the highest cardiac output. This example demonstrates the necessity of a coupled simulation for these types of case studies.

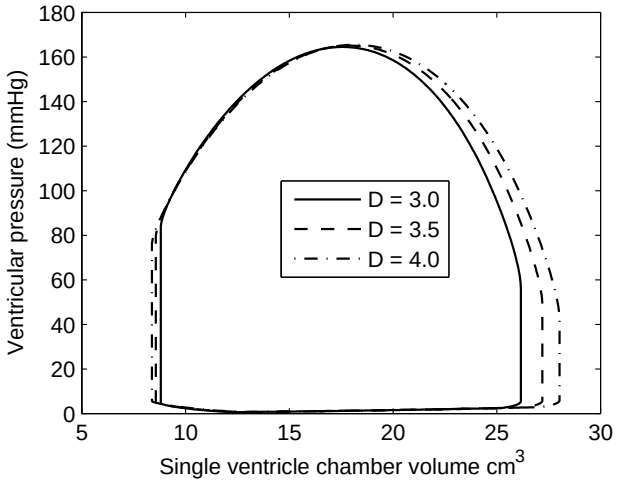

Figure 2.13: Ventricular pressure-volume loop of the LPN shown in Figure 2.11 with three different shunt sizes.

To compare the computational cost of the multidomain method with monolithic BCs, we also performed a simulation with the same geometry and resistance BCs. The resistance values are tuned to obtain the same average pressure at the outlets as the multidomain simulation. The LPN is replaced with resistance BCs at the outlets and a prescribed uncoupled velocity, which is duplicated from the multidomain simulation results, at the inlet of the AA. Comparing the computational costs of two methods for pure resistance BCs, the partitioned approach cost 9% more. However, comparing to the simulation with Windkessel BCs, the partitioned approach cost 9% less (44 min versus 48 min). These small differences indicate a negligible difference in cost between the proposed partitioned and monolithic approaches. The number of nonlinear iterations per cycle was almost the same (0.3% difference in number of iterations), which indicates insignificant

differences between the two approaches.

For the original simulation with LPN shown in Figure 2.11, five cardiac cycles were simulated with an average of 7.5 iterations per time step. This required 7,503 iterations per cycle in total, which took 38 min/cycle on a parallel 48 $\times$ 2.4 GHz processor cluster. Comparing these values to the case with pure resistance BCs using a monolithic approach, the LPN simulation required 22% more iterations per cycle, while each cycle cost 55% less overall. This is because the multidomain problem has a tangent matrix with a lower condition number, which reduces the number of internal LS iterations, reducing its overall cost.

This example suggests the presented method can be used with multiple outlets and a complicated LPN with no significant additional computing cost. The semi-implicit implementation of the coupled Neumann boundaries formulation inside the iterative loop resulted in a stable solution with a time step size that is an order of magnitude higher than previous work, in which a similar problem was studied [25].

2.5 Discussion

The multidomain approach presented in this chapter provides both detailed hemodynamic information in the 3D domain of interest, and global hemodynamic information in the circulatory system. We have presented a modular and flexible framework for coupling 3D FE simulations to LPN models for cardiovascular simulation. In this framework, one can use either Dirichlet or Neumann coupled BCs, depending on the type of LPN model employed. This method can be applied in a range of patient specific blood flow simulations, in which global information about circulatory dynamics is required. A separate numerical solver for the LPN, with a specific protocol for passing pressure and flow information at the boundaries, enables convenient implementation for legacy solvers in which the LPN can be changed or reconfigured without recompiling the 3D solver code.

Depending on the type of nonlinear elements in the 0D model, time step sizes, and other numerical parameters, either an implicit, semi-implicit, or explicit

coupling approach can be used. Based on our results, the semi-implicit approach seems the most attractive choice, since it provides a more stable, yet cost-effective solution. In the explicit approach, a less costly scheme can be obtained that does not change the non-zero pattern of the sparse tangent matrix. However, this proves to be less stable with a lower convergence rate that increases the overall cost. By including only the diagonal part of $\boldsymbol{M}$ in the tangent matrix, which is generally a good approximation of the full matrix, we obtain a system of equations with good convergence. In doing so, off-diagonal elements of $\boldsymbol{M}$ that would decrease the sparsity of the tangent matrix and complicate parallelization of LS are neglected. Implementation of this approach requires only minor modifications to a Navier-Stokes solver in which simple BCs such as resistance models are already implemented with a monolithic approach. Note that for these coupled Neumann boundaries, backflow stabilization allowed us to perform this coupling, where other methods may cause simulation divergence [59].

Conservation of mass can be directly satisfied through the external surfaces (via 0D domain), if the coupled Dirichlet BC is imposed for all the external surfaces. Implementation of this method does not not require any changes to the 3D solver, compared to a classic Dirichlet BC other than passing the flow rate and pressure information. Comparing this approach with the Neumann approach we obtained improved convergence rates and stability, independent of the time-step size. On the other hand, the Dirichlet BC approach requires knowledge of the velocity profile, which is not usually available. This requires an assumption that may change the local velocity solution and possibly the pressure field in the entire domain.

Use of a multidomain method enables prediction of important hemodynamic parameters in the entire circulatory system that can be relevant to clinical decision making and surgical planning. One example is selecting between surgical options for single ventricle patients, in which prior explicitly coupled version of this method proved to be important for clinical applications [25, 26, 79]. In addition, the combination of this type of multidomain simulation with formal design optimization methods provides a powerful tool that can assist in surgical planning, while accounting for the changing dynamic response of the heart and cardiovascular

system [80].

Although, in comparison with 1D/3D coupling, the 0D/3D coupling cannot predict wave propagation, it is the only feasible option for modeling vessels outside of the 3D domain with no available geometrical information, as is often the case in image-based modeling. However we note that, the same implicit modular approach described in this work could be used for 1D/3D coupling.

Also, the dynamic response of an LPN can be modified to incorporate non periodic phenomena [29] and auto-regulatory mechanisms [81] to model exercise conditions. Due to the lack of available clinical data, specifying parameter values in an elaborate LPN is a challenging issue [82], and usually restricted to Windkessel type models [83, 84, 85].

Acknowledgements

The authors wish to thank Tain-Yen Hsia for providing the clinical impetus for the present work, Giancarlo Pennati, Francesco Migliavacca, and Sethuraman Sankaran for sharing their expertise in the LPN modeling. This chapter, in full, is a reprint of the material as it appears in A modular numerical method for implicit 0D/3D coupling in cardiovascular finite element simulations in *Journal of Computational Physics*, 224, 63-79, 2013. Authors are M. Esmaily-Moghadam, I. Vignon-Clementel, R. Figliola, and A. Marsden. The dissertation author was the primary investigator and author of this paper.

Chapter 3

Methods for Prevention of Backflow Divergence

The occurrence of backflow divergence is a well-known but not sufficiently addressed problem in the field of cardiovascular flow simulation. This problem usually arises in large vessels that are exposed to backflow in 3D and 2D flow simulations. There are three main situations that lead to numerical divergence caused by backflow. First, backflow divergence can result from bulk reversal of the flow through an outlet, such that there is negative flow over the entire outlet face. Second, there may be localized areas of flow reversal on an outlet face with bulk outward positive flow. And third, the use of multiscale modeling (e.g. using closed-loop lumped parameter 0D models [26, 86], or 1D models [87, 53, 29, 54] coupled to the 3D model) may necessitate the passing of pressure and flow information for which there is a lack of velocity profile information, leading to numerical instabilities on either the coupled inflow or outflow faces. All of these numerical instabilities emanate from the use of Neumann BCs on the outlet faces, for which velocity profile information is not specified [88, 47, 89].

Bulk backflow (complete flow reversal at an outlet) is a physiologic and commonly occurring phenomenon in the cardiovascular system in both healthy and diseased states. It often occurs in vessels during diastole and flow deceleration, particularly in certain regions. Thus, accurately capturing backflow phenomenon is essential for reproducing realistic conditions in many cardiovascular problems.

Examples of physiologic flow reversal include flow in the descending abdominal aorta during diastole [28, 29], flow reversal in the brachiocephalic artery after the stage 1 repair for single-ventricle heart patients (as was observed in the MBTS simulation in Chapter 2) [25] and reversed flow due to respiratory effects in Fontan patients [90].

Backflow divergence due to local flow separation or flow recirculation is commonly caused by complex geometries such as the presence of stenosis, anastomoses, or increased cross sectional area, near the outlets of a model. These geometric features often lead to either steady or unsteady separation regions close to the outflow faces of a model, particularly at peak systolic flow. Similarly, geometric features can also lead to vortex shedding, and convection of vortices through the outflow faces, also leading to backflow divergence.

Multiscale modeling, in which a closed-loop lumped parameter network of ODEs is coupled to the inflow and outflow faces, usually requires Neumann BCs on both inflows and outflows. As we observed in Chapter 2, in these situations, it is common that flow reversal is dictated by the pressure passed to the 3D model, causing a bulk inward flow without prescribing velocity profile information. In these situations, instabilities can occur, particularly in cases with rapidly changing dynamics that may alternate between positive and negative flow within a cardiac cycle.

Simulation divergence due to the above causes, for either total or partial flow reversal on an outlet face, requires careful consideration of the outflow BCs. Since it is assumed that the inflow BC is given, altering the inlet flow wave form to prevent backflow is not considered to be a viable solution [91, 92]. Use of a mixed BC [93, 94], in which a Dirichlet BC is used for the normal component of the velocity (either on the entire outlet or only in the region with backflow) along with a Neumann BC for tangential velocity components, requires extra information about the velocity profile and the flow rate magnitude, which is generally unknown for the outlets.

The simplest solution to the backflow issue is to artificially elongate the outlets by adding long straight sections, thereby dissipating the vortices before they

reach the outlet. While this has been commonly used in simulations [69, 32, 95] this method poses several major problems. First, it cannot be used as a solution for the case of total flow reversal at the outlet due to conservation of mass. Second, the addition of artificial extensions to the outlets has potential to change local hemodynamics, particularly in patient specific models or in multiscale modeling networks, where information as the boundary faces are coupled. And third, there is a non-negligible additional computational cost incurred by the need to mesh and simulate long outlet extensions. This added cost increases for high Reynolds number flows, since longer extensions will be needed to dissipate the vortices. Another option is to add additional vessels to the model until the flow becomes unidirectional and the Reynolds number at the outlet is reduced [96]. While this method has proven to be effective in patient-specific cases, it can only be used in a non-artificial way if the image resolution is adequate enough to permit inclusion of additional levels of branching. Additionally, this method increases the model generation and computational costs significantly. Due to these issues, we will not consider outlet extensions or additional branches as viable methods in this chapter.

Apart from model extensions, there are three alternate methods currently in use for solving the issue of backflow divergence in FE solvers.

1. Modifying the weak formulation by adding a backflow stabilization term for the Neumann boundaries [30].

2. Confining the backflow velocity to a desired direction, e.g. normal direction.

3. Using Lagrange multipliers for constraining the velocity profile to an assumed form [27].

The issue of backflow divergence has been addressed in previous work of Kim et al [27]. However, a thorough and quantitative comparison of these three methods using a single code has not been previously performed. In this chapter we present a detailed comparison of these methods and compare their impact on the flow physics, computational cost, implementation effort, and robustness. The weak formulation is presented and then the modified formulation is discussed for each method. To produce an accurate comparison between the three methods,

identical solver numerics, meshes, fluid properties, and inflow BCs are used. The three backflow treatment methods are illustrated using three model problems which have relevance to blood flow simulation, as well as other internal flow problems in CFD, such as combustion simulations and duct flows.

First, a classic cylindrical expansion is studied with two exit lengths and two Reynolds numbers. This illustrates the case of backflow due to a localized steady separation region. Second, a 90-degree bend is studied with a physiologic unsteady inlet flow wave-form. This illustrates the case of backflow due to an asymmetric outlet velocity profile, as well as diastolic bulk flow reversal. The last case is a patient-specific model of an aorta, for which the untreated simulation diverges due to flow reversal during diastole. For this case, a non-ideal cut of an outlet is also considered to investigate the robustness of the proposed methods.

3.1 Methods for backflow treatment

In this section, we present the numerical formulations of the three methods, based on previous work. The pros and cons of the three methods are as follows.

Outlet stabilization has been proposed by Bazilevs et al. and used previously in cardiovascular applications in [30]. Advantages of this method include accuracy, robustness, ease of implementation, and little to no additional computational cost. Cons of the method are the potential to alter the local flow dynamics due to the addition of an artificial traction component opposite to the direction of the flow. However, as shown in the results section, these effects turn out to be minimal.

Confining the velocity profile to the normal direction is commonly used for stabilization in commercial flow solvers. While it has been effectively used in previous work, it has the obvious disadvantage of directly changing the local flow field if the assumed flow direction is not aligned with the flow. However, by choosing a proper direction, this method can cause little to no artifact in the flow field. The main disadvantages of this method are a lack of stability, as compared with the two other methods, which will be demonstrated in the results section.

Recent progress on backflow stabilization was made through the introduction of the Lagrange multiplier method for constraining the velocity profile of outlets. In the work of Kim et al. [27], this method was shown to have little effect on the local flow field, and effectively stabilize simulations that otherwise diverged. However, potential disadvantages of this method include complexity of implementation, the need for adjustable parameters, and significantly increased computational cost. Our work aims to build on this recent work by offering an alternative through the use of the stabilization method.

The FE framework, described in Section 2.1, is used for discretization of Navier-Stokes equations in space and time and obtaining the linear system of equations.

3.1.1 Outlet stabilization

In this section, we follow the implementation of Bazilevs et al. [30] for the addition of stabilization terms on the outflow boundaries. The weak form in Equation (2.7) is vulnerable to backflow divergence. To obtain a more stable weak form in the regions with backflow, an additional convective traction is added. The parameter β presents a modification to the method proposed in [30]. The original formulation, presented in [30], is equivalent to the current formulation for $\beta = 1$. In this chapter, we present a modification of this method in which a fraction of this term is added, and a more stable method is obtained. From our numerical experience, this coefficient allows us to have a stable solution for larger time-step values compared to the $\beta = 1$ case, when there is significant flow reversal. The stabilization term can be defined as follows

$$\tilde{B}(\boldsymbol{w}, q; \boldsymbol{u}, p) = B(\boldsymbol{w}, q; \boldsymbol{u}, p) - \int_{\Gamma_\mathrm{h}} \beta u_{\mathrm{n\_}} \rho \boldsymbol{w} \cdot \boldsymbol{u} \mathrm{d}\Gamma, \tag{3.1}$$

where β is a positive coefficient between 0.0 and 1.0. For small values of β, this method is less intrusive and also stable in numerical experiments over a larger

range of time steps. In Equation (3.1), u_{n_-} is defined as,

$$u_{\mathrm{n}_-} \equiv \frac{1}{2}\left(\boldsymbol{u}\cdot\boldsymbol{n} - |\boldsymbol{u}\cdot\boldsymbol{n}|\right) = \begin{cases} \boldsymbol{u}\cdot\boldsymbol{n} & \boldsymbol{u}\cdot\boldsymbol{n} < 0 \\ 0 & \boldsymbol{u}\cdot\boldsymbol{n} \geq 0. \end{cases} \tag{3.2}$$

Considering the weak form of Equation (2.30), since the $-\beta u_{\mathrm{n}_-}\boldsymbol{u}\cdot\boldsymbol{u}$ term is always positive, the energy dissipation added by this term is proportional to the degree of backflow velocity. In physical terms, the added term in Equation (3.1) is an outward traction, opposite the direction of backflow, which pushes the flow in the direction of the outward normal (Figure 3.1). In this sense, this term provides the *missing* convective flow information from outside of the computational domain during flow reversal.

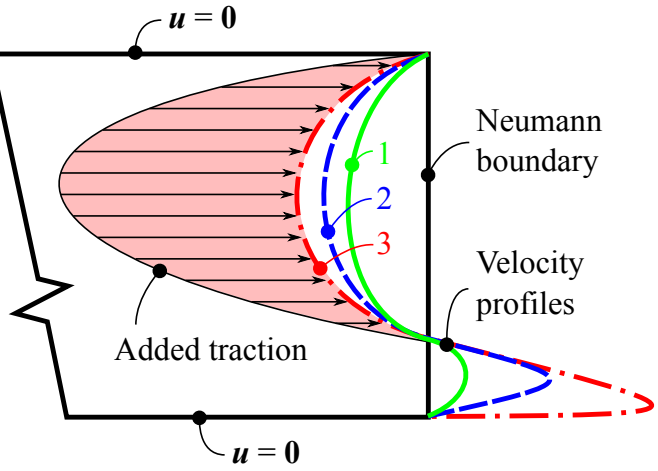

Figure 3.1: Schematic of a 2D model with backflow at a Neumann boundary. Three velocity profiles (green/solid, blue/dashed, and red/dot-dash) are shown with different levels of reversal flow, but similar net-flow. All three profiles can satisfy conservation of mass, causing the flow to become unstable as it transitions from green toward red profile. This issue is resolved by adding an outward traction proportional to the inward velocity.

3.1.2 Normal velocity constraint

In this method, the velocity is constrained to be in a particular direction, e_i, which is usually set to the surface normal direction. Therefore, a zero Dirichlet velocity is imposed for the tangential directions. Although the normal velocity

BC formulation can be found in standard FE text books [97], we have included the formulation here for the sake of completeness. The momentum equation of the outlet nodes is modified such that the two tangential velocity components are zero, but the momentum equation is unchanged in the normal direction. Let us define a rotation matrix $\boldsymbol{T}$ by,

$$\boldsymbol{T} = \begin{bmatrix} \boldsymbol{t}_1 \\ \boldsymbol{t}_2 \\ \boldsymbol{t}_3 \end{bmatrix}, \tag{3.3}$$

where $\boldsymbol{t}_2$ and $\boldsymbol{t}_3$ are the directions orthogonal to the vector $\boldsymbol{t}_1$. To confine the velocity in the normal direction, $\boldsymbol{t}_1$, $\boldsymbol{t}_2$ and $\boldsymbol{t}_3$ in Equation (3.3) are simply replaced by $\boldsymbol{n}$ and its orthogonal vectors. Multiplying Equation (2.14) by $\boldsymbol{T}$ in the element level rotates it to the normal and tangential coordinates. From Equation (2.14), for node b at the outlet surface we have

$$T^{ij} k^{ab,jk} T^{lk} T^{lp} y_{\mathrm{u}}^{b,p} + T^{ij} g^{ab,j} y_{\mathrm{p}}^{b} = -T^{ij} r_{\mathrm{m}}^{a,j}, \tag{3.4}$$

where $\boldsymbol{k}$ and $\boldsymbol{g}$ are element stiffness matrices and $\boldsymbol{r}_{\mathrm{m}}$ is the momentum element residual vector, obtained from local assembling of Equations (2.18) and (2.10). To eliminate tangential components of $T^{ij} y_{\mathrm{m}}^{b,j}$, the stiffness matrices and residual vector are replaced by

$$\begin{aligned} \tilde{k}^{ab,ij} &= T^{\hat{i}k} k^{\hat{a}\hat{b},kl} T^{\hat{j}l} \delta^{\hat{i}\hat{j}} \delta^{\hat{a}\hat{b}}, \\ \tilde{g}^{ab,i} &= T^{\hat{i}j} g^{\hat{a}\hat{b},j} \delta^{\hat{i}1} \delta^{\hat{a}\hat{b}}, \\ \tilde{r}_{\mathrm{m}}^{a,i} &= T^{\hat{i}j} r_{\mathrm{m}}^{a,j} \delta^{\hat{i}1}. \end{aligned} \tag{3.5}$$

where δ^{ij} is the Kronecker's delta, equal to one for $i = j$ and zero for $i \neq j$. There is no summation over the indices with the hat notation, e.g. $\hat{i}$.

Substituting Equation (3.5) into (3.4) and multiplying by $\boldsymbol{T}^{\mathrm{T}}$ to rotate back to original coordinates, we have

$$T^{ji} \tilde{k}^{ab,jk} T^{kp} y_{\mathrm{m}}^{b,p} + T^{ji} \tilde{g}^{ab,j} y_{\mathrm{p}}^{b} = -T^{ji} \tilde{r}_{\mathrm{m}}^{a,j}, \tag{3.6}$$

which can be rewritten as

$$\bar{k}^{ab,ji} y_{\mathrm{m}}^{b,i} + \bar{g}^{ab,j} y_{\mathrm{p}}^{b} = -\bar{r}_{\mathrm{m}}^{a,j} \,:\, b \in \partial_{\mathrm{h}}\Omega, \tag{3.7}$$

so that the modified stiffness matrices, $\bar{\boldsymbol{k}}$, $\bar{\boldsymbol{g}}$, and residual vector, $\bar{\boldsymbol{r}}_{\mathrm{m}}$, are defined by

$$\bar{k}^{ab,ij} = T^{ki}\tilde{k}^{ab,kl}T^{lj},$$

$$\bar{g}^{ab,i} = T^{ji}\tilde{g}^{ab,j},$$

$$\bar{r}_{\mathrm{m}}^{a,i} = T^{ji}\tilde{r}_{\mathrm{m}}^{a,j}. \tag{3.8}$$

By using Equations (3.3)-(3.5) and (3.8), the modified element stiffness matrices and residuals are found from $\boldsymbol{k}$, $\boldsymbol{g}$ and $\boldsymbol{r}_{\mathrm{m}}$ and can be assembled into the global matrices and vector. One might add another requirement of $\boldsymbol{u}^b \cdot \boldsymbol{n}^b < 0$ to Equation (3.7), in order to only effect the nodes with inward velocity (i.e. defining this equation only on $\partial_{h\_}\Omega$). But for this study, we restrict all the nodes on the outlet surface to obtain a more stable and general form. It should be noted that while commercial solvers often have an option for normal velocity constraints, it is impossible to guarantee identical implementation since this information is typically proprietary.

3.1.3 Constraining the velocity profile

The concept of this method is to assume a particular velocity profile, e.g. parabolic, for the outlet and then constrain the solution to converge to this assumption. This is achieved by adding penalties to the residual vector for deviation from this assumption. To this end, the following constraints are enforced using the augmented Lagrange multiplier method as in the work of Kim et al. [27].

$$c_1 = \alpha\left(\boldsymbol{u}\cdot\boldsymbol{n} - \phi, \boldsymbol{u}\cdot\boldsymbol{n} - \phi\right)_{\partial_{\mathrm{h}}\Omega} = 0,$$

$$c_2 = \alpha\left(\boldsymbol{u}\cdot\boldsymbol{t}_2, \boldsymbol{u}\cdot\boldsymbol{t}_2\right)_{\partial_{\mathrm{h}}\Omega} = 0,$$

$$c_3 = \alpha\left(\boldsymbol{u}\cdot\boldsymbol{t}_3, \boldsymbol{u}\cdot\boldsymbol{t}_3\right)_{\partial_{\mathrm{h}}\Omega} = 0, \tag{3.9}$$

where $\boldsymbol{t}_2$ and $\boldsymbol{t}_3$ are tangential surface vectors and $\phi(\boldsymbol{x}, t)$ is the velocity profile to be imposed,

$$\phi = \left(\frac{(\boldsymbol{u},\boldsymbol{n})_{\partial_{\mathrm{h}}\Omega}}{(1,1)_{\partial_{\mathrm{h}}\Omega}}\right)\left(\frac{n+2}{n}\right)\left(1 - (\frac{r}{R})^n\right), \tag{3.10}$$

where n is the velocity profile polynomial order defined by the user, $r(\boldsymbol{x})$ is the distance from the center of the face, and R is the surface radius defined by the user. Also, α which is used to nondimensionalize Equation (3.9) is,

$$\alpha = \frac{(1,1)_{\partial_{\mathrm{h}}\Omega}}{\bar{Q}^2}, \tag{3.11}$$

where $\bar{Q}$ is a user-defined estimate of the average flow rate through the surface. Note that the definition of Equation (3.10) implies the requirement of circular outlet cross sections, although this is not strictly required for use in all problems.

Having c_i from Equation (3.9), a weak form obtained from the following equation is included in the formulation for all the constrained surfaces (see [27]),

$$-\lambda_i c_i + \frac{1}{2}\kappa_i c_i^2 + \sigma_i \lambda_i^2 = 0, \tag{3.12}$$

where λ, κ, and σ are Lagrange multipliers (part of the solution vector), user-defined penalty numbers, and regularization parameters, respectively. The regularization parameters, which are chosen to be small, are used to prevent an ill-conditioned stiffness matrix.

3.2 Backflow treatment test results

The adopted model construction process is described in Section 2.3. Models for the first two cases are idealized and third case is patient-specific. A Dirichlet BC is imposed at the inlet with a parabolic velocity profile in all cases. At the outlet, when a zero traction Neumann BC is imposed, all components of the traction are set to zero, i.e. $h_i = 0$ in Equation (2.5). An implicit method (the coupled multidomain method) is adopted for RCR outlet BCs, in which the derivative of the imposed pressure at each time step is considered in the stiffness matrix [29, 29]. The same number of non-linear iterations are used for all methods. All three methods for outflow treatment were implemented in the same code with identical numerics and meshing, allowing for an *apples-to-apples* comparison of the three methods. The implementation of the Lagrange method used in this work was done by Kim et al., and included in the open source release of the Simvascular package.

For all the case studies, the β value in Equation (3.1) is equal to 0.2. The profile order, i.e. n in Equation (3.10), is equal to 2 for all Lagrange cases, corresponding to a parabolic profile, unless stated otherwise. The penalty numbers, κ, are also set to 10^6, unless stated otherwise. Also, $\boldsymbol{t}_1$ is set to the surface normal vector, $\boldsymbol{n}$, in Equation (3.3).

3.2.1 Cylinder with expansion

The first case study is a cylinder with an expansion, as shown in Figure 3.2. The inlet and outlet diameters are 5 and 10 mm, respectively. The lengths of the inlet and expansion sections are 10 and 5 mm, respectively. Two lengths, 15 and 30 mm, are used for the outlet sections in the short and extended models, respectively. The short and extended models are meshed with 215,910 and 320,157 tetrahedral linear elements, respectively. The results are presented based on the inlet Reynolds number with a steady inflow rate. A zero traction BC is imposed for the outlet. As shown in Figure 3.3, the expansion in cross section produces a recirculation region which causes backflow at the outlet at high Reynolds numbers.

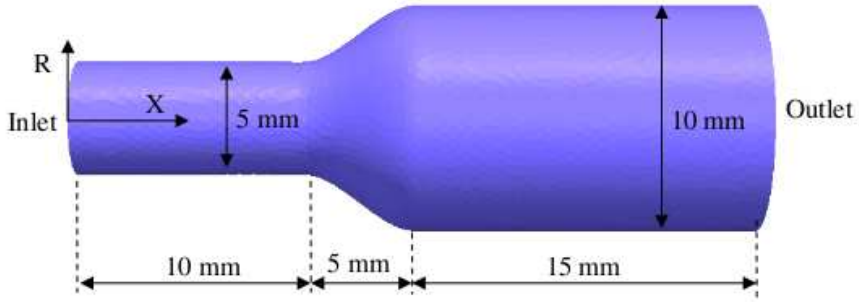

Figure 3.2: Short solid model for first case study with 15 mm outlet section.

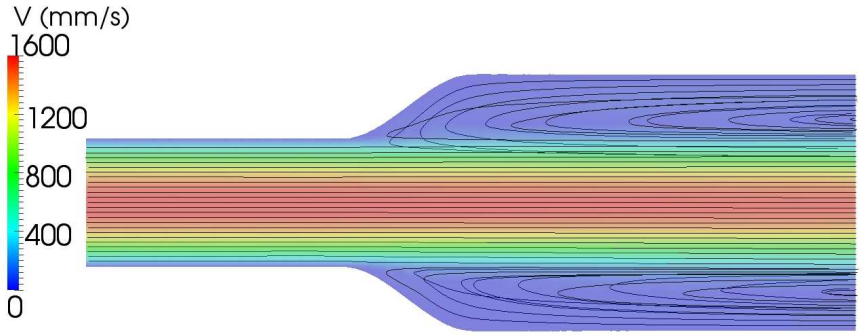

Figure 3.3: Velocity contours and stream lines at Re = 1000 for first case study illustrating stable vortices at the outflow face.

Extended model

This simulation is done with the extended model and an inlet Reynolds number of 1000. At this Reynolds number and model length there is a very small amount of backflow, and the simulation is stable with no boundary treatment. A comparison of simulation results is shown in Figure 3.4 for the no boundary treatment case and the three treatment methods. The pressure and velocity at the centerline and the outlet are plotted in this figure.

We observe that the stabilization and normal constraint method results are very close to the no-treatment case. However, the Lagrange method failed to match to the no-treatment case results. Although this method does not change the velocity in the region far from the outlet (see Figure 3.5), the velocity profile is changed significantly at the outlet, as expected. The changes in the velocity profile at the outlet are responsible for changes in the outlet pressure as well. The reduction of velocity at the center and its increase in the peripheral region requires higher and lower pressure in those areas, respectively, to satisfy the momentum equations. This change in pressure is propagated throughout the model.

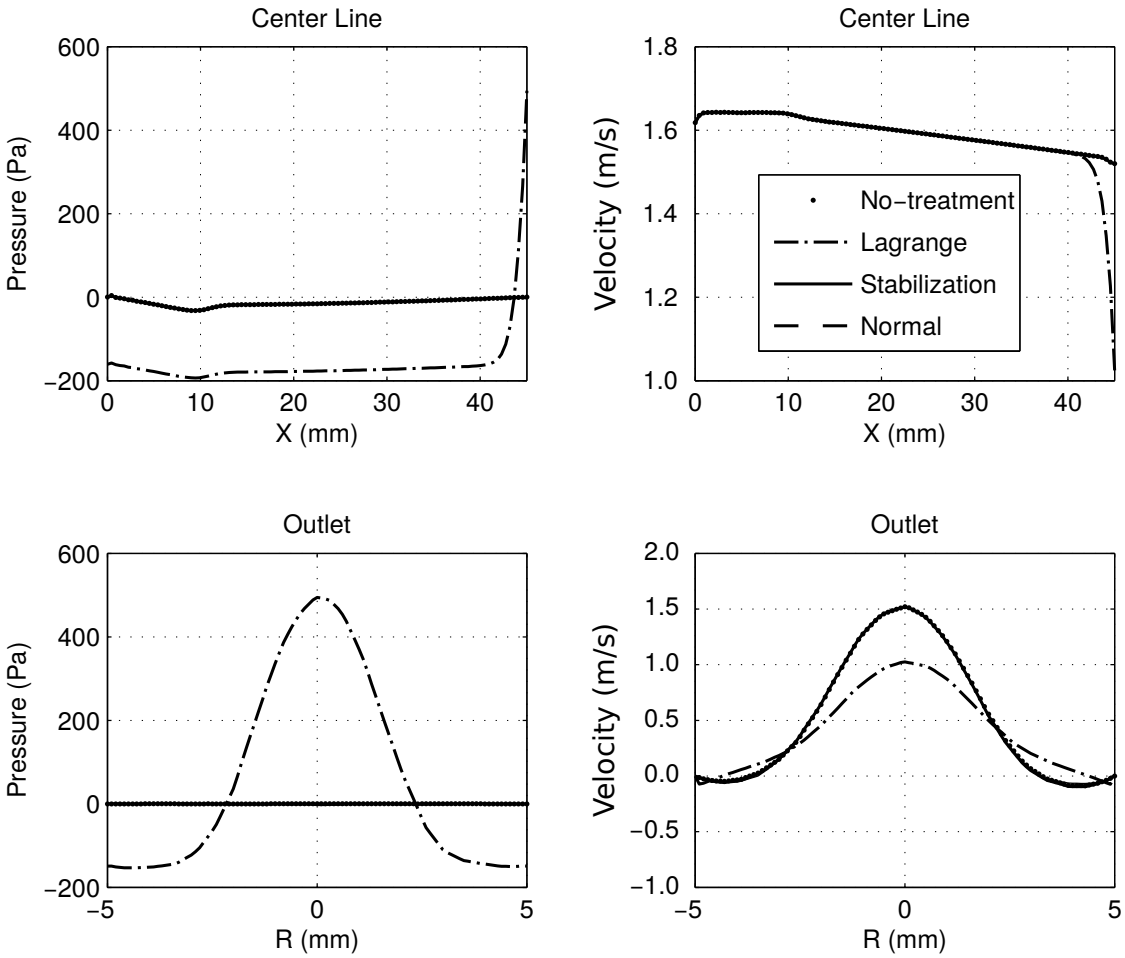

Figure 3.4: Velocity and pressures for the extended model at the centerline and outlet section at Re = 1000

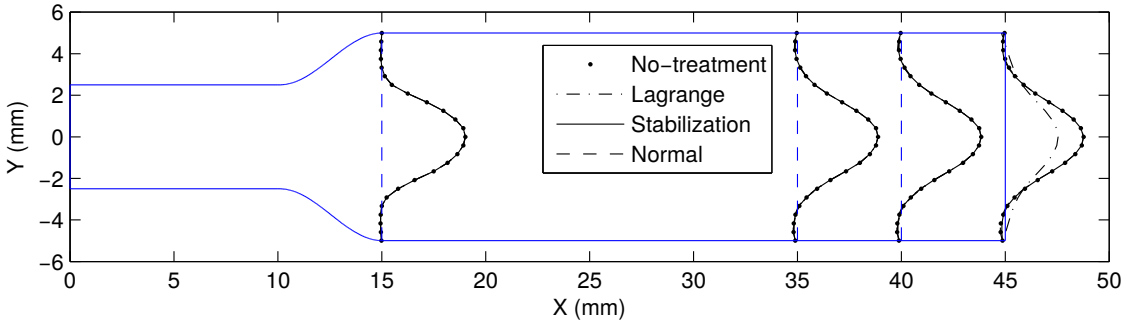

Figure 3.5: Velocity profiles at x=15, 35, 40 and 45 mm in the extended model at Re = 1000.

From Figure 3.4 it is clear that the Lagrange method has a significant effect on the flow physics. To magnify the difference between the normal constraint and the stabilization method, deviation of these methods from the no-treatment case is shown in Figure 3.6 as the percent error. This figure suggests that in this case the stabilization method has a larger impact on the flow than the normal constraint method. This may be a result of the added traction from the stabilization term, which opposes the inward flow.

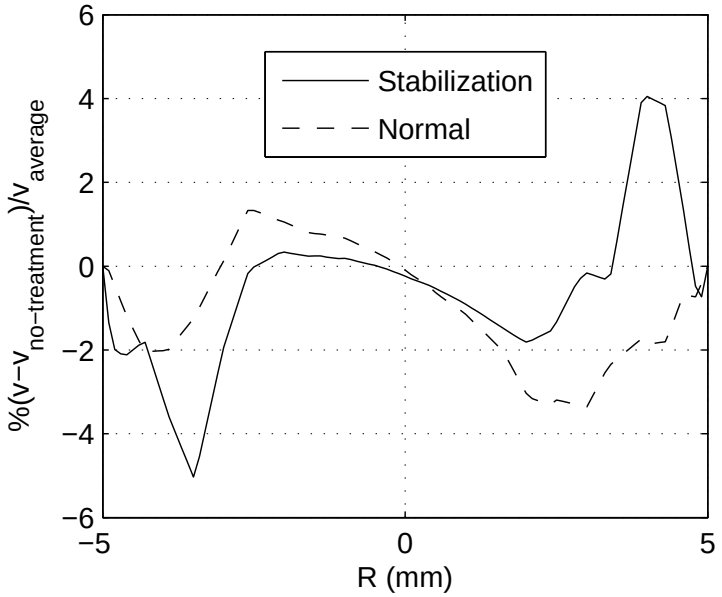

Figure 3.6: Differences in velocity for the normal constraint and stabilization methods compared to no-treatment case at the outlet of the extended model at Re = 1000

To obtain a more global picture of the effect of these methods on the flow, the outlet and inlet energy fluxes and average pressures are tabulated (Table 3.1). Wall time is the parallel simulation time with 8 processors under the same circumstances for all cases. This table also confirms the results shown in Figures 3.4 and 3.6. Comparing the stabilization and normal constraint methods, the normal constraint is slightly less intrusive, but more costly. The Lagrange method has the highest impact on the flow with highest computational cost. Use of a higher profile order in the Lagrange method slightly reduces the effect on the flow physics.

The same is also true for lower penalty numbers, but this will also decrease the robustness of the method.

Table 3.1: Comparison of the average pressure and energy fluxes for all methods with the extended model at Re = 1000. t_{sim} denotes simulation execution in wall clock time.

Methods	t_{sim} (s)	$\bar{P}_{\text{in}}$ (Pa)	$\bar{P}_{\text{out}}$ (Pa)	$\dot{E}_{\text{in}}$ (mW)	$\dot{E}_{\text{out}}$ (mW)	$-\dot{E}_{\text{out}}/\dot{E}_{\text{in}}$ (%)
No-treatment	379	1.90	-0.029	-10.89	8.70	79.9
Stabilization	394	0.26	-0.32	-10.87	8.70	79.9
Normal	399	1.72	-0.284	-10.89	8.69	79.8
Lagrange	537	-160	-63.3	-8.36	5.48	65.6
Lagrange ($n = 5$)	532	-128	-30.4	-8.85	6.01	69.4
Lagrange ($\kappa = 10^5$)	523	-57.1	-26.6	-9.97	7.66	76.8

Short model

The short model with no treatment at a Reynolds number of 1000 is not stable. The results shown in Figure 3.7 are analogous to Figure 3.4. The zero traction BC is not satisfied for the Lagrange method. As expected, the outlet velocity profile for this method is closer to a parabolic profile.

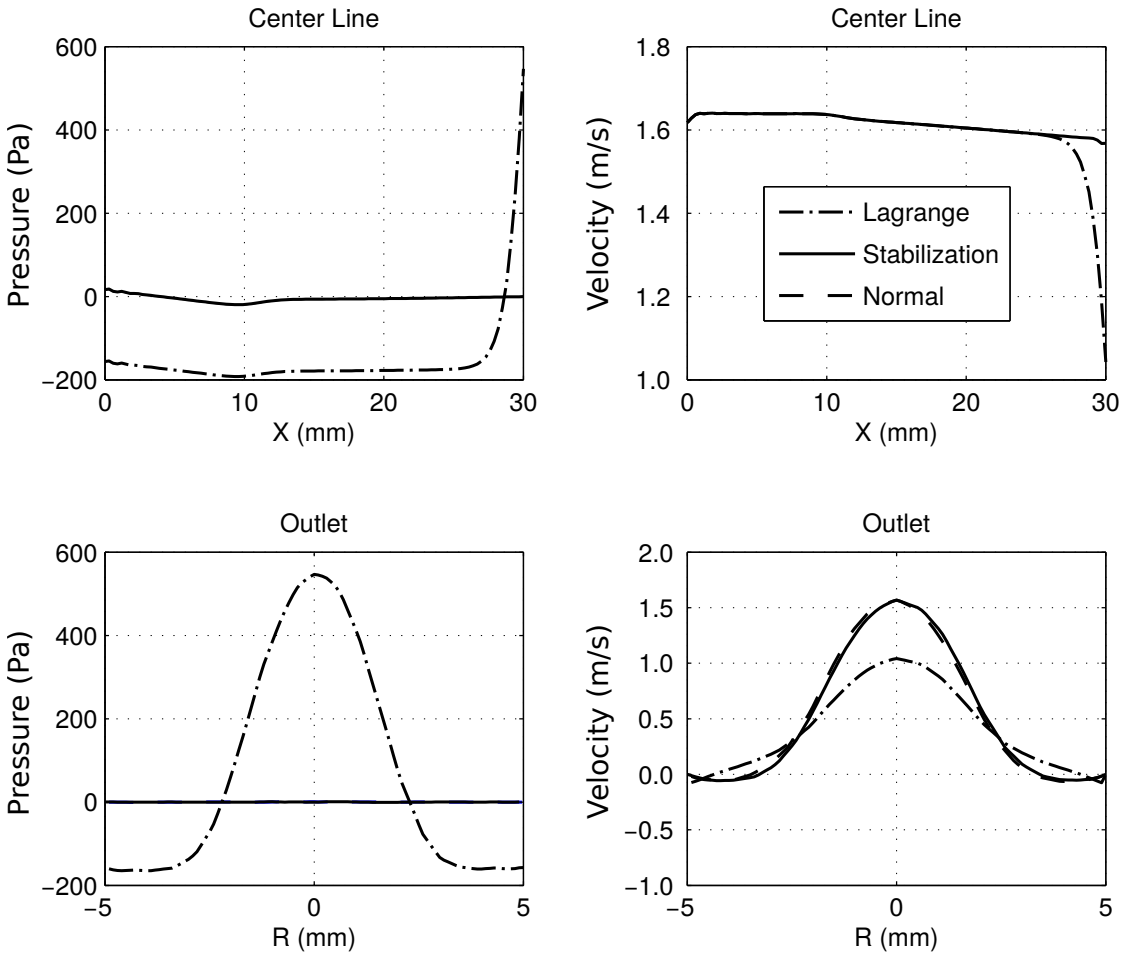

Figure 3.7: Velocity and pressures for the short model at Re = 1000

Higher Reynolds number

Figure 3.8 shows the results for the short model at a Reynolds number of 5000. In this figure, the Lagrange method velocity results are closer to the other two. However, the pressure at the centerline is lower at the inlet and rapidly increases at the outlet. This suggests lower pressure energy dissipation in this method as compared with the others. To obtain stable results, the time-step size is reduced to 10^{-3} from 10^{-2} for the lower Reynolds number case. When increasing the Reynolds number further to 2×10^4, the Lagrange (keeping the penalty numbers and profile order unchanged) and normal constraint methods are no longer stable,

where the stabilization method remains stable. For the stabilization method, we found that for lower β values, the solution was stable for higher time-step values.

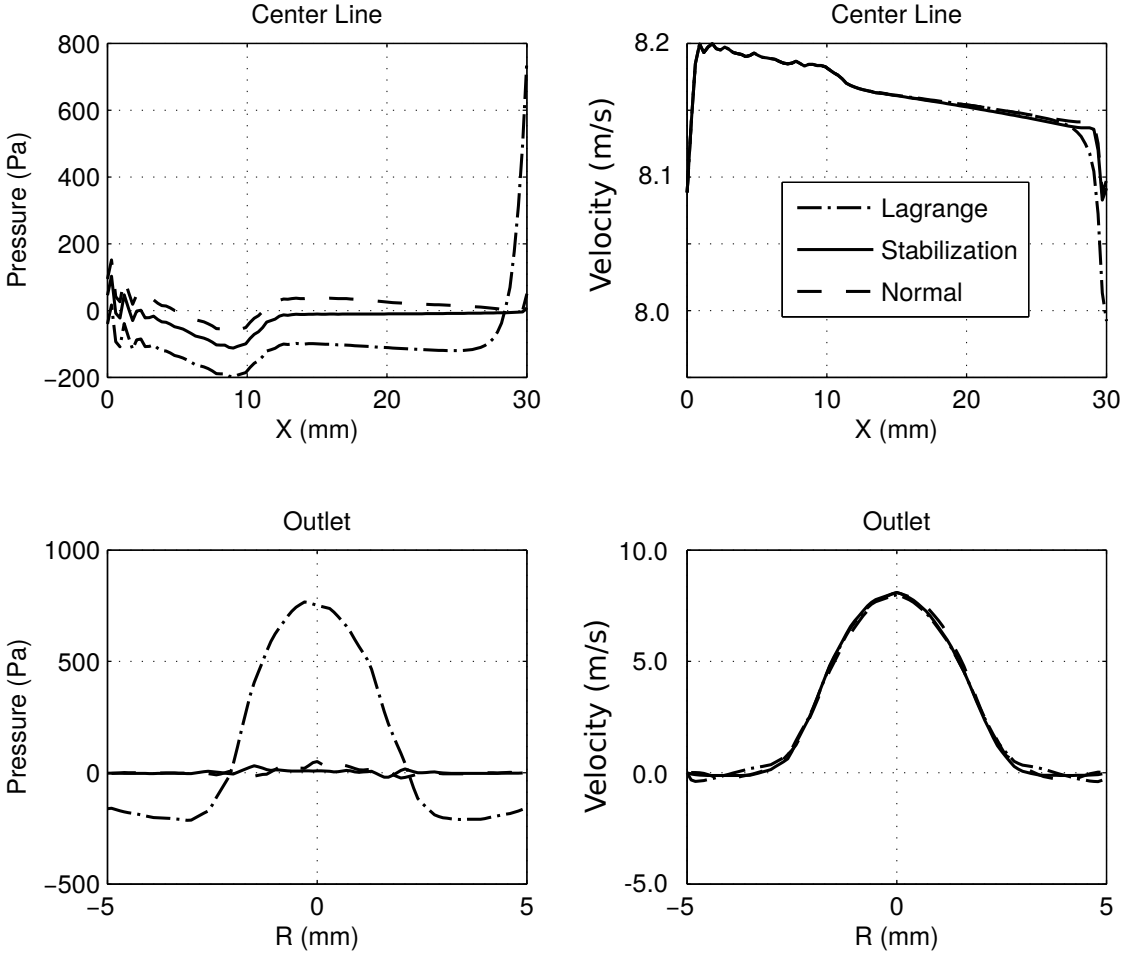

Figure 3.8: Velocity and pressures for the short model at Re = 5000

Considering the centerline velocity at Re = 1000 and 5000 in Figures 3.7 and 3.8, the impact of the both the stabilization and normal constraint methods on the centerline velocity increases with the Reynolds number. This can be inferred by the sharp reduction of the centerline velocity at the outlet at Re = 5000. Also, the centerline pressure of these two methods does not match as well at Re = 5000 as it does at Re = 1000.

3.2.2 Right angle bend

The second example illustrates pulsatile flow through a right-angle bend. The radius of the bend centerline is 10 mm and its diameter is 5 mm. This is a common shape in the arterial system, e.g. in a child's descending aorta. This simulation is done with a time-step equal to 10^{-4} over 1 s with three nonlinear iterations per time-step. The inflow wave-form is physiological, with a cardiac cycle time of 0.5 s [16]. This wave form (Q_1) and the model are shown in Figure 3.9. The average flow rate was scaled to produce an average Re = 2500. This high Reynolds number is chosen to challenge the robustness of these methods, and is above the normal physiologic range. However, high Reynolds number such as this can occur in the other applications, such as flow simulation through pipes and ducts. Analogous to the previous case, a zero traction BC is set for the outlet. Both the normal constraint and the no-treatment cases were unstable.

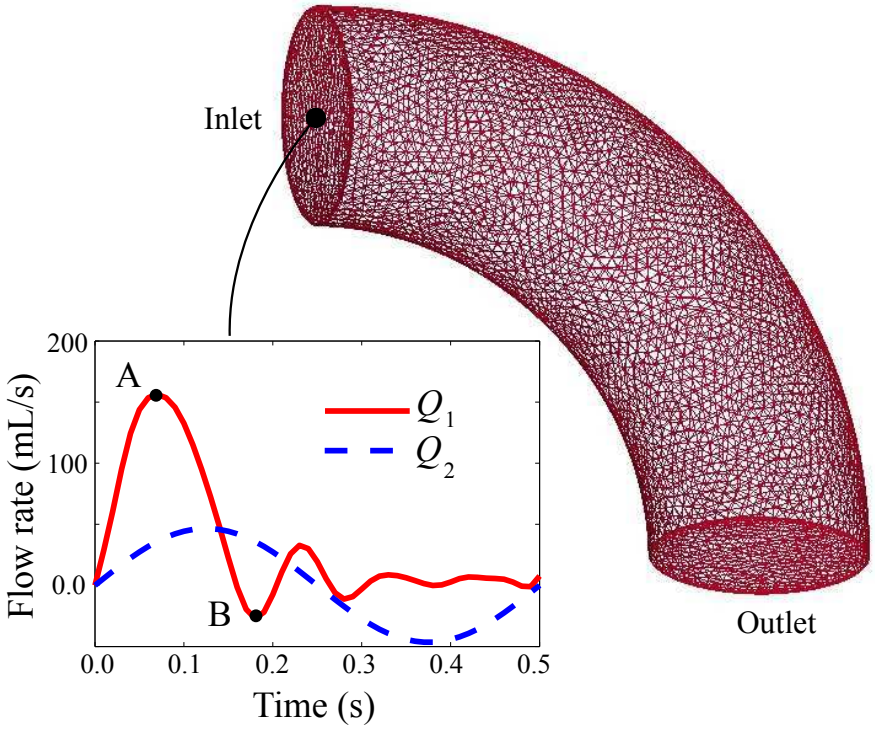

Figure 3.9: Second case study geometric model and inflow waveforms.

Table 3.2: Comparison between the average pressure and energy fluxes of the curved model at average $Re = 2500$ for case study two.

Method	$\bar{P}_{\text{in}}$ (Pa)	$\bar{P}_{\text{out}}$ (Pa)	$\dot{E}_{\text{in}}$ (W)	$\dot{E}_{\text{out}}$ (W)	$-\dot{E}_{\text{out}}/\dot{E}_{\text{in}}$ (%)
Stabilization	1192	-24.1	-1.585	1.372	86.5
Normal	-	-	-	-	-
Lagrange	1781	433.7	-1.584	1.323	83.5

From Table 3.2, the Lagrange method results show large differences in the inlet and outlet pressures compared to the stabilization method results. Similar to the previous cases, the zero traction BC at the outlet is not satisfied for the Lagrange method. This is due to the added normal traction at the outlet, which increases the pressure at the outlet nodes, for the Lagrange method. This pressure propagates through the model, causing higher pressure at the inlet as well.

The inflow wave form was changed to a more critical case of $\frac{\pi^2}{8} D\nu \text{Re} \sin(2\pi t/T)$, where the T, D, ν, and Re are one cycle period, inlet diameter, fluid kinematic viscosity, and average Reynolds number, respectively. This inflow wave form has more backflow, as shown by Q_2 in Figure 3.9. The Reynolds number is set to 2000. At this Reynolds number the normal constraint simulation diverged. The Lagrange constraint case remained stable, but the result was physically unrealistic, with a high pressure oscillation through the cardiac cycle. The stabilization method result, on the other hand, was stable and the solution residual was low.

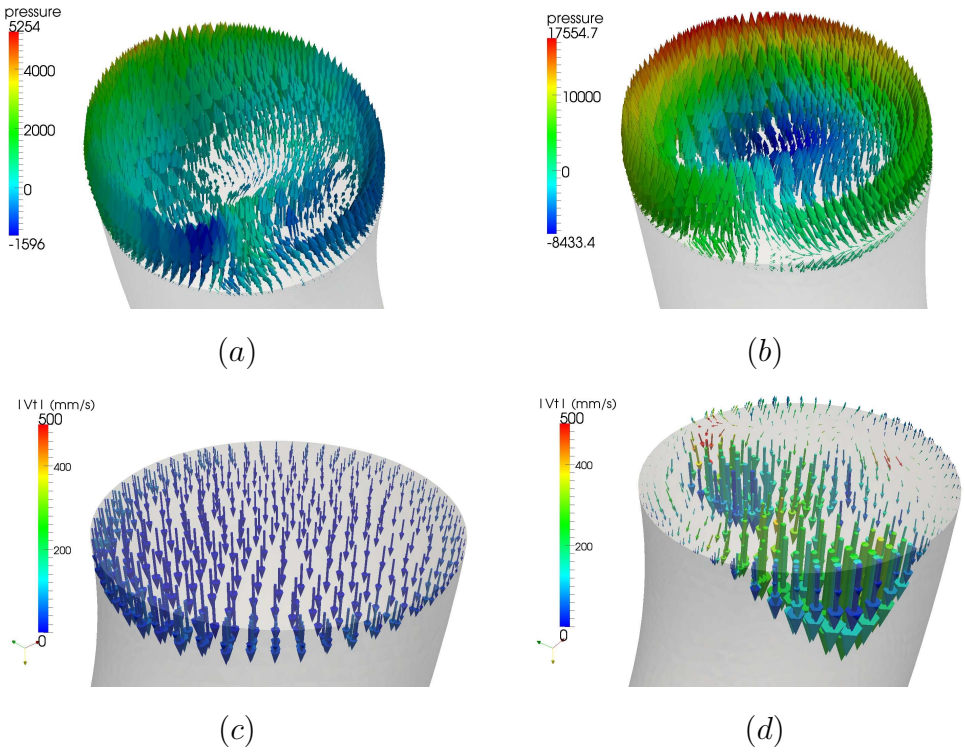

Figure 3.10: Second case study, outlet velocity vectors at peak flow (point A in Figure 3.9) colored by pressure (Pa) using (a) stabilization method and (b) Lagrange method; and velocity vectors after deceleration (point B in Figure 3.9) colored by tangential velocity for (c) stabilization method and (d) Lagrange method.

Figure 3.10 illustrates the larger differences in the outlet velocity vector found using the Lagrange and stabilization methods. The vectors in Figure 3.10(b) which are colored by pressure, clearly show the low artificial pressure at the center of the outlet which tends to increase the velocity at the center to achieve the desired parabolic profile. This is also true for the region of the outlet with high velocity close to the wall, which has a higher artificial pressure. The residual value is low for the stabilization method over the entire cycle, but the residual increases in diastole for the Lagrange method. This is the reason that after deceleration (i.e. point B in Figure 3.9) the velocity vectors shown in (d) are inconsistent with part (c) of Figure 3.10.

3.2.3 Patient-specific aorta model

The final case study is an aortic arch model constructed from CT data of a healthy, 62 year-old male patient, which is shown in Figure 3.11. In addition to the aorta, three branches of the brachiocephalic artery, the left common carotid artery, and the left subclavian artery are included in the model. Physiologic RCR BCs are imposed at all outlets [29, 51]. The sum of proximal and distal resistances for each branch is tuned based on the flow rate in the branches, which assumed to be proportional to the outlet surface areas. The proximal resistances are assumed to be 10% of their corresponding distal resistances. The total resistance is tuned to obtain an average pressure of 100 mmHg for the AA, a typical physiologic value. The capacitances are tuned to obtain a pressure amplitude between 80-120 mmHg at the outlets. To achieve mesh independence, the mesh is adapted twice based on element residual values [98]. The final mesh contains approximately 2 million tetrahedral elements. A Dirichlet BC is imposed at the inlet, i.e. AA, with the flow waveform shown in Figure 3.11 [51]. All the outlets are constrained for the Lagrange method with a profile order of 5. Also, $\bar{Q}$ in Equation (3.11) was tuned to the exact values obtained from the stabilization methods results, giving the Lagrange method an exact initial guess for the flow rates at each outlet.

The flow rate is negative for a significant portion of the cycle for the three upper branches (flow rate plots in Figure 3.11), but not for the descending aorta. This backflow results in an unstable solution for the no-treatment case, and the normal constraints case also diverged after 25% of the cardiac cycle.

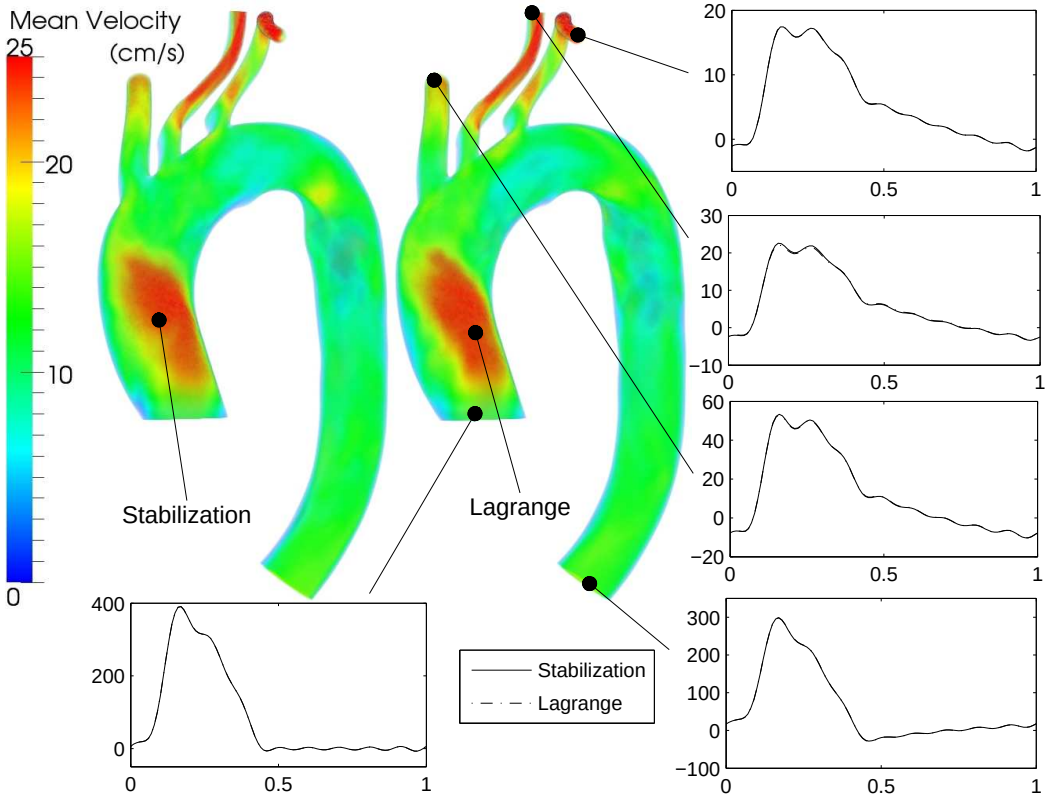

Figure 3.11: Flow rates (mL/s versus time) of the outlets obtained from the stabilization and Lagrange methods results. The volumetric contours of time-averaged velocity magnitude are shown for the stabilization and the Lagrange methods.

Since there is no significant flow reversal in the descending aorta, the stabilization method does not have any effect on this outlet. This is also true at flow peak for the other branches, when there is no backflow at these outlets. Comparing the flow traces of the Lagrange and stabilization methods shows no significant difference between the results. Assuming the stabilization method results are close to the supposed no treatment case results, it can be concluded that the Lagrange method does not change the flow split values in this case. This is mainly due to the fact that the flow split is determined by the BCs, rather than the 3D model hemodynamics. This can be simply deduced by comparing the pressure loss through the model to the pressure loss at the boundaries (see Figure 3.12).

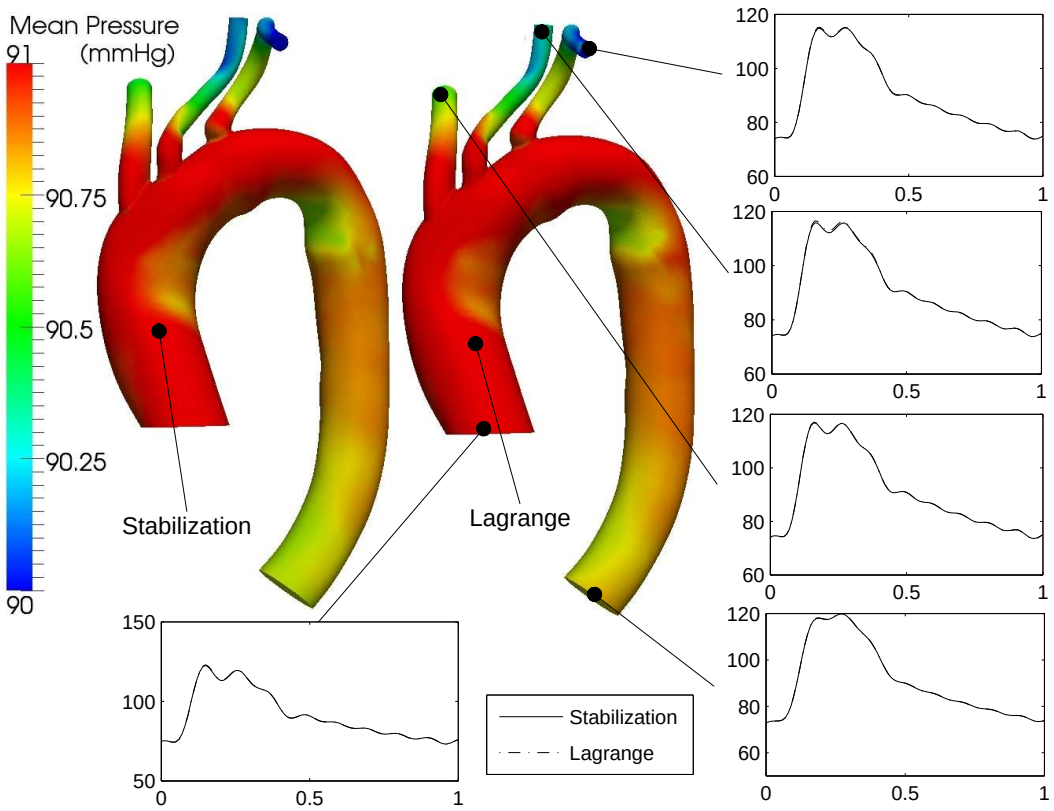

Figure 3.12: Pressure plots (mmHg versus time) at the outlets obtained from the Lagrange and stabilization methods. The time-averaged pressure contours at the surface are shown for the stabilization and the Lagrange methods.

As seen in this figure, the pressure loss in the model is on the order of 1 mmHg, while the mean pressure imposed by the BCs is approximately 90 mmHg. Since the intrusion of the Lagrange method on the pressure field is of the same order as pressure loss in the model, the variation in the pressure field is too small to significantly affect the flow split. Hence, the flow split between the branches is roughly inversely proportional to the sum of distal and proximal resistances.

However, if the Lagrange parameters are not tuned properly, the Lagrange results can be drastically different from the stabilization results. The importance of tuning the Lagrange parameters is deducible from Table 3.3. The results in this table are obtained from steady state simulations with zero traction BCs for the outlets. In the cases shown, the Lagrange method produces significantly different

flow splits compared to the no treatment case, and the difference is made worse if the Lagrange method parameters are not tuned properly (see Table 3.3).

Table 3.3: The effect of tuning Lagrange parameters on the solution. The flow rates are in (mL/s) and pressures are in (Pa). Case I simulation is performed with no treatment of the BC. Case II simulation is performed using Lagrangian constraint with tuned $\bar{Q}$ obtained from the no-treatment case, and $n = 2$. Case III simulation is performed using Lagrangian constraint with tuned $\bar{Q}$ obtained from the no-treatment case, and $n = 5$. Case IV simulation is performed using Lagrangian constraint with untuned $\bar{Q}$, and $n = 2$. In latter case, $\bar{Q}$ is estimated based on the outlet surface area and AA flow rate. Note that the stabilization results are identical to the no-treatment case, since there is no backflow at the outlets. aa: ascending aorta; aod: descending aorta; ba: brachiocephalic artery; lsa: left subclavian artery, lcca: left common carotid artery.

Case	$\bar{Q}_{\text{aa}}$	$\bar{Q}_{\text{aod}}$	$\bar{Q}_{\text{ba}}$	$\bar{Q}_{\text{lsa}}$	$\bar{Q}_{\text{lcca}}$	$\bar{P}_{\text{aa}}$	$\bar{P}_{\text{aod}}$	$\bar{P}_{\text{ba}}$	$\bar{P}_{\text{lsa}}$	$\bar{P}_{\text{lcca}}$
I	-50.0	38.7	7.63	1.41	2.27	14.5	0.014	0.35	0.33	0.55
II	-50.0	40.2	7.11	1.79	0.87	15.5	0.795	2.54	4.39	6.04
III	-50.0	43.6	5.23	0.86	0.34	13.8	-0.017	7.15	8.71	9.37
IV	-50.0	46.0	3.19	0.43	0.36	15.2	0.610	11.5	12.4	10.3

The contours of WSS magnitude for the steady state case with zero traction BCs are shown in Figure 3.13. The Lagrange contours are obtained from the case IV simulation in Table 3.3. The changes in the velocity field have caused large changes in the WSS in the upper branches. In these branches the Lagrange method predicts a lower flow rate, and hence a lower WSS. However, in the AA the WSS predictions are very close, due to the identical flow rates at the inlet.

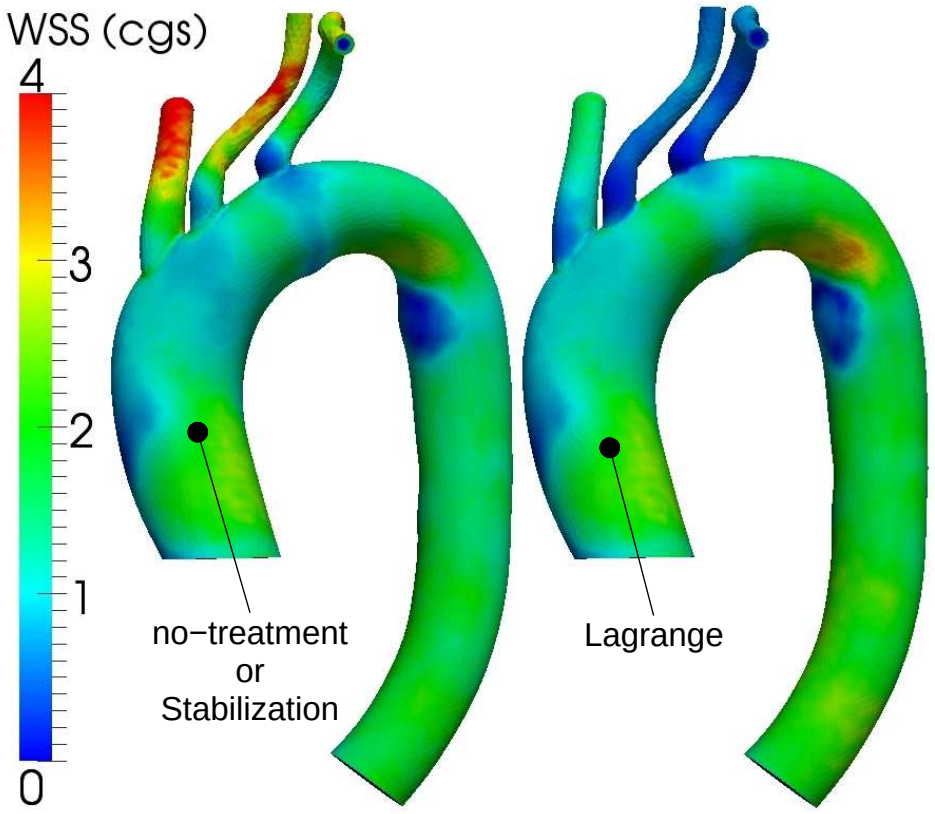

Figure 3.13: The WSS contours obtained from the no-treatment and the Lagrange methods results. These results correspond to a steady state, zero traction BC simulation. The $\bar{Q}$ is untuned for the Lagrange method with $n = 2$ (case IV in Table 3.3). The Lagrange method predicts lower WSS in the upper branches due to the lower flow rates in these branches. However, the WSS is nearly unaffected for the aortic arch.

To illustrate issues with robustness of the proposed methods, we present a case in which we alter the cross sectional cut of one of the model outlets. This represents a situation in which the outlet section cannot be cut perpendicular to the flow direction for reasons related to model construction or lack of image data. Also, due to unsteady flow phenomenon, the primary flow direction at a given outlet can change over the cardiac cycle. Thus, there may be no unique direction for the outlet normal that remains aligned with the flow direction during the entire cycle. The situation is even more challenging when fluid-structure interaction modeling

is employed for cardiovascular simulation (see, e.g.,[99, 100, 101, 102]).

To investigate the robustness of the methods under these non-ideal circumstances, the brachiocephalic outlet is intentionally cut in an off-normal direction to the vessel centerline (see Figure 3.14). Therefore, the normal constraint direction is not aligned with the flow direction. Also, the outlet cross section is elliptical, which differs from the assumed circular cross section in Equation (3.10). This leads to divergence of the normal constraint simulation after 15% of the cardiac cycle. Compared to the previous case, this demonstrates the sensitivity of the normal constraint method to the outlet cut angle. Without tuning the Lagrange method parameters, the simulation diverges. This is likely a result of inconsistency between the outlet cross section and the assumed cross section in Equation (3.10). The stabilization method remains stable for this case, and the time-averaged WSS and pressure contours are smooth, matching well with the previous results. This result indicates improved robustness of the stabilization method in non-ideal circumstances compared to the other two methods.

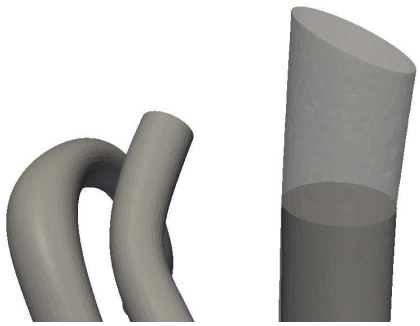

Figure 3.14: The brachiocephalic artery with normal and angled cut.

3.3 Discussion

The overall performance of the three treatment methods can be compared in terms of robustness, impact on the flow physics, computational cost, implementation effort and ease-of-use aspects.

Comparing the robustness of the three methods used for backflow treatment, the stabilization method performed the best. Robustness was tested by varying the Reynolds number and length of geometry in case study 1, by adding flow pulsatility with backflow in case study 2, and by varying the outlet cut plane in case study 3. For all these cases, the stabilization method produced a numerically stable solution without the need for parameter adjustment. In examining the residuals of the numerical solution, we find that the Lagrange method was stable while the normal constraint method failed for the second and third case studies. However, the residual was still high for the Lagrange method compared to the stabilization method in the second case study, and the obtained solution deviated substantially from the stabilization method results. Both the normal constraint method and the Lagrange method, depending on the formulation, can place additional requirements on the model geometry compared to the stabilization method. The normal constraint method failed faster in case study 3 when the outlet section was not cut properly. Since a circular cross section at the outlets was assumed, the untuned Lagrange method also failed.

Perhaps the most important measure of performance is the impact of the outlet treatment on the flow physics. In this case, the stabilization method outperformed the Lagrange and normal constraint methods. Although the stabilization method can change the pressure slightly due to the added traction, this effect does not appear to be significant, especially when examining the velocity vectors. The stabilization method has absolutely no impact on the flow when there is no backflow. This is also true for the normal constraint if the normal constraint equation is considered only for $\partial_{h\_}\Omega$, i.e. where $\boldsymbol{u}^a \cdot \boldsymbol{n}^a < 0$.

For all cases examined in this chapter, the Lagrange method had a significant impact on the velocity profile at the constrained outlet. While the effect on the velocity profile shape was restricted to a local region near the outlet, there were important effects on other quantities including pressure and energy loss that propagated globally. Our results showing only local changes in the velocity profile agreed with the previous work of Kim et al [27]. However, to satisfy the momentum equations, the Lagrange method also resulted in large changes to the pressure at

the boundary, which affected the pressure globally throughout the model in case studies 1 and 2. This causes an error in the predicted pressure field in regions far from the constrained boundaries.

Our results suggest that the effect of the Lagrange method on the flow field depends on the type of BCs used. Specifically, the Lagrange results were more accurate when physiologic non-zero traction BCs are used, as compared to the zero traction BCs. When using RCR BCs in case study 3, the pressure changes due to the Lagrange constraint were small compared to the overall mean pressures imposed by the BCs, and therefore, the resulting changes in both flow rate and pressure were not significant. However, the excellent agreement obtained with the Lagrange method for this case required tuning the $\bar{Q}$ values using the stabilization results, and the results were highly variable without tuning. These results also suggest that the Lagrange method may be less suited to problems with lower overall mean pressure, such as venous flow simulations. Decreasing the penalty numbers can decrease the impact of the Lagrange method on the flow physics, but it will also decrease the robustness of this method.

Comparing the results for computational cost, the normal constraint and stabilization methods do not add any significant additional cost, whereas, the Lagrange method can add up to 50% to the computational cost, depending on the problem. This increased cost is due to the additional elements inside the solution vector, i.e. Lagrange multipliers, as well as added blocks inside the stiffness matrix.

The implementation effort required for the normal constraint and stabilization methods are both minimal, because the structure of the stiffness matrix and the linear solver need not be modified for either method. The implementation of the normal constraint method requires somewhat more effort because the rotation matrix must be formed for each element, and also specific blocks of the element stiffness matrix and residual vector should be modified. Due to the new entries in the solution vectors and the changes in the structure of the tangent matrix, the Lagrange method requires the highest implementation effort.

Considering the ease-of-use aspect, the normal constraint and stabilization methods are fairly simple to use. However, the Lagrange method requires the use

of several user-defined parameters. For example, the quantity $\bar{Q}$ in Equation (3.11) must be estimated and specified by the user prior to the running the simulation, while this parameter should be a simulation result. In practice, this may required a time-intensive iterative procedure. It should be noted that drastic changes in these parameters can have profound effect on the final simulation results, even with RCR BCs.

Acknowledgements

We gratefully acknowledge the use of software from the Simvascular open source project through Simbios (http://simtk.org), as well as the expertise of Dr. Nathan Wilson. The authors gratefully acknowledge Dr. Hyun Jin Kim for her help regarding the Lagrange method coding and implementation.

This chapter, in full, is a reprint of the material as it appears in A comparison of outlet boundary treatments for prevention of backflow divergence with relevance to blood flow simulations in *Computational Mechanics*, 48(3), 277-291, 2011. Authors are M. Esmaily-Moghadam, Y. Bazilevs, I. Vignon-Clementel, and A. Marsden. The dissertation author was the primary investigator and author of this paper.

Chapter 4

A Preconditioning Method for Multidomain Simulations

Solution of linear systems of equations arising in the discretization of the incompressible Navier-Stokes equations remains an active area of research. Using direct solvers for time-dependent cardiovascular simulations is not viable due to high computational cost, poor scalability, and large memory requirements. Iterative solution methods are therefore the strategy of choice for this class of problems. In cardiovascular simulations, high outflow resistances, high Reynolds numbers, and long, thin blood vessel geometry all contribute to ill-conditioning of the underlying linear system.

Cardiovascular blood flow simulations mandates the use of a multidomain approach to model the multiscale behavior of the cardiovascular system. As detailed in Chapter 2, in this approach the 3D CFD domain is typically coupled to a reduced dimension (RD) model, which acts as a BC for the 3D domain and vice versa. In this context, the RD domain can be a simple impedance or resistance, Windkessel model, 1D network of vessels, or a sophisticated 0D LPN [29, 80, 49, 53, 25]. To couple the RD and 3D domains, both explicit or implicit methods have been used. Implicit methods offer advantages due to superior numerical stability and lower computational cost [49, 50, 103], while offering equivalent modularity [33].

The developed method in Chapter 2 for implicit coupling have achieved

stability by calculating the relation between flow and pressure, hence predicting the influence of the RD domain in the 3D domain. This produces a contribution from the RD domain in the 3D domain tangent matrix. For many physiological scenarios, this contribution is much larger than that from the 3D domain. From a physical point of view, in these scenarios the flow inside the 3D domain is mainly determined by the BCs rather than the geometry of the 3D domain. In this chapter we show that the contribution to the LHS matrix from the RD domain produces an ill-conditioned matrix, which introduces new challenges in the LS. This issue becomes more critical as the mesh size is reduced. To resolve this issue, we propose a specialized preconditioner (PC) to reduce the tangent matrix condition number and remove the dependence of the simulation cost on the BCs.

Designing good preconditioning techniques for flow computations, especially those with stabilized methods, attracted much attention (see, for example, [104, 105, 106, 107, 108, 109, 110, 111]). There exist several challenges facing linear equation solvers for incompressible flow in general [112], and for cardiovascular fluid mechanics applications in particular [113]. Challenges associated with flows in spatial domains that are longer in one dimension than the others (e.g., networks of pipes or blood vessels) were addressed in [114], while the work in [115, 116] focused on the difficulties encountered in cardiovascular applications involving high-aspect-ratio boundary-layer elements. Furthermore, using a general purpose PC, such as those available in standard open source linear equation solver packages is not effective for the aforementioned multidomain problem. These PCs are either too costly or are not effective in reducing the condition number of the tangent matrix, hence producing additional overall computational cost (e.g. see [117, 118]). Another approach is to generate an orthogonal space based on the previous iterations and use it to find the part of the solution that lives in that space. This method cannot be used with multiple Newton nonlinear iterations and is often inefficient when the LS requires more iterations (stiffer problems) [119]. For an efficient LS algorithm, it is critical to design an efficient PC, because the overall algorithm performance can be significantly degraded by even a minor overhead cost in the PC.

In this chapter we introduce an effective PC that reduces computational

cost associated with implicit multidomain simulations. This PC is tested in an efficient LS, also presented in this chapter, to demonstrate its minimal overhead and combined algorithm effectiveness. We first show the contribution of the RD domain to the tangent matrix. We then construct a PC based on this contribution, and demonstrate its use inside the LS where the increments of the flow and pressure variables are computed simultaneously. Using a set of clinically relevant examples, we examine the efficiency of the proposed algorithm by comparing its performance to the non-preconditioned case as well as standard GMRES [120, 121], achieving an order of magnitude improvement in performance.

4.1 A PC for coupled Neumann BCs

Here we follow the FE framework, described in Section 2.1, for discretization of Navier-Stokes equations in space and time and obtaining the linear system of equations. We saw two types of BCs are imposed in the 3D domain: 1) Dirichlet BC, which is an essential BC on the velocity, and 2) Neumann BC, which is a weakly imposed traction. Since for a Dirichlet BC velocity is directly imposed, this type of BC does not incur extra computational cost or instability. A Neumann BC, however, can lead to higher computational cost and instabilities. Therefore, for the purpose of developing the PC, we only consider coupled Neumann BCs in this chapter.

In the case of a coupled Neumann boundary, the contribution of coupled BCs to the LHS matrix is calculated by Equation (2.30), which is

$$\boldsymbol{K}_{\mathrm{bc}}^{ab} = \sum_{k=1}^{n_{\mathrm{bc}}} \sum_{l=1}^{n_{\mathrm{bc}}} \gamma \Delta t M^{kl} \int_{\Gamma^k} N^a \boldsymbol{n} \mathrm{d}\Gamma \otimes \int_{\Gamma^l} N^b \boldsymbol{n} \mathrm{d}\Gamma. \tag{4.1}$$

From Equation (2.14), we define

$$\boldsymbol{K}_{\mathrm{mc}} \boldsymbol{y} = -\boldsymbol{R}, \tag{4.2}$$

$$\boldsymbol{K}_{\mathrm{mc}} = \begin{bmatrix} \boldsymbol{K} & \boldsymbol{G} \\ \boldsymbol{D} & \boldsymbol{L} \end{bmatrix} \tag{4.3}$$

where $\boldsymbol{K}_{\mathrm{mc}}$ is the tangent (stiffness) matrix containing the blocks of momentum and continuity tangent matrices ($\boldsymbol{K}$, $\boldsymbol{G}$, $\boldsymbol{D}$, and $\boldsymbol{L}$).

We decompose the tangent matrix $\boldsymbol{K}$ into

$$\boldsymbol{K} = \hat{\boldsymbol{K}} + \boldsymbol{K}_{\mathrm{bc}}, \tag{4.4}$$

in which $\hat{\boldsymbol{K}}$ is the 3D domain interior contribution and $\boldsymbol{K}_{\mathrm{bc}}$ is the BC contribution (Equation (4.1)). $\hat{\boldsymbol{K}}$ is a non-singular matrix, while $\boldsymbol{K}_{\mathrm{bc}}$ is a linear combination of n_{bc} vectors and has only n_{bc} non-zero eigenvalues. Hence, the condition number of $\boldsymbol{K}$ (and also $\boldsymbol{K}_{\mathrm{mc}}$) highly depends on the relative norm of these two matrices. Increasing the resistance of the coupled Neumann BC (i.e. $\boldsymbol{M}$), the entries of $\boldsymbol{K}$ will be dominated by only a few eigenvalues of $\boldsymbol{K}_{\mathrm{bc}}$, producing an ill-conditioned matrix. This causes poor performance of standard iterative methods, with a large number of iterations required for convergence. Because $\boldsymbol{K}$ is dominated by only a few eigenvalues when the entries of $\boldsymbol{K}_{\mathrm{bc}}$ are much larger than $\hat{\boldsymbol{K}}$, we can exploit this to construct a PC. We do this using the Sherman-Morrison formula [122]. Since only the diagonal entries of $\boldsymbol{M}$ are considered, we define

$$\mathcal{R}^i \equiv \gamma \Delta t M^{ij} \delta^{ij}, \tag{4.5}$$

where no sum is taken on i. Also defining

$$\boldsymbol{S}^k \equiv \int_{\Gamma^k} N(\boldsymbol{x}) \boldsymbol{n} \mathrm{d}\Gamma, \tag{4.6}$$

Equation (4.1) can be rewritten as

$$\boldsymbol{K}_{\mathrm{bc}} = \sum_{k=1}^{n_{\mathrm{bc}}} \mathcal{R}^k \boldsymbol{S}^k \otimes \boldsymbol{S}^k. \tag{4.7}$$

Defining the operator $\mathcal{D}$ to select the diagonal entries of a matrix, we define

$$\hat{\boldsymbol{K}}_{\mathrm{d}} \equiv \mathcal{D}(\hat{\boldsymbol{K}}), \tag{4.8}$$

$$\boldsymbol{K}_{\mathrm{d}} \equiv \hat{\boldsymbol{K}}_{\mathrm{d}} + \boldsymbol{K}_{\mathrm{bc}}. \tag{4.9}$$

We seek a matrix $\boldsymbol{H}$, such that

$$\boldsymbol{H} \simeq \boldsymbol{K}^{-1}. \tag{4.10}$$

Instead we find a matrix $\boldsymbol{H}$, such that

$$\boldsymbol{H}\boldsymbol{K}_{\mathrm{d}} = \boldsymbol{I}. \tag{4.11}$$

To normalize $\hat{\boldsymbol{K}}_{\mathrm{d}}$, a symmetric Jacobi PC is used

$$\boldsymbol{W} \equiv (\hat{\boldsymbol{K}}_{\mathrm{d}})^{-\frac{1}{2}}. \tag{4.12}$$

Hence the normalized $\boldsymbol{K}_{\mathrm{d}}$ is defined as

$$\tilde{\boldsymbol{K}}_{\mathrm{d}} \equiv \boldsymbol{W}\boldsymbol{K}_{\mathrm{d}}\boldsymbol{W}. \tag{4.13}$$

From Equations (4.9)-(4.13)

$$\tilde{\boldsymbol{K}}_{\mathrm{d}} = \boldsymbol{I} + \tilde{\boldsymbol{K}}_{\mathrm{bc}}. \tag{4.14}$$

From Equation (4.7) we have

$$\tilde{\boldsymbol{K}}_{\mathrm{bc}} = \sum_{i=1}^{n_{\mathrm{bc}}} \mathcal{R}^i \tilde{\boldsymbol{S}}^i \otimes \tilde{\boldsymbol{S}}^i, \tag{4.15}$$

$$\tilde{\boldsymbol{S}}^i \equiv \boldsymbol{W}\boldsymbol{S}^i. \tag{4.16}$$

Defining

$$\tilde{\boldsymbol{H}} \equiv \boldsymbol{W}^{-1}\boldsymbol{H}\boldsymbol{W}^{-1}, \tag{4.17}$$

it can be shown that

$$\tilde{\boldsymbol{H}}\tilde{\boldsymbol{K}}_{\mathrm{d}} = \boldsymbol{I}. \tag{4.18}$$

From Equations (4.14), (4.15), and (4.18)

$$\tilde{\boldsymbol{H}} + \sum_{i=1}^{n_{\mathrm{bc}}} \mathcal{R}^i \tilde{\boldsymbol{H}}\tilde{\boldsymbol{S}}^i \otimes \tilde{\boldsymbol{S}}^i = \boldsymbol{I}. \tag{4.19}$$

Since $\Gamma^i \cap \Gamma^j = \{\}$, multiplying Equation (4.19) by $\tilde{\boldsymbol{S}}^j$ produces

$$\tilde{\boldsymbol{H}}\tilde{\boldsymbol{S}}^j = \frac{\tilde{\boldsymbol{S}}^j}{1 + \mathcal{R}^j \|\tilde{\boldsymbol{S}}^j\|^2}. \tag{4.20}$$

From Equation (4.20) we then have

$$\sum_{j=1}^{n_{\mathrm{bc}}} \mathcal{R}^j \tilde{\boldsymbol{H}}\tilde{\boldsymbol{S}}^j \otimes \tilde{\boldsymbol{S}}^j = \sum_{j=1}^{n_{\mathrm{bc}}} \left[\frac{\mathcal{R}^j \tilde{\boldsymbol{S}}^j \otimes \tilde{\boldsymbol{S}}^j}{1 + \mathcal{R}^j \|\tilde{\boldsymbol{S}}^j\|^2} \right]. \tag{4.21}$$

The normalized PC is found by combining Equations (4.19) and (4.21)

$$\tilde{\boldsymbol{H}} = \boldsymbol{I} - \sum_{j=1}^{n_{\mathrm{bc}}} \left[\frac{\mathcal{R}^j \tilde{\boldsymbol{S}}^j \otimes \tilde{\boldsymbol{S}}^j}{1 + \mathcal{R}^j \|\tilde{\boldsymbol{S}}^j\|^2} \right], \tag{4.22}$$

which after multiplying by $\boldsymbol{W}$ on the left and right is

$$\boldsymbol{H} = (\hat{\boldsymbol{K}}_{\mathrm{d}})^{-1} - \sum_{j=1}^{n_{\mathrm{bc}}} \left[\frac{\mathcal{R}^j((\hat{\boldsymbol{K}}_{\mathrm{d}})^{-1}\boldsymbol{S}^j) \otimes ((\hat{\boldsymbol{K}}_{\mathrm{d}})^{-1}\boldsymbol{S}^j)}{1 + \mathcal{R}^j \|(\hat{\boldsymbol{K}}_{\mathrm{d}})^{-\frac{1}{2}}\boldsymbol{S}^j\|^2} \right]. \tag{4.23}$$

We note that $\boldsymbol{H}$ reduces to a Jacobi PC if there are no coupled Neumann BCs. When the norm of $\boldsymbol{M}$ is large, Equation (4.23) is a good approximation for $\boldsymbol{K}^{-1}$ and can be calculated directly from $\hat{\boldsymbol{K}}$ and $\boldsymbol{K}_{\mathrm{bc}}$ with negligible computational cost.

The proposed PC in Equations (4.22)-(4.23) is straightforward to implement in a parallelized code. Generally all the nodes of a boundary reside in a single processor, causing all the nonzero entries of $\boldsymbol{S}^i$ to be allocated to that processor. In this case, the product of $\boldsymbol{H}$ and a vector does not require any communication between processors. If a boundary j is divided between two or more processors, only a single dot product (already implemented in most LS) with collective communication must be calculated for the boundary j. In the following section we will see how this PC can be used inside the LS.

4.2 Bi-partition iterative algorithm

From Equation (2.14) we look for $\boldsymbol{y}_{\mathrm{u}}$ and $\boldsymbol{y}_{\mathrm{p}}$ that satisfies

$$\begin{bmatrix} \boldsymbol{K} & \boldsymbol{G} \\ \boldsymbol{D} & \boldsymbol{L} \end{bmatrix} \begin{bmatrix} \boldsymbol{y}_{\mathrm{u}} \\ \boldsymbol{y}_{\mathrm{p}} \end{bmatrix} = - \begin{bmatrix} \boldsymbol{R}_{\mathrm{m}} \\ \boldsymbol{R}_{\mathrm{c}} \end{bmatrix}. \tag{4.24}$$

Since $\boldsymbol{K}$ is non-singular we have

$$\begin{bmatrix} \boldsymbol{K}^{-1} & 0 \\ 0 & \boldsymbol{I} \end{bmatrix} \begin{bmatrix} \boldsymbol{K} & \boldsymbol{G} \\ \boldsymbol{D} & \boldsymbol{L} \end{bmatrix} \begin{bmatrix} \boldsymbol{y}_{\mathrm{u}} \\ \boldsymbol{y}_{\mathrm{p}} \end{bmatrix} = - \begin{bmatrix} \boldsymbol{K}^{-1} & 0 \\ 0 & \boldsymbol{I} \end{bmatrix} \begin{bmatrix} \boldsymbol{R}_{\mathrm{m}} \\ \boldsymbol{R}_{\mathrm{c}} \end{bmatrix}, \tag{4.25}$$

so that

$$\begin{bmatrix} \boldsymbol{I} & \boldsymbol{K}^{-1}\boldsymbol{G} \\ \boldsymbol{D} & \boldsymbol{L} \end{bmatrix} \begin{bmatrix} \boldsymbol{y}_{\mathrm{u}} \\ \boldsymbol{y}_{\mathrm{p}} \end{bmatrix} = - \begin{bmatrix} \boldsymbol{K}^{-1}\boldsymbol{R}_{\mathrm{m}} \\ \boldsymbol{R}_{\mathrm{c}} \end{bmatrix}. \tag{4.26}$$

To obtain a triangular structure we multiply both sides by a lower triangular matrix such that

$$\begin{bmatrix} \boldsymbol{I} & 0 \\ -\boldsymbol{D} & \boldsymbol{I} \end{bmatrix} \begin{bmatrix} \boldsymbol{I} & \boldsymbol{K}^{-1}\boldsymbol{G} \\ \boldsymbol{D} & \boldsymbol{L} \end{bmatrix} \begin{bmatrix} \boldsymbol{y}_{\mathrm{u}} \\ \boldsymbol{y}_{\mathrm{p}} \end{bmatrix} = - \begin{bmatrix} \boldsymbol{I} & 0 \\ -\boldsymbol{D} & \boldsymbol{I} \end{bmatrix} \begin{bmatrix} \boldsymbol{K}^{-1}\boldsymbol{R}_{\mathrm{m}} \\ \boldsymbol{R}_{\mathrm{c}} \end{bmatrix}, \tag{4.27}$$

and hence

$$\begin{bmatrix} \boldsymbol{I} & \boldsymbol{K}^{-1}\boldsymbol{G} \\ 0 & \boldsymbol{S} \end{bmatrix} \begin{bmatrix} \boldsymbol{y}_{\mathrm{u}} \\ \boldsymbol{y}_{\mathrm{p}} \end{bmatrix} = - \begin{bmatrix} \boldsymbol{K}^{-1}\boldsymbol{R}_{\mathrm{m}} \\ \boldsymbol{R}_{\mathrm{c}} - \boldsymbol{D}\boldsymbol{K}^{-1}\boldsymbol{R}_{\mathrm{m}} \end{bmatrix}, \tag{4.28}$$

in which

$$\boldsymbol{S} = \boldsymbol{L} - \boldsymbol{D}\boldsymbol{K}^{-1}\boldsymbol{G} \tag{4.29}$$

is the Schur compliment. Since having the Schur compliment as the LHS matrix involves solving another linear system of equations, solving Equation (4.28) in the form shown is expensive and impractical. Hence, $\boldsymbol{K}^{-1}$ is generally replaced by $(\hat{\boldsymbol{K}}_{\mathrm{d}})^{-1}$, which, as we will show, is a reasonable choice only in the absence of $\boldsymbol{K}_{\mathrm{bc}}$. Here we use Equation (4.23) as a PC and as an approximation for $\boldsymbol{K}^{-1}$. Also in the case that the system has $\boldsymbol{K}$ on the LHS, $\boldsymbol{H}$ is used as a PC to improve convergence. A symmetric Jacobi PC can also be used to normalize $\boldsymbol{K}_{\mathrm{mc}}$ and $\boldsymbol{y}$. Putting these together, given $\hat{\boldsymbol{K}}$, $\boldsymbol{K}_{\mathrm{bc}}$, $\boldsymbol{G}$, $\boldsymbol{D}$, $\boldsymbol{L}$, $\boldsymbol{y}_{\mathrm{u}}$, $\boldsymbol{y}_{\mathrm{p}}$, ϵ_{cg}, ϵ_{gm}, and ϵ, the steps of implementation are as follows:

1. Use a symmetric Jacobi PC to normalize $\boldsymbol{K}_{\mathrm{mc}}$ and $\boldsymbol{y}$ such that

$$\boldsymbol{W}_{\mathrm{m}} = \mathcal{D}(\hat{\boldsymbol{K}})^{-\frac{1}{2}}, \tag{4.30}$$

$$\boldsymbol{W}_{\mathrm{c}} = \mathcal{D}(\boldsymbol{L})^{-\frac{1}{2}}, \tag{4.31}$$

$$\boldsymbol{K} \leftarrow \boldsymbol{W}_{\mathrm{m}}\boldsymbol{K}\boldsymbol{W}_{\mathrm{m}}, \tag{4.32}$$

$$\boldsymbol{G} \leftarrow \boldsymbol{W}_{\mathrm{m}}\boldsymbol{G}\boldsymbol{W}_{\mathrm{c}}, \tag{4.33}$$

$$\boldsymbol{D} \leftarrow \boldsymbol{W}_{\mathrm{c}}\boldsymbol{D}\boldsymbol{W}_{\mathrm{m}}, \tag{4.34}$$

$$\boldsymbol{L} \leftarrow \boldsymbol{W}_{\mathrm{c}}\boldsymbol{L}\boldsymbol{W}_{\mathrm{c}}, \tag{4.35}$$

$$\boldsymbol{y}_{\mathrm{u}} \leftarrow \boldsymbol{W}_{\mathrm{m}}\boldsymbol{y}_{\mathrm{u}}, \tag{4.36}$$

$$\boldsymbol{y}_{\mathrm{p}} \leftarrow \boldsymbol{W}_{\mathrm{c}}\boldsymbol{y}_{\mathrm{p}}, \tag{4.37}$$

   in which $\leftarrow$ is the assignment operator. Note $\boldsymbol{W}_{\mathrm{m}}$ and $\boldsymbol{W}_{\mathrm{c}}$ can be employed inside the iterative algorithm as well, leaving the $\boldsymbol{K}_{\mathrm{mc}}$ blocks unchanged. We found that directly applying Jacobi PC to the tangent matrix is more computationally efficient.

2. Use the GMRES method to solve for un-corrected $\boldsymbol{y}_{\mathrm{u}}$. Use $\boldsymbol{H}$ as PC and ϵ_{gm} as tolerance

$$(\boldsymbol{HK})\boldsymbol{y}_{\mathrm{u}} = -\boldsymbol{HR}_{\mathrm{m}}. \tag{4.38}$$

Note, since the Jacobi PC is already applied to $\boldsymbol{K}$, $\hat{\boldsymbol{K}}_{\mathrm{d}} = \boldsymbol{I}$ and Equation (4.22) can be used directly instead of (4.23) to compute $\boldsymbol{H}$.

3. Compute the corrected continuity residual

$$\tilde{\boldsymbol{R}}_{\mathrm{c}} \leftarrow -\boldsymbol{R}_{\mathrm{c}} - \boldsymbol{D}\boldsymbol{y}_{\mathrm{u}}. \tag{4.39}$$

4. Approximate $\boldsymbol{K}^{-1}$ by $\boldsymbol{H}$ and use ϵ_{cg} as tolerance to solve for $\boldsymbol{y}_{\mathrm{p}}$

$$(\boldsymbol{L} - \boldsymbol{DHG})\boldsymbol{y}_{\mathrm{p}} = \tilde{\boldsymbol{R}}_{\mathrm{c}}. \tag{4.40}$$

As discussed in Section 2.1, $\boldsymbol{D}$ is the approximate transpose of $\boldsymbol{G}$. In Equation (4.40) we set $\boldsymbol{D} = \boldsymbol{G}^{\mathrm{T}}$, which allows us to solve the linear system using the conjugate gradient (CG) method. Otherwise, the bi-conjugate gradient method can be used.

5. Correct $\boldsymbol{y}_{\mathrm{u}}$ using

$$\tilde{\boldsymbol{R}}_{\mathrm{m}} \leftarrow \boldsymbol{G}\boldsymbol{y}_{\mathrm{p}}, \tag{4.41}$$

$$(\boldsymbol{HK})\tilde{\boldsymbol{y}}_{\mathrm{u}} = \boldsymbol{H}\tilde{\boldsymbol{R}}_{\mathrm{m}}, \tag{4.42}$$

$$\boldsymbol{y}_{\mathrm{u}} \leftarrow \boldsymbol{y}_{\mathrm{u}} - \tilde{\boldsymbol{y}}_{\mathrm{u}}. \tag{4.43}$$

Note the second call to the GMRES solver in Equation (4.42).

6. If $\|\boldsymbol{K}_{\mathrm{mc}}\boldsymbol{y} - \boldsymbol{R}\| > \epsilon\|\boldsymbol{R}_{\mathrm{i}}\|$, in which $\boldsymbol{R}_{\mathrm{i}}$ is the initial preconditioned residual vector, update $\boldsymbol{y}$ and $\boldsymbol{R}$ and repeat step 3-6, otherwise go to step 8.

7. Apply the Jacobi PC to obtain the final solution

$$\boldsymbol{y}_{\mathrm{u}} \leftarrow \boldsymbol{W}_{\mathrm{m}}\boldsymbol{y}_{\mathrm{u}}, \tag{4.44}$$

$$\boldsymbol{y}_{\mathrm{p}} \leftarrow \boldsymbol{W}_{\mathrm{c}}\boldsymbol{y}_{\mathrm{p}}. \tag{4.45}$$

In total this algorithm involves 2 GMRES solves and 1 CG solve. Generally, the quality of the CG solve determines how well the continuity equation is satisfied. Neglecting $\boldsymbol{H}$ (i.e. replacing it by $\boldsymbol{I}$) leads to a velocity field that poorly satisfies the continuity equation. We refer to this case as *without PC (woPC)* and the full algorithm as *with PC (wPC)* in the results section. We refer to the case in which $\boldsymbol{K}_{\text{mc}}$ is preconditioned by a symmetric Jacobi PC and solved by GMRES as *GMRES* in the results section. Tolerances for the wPC method are $\epsilon = 0.4$, $\epsilon_{\text{cg}} = 0.2$, and $\epsilon_{\text{gm}} = 0.01$. Due to convergence issues, ϵ tolerance is reduced to 0.2 for the woPC method. Since the continuity equation is satisfied at lower tolerances for the GMRES method, ϵ is set to 0.05 for this case. We compare the performance of these methods on several examples in the next section.

4.3 PC test results

To illustrate the performance of the proposed PC method and test the proposed algorithm, three example problems were chosen: 1) A cylindrical pipe model, 2) a thoracic aorta model with detailed coronary artery anatomy, 3) a multidomain closed-loop model of a single ventricle heart patient. In the first case study, we show the effect of the PC on the tangent matrix condition number by varying the outflow resistance value. We also study the dependence of tangent matrix stiffness on the mesh size. The mesh dependency of the proposed method is studied by using a wide range of mesh sizes. We test the algorithm performance in the second case study with a more complex geometry and higher number of elements (larger tangent matrix) at different time step sizes. This model, which contains long and thin branches of the coronary arteries, is intended to test the effectiveness of the proposed method for this class of problems. Using a complex multidomain model, the performance and robustness of the algorithm is tested in the third case study.

4.3.1 Cylindrical model with variable resistance

The first case study is a cylinder with a resistance outlet BC and steady inflow Dirichlet BC. The cylinder diameter and length are 5 and 30 cm, respectively (Figure 4.1).

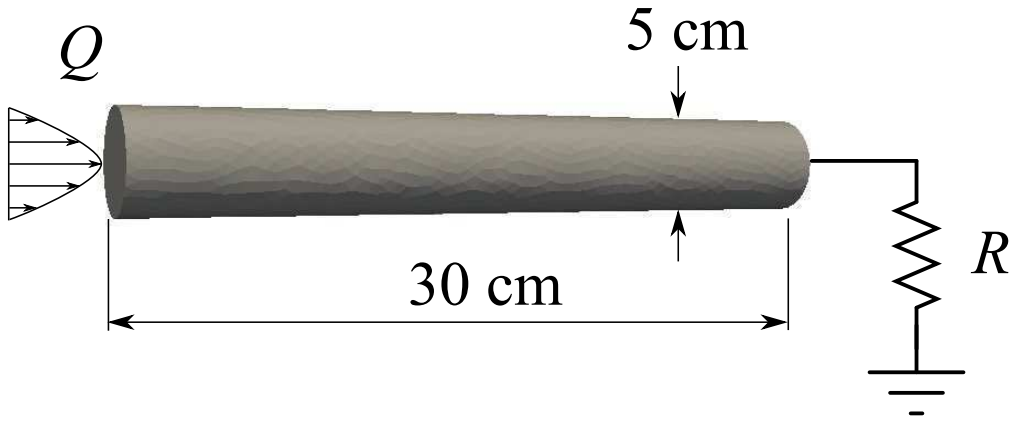

Figure 4.1: The cylindrical model with resistance outlet BC and prescribed inflow BC.

The simulation was run on four processors for 0.5 s with a time step size of 50 ms. This large time step size was selected to produce a stiff LHS matrix, hence testing the proposed method in an extreme situation. The non-linear iterations continued until $\frac{\|\boldsymbol{R}\|}{\|\boldsymbol{R}_0\|} < 10^{-3}$, where $\boldsymbol{R}_0$ is the residual vector at $t = 0$, or the number of iterations exceeded 8. The model was meshed with 331K tetrahedral linear elements producing over 14M non-zero entries in the tangent matrix. A parabolic velocity profile was prescribed on the inflow face with an average value of 10 cm/s, producing Re = 1325. The resistance value was varied over a range of values to study the effect of the PC on the computational cost. Our results show that the simulation cost with the preconditioned matrix is nearly independent of the outflow resistance value, whereas without the PC the cost goes up significantly with increasing resistance (Figure 4.2). Comparing the computational cost of the woPC case to GMRES case at low resistances demonstrates the effectiveness of the LS algorithm. At higher resistances, the woPC algorithm was unstable. With an outlet resistance of 1000 g/(s cm^4) the simulation diverged and is not shown. In

the woPC simulation, the time step size was reduced to 10 ms for resistance 100 g/(s cm^4) to obtain a stable solution.

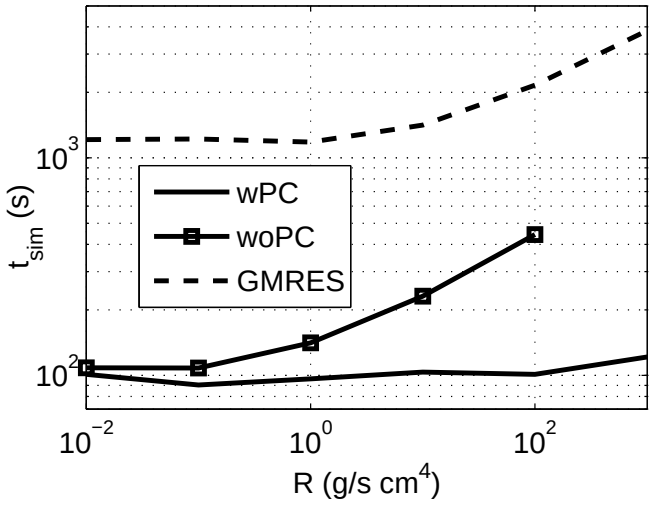

Figure 4.2: The effect of boundary resistance on the computational cost. Using the PC has produced a nearly independent simulation cost from the resistance value, reducing the cost significantly compared to without PC or GMRES at higher resistances.

To perfectly satisfy the continuity equation, the outlet flow rate must be equal to the inlet flow rate. The normalized difference between these two flow rates at $t = 0.5$s is shown in Figure 4.3 as a function of outlet resistance. Although a smaller ϵ value was used for the GMRES method, the woPC and wPC methods have satisfied the continuity equation more accurately at all resistance values.

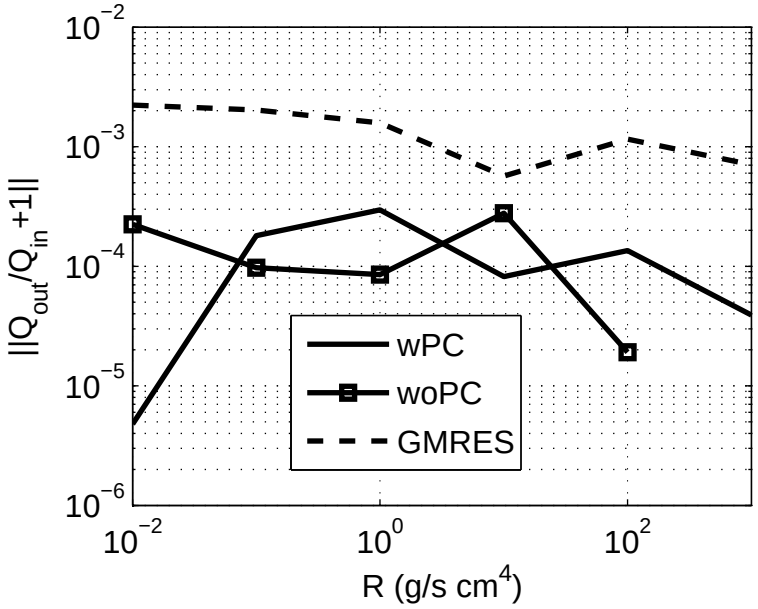

Figure 4.3: The effect of boundary resistance on the continuity equation solution error.

To study the effect of mesh resolution on LS performance, we used the cylinder model with a resistance value of 10 g/(s cm^4). The model was meshed with 24, 109, 331, 1449 K tetrahedral elements, producing 1.11, 4.82, 14.18, and 60.41 M non-zero entries in the LHS matrix.

Increasing the number of elements by 1 order of magnitude, the wPC method had the best speedup by 1.6 orders of magnitude increase in the computational cost. The increase in the computational cost was 1.7 and 1.9 orders of magnitude for the woPC and GMRES, respectively (Figure 4.4).

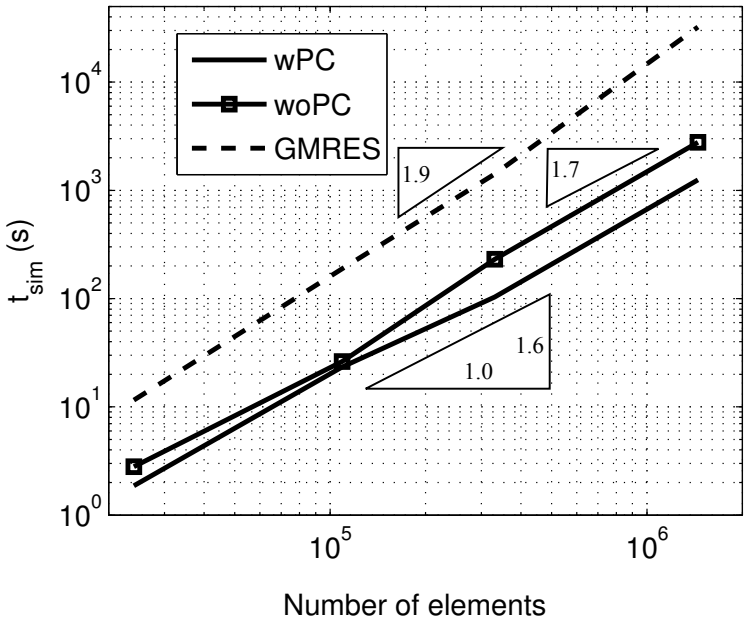

Figure 4.4: The effect of mesh size on the computational cost.

Comparing to the standard theoretical Poiseuille solution, ΔP_{th}, the errors in the simulated pressure drop at $t = 0.5$ s are shown in Figure 4.5. This error depends on the quality of the momentum equation solution. Due to the lower tolerance of the GMRES method, this method generally predicts pressure drop more accurately.

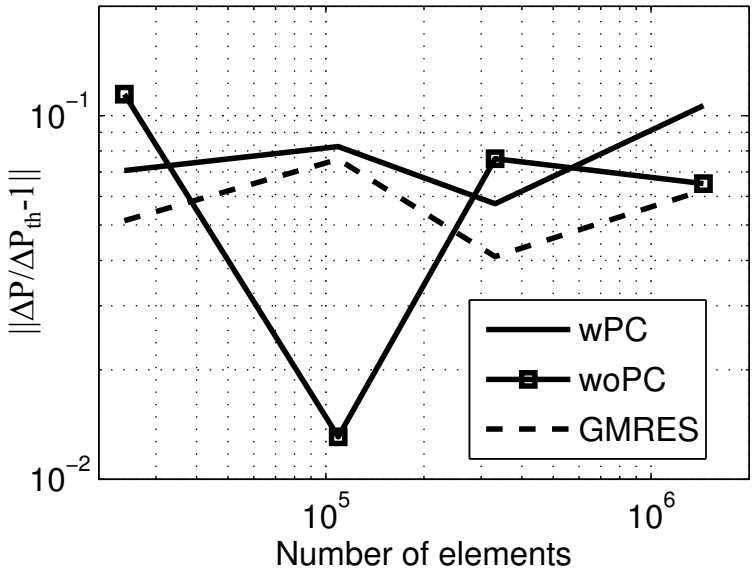

Figure 4.5: The effect of mesh size on the pressure drop prediction error.

To study the effect of the PC on the convergence rate of GMRES calls in the full algorithm, we consider a case with the mesh with 109 K elements and outlet resistance of 1000 g/(s cm^4). The error in GMRES solves (Equations (4.38) and (4.42)) versus iteration number is shown in Figure 4.6. In this case, applying the PC is equivalent to a single iteration of the GMRES solver, hence reducing the number of iterations by one for each GMRES call. This suggests that at negligible computation cost a major reduction in the residual can be obtained by applying the PC. As a result, major improvement in overall convergence is obtained by including $\boldsymbol{H}$ in Equation (4.40).

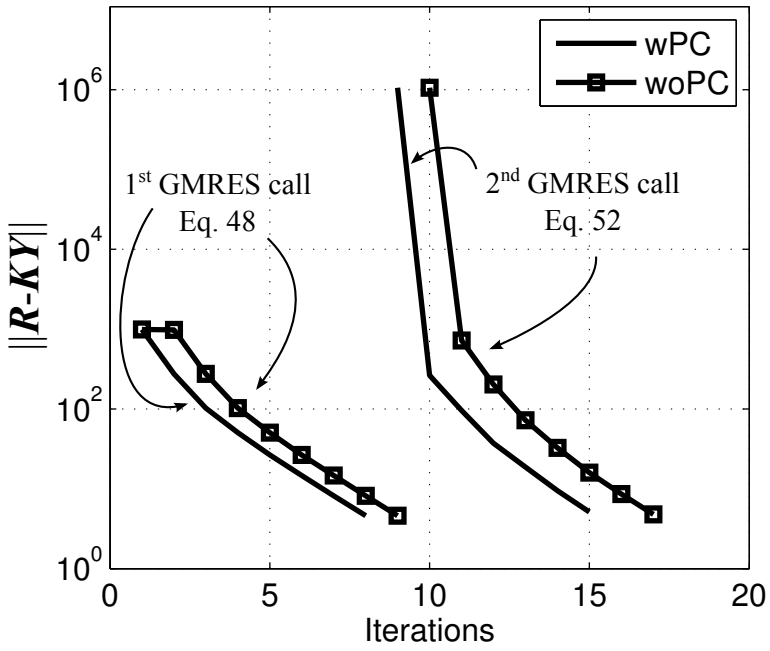

Figure 4.6: The effect of including $\boldsymbol{H}$ (wPC) and replacing it by $\boldsymbol{I}$ (woPC) on the convergence rate of GMRES calls in Equations (4.38) and (4.42).

4.3.2 Aorta model

The second case study is a patient specific model of an aorta with coronary arteries (Figure 4.7) in a patient with Kawasaki disease [41, 77]. The BCs are resistances at 15 outlets and a Dirichlet steady flow condition at the inlet. The inlet flow and outlet resistances are based on physiological values [41]. The inlet flow rate is 13.29 cm^3/s and outlet resistances are 3.7×10^5, 3.5×10^3, $1.25-1.75\times10^4$ $\mathrm{g}/(\mathrm{s\ cm}^4)$ for the coronary arteries, the descending aorta, and the head and neck vessels, respectively. Since this model has longer branches, it is a good candidate for evaluating the performance of the proposed method subjected to abrupt changes of the inlet flow rate that need to travel from the inlet to the outlets. Hence to examine only these transient effects in the measured performance, we chose not to continue this simulation longer that 0.01 s. The simulation was run on 64 processors with a time step size of 1 ms and 0.2 ms. Similar to Section 4.3.1, the non-linear iterations were continued until the relative norm of the residual

vector reduced to 10^{-3} or the number of iterations exceeded 8. Using boundary layer meshing and a denser mesh for smaller branches produced 2.7 M tetrahedral elements for this model (Figure 4.7).

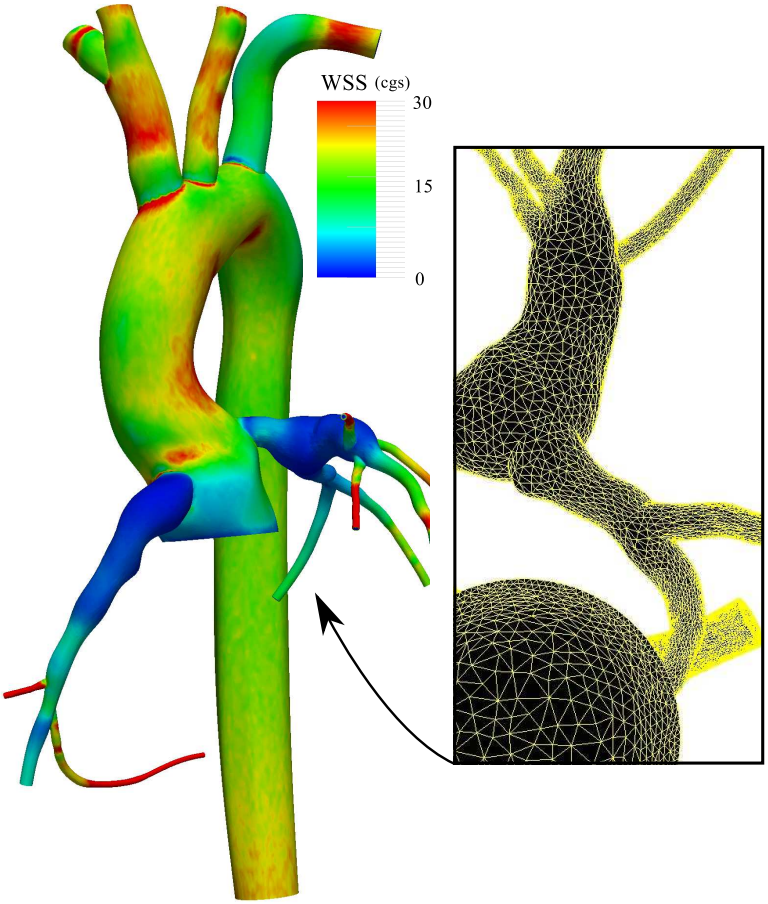

Figure 4.7: The patient specific model with coronary arteries. WSS contour and adapted tetrahedral mesh are shown.

As shown in Table 4.1, using the PC has reduced the simulation time by a factor of 7.8 for $\Delta t = 0.2$ ms and 15.6 for $\Delta t = 1$ ms compared to the standard GMRES method, and by a factor of 3.3 compared to the method without PC. Due to the high resistance values, a time step size of 1 ms produces a relatively ill-conditioned tangent matrix, causing the woPC case to diverge and GMRES to take a long time to converge. With the same time step size, wPC is still efficient

Table 4.1: Comparison between simulation times and *err* at different time step sizes, Δt, using the coronary model. t_{sim} denotes the simulation time and the error (err) is defined as $10^5 |Q_{\text{in}}^{-1} \sum_{i=1}^{16} Q^i|$.

method	Δt (ms)	t_{sim} (s)	err
wPC	0.2	560	2.798
woPC	0.2	1850	2.655
GMRES	0.2	4389	13.99
wPC	1	284	1.534
woPC	1	-	-
GMRES	1	4435	32.05

and stable. For the woPC case, ϵ_{cg} is reduced to 0.1 at 0.2 ms time step size to obtain a stable solution. As in the previous case, the wPC and woPC methods satisfy the continuity equation better than the GMRES method.

Since the norm of the residual has reduced below the specified limit for all simulations, results confirm that little difference was found between the three methods (Figure 4.8).

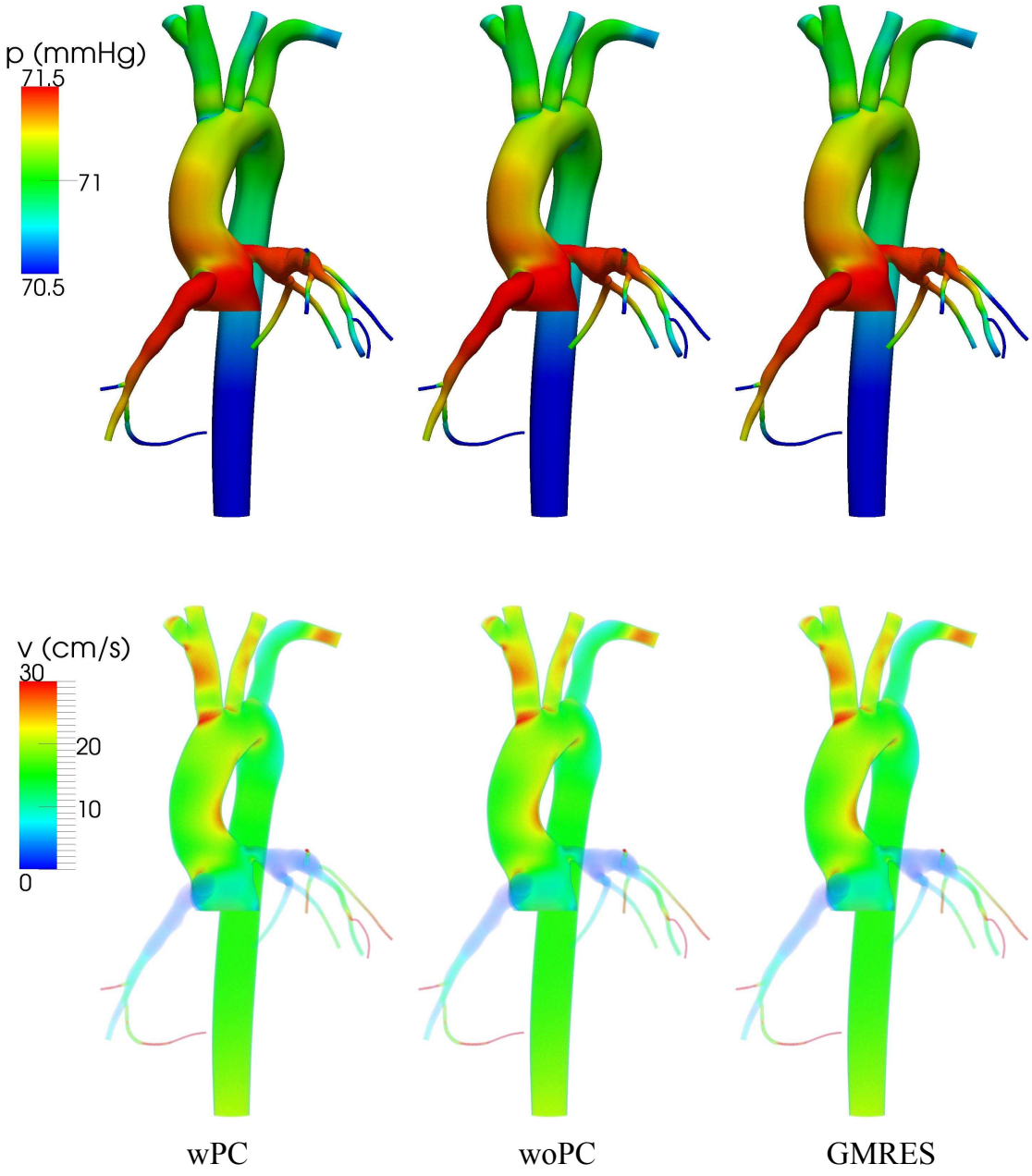

Figure 4.8: Pressure contours and volume-rendered velocities for the coronary model, using the results of simulation with $\Delta t = 0.2$ ms.

Table 4.2: Comparison of simulation times, cardiac output (CO) and average aortic pressure ($\bar{P}_{\text{AA}}$), using the multidomain model with different LS methods. t_{sim} denotes the simulation time.

method	t_{sim} (s)	CO (L/min)	$\bar{P}_{\text{AA}}$ (mmHg)
wPC	2087	1.1403	45.31
woPC	4119	1.1407	45.25
GMRES	9114	1.1403	45.46

4.3.3 Single-ventricle multidomain model

In the third example we consider an idealized post surgical anatomy of a single ventricle heart patient, presented in Section 2.4.4. Flow simulations were performed using a multidomain approach, in which the 0D domain consists of a LPN that models the heart and downstream circulation (Figure 2.11) [16, 25, 80]. All outlets are coupled Neumann boundaries and the inlet, i.e. the AA, is a coupled Dirichlet boundary in this case. Due to the presence of reversed flow at the outlets, stabilization method described in Section 3.1.1 is used at the coupled Neumann boundaries to avoid rapid simulation divergence.

An interior maximum element edge length of 0.625mm was chosen for this study. The maximum edge length for the coronary artery wall was 0.25mm and the maximum edge length for the other walls was 0.5mm, producing approximately 340K elements. The simulation was run on 32 processors for five cardiac cycles (2.5 s) with a time step size of 1 ms. Similar to Section 4.3.1, the non-linear iterations were continued until the norm of the residual vector reduced to 10^{-3} or the number of iterations exceeded 8.

The costs of GMRES and woPC simulations were 2.0 and 4.3 times higher than the wPC (Table 4.2) simulation. The differences between the predicted cardiac output and average aortic pressures were well below the clinically accepted tolerances, with qualitatively indistinguishable differences (Figure 4.9). The outlet flow waveforms were also very similar for all methods.

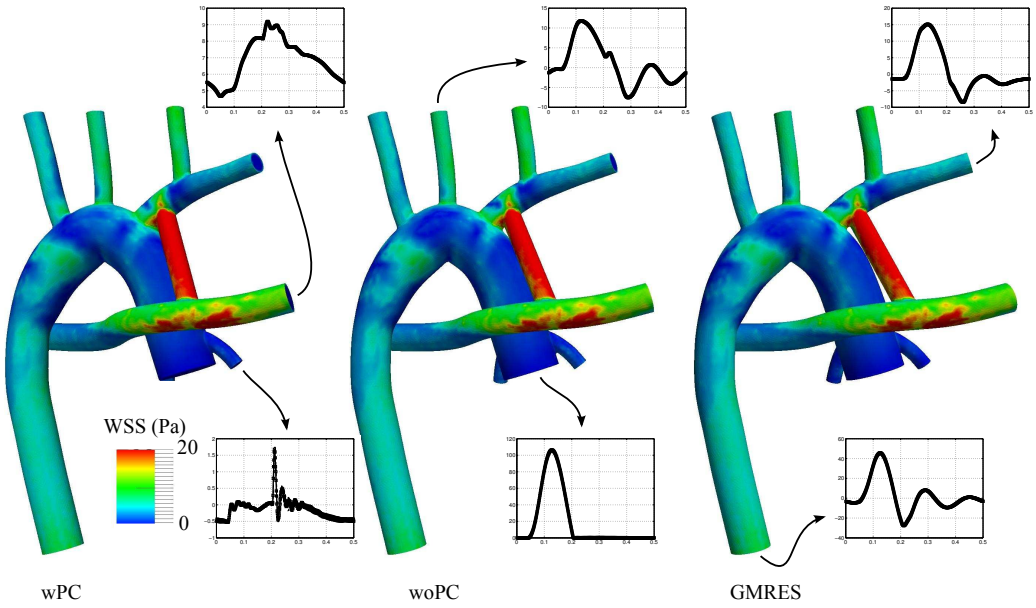

Figure 4.9: The multidomain model outlet flow rates (in cm^3/s) versus time and WSS at peak systole.

4.4 Discussion

Due to the wide range of scales and nonlinearities, efficient solution of the Navier-Stokes equations is computationally challenging. In the context of cardiovascular simulations, the pressure drop inside the model is typically orders of magnitude lower than the boundary pressure. The dependence of boundary pressure on flow rate, as is the case for the coupled Neumann boundaries, introduces a small number of eigenvalues into the tangent matrix with significant effect on the solution. For instance, the flow split in a bifurcation highly depends on the BCs used for the daughter branches rather than the 3D geometry. This is shown by an example in Figure 4.10, which is a schematic of flow in a parent branch that bifurcates to two branches, each coupled to a resistance. We showed that high resistance values produce an ill-conditioned tangent matrix that increases computational cost significantly. We also showed that a PC can be employed for the coupled Neumann BC that exploits the presence of a few dominant eigenvalues

in the tangent matrix to dramatically improve LS efficiency. This PC greatly improves the condition number of the tangent matrix, hence reducing the number of iterations and computational cost.

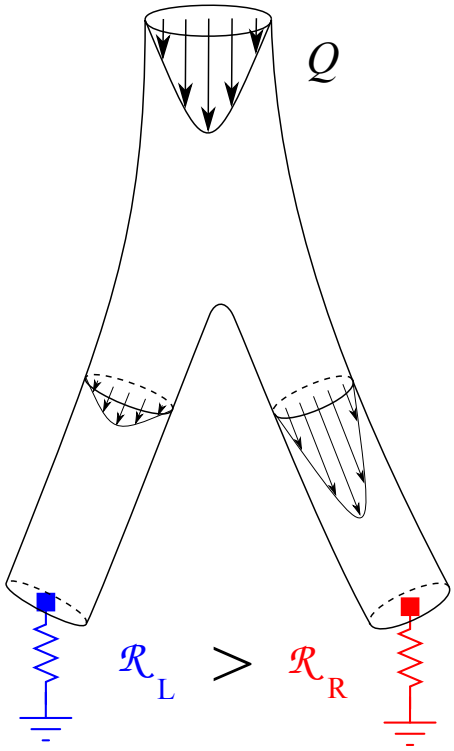

Figure 4.10: Schematic of flow in a bifurcating vessel with resistance BC at outlets and inflow condition at the inlet. For high resistance values, flow split to the right and left branches highly depends on the BC, rather than the 3D geometry.

Perturbations on one side of a domain travel through to the other side to affect the solution on the other side. From this perspective, the continuity equation has a significant impact on the overall solution quality. The standard GMRES method is designed to minimize the norm of the residual vector, regardless of how essential the solution quality is of each particular equation (continuity vs. momentum). Hence, for the GMRES method a very tight tolerance is required to sufficiently reduce the momentum equation residual before reducing the continuity equation residual, even after using the Jacobi PC. In the proposed method, a combination of iterative solvers, i.e. CG and GMRES, is used as the main algorithm.

In this method, the tangent matrix is decomposed into sub-blocks and velocity and pressure are solved separately. Having a symmetric Schur compliment allows use of the CG algorithm, which is an effective iterative method to deal with the continuity equation. This allows a relief on the tolerance, reducing the overall computational cost furthermore. At lower resistances or in the absence of coupled Neumann BCs, this method was shown to be effective by reducing the computational cost by an order of magnitude compared to the pure GMRES method. This method showed better scalability characteristics with mesh size (size of tangent matrix) compared to GMRES alone.

The combination of the proposed LS and PC provides a powerful algorithm that can be applied to a wide range of problems, including those with coupled Neumann boundaries and stiff problems with large time step sizes, by improving the tangent matrix condition number, solving the continuity equation more accurately, and significantly reducing the computational cost. This increase in efficiency could have far reaching implications for numerous cardiovascular disease and device applications, enabling solutions of larger and more detailed models, or higher throughput of simulations in studies with a larger number of patients.

Acknowledgements

This chapter, in full, is a reprint of the material as it appears in A new preconditioning technique for implicitly coupled multidomain simulations with applications to hemodynamics, *Computational Mechanics*, 2013, DOI: 10.1007/s00466-013-0868-1. Authors are M. Esmaily-Moghadam, Y. Bazilevs, and A. Marsden. The dissertation author was the primary investigator and author of this paper.

Chapter 5

Parallel Algorithms for Iterative Linear Solvers

Large systems of linear equations arise in many areas of computational science and engineering. They are often a byproduct of a finite-difference, finite-volume, or finite-element discretization of partial differential equations (PDEs) governing the behavior of a given physical system. The software written for a given set of PDEs typically assembles the linear equation system, which is then passed to a LS to produce the discrete solution. Solving large linear systems of equations is a computationally demanding process that often requires using high performance parallel computing. For large problems, due to memory limitations and scalability issues, an iterative LS is generally preferred to its direct counterpart, especially for the solution of time-dependent PDEs.

Parallel processing is utilized to offset the high computational cost of large-scale PDE-based simulations. However, designing efficient parallel algorithms for this class of problems remains a challenge and continues to attract significant attention in the community [34, 35, 36]. In PDE-based simulations, to ensure the required continuity of the solution field, a significant portion of the total computational time is spent in the inter-processor communications. In particular, most of the inter-processor communications occur inside the LS, where the entire discrete solution, although partitioned between the processors, is calculated simultaneously using global operations. Global operations require collective or processor-to-

processor communications that are costly, in large part due to the need for waiting before sending or receiving messages. This wait time, in turn, contributes a large portion of the overall wall-clock time for multi-processor simulations. In addition, for large problems, the overall communication time can further increase because of a larger number of processors employed.

In this chapter we present an algorithm for efficient handling of parallel algebraic operations in iterative solvers. By mapping the sparse matrix row and column indices on each processor, a *low-entropy data structure* is obtained that leads to efficient and scalable parallel communications.

The chapter is outlined as follows. In Section 5.1, after briefly recalling the basic concepts, we present and explain an algorithm to produce the appropriately sorted node list. We then show how to use the sorted node list to perform algebraic operations commonly used in iterative LS: matrix-vector product and vector inner product. The proposed approach allows some overlap between communication and computation, which is key for improving parallel efficiency. In Section 5.2, we test the method using three incompressible flow example problems. A FE discretization is employed and the cases are tested using a wide range of mesh sizes and processor numbers. To establish a baseline for the performance of the proposed algorithm, the results are compared with PETSc [123]. The advantages of using the low-entropy data structure are clearly demonstrated using the numerical examples.

5.1 Sorted data structure

In this section, we discuss a general approach for performing basic algebraic operations in parallel, present the data sorting algorithm, and describe its implementation. Assuming that the underlying PDE is scalar-valued, we associate the unknowns in the linear system of equations with the mesh nodes. As a result, the terms *node* and *entry* may used interchangeably. This is done for simplicity of exposition and is not a requirement of the proposed method. In what follows, subscripts g and s are generally used to denote the global and sorted counterparts, respectively. Indices i, j, and k are used for processor IDs, and p and q for node

IDs.

5.1.1 Basic concepts

The first step in solving a PDE in parallel is to partition the mesh and assign each processor to a partition (i.e., a subdomain). As a result, in what follows, the terms *processor ID* and *partition number* will have the same meaning. There are two choices for mesh partitioning, namely, node-based (also called vertex-based) and element-based, in which elements and nodes are shared between adjacent processors, respectively.

We adopt the element-based partitioning approach. The physical domain $\Omega \subset \mathbb{R}^{\text{nsd}}$ is partitioned into a set of non-overlapping subdomains Ω^i as

$$\bigcup_{i=1}^{n_{\text{p}}} \Omega^i = \Omega, \tag{5.1}$$

$$\Omega^i \cap \Omega^j = \Gamma^{ij}, \tag{5.2}$$

where n_{p} is the number of subdomains assumed to be equal to the number of MPI processors, and Γ^{ij}, an $\text{nsd}-1$-dimensional manifold in $\mathbb{R}^{\text{nsd}}$, is the boundary between the subdomains i and j. In this case, the information corresponding to nodes on Γ^{ij} is shared between the processors.

We denote a linear system of equations by

$$\boldsymbol{A}\boldsymbol{x} = \boldsymbol{b}, \tag{5.3}$$

where $\boldsymbol{A}$ is an $n \times n$ LHS matrix, $\boldsymbol{b}$ is an $n \times 1$ right-hand-side vector, and $\boldsymbol{x}$ is an $n \times 1$ solution vector.

After assembling the matrix and vector regardless of the neighboring subdomains, each processor contains a part of $\boldsymbol{A}$ and $\boldsymbol{b}$,

$$\sum_{i=1}^{n_{\text{p}}} \boldsymbol{A}_{\text{g}}^i = \boldsymbol{A}, \tag{5.4}$$

$$\sum_{i=1}^{n_{\text{p}}} \boldsymbol{b}_{\text{g}}^i = \boldsymbol{b}, \tag{5.5}$$

where $\boldsymbol{A}^i_{\mathrm{g}}$ and $\boldsymbol{b}^i_{\mathrm{g}}$ are the global representations of the contributions of Ω^i to the LHS matrix and right-hand-side vector, respectively.

Denoting the number of non-zero entries in $\boldsymbol{b}^i_{\mathrm{g}}$ by n^i, the non-zero entries of $\boldsymbol{b}^i_{\mathrm{g}}$ can be mapped to a local vector, $\boldsymbol{b}^i$, using a permutation matrix $\boldsymbol{P}^i$ as

$$\boldsymbol{b}^i = \boldsymbol{P}^i \boldsymbol{b}^i_{\mathrm{g}}. \tag{5.6}$$

The transpose of the permutation matrix may be written as

$$\boldsymbol{P}^{i\mathrm{T}} = \left[\mathbf{1}^{a^i(1)}\ \mathbf{1}^{a^i(2)}\ \cdots\ \mathbf{1}^{a^i(n^i)}\right], \tag{5.7}$$

where $\mathbf{1}^p$ is a vector with a unit entry at location p, i.e.,

$$1^p(q) = \begin{cases} 0 & q \neq p \\ 1 & q = p, \end{cases} \tag{5.8}$$

and $\boldsymbol{a}^i$ is the unsorted list of all nodes in subdomain Ω^i. Similarly, the LHS may be written as

$$\boldsymbol{A}^i = \boldsymbol{P}^i \boldsymbol{A}^i_{\mathrm{g}} \boldsymbol{P}^{i\mathrm{T}}, \tag{5.9}$$

where $\boldsymbol{A}^i$ is the local counterpart of $\boldsymbol{A}^i_{\mathrm{g}}$.

In general, the distribution of non-zero entries in $\boldsymbol{b}^i_{\mathrm{g}}$, or a particular column or row of $\boldsymbol{A}^i_{\mathrm{g}}$ does not follow a specific rule. Hence, the shared entries between $\boldsymbol{b}^i$ and $\boldsymbol{b}^j$ are randomly distributed among the unshared entries. From the point of view of inter-processor communication this randomness has some drawbacks. A random distribution requires random fetches from the main memory during the communications, which reduces the cache hit ratio. Furthermore, shared entries need special handling that largely depends on the nature of the algebraic operations performed. In what follows, we present a local-to-global node mapping that removes the above mentioned drawbacks, and leads to a reduced communication overhead.

5.1.2 Local data representation

The most common algebraic operations that take place in iterative linear algebra solvers can be divided into three groups:

1. Addition and scaling of vectors. These operations are simple and produce mathematically consistent results regardless the node ordering.

2. Calculation of vector inner products and norms. In this group of operations special care must be taken when handling the shared entries of $\boldsymbol{b}^i$ and $\boldsymbol{b}^j$. A traditional approach is to send the shared entries from processor j to processor i, set the shared entries on j to zero, perform the operation on the vectors local to the processors, and sum the values on all processors to obtain the final result.

3. Calculation of matrix-vector products. Special care is also required here since the shared rows in $\boldsymbol{A}^i$ only contain a part of the corresponding rows in $\boldsymbol{A}$, which is a consequence of element-based partitioning. Traditionally, the product $\boldsymbol{y} = \boldsymbol{A}\boldsymbol{x}$ is calculated in parallel using four steps: First, it is ensured that shared entries of $\boldsymbol{x}^i$ and $\boldsymbol{x}^j$ have the same values; Second, the local-to-processor matrix-vector products are performed; Third, the shared entries of $\boldsymbol{y}^i$ and $\boldsymbol{y}^j$ are added; Finally, the results are "scattered" back to processors i and j.

To obtain a more favorable substrate for the second and third group of operations, we start from the list of global node IDs $\boldsymbol{a}^i$, and modify it to produce a sorted list $\boldsymbol{a}^i_{\mathrm{s}}$ using the mapping $\boldsymbol{\mathcal{M}}^i$, where

$$p_{\mathrm{s}} = \mathcal{M}^i(p), \tag{5.10}$$

$$a^i_{\mathrm{s}}(p_{\mathrm{s}}) = a^i(p), \tag{5.11}$$

and $p, p_{\mathrm{s}} \in \{1, \ldots, n^i\}$. In practice, $\boldsymbol{\mathcal{M}}^i$ is a pointer array with length n^i that orders the local representation of data. The mapping $\boldsymbol{\mathcal{M}}^i$ is found, such that, given n^i and $\boldsymbol{a}^i$, the following holds:

1. The owner of a node p shared between m processors $\{i^1, \cdots, i^m\}$ is i^m, given $i^m > i^j \ \forall j \in \{1, \cdots, m-1\}$. In this case, processor i^m is called the owner of p and $i^j \ \forall j \neq m$ will only keep a copy of node p.

2. The conditions
$$\left.\begin{array}{c} a_{\mathrm{s}}^i(p) \in \boldsymbol{a}_{\mathrm{s}}^j \\ a_{\mathrm{s}}^i(q) \notin \boldsymbol{a}_{\mathrm{s}}^k \; \forall k \neq i \\ i < j \end{array}\right\} \Rightarrow q < p, \tag{5.12}$$
are satisfied. In this case p is possibly owned by j, and q is "only" owned by i.

3. The conditions
$$\left.\begin{array}{c} a_{\mathrm{s}}^i(p) \in \boldsymbol{a}_{\mathrm{s}}^j \\ a_{\mathrm{s}}^i(q) \notin \boldsymbol{a}_{\mathrm{s}}^k \; \forall k \neq i \\ j < i \end{array}\right\} \Rightarrow p < q, \tag{5.13}$$
are satisfied similar to those in Equation (5.12), which ensure that entries shared by the lower- and higher-numbered processors are located in the beginning and end of the vector, respectively. Note that both p and q are owned by i in Equation (5.13).

Equation (5.12) presents a more relaxed set of conditions compared to those presented in [124], which are repeated here for convenience:
$$\left.\begin{array}{c} a_{\mathrm{s}}^i(p) \in \boldsymbol{a}_{\mathrm{s}}^j \\ a_{\mathrm{s}}^i(q) \in \boldsymbol{a}_{\mathrm{s}}^k \\ j < k \end{array}\right\} \Rightarrow p < q. \tag{5.14}$$
Equation (5.14) ensures a fully sorted vector from low to high processor ID on any processor i, while Equations (5.12) and (5.13) only mandate unowned entries to be located at the end, and owned, shared entries at the beginning of the vector (see Figure 5.1 for an illustration). This simplifies the computation of $\boldsymbol{\mathcal{M}}$, specifically in cases that an entry is shared between more than two processors, hence eliminating the need to track these entries and to use an extra hash table.

We denote the last owned shared entry by n_{s}^i and the last owned unshared entry by n_{o}^i, i.e.,
$$n_{\mathrm{s}}^i = \sup\left\{p \in \{1, \ldots, n^i\} : \boldsymbol{a}_{\mathrm{s}}^i(p) \in \boldsymbol{a}_{\mathrm{s}}^j, j < i\right\}, \tag{5.15}$$
and
$$n_{\mathrm{o}}^i = \sup\left\{p \in \{1, \ldots, n^i\} : \boldsymbol{a}_{\mathrm{s}}^i(p) \notin \boldsymbol{a}_{\mathrm{s}}^j, \forall j \neq i\right\}. \tag{5.16}$$

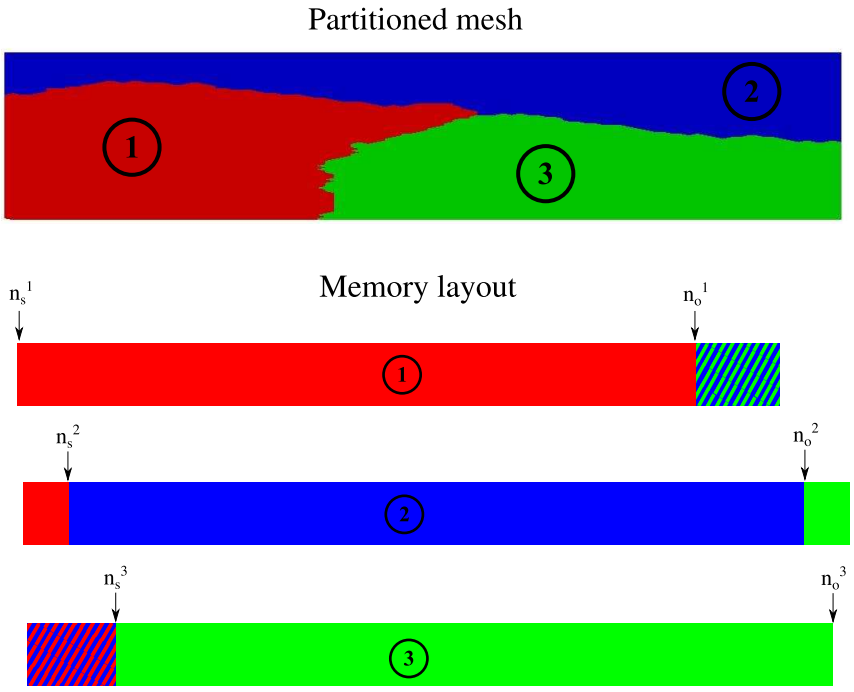

Figure 5.1: Data distribution in memory for a partitioned mesh with 3 processors. Encircled numbers denote processor IDs. The initial and final segments of vectors are shared by lower and higher processors, respectively. Hatched areas with multiple colors show segments of vectors that contain entries shared with processors with corresponding colors.

Note that

$$n_{\mathrm{s}}^i = \inf\left\{p \in \{1,\ldots,n^i\} : \boldsymbol{a}_{\mathrm{s}}^i(p) \notin \boldsymbol{a}_{\mathrm{s}}^j, \forall j \neq i\right\} - 1, \tag{5.17}$$

and

$$n_{\mathrm{o}}^i = \inf\left\{p \in \{1,\ldots,n^i\} : \boldsymbol{a}_{\mathrm{s}}^i(p) \in \boldsymbol{a}_{\mathrm{s}}^j, i < j\right\} - 1. \tag{5.18}$$

(See Figure 5.1 for an illustration.)

Given $\boldsymbol{a}^i$, n^i, n, and n_{p}, we obtain $\boldsymbol{\mathcal{M}}^i$ as follows:

1. Construct a global-to-local array $\boldsymbol{a}_{\mathrm{g}}^i$ with size n that is initialized to zero and communicate $\{\boldsymbol{a}^1,\ldots,\boldsymbol{a}^{n_{\mathrm{p}}}\}$ between all processors to construct an $\max(n^i)\times n_{\mathrm{p}}$-dimensional array $\boldsymbol{d}^i$ as:

```
a_g^i ← 0
do p = 1, ··· , n^i
   a_g^i(a^i(p)) ← p
   do j = 1, ··· , n_p
      d^i(p, j) ← a^j(p)
```

2. Construct the shared segments of $\boldsymbol{a}_{\mathrm{s}}^i$ as:

```
n_s^i ← 0
n_o^i ← n^i
do j = n_p, ··· , 1
   if j ≠ i
      do p = 1, ··· , n^j
         p_g ← d^i(p, j)
         q ← a_g^i(p_g)
         if q ≠ 0
            if d^i(q, i) ≠ 0
               d^i(q, i) ← 0
               if j < i
                  n_s^i ← n_s^i + 1
                  a_s^i(n_s^i) ← p_g
               else
                  a_s^i(n_o^i) ← p_g
                  n_o^i ← n_o^i − 1
```

Note the third *if* statement and the assignment statement that follows it, where $\boldsymbol{d}^i(:, i)$ is used to make sure that the nodes are included in $\boldsymbol{a}^i_{\mathrm{s}}$ only once.

3. Construct the rest of $\boldsymbol{a}^i_{\mathrm{s}}$, the segment that contains nodes only owned by i, as:

```
q ← n_s^i + 1
do  p = 1, ··· , n^i
   p_g ← d^i(p, i)
   if  p_g ≠ 0
      a_s^i(q) ← p_g
      q ← q + 1
```

4. Reconstruct the global-to-local array $\boldsymbol{a}^i_{\mathrm{g}}$ based on the sorted list $\boldsymbol{a}^i_{\mathrm{s}}$, and calculate the mapping array as:

```
do  p = 1, ··· , n^i
   a_g^i(a_s^i(p)) ← p

do  p = 1, ··· , n^i
   M^i(p) ← a_g^i(a^i(p))
```

Remarks:

1. The above algorithm assumes that all arrays start from index 1, which is the Fortran default.

2. As superscript i suggests, all arrays are processor-specific, and calculations are performed independently on all processors.

3. The proposed method is not memory intensive. The largest arrays employed, $\boldsymbol{a}^i_{\mathrm{g}}$ and $\boldsymbol{d}^i$, are approximately n bytes each. This value is independent of the number of processors, hence the memory requirements do not increase with n_{p}.

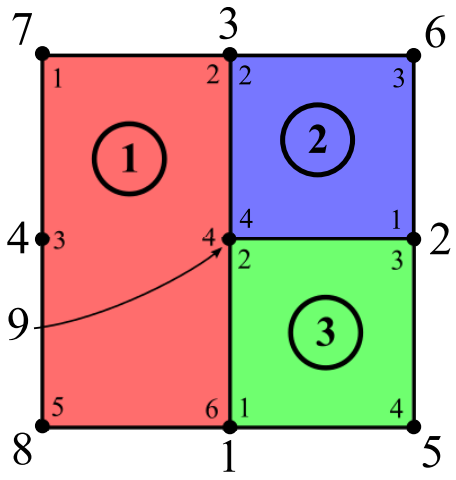

Figure 5.2: An example of a mesh with 9 nodes partitioned to three subdomains that are denoted by encircled numbers. The global and local node IDs are shown using the numbers outside and inside of the box, respectively. For example, node 9 (central node) is local node 2 on processor 3 and 4 on processors 1 and 2.

4. The number of operations is also proportional to n on each processor, therefore the wall-clock time for the calculations is independent of n_{p} as well. This is confirmed by the test cases reported in the numerical results section.

We present a simple example to illustrate the node numbering scheme and the data structures employed. We consider a 2D four-element and nine-node mesh decomposed into three processors, with $n^1 = 6$, $n^2 = 4$, and $n^3 = 4$ (see Figure 5.2 for an illustration). Assuming an unsorted list of nodes for each partition,

$$\boldsymbol{a}^1 = \begin{bmatrix} 7 \\ 3 \\ 4 \\ 9 \\ 8 \\ 1 \end{bmatrix}, \boldsymbol{a}^2 = \begin{bmatrix} 2 \\ 3 \\ 6 \\ 9 \end{bmatrix}, \boldsymbol{a}^3 = \begin{bmatrix} 1 \\ 9 \\ 2 \\ 5 \end{bmatrix}, \tag{5.19}$$

we use the above algorithm to obtain

$$\boldsymbol{a}_{\mathrm{s}}^1 = \begin{bmatrix} 7 \\ 4 \\ 8 \\ 3 \\ 9 \\ 1 \end{bmatrix}, \boldsymbol{a}_{\mathrm{s}}^2 = \begin{bmatrix} 3 \\ 6 \\ 2 \\ 9 \end{bmatrix}, \boldsymbol{a}_{\mathrm{s}}^3 = \begin{bmatrix} 2 \\ 9 \\ 1 \\ 5 \end{bmatrix}, \tag{5.20}$$

and

$$\boldsymbol{\mathcal{M}}^1 = \begin{bmatrix} 1 \\ 4 \\ 2 \\ 5 \\ 3 \\ 6 \end{bmatrix}, \boldsymbol{\mathcal{M}}^2 = \begin{bmatrix} 3 \\ 1 \\ 2 \\ 4 \end{bmatrix}, \boldsymbol{\mathcal{M}}^3 = \begin{bmatrix} 3 \\ 2 \\ 1 \\ 4 \end{bmatrix}. \tag{5.21}$$

In this example, $n_{\mathrm{s}}^1 = 0$, $n_{\mathrm{o}}^1 = 3$, $n_{\mathrm{s}}^2 = 1$, $n_{\mathrm{o}}^2 = 2$, $n_{\mathrm{s}}^3 = 3$, and $n_{\mathrm{o}}^3 = 4$. There are two shared nodes between any two processors, hence two blocks of data with length two are sent and received in a communication after a matrix-vector product. More discussion is given in the what follows.

Benefits for vector inner-product and norm computations. In the computation of a vector norm that is mapped by $\boldsymbol{\mathcal{M}}^i$, only locally owned entries are considered. In practice this can be achieved by simply setting the upper limit of the nested loop to n_{o}^i instead of n^i. This is a valid approach since all the entries following n_{o}^i are owned by other processors and will be included in the calculations exactly once. As a result, the entries of $\boldsymbol{b}^i(p),\ p \in \{n_{\mathrm{o}}^i + 1, \cdots, n^i\}$ do not have any effect on the norm or dot product calculation and may retain any value. This is in contrast to the traditional method that requires setting those entries to zero to avoid computing a single entry twice. The proposed renumbering reduces extra computations associated with the assignment of the entries $n_{\mathrm{o}}^i + 1$ to n^i to zero and looping over them. Also, depending on how an iterative LS is implemented, the proposed mapping can reduce the amount of data communicated between the

processors. Note that $\sum_{i=1}^{n_\mathrm{p}} n_\mathrm{o}^i = n$ is the number of nodes participating in the inner-product computation. It is coincident with the total number of nodes in the mesh, and is independent of the number of mesh partitions n_p.

Benefits for matrix-vector product computations. Using the sorted list of nodes is also beneficial in matrix-vector products. The benefits are achieved by using non-blocking communications calls overlapped with computations. The parallel procedure involves the following steps:

1. Perform the matrix-vector products at the processor level for the shared rows, from 1 to n_s^i and from $n_\mathrm{o}^i + 1$ to n^i.

2. Wait for the send requests.

3. Copy the resulting values in the shared entries to the buffer, and call non-blocking processor-to-processor send and receive routines.

4. While the messages are being delivered, calculate the unshared rows, from $n_\mathrm{s}^i + 1$ to n_o^i.

5. Wait for the receive requests.

6. Add the received values to the corresponding vector entries.

Note that the communicated data is first copied to a separate buffer, and the send buffer is used again only during the next call to the routine. By that time the message from the former call has been delivered, and, as a result, there is no time delay in step 2 above. Step 5, however, may be associated with significant overhead, especially when there is an imbalance in the amount of floating-point operations performed on each processor. This issue may be partly mitigated by massive computations performed in step 4. Generally, step 4 contains the majority of floating-point operations, because the number of internal nodes in a mesh partition is much larger than that on a shared boundary.

Using the sorted data structure, all the vectors can be kept in a *communicated*

state. Combining inter-processor communications with the matrix-vector product routine as detailed above produces values at the shared vector entries that are equal to the sum of the contributions of all the subdomains. This is identical to what a sequential algorithm would produce. As a result, to parallelize a sequential LS, only operations such as norm, inner product, and matrix-vector product need to be replaced by their parallel counterparts, without changing the main algorithm.

5.1.3 Implementation

Generally the ordering of unknowns is determined by the mesh generator rather than the LS itself. Hence, the linear system of equations that is received by the LS typically has a random order. In order to benefit from ordered data structure, data passed through the interface to the LS must be mapped. This operation has a negligible computational cost for vectors as it requires $O(n^i)$ operations on each processor.

Denoting $\boldsymbol{b}^i$ as the unordered input and $\boldsymbol{x}^i_{\mathrm{s}}$ as the ordered output, the data mapping at the interface to the LS is as follows:

do $p = 1, \cdots, n^i$
$\quad b^i_{\mathrm{s}}(\mathcal{M}^i(p)) \leftarrow b^i(p)$

do $p = 1, \cdots, n^i$
$\quad x^i(p) \leftarrow x^i_{\mathrm{s}}(\mathcal{M}^i(p))$

All the computations inside the LS are now performed on the sorted data and no extra mappings are required.

Mapping the matrix $\boldsymbol{A}^i$ is more costly as the number of non-zeros, n^i_{nz}, is generally much larger than n^i. This extra computational cost may be avoided by adopting a specialized compressed sparse row (CSR) format [117]. Given an unsorted array of non-zero values on processor i, the matrix $\boldsymbol{A}^i$, an unsorted array of indices of the first nonzero element of each row, $\boldsymbol{I}^i$, and an unsorted array of the column indices of each entry of $\boldsymbol{A}^i$, $\boldsymbol{J}^i$, the sorted pointers are calculated as

do $p = 1, \cdots, n^i$
$\quad p_{\mathrm{s}} \leftarrow \mathcal{M}^i(p)$

$I^i_{\rm s}(1,p_{\rm s}) \leftarrow I^i(p)$
$I^i_{\rm s}(2,p_{\rm s}) \leftarrow I^i(p+1)-1$

do $p = 1, \cdots, n^i_{\rm nz}$
$J^i_{\rm s}(p) \leftarrow \mathcal{M}^i(J^i(p))$

Here $I^i_{\rm s}(1,p)$ and $I^i_{\rm s}(2,p)$ point to the first and last element of row p, and $J^i_{\rm s}(p)$ is the column index in the sorted format. With this transformation, there is no need to map $\boldsymbol{A}^i$, as the matrix-vector product $\boldsymbol{y}^i_{\rm s} = \boldsymbol{A}^i \boldsymbol{x}^i_{\rm s}$ may be expressed as:

$\boldsymbol{y}^i_{\rm s} \leftarrow 0$
do $p_{\rm s} = 1, \cdots, n^i$
  do $q = I^i_{\rm s}(1,p_{\rm s}), \cdots, I^i_{\rm s}(2,p_{\rm s})$
    $y^i_{\rm s}(p_{\rm s}) \leftarrow y^i_{\rm s}(p_{\rm s}) + A^i(q) x^i_{\rm s}(J^i_{\rm s}(q))\,,$

which is similar to a conventional sparse matrix-vector product.

Remarks:

1. The operator $\boldsymbol{I}^i_{\rm s}$ acts in the sorted domain and produces an unsorted codomain, while $\boldsymbol{J}^i_{\rm s}$ operates on the unsorted domain and produces a sorted codomain.

2. Since $\boldsymbol{\mathcal{M}}^i$ depends on the mesh connectivity and partitioning, $\boldsymbol{\mathcal{M}}^i$, $\boldsymbol{I}^i_{\rm s}$, and $\boldsymbol{J}^i_{\rm s}$ are calculated only when the mesh or partitioning are changed. To solve multiple linear systems of equations that are based on the same mesh, as is the case of time dependent simulations, the LS is initialized only once by calculating $\boldsymbol{\mathcal{M}}^i$, $\boldsymbol{I}^i_{\rm s}$, and $\boldsymbol{J}^i_{\rm s}$, and called each time with different $\boldsymbol{A}^i$ and $\boldsymbol{b}^i$. In this case, the extra cost associated with the LS initialization is typically negligible compared to the cost of the entire simulation.

3. Only $\boldsymbol{\mathcal{M}}^i$, $\boldsymbol{I}^i_{\rm s}$, and $\boldsymbol{J}^i_{\rm s}$ need to be stored, resulting in no additional significant memory requirements.

4. In the case of multiple degrees-of-freedom per node, $\boldsymbol{A}^i$ and $\boldsymbol{b}^i$ may be allocated with an extra dimension that can be unrolled in operators for improved performance.

5.2 Results

The proposed algorithms are implemented in an efficient in-house LS written in Fortran that contains several iterative methods, such as conjugate gradient [125], generalized minimum residual (GMRES) [120], and a specialized algorithm for solving the linear system of equations obtained from the FE discretization of the Navier–Stokes equations of incompressible flows [126]. This LS is used in several studies that involve solving Navier–Stokes and advection–diffusion equations [59, 80, 33, 127]. In-house MUPFES solver is used to form the linear systems of equations, i.e., for constructing $\boldsymbol{A}^i$, $\boldsymbol{I}^i$, $\boldsymbol{J}^i$, $\boldsymbol{b}^i$, and $\boldsymbol{a}^i$. The results are verified for mathematical consistency by checking that all algebraic operations yield identical results for the parallel code and its serial counterpart. All the test cases were run on the Kraken machine at the university of Tennessee using an allocation from XSEDE program. Kraken is a massively parallel processing machine that uses 2.6 GHz AMD Opteron processors with 1.33 Gbytes of memory per core. There are in total 9,408 computing nodes and 112,896 computing cores. Compute nodes are interconnected via a Cray SeaStar2+ router [128]. Kraken's default MPI library was employed in our computations.

Three models are considered: small, medium, and large. The small model is a 3D cylinder that is meshed with 25K linear tetrahedral elements, producing 5.5K nodes and 81K non-zero entries in $\boldsymbol{A}$ (see Figure 5.3-(a)). The medium model is a 2D duct that is meshed with 14K bi-quadratic quadrilateral elements, producing 55K nodes and 890K non-zero entries in $\boldsymbol{A}$ (see Figure 5.3-(b)). The largest model is a 3D patient-specific aorta model from [41] that is meshed with 2.7M linear tetrahedral elements, producing 510K nodes and 7.4M non-zero entries in $\boldsymbol{A}$ (see Figure 5.3-(c)). The models are selected such that the number of unknowns varies by about one order of magnitude from case to case. The models are partitioned using ParMetis [129]. The number of partitions is chosen to be a power of two, that is, $n_{\mathrm{p}} = 2^i \; i \in \{0, \cdots, 11\}$.

To examine the influence of the compiler on the performance of the proposed method, we consider the small model, and use *pgi*, *Intel*, and *gnu* compilers to generate three separate executables. One hundred sparse matrix-vector products

(a) (b) (c)

Figure 5.3: Test cases: (a) 3D cylindrical model with n_{p}=8 and n=5.5K, (b) 2D model of a duct with n_{p}=16 and n=55K, and (c) 3D aortic model with n_{p}=32 and n=510K.

are performed for each case, and the results are presented in Figure 5.4. The results show that all compilers give a similar performance when running in serial. However, as the number of processors is increased, the *pgi* compiler gives the least consistent performance. Based on this study, the *Intel* compiler is chosen for the rest of the computations presented in this chapter.

To test the performance of present method, we compare the ordered data structure (ODS) with PETSc library [123], a Cray PETSc 3.2.00 release equivalent to a 3.2-p5 release by the Argonne National Laboratory. Since there are inconsistencies between implementation of iterative algorithms, only basic algebraic operations, matrix-vector product and vector norm, are considered in this comparison. To test the performance of the matrix-vector product operation using the new data structures, one hundred matrix-vector products using all three models were computed and t_{tot} was measured. t_{tot} is defined as the sum of all processors' computation and communication time. The speedup is calculated using the formula $t_{\mathrm{tot}}\,|_{n_{\mathrm{p}}=1}\,(t_{\mathrm{tot}})^{-1}\,n_{\mathrm{p}}$. The results presented in Figure 5.5 indicate that the present method significantly outperforms PETSc. While at a lower number of processors the communication overhead is negligible and speedup is close to ideal,

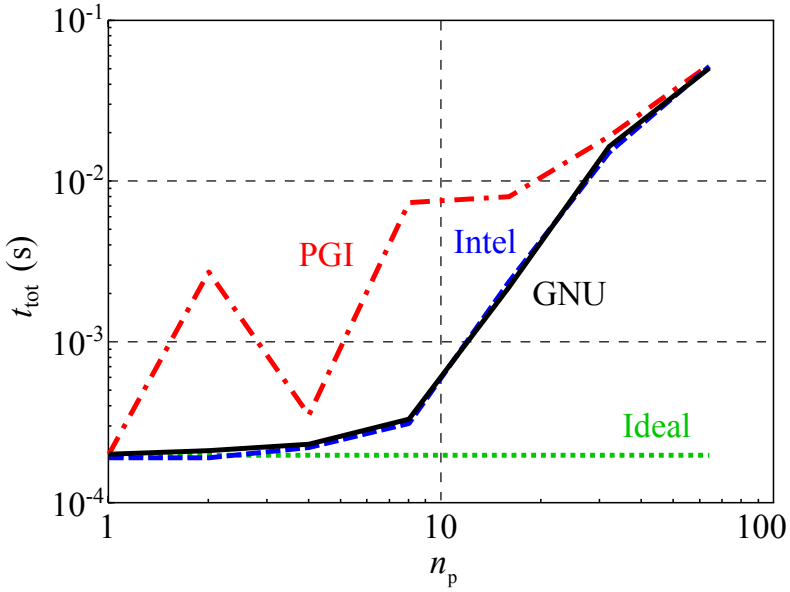

Figure 5.4: Influence of the compiler on the performance of the sparse matrix-vector product. One hundred matrix-vector products were performed, and program execution time t_{tot} is plotted versus the number of processors employed. The time t_{tot} is measured as the sum of all processor wall clock times. Fortran compilers from *pgi*, *Intel*, and *gnu*, versions 11.9-0, 12.1.2, and 4.6.2, respectively, were used. These are the default compilers on Kraken at the present time. While *gnu* and *Intel* compilers gave very similar performance, the *pgi* compiler produced the least consistent results.

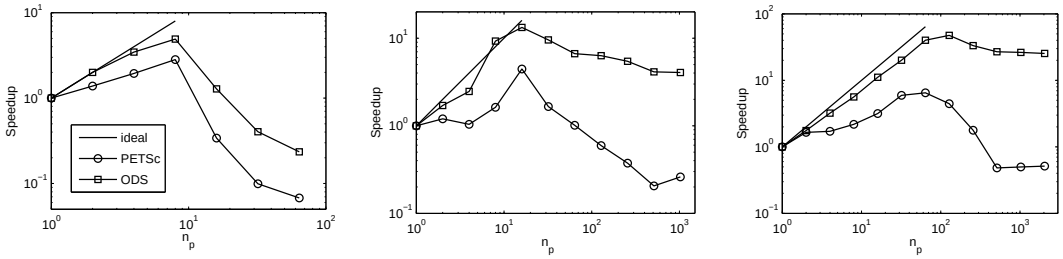

Figure 5.5: Speedup in matrix vector product versus number of processors using matrices with (a) $n = 5.5$K, (b) $n = 55$K, (c) $n = 510$K (Figure 5.3). PETSc refers to the Cray PETSc 3.2.00 release equivalent to 3.2-p5 release by Argonne National Laboratory. ODS (ordered data structure) refers to the present method. In all cases, the introduced method performs significantly better than PETSc at a higher number of processors.

at a higher number of processors the communications overhead presents a major computational cost and leads to saturation. In all cases the present method gave better speedup than PETSc. For the largest model the saturation was delayed for the present method: The highest speedup was achieved for $n_{\mathrm{p}} = 128$, compared to PETSc's $n_{\mathrm{p}} = 64$.

To compare the methods in terms of minimal time to completion of a matrix-vector product operation, the cases of n_{p} =8, 16, and 64 are considered for the small, medium, and large model, respectively (see Table 5.1). These correspond to near-peak performance of both methods (see Figure 5.5). The results show that by increasing the problem size the difference between the peak performance of the present method and PETSc also increases: The higher the number of partitions, the better ODS performs relative to PETSc. The improvement for the small, medium, and large model is 65%, 177%, and 516%, respectively.

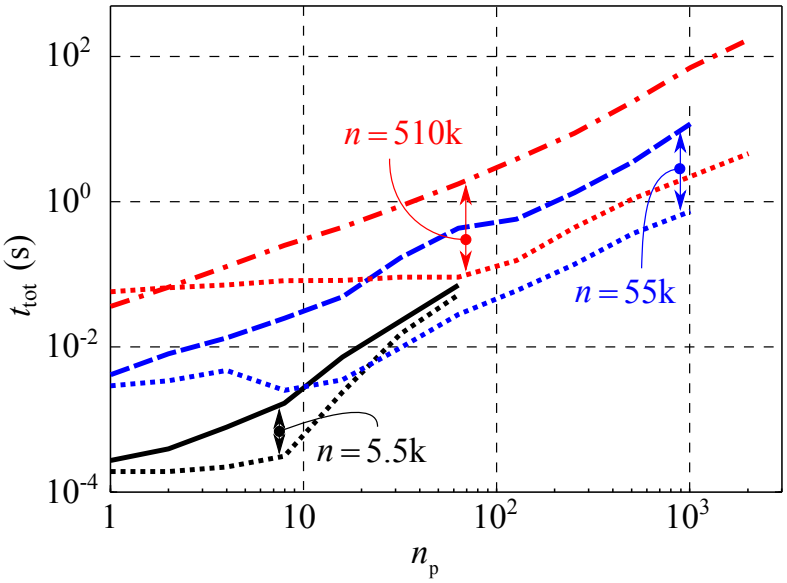

Figure 5.6: The total cost of initialization, i.e. computing $\boldsymbol{\mathcal{M}}^i$, $\boldsymbol{I}_{\text{s}}^i$, $\boldsymbol{J}_{\text{s}}^i$, and communication data structure for the models shown in Figure 5.3. Solid lines are initialization cost and dotted lines are a single matrix-vector product cost, shown here as the reference.

Table 5.1: Performance of PETSc and presented method (ODS), for the three problem sizes (based on Figure 5.5). t_{tot} is the total cost of computing a single matrix-vector product.

Case	n_{p}	n	t_{tot} (ms)	
			PETSc	ODS
a	8	5.5K	0.51	0.31
b	16	55K	9.7	3.5
c	64	510K	561	91

The initialization costs, that is, the costs of calculating $\boldsymbol{\mathcal{M}}^i$, $\boldsymbol{I}_{\text{s}}^i$, $\boldsymbol{J}_{\text{s}}^i$, and constructing the data structures for inter-processor communications, are plotted in Figure 5.6. The initialization costs may be up to 30 times higher than performing a single matrix-vector product. However, these costs increase almost linearly with n_{p}, resulting in wall-clock time that is almost independent of the number of processors. For the three cases considered in this study, the initialization stage always took less than 0.1 s in wall-clock time, which is negligible, especially for time-dependent problems.

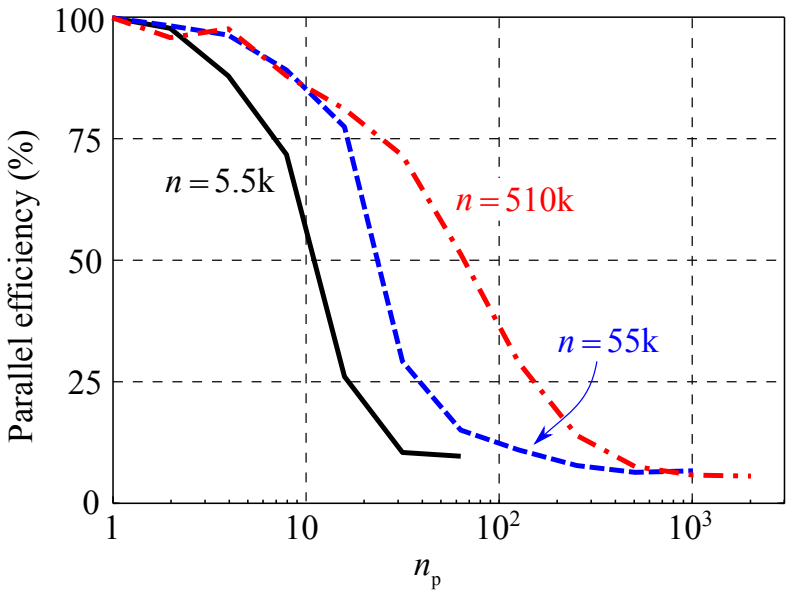

Figure 5.7: The parallel efficiency of the matrix-vector product versus the number of partitions for the models shown in Figure 5.3.

Parallel efficiency of the matrix-vector product, defined as the percentage ratio of the time spent on floating-point operations to the total time t_{tot} is calculated for the present method, and the results are plotted in Figure 5.7. As expected, there is a sharp drop in efficiency as n_{p} increases. The minimum total time for performing a matrix-vector product (i.e., the peak performance) generally occurs before parallel efficiency drops below 50%.

The theoretical reduction in the number of floating point operations in a vector inner product, obtained by ODS, is equal to $n^i - n_{\text{o}}^i$ in partition i. Hence, the relative saving can be calculated as

$$\left(\sum_{i=1}^{n_{\text{p}}} n^i\right)^{-1} \sum_{i=1}^{n_{\text{p}}} (n^i - n_{\text{o}}^i), \tag{5.22}$$

which is plotted in Figure 5.8. Increasing the number of partitions increases the number of nodes on the boundaries of partitions and leads to more significant savings. At peak performance (for n_{p} reported in Table 5.1), this translates to approximately a 10% reduction in computations for all the test cases.

To test the performance of presented method when it is incorporated into a

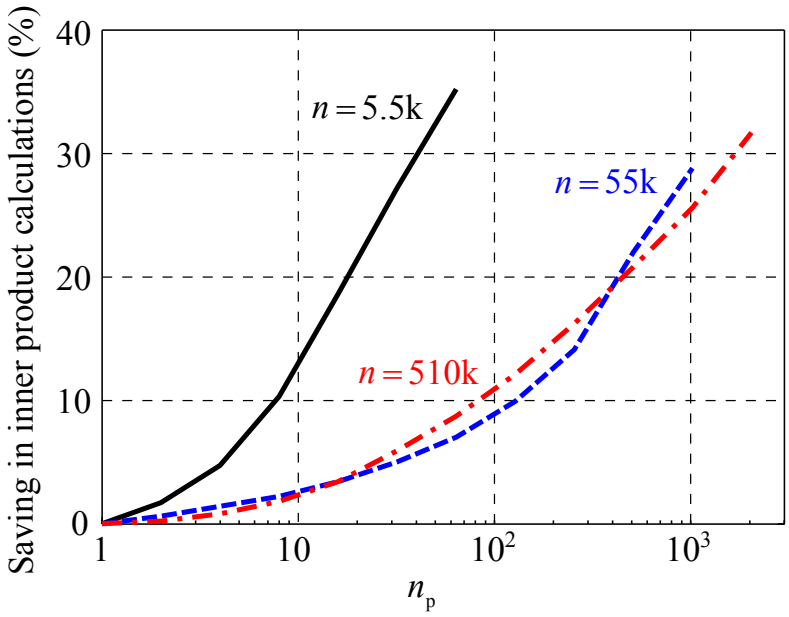

Figure 5.8: Theoretical saving in norm and dot product calculation, i.e. $1 - \left(\sum_{i=1}^{n_p} n^i\right)^{-1} n$, versus the number of partitions for the models shown in Figure 5.3.

PDE solver, blood flow in the aorta model (Figure 5.3-(c)) is simulated. Blood flow governing equations (Navier-Stockes) are reduced to a system of linear equations using finite-element method and an implicit time integration scheme [65, 66, 67]. The resulting linear system has four degrees of freedom per node, one for pressure and three for velocity. Hence, vectors and matrices containing floating values are allocated with an extra dimensions. A Schur complement is formed by decomposing matrix $\boldsymbol{A}$ to four blocks, allowing velocity and pressure to be solved seperately at the linear solver level. Based on physiological values, resistance boundary condition is imposed at all outlets and steady inflow boundary condition is imposed at the inlet (See Chapter 2). In presence of resistance boundary conditions, the specialized preconditioner discussed in Chapter 4 is employed to improve convergence rate of the iterative solver. The time step size is set to 1 ms and simulation is continued for 10 time step.

The cost of simulating one time step along with parallel speedup is shown in Figure 5.9. This figure shows a good scalability of presented method upto 64 processors, in which $n^i \approx 8$k. Increasing n_p from 64 to 100, reduces parallel

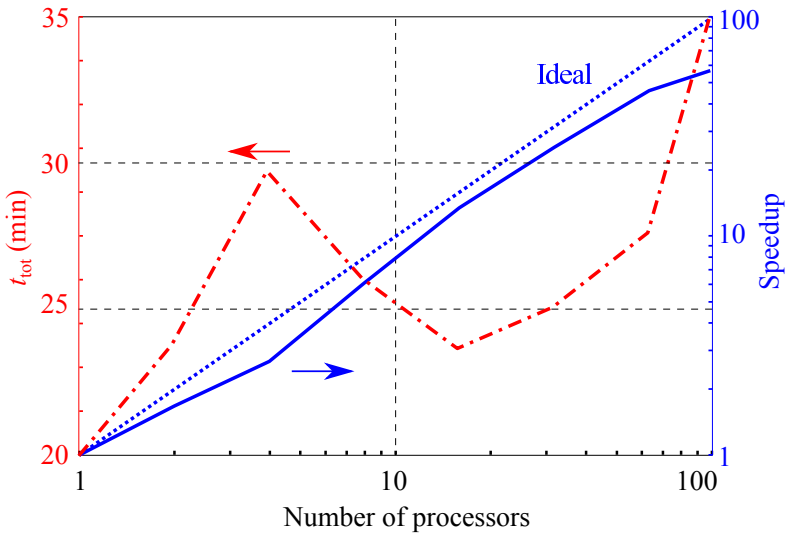

Figure 5.9: The aorta model fluid-flow simulation cost and parallel speedup. Red/dash-dot curve (corresponding to the left y-axis) shows the cost, which is calculated as the total CPUT time per each time step. Blue/solid curve (corresponding to the right y-axis) is the parallel speedup. Ideal speedup is shown by a blue/dotted line.

efficiency from 72% to 57%. Despite this drop in efficiency, simulation wall-clock time decreases by 19% when increasing n_{p} from 64 to 100.

Acknowledgments

This chapter, in full, is a reprint of the material as it appears in Efficient and Highly Scalable Parallel Algorithms for Iterative Linear Solvers in *Parallel Computing*. Authors are M. Esmaily-Moghadam, Y. Bazilevs, and A. Marsden. The dissertation author was the primary investigator and author of this paper.

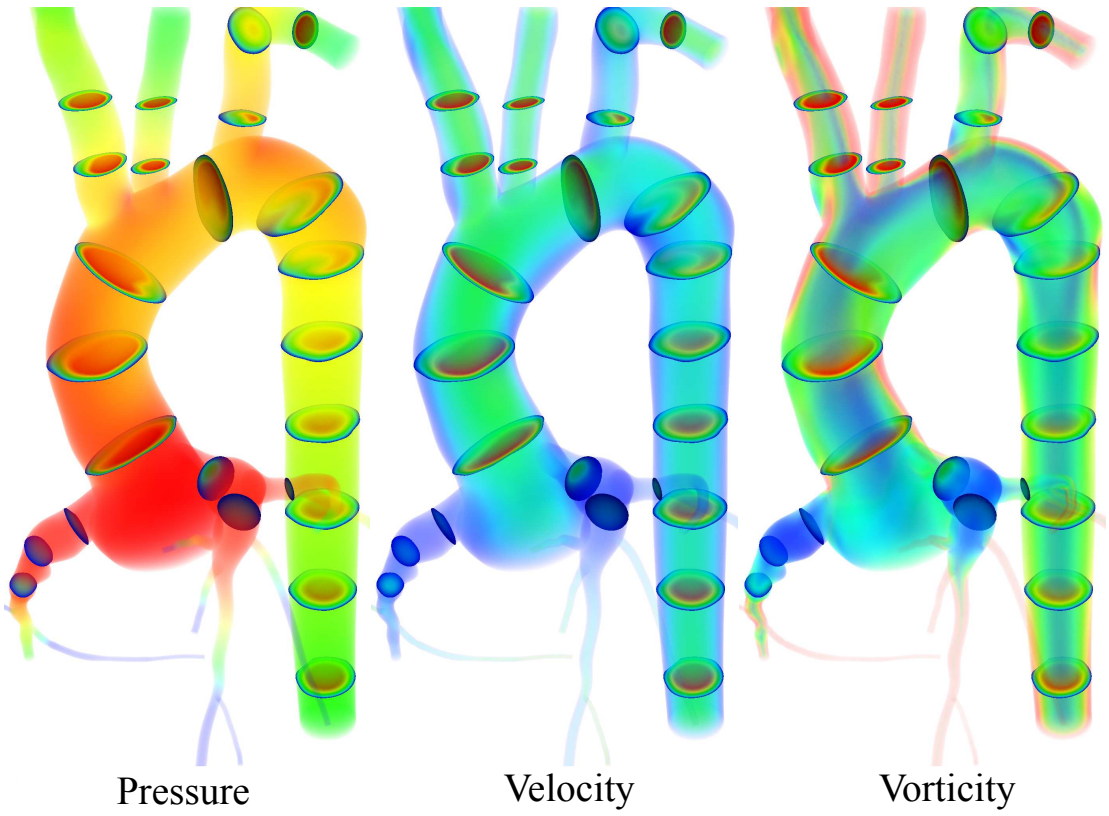

Figure 5.10: Simulation results of the aorta model. Velocity is shown at several slices with volumetric rendering of pressure (left), velocity magnitude (center), and vorticity magnitude (right).

Chapter 6

A Non-discrete Method for Computation of RT

Cardiovascular simulations typically require post processing analysis to determine hemodynamic parameters of clinical or physiological significance. These include, among others, WSS and strain, energy loss, oscillatory shear index, flow distribution, and particle RT. While most of these can be directly computed from the flow field, particle RT calculations currently require additional post processing simulations.

RT and WSS are known to be linked to thrombus formation, which is a serious clinical issue in numerous pediatric and adult cardiovascular disease applications, including stroke, embolism, myocardial infarction, bypass graft failure, device design, and congenital heart disease. Thrombus formation is a multi-factorial process involving complex chemistry, vascular biology, and hemodynamics. These complexities underscore the need for simpler hemodynamic surrogates to assess thrombotic risk.

High WSS is known to cause platelet activation, hemolysis, and endothelial cell damage and is associated with thrombotic risk [130, 131, 132]. Red blood cell damage has been reported for WSS values in range of 120 to 300 (dyne/cm^2) [133, 134, 135]. On the other hand, recirculation regions associated with lower WSS and high RT, in combination with previous exposure to high shear stress, may also increase the risk of thrombus formation [37, 38]. Many prior studies report

WSS as an important parameter for comparison of different anatomies and clinical scenarios [31, 32, 17, 78]. This measure partly accounts for the time-history of red blood cell exposure to altered shear conditions. In this context, RT calculation is a measure of the degree of fluid entrapment in a specific region, providing a time scale for the thrombus formation process to occur.

RT calculation is a non-trivial problem with numerous previous definitions proposed in the literature, each of which produces different values. To obtain a measure of RT in a region of interest, most prior studies have proposed a discrete formulation in which particles are released in the flow and their locations are traced over time [39, 40, 41, 42, 43]. RT is then calculated based on the time each individual particle spends in the region of interest. RT results obtained from these approaches depend on the number of particles used, often requiring a large number of particles to obtain a smooth spatial distribution. Results can also be highly effected by seeding location, which is typically upstream of the region of interest, inside the region of interest, or at the model inlet [39, 40, 42]. Typically, several particle-tracking simulations are needed for pulsatile flow conditions, since the particle initiation time (e.g. relative to the cardiac cycle) affects the results of the RT calculation [39, 40]. To mitigate this drawback, particles are often continuously released at the inflow boundary, however the spatial distribution of seeded particles may not follow the non-uniform velocity distribution at the inlet [42].

Another drawback of discrete methods is mesh dependency. Because it is often necessary to calculate the time that particles spend inside individual mesh elements, results may depend on the mesh orientation relative to streamlines in the flow. For example, a particle may spend longer in an element that is oriented in the direction of the flow, as shown schematically in Figure 6.1, producing an artificially higher value of RT. This drawback is more critical for adapted meshes with anisotropic elements. Additionally, particle methods typically require special treatment for particles close to the wall, for example by adding a small wall-normal velocity to prevent particles from getting stuck on the no-slip boundary. In this chapter we offer an alternative approach that avoids the need for large

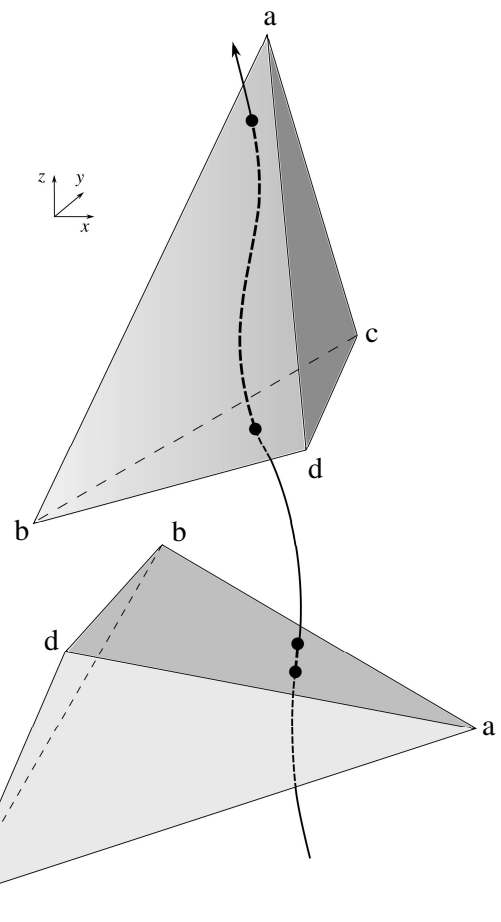

Figure 6.1: Schematic of two possible element orientations. Using a discrete approach, the top orientation produces an artificially higher value of RT compared to the bottom orientation of element *abcd*.

particle numbers with uncertain temporal and spatial resolution, and allows for a continuous and mesh-independent representation of RT.

Non-discrete methods for RT calculation were first introduced for environmental engineering with applications in sedimentation and biology. These method are based on the solution of an advection-diffusion equation with a non-zero source term [136, 137]. There are currently a number of competing definitions of RT in the cardiovascular simulation literature, with no clear consensus. To track contrast agent, Rayz et al. solved an advection equation with a zero source term [138]. Narracott et al. calculated RT to model clot formation in a stenosis using an advection-diffusion equation with a non-zero source term [139]. In that study a

non-zero source term was used for the entire computational domain and dye was advected from the inlet, so the value of RT depended on the distance from the model inlet to the region of interest. In this chapter, we start from two intuitive definitions for RT and go on to develop new non-discrete methods that attempt to address the drawbacks of prior methods. Because we rely on a continuous solution of an advection-diffusion problem, this new method is not limited by the spatial and temporal resolution requirements of particle based methods. Since the present method does not rely on the elements for calculating RT, apart from numerical accuracy of the original solution, the formulation of this method is mesh-independent. This approach also allows one to capture the diffusion process in the boundaries of a region of interest. We also show that for special cases RT can be directly obtained from the velocity field without extra post-processing simulations. We also show that the value obtained from this approach provides a lower bound for the RT value calculated from the advection-diffusion problem.

In previous studies, WSS and RT have been viewed as independent surrogates for thrombotic risk. However, it is clear that these quantities are not physically independent. To quantify the relationship between RT and WSS, a range of clinical scenarios is considered and the correlation between measures of RT and WSS is reported.

6.1 RT calculation

In this section, starting with both existing and slightly modified RT definitions, a mathematical model is constructed and then simplified to obtain a new formulation for calculating RT. We consider two approaches for calculating RT in a region of interest. In the first, we solve an advection-diffusion equation to compute temporally and spatially averaged RT for fluid inside a region of interest. In the second, we calculate the temporally and spatially averaged RT for fluid entering and leaving a region of interest using a control volume approach. In other words, in the first method we examine fluid inside a certain region of interest and calculate the time it has stayed in that region, while in the second method we examine the

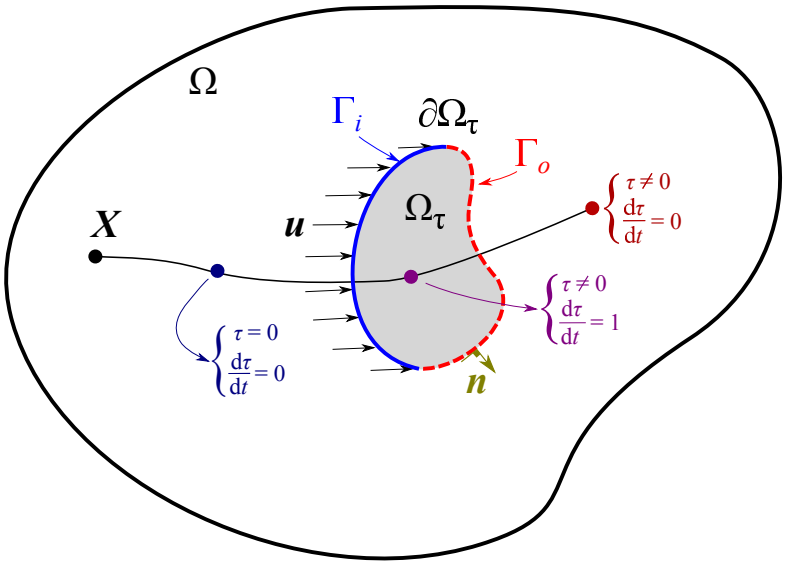

Figure 6.2: 2D schematic of region of interest Ω_τ in the computational domain Ω. A single Lagrangian particle originating at $\boldsymbol{X}$ is shown at three locations, each with different time derivative.

boundaries of the region of interest and examine the RT of the fluid passing over these boundaries.

As shown in Figure 6.2, we denote the time a fluid particle has been in the region of interest, $\Omega_\tau \subset \mathbb{R}^{\text{nsd}}$, by $\tau(\boldsymbol{x}, t) : \Omega \times \mathbb{R}^+ \to \mathbb{R}^+$, in which $\mathbb{R}^+ = \mathbb{R} \geq 0$. For fluid that has never entered the region of interest, $\tau = 0$. As soon as a fluid particle enters the region of interest, τ is incremented in time. Hence in a Lagrangian framework

$$\left.\frac{\mathrm{d}\tau}{\mathrm{dt}}\right|_{\boldsymbol{X}} = H(\boldsymbol{x}), \tag{6.1}$$

where $\boldsymbol{X} \in \Omega$ is the origin of a fluid particle and $H(\boldsymbol{x}) : \Omega \to \{0, 1\}$ is defined as

$$H(\boldsymbol{x}) := \begin{cases} 1 & \boldsymbol{x} \in \Omega_\tau \\ 0 & \boldsymbol{x} \notin \Omega_\tau. \end{cases} \tag{6.2}$$

This definition is identical to the formulation in [136], if $\Omega_\tau = \Omega$ or $H = 1$ is assumed. Note that with this assumption $\tau(\boldsymbol{x})$ varies with the distance of point $\boldsymbol{x}$ from the inlet. Since we generally wish to calculate RT in a specific region of interest, we assume $\Omega_\tau \neq \Omega$. Defining the operator $\mathcal{L}(\tau; \boldsymbol{u}) : \mathbb{R}^+ \times \mathbb{R}^{\text{nsd}} \to \mathbb{R}$ as

follows

$$\mathcal{L} := \frac{\partial \tau}{\partial t} + \boldsymbol{u} \cdot \nabla \tau - \nabla \cdot \kappa \nabla \tau - H, \tag{6.3}$$

and accounting for diffusion, Equation (6.1) in an Eulerian framework is

$$\mathcal{L}(\tau; \boldsymbol{u}) = 0. \tag{6.4}$$

To derive Equation (6.4), it is assumed that there are enough particles to use a continuum mechanics formulation. Also it is assumed that particles follow the pathlines in the flow or $\frac{\partial \boldsymbol{x}}{\partial t} = \boldsymbol{u}$. In Equation (6.3), $\boldsymbol{u}(\boldsymbol{x}, t) = \{\boldsymbol{u} \mid \boldsymbol{u}(\cdot, t) \in H^1(\Omega)^{\text{nsd}}, t \in \mathbb{R}^+, \ \boldsymbol{u}(\boldsymbol{x}, t+T) = \boldsymbol{u}(\boldsymbol{x}, t)\}$, is a periodic velocity field obtained from solving the Navier-Stokes equations in the 3D domain, and κ is the physical diffusion coefficient. In this study, the physical diffusion coefficient is set to zero because it is negligible.

Equation (6.4) is an advection-diffusion equation with a non-zero source term that is solved in a post-processing step to find τ. This PDE equation can be solved using various numerical methods, including a FE approach. Using a FE method, we find $\tau \in \mathcal{S}_{\text{h}}$ such that for all $q \in \mathcal{S}_{\text{h}}$, in which $\mathcal{S}_{\text{h}} = \{s \mid s(\boldsymbol{\cdot}, t) \in H^1(\Omega), t \in (0, nT], \ s = 0 \text{ on } \Gamma_{\text{g}}\}$, the following stabilized weak form holds [140]

$$\int_\Omega q \cdot (\frac{\partial \tau}{\partial t} + \boldsymbol{u} \cdot \nabla \tau) \, \mathrm{d}\Omega + \int_\Omega \nabla \mathrm{q} \cdot \tilde{\kappa} \nabla \tau \, \mathrm{d}\Omega + \sum_{\text{e}} \int_{\Omega_{\text{e}}} \nabla \mathrm{q} \cdot \boldsymbol{u} \tau_{\text{m}} \mathcal{L} \, \mathrm{d}\Omega = 0, \tag{6.5}$$

where $n \in \mathbb{N}$ is the number of simulated cycles and $\tau_{\text{m}} \in \mathbb{R}^+$ and $\tilde{\kappa} \in \mathbb{R}^+$ are defined as,

$$\tau_{\text{m}}(\boldsymbol{x}, t) := \frac{1}{\sqrt{4/\Delta t^2 + \boldsymbol{u}^T \boldsymbol{\xi} \boldsymbol{u} + 3\tilde{\kappa}^2 \boldsymbol{\xi} : \boldsymbol{\xi}}}, \tag{6.6}$$

$$\tilde{\kappa}(\boldsymbol{x}, t) := \kappa + \kappa_{\text{DC}} = \kappa + \frac{|\mathcal{L}|}{2\sqrt{\nabla \tau^T \boldsymbol{\xi} \nabla \tau}}, \tag{6.7}$$

where $\boldsymbol{\xi} \in \mathbb{R}^{\text{nsd} \times \text{nsd}}$ is the Jacobian that maps between the parent and physical domains [141], and $\kappa_{\text{DC}} \in \mathbb{R}^+$ is a discontinuity capturing diffusion coefficient. This residual based coefficient goes to zero as $\mathcal{L}$ goes to zero, and is minimally intrusive where $\nabla \tau$ is maximal. This is added to improve the solution by removing the overshoot and undershoot adjacent to a jump in τ [140, 142]. The last term in

Equation (6.5) is a non-linear function of τ, therefore multiple nonlinear iterations are performed at each time step to obtain convergence (3 iterations are used in our computations). A Dirichlet BC is imposed on inlets and outlets with backflow and a Neumann BC with zero flux is imposed on the walls. The Dirichlet BC is imposed on outlets with partial backflow to prevent any possible divergence of the simulations or unrealistic solution. Note that in the studied scenarios since advection is much stronger than diffusion, the imposed value on the outlets in the presence of outward flow have a negligible effect on the interior solution.

The first measure of RT, $RT_1 \in \mathbb{R}^+$, is calculated by averaging τ over $\Omega_\tau \times ((n-1)T, nT]$ so that

$$RT_1 = \frac{1}{T}\int_{(n-1)T}^{nT} \frac{1}{V_{\Omega_\tau}} \int_{\Omega_\tau} \tau(\boldsymbol{x}, t)\mathrm{d}\Omega\mathrm{dt}, \tag{6.8}$$

where

$$V_{\Omega_\tau} := \int_{\Omega_\tau} \mathrm{d}\Omega. \tag{6.9}$$

The number of simulated cycles, n, is selected such that the transient part of the solution is damped and τ is a periodic function of time. To ensure periodicity, RT_1 is calculated from Equation (6.8) and the result is compared to its preceding cycle.

The second measure of RT, RT_2, is calculated based only on the particles that are entering and leaving Ω_τ. We define $\Gamma_\mathrm{o}(t) = \{\boldsymbol{x} \mid \boldsymbol{x} \in \partial\Omega_\tau,\ \boldsymbol{u}\cdot\boldsymbol{n} \geq 0\}$ and $\Gamma_\mathrm{i}(t) = \{\boldsymbol{x} \mid \boldsymbol{x} \in \partial\Omega_\tau,\ \boldsymbol{u}\cdot\boldsymbol{n} < 0\}$, in which $\boldsymbol{n}(\boldsymbol{x})$ is the outward normal vector to Ω_τ. Note that $\Gamma_\mathrm{i} \cup \Gamma_\mathrm{o} = \partial\Omega_\tau$ and $\Gamma_\mathrm{i} \cap \Gamma_\mathrm{o} = \{\}$ and the total time spent in Ω_τ by the fluid is equal to the increase in τ from Γ_i to Γ_o. We let $\bar{Q} \in \mathbb{R}^+$ be the average flow into Ω_τ in time T, so that the continuity equation gives

$$\bar{Q} := \frac{1}{T}\int_{(n-1)T}^{nT} \int_{\Gamma_\mathrm{o}(t)} \boldsymbol{u}\cdot\boldsymbol{n}\ \mathrm{d}\Gamma\mathrm{dt}. \tag{6.10}$$

Considering a non-uniform distribution of τ and $\boldsymbol{u}$ over $\partial\Omega_\tau$, we have

$$RT_2 := \frac{1}{T\bar{Q}}\int_{(n-1)T}^{nT} \left[\int_{\Gamma_\mathrm{o}(t)} \tau|\boldsymbol{u}\cdot\boldsymbol{n}|\ \mathrm{d}\Gamma - \int_{\Gamma_\mathrm{i}(t)} \tau|\boldsymbol{u}\cdot\boldsymbol{n}|\ \mathrm{d}\Gamma - \int_{\partial\Omega_\tau} \kappa\nabla\tau\cdot\boldsymbol{n}\ \mathrm{d}\Gamma\right]\mathrm{dt}, \tag{6.11}$$

which is a temporally and spatially weighted average of the increase in τ from Γ_i

to Γ_{o}. Considering the definition of Γ_{i} and Γ_{o},

$$RT_2 = \frac{1}{T\bar{Q}} \int_{(n-1)T}^{nT} \int_{\partial\Omega_\tau} (\tau \boldsymbol{u} - \kappa \nabla \tau) \cdot \boldsymbol{n} \, \mathrm{d}\Gamma \mathrm{d}t. \tag{6.12}$$

Integrating Equation (6.4) over $\Omega_\tau \times [(n-1)T, nT]$ gives

$$\int_{\Omega_\tau} (\tau(\boldsymbol{x}, nT) - \tau(\boldsymbol{x}, (n-1)T)) \, \mathrm{d}\Omega$$

$$+ \int_{(n-1)T}^{nT} \int_{\Omega_\tau} (\boldsymbol{u} \cdot \nabla \tau - \nabla \cdot \kappa \nabla \tau - H) \, \mathrm{d}\Omega \mathrm{d}t = 0. \tag{6.13}$$

The first integral in Equation (6.13) vanishes due to cyclic periodicity, as is typically the case in cardiovascular simulations. Integrating H and applying the divergence theorem to the second integral gives

$$\int_{(n-1)T}^{nT} \int_{\partial\Omega_\tau} (\tau \boldsymbol{u} - \kappa \nabla \tau) \cdot \boldsymbol{n} \, \mathrm{d}\Gamma \mathrm{d}t - \int_{(\mathrm{n}-1)\mathrm{T}}^{\mathrm{nT}} \int_{\Omega_\tau} (\tau \nabla \cdot \boldsymbol{u}) \, \mathrm{d}\Omega \mathrm{d}t = \mathrm{V}_{\Omega_\tau}\mathrm{T}. \tag{6.14}$$

Considering the continuity equation, the second integral in Equation (6.14) is zero, hence,

$$\int_{(n-1)T}^{nT} \int_{\partial\Omega_\tau} (\tau \boldsymbol{u} - \kappa \nabla \tau) \cdot \boldsymbol{n} \, \mathrm{d}\Gamma \mathrm{d}t = \mathrm{V}_{\Omega_\tau}\mathrm{T}. \tag{6.15}$$

From Equations (6.12) and (6.15),

$$RT_2 = \frac{V_{\Omega_\tau}}{\bar{Q}}. \tag{6.16}$$

This result is a very simple formula for calculating RT, which requires measuring only the volume of a region interest, V_{Ω_τ}, and the average flow passing through the boundaries of the region of interest in a cycle, $\bar{Q}$. This result is identical to the definition of flushing time that has applications in environmental flows [143, 144]. Note that this measure of RT does not require solving the advection-diffusion problem and can be directly calculated from the velocity field at the boundaries of the region of interest, i.e. all $\boldsymbol{u}(\boldsymbol{x}, t)$ such that $\boldsymbol{x} \in \partial\Omega_\tau$. Since the incompressibility assumption was used to derive Equation (6.15), Equation (6.16) is only valid for incompressible flows, while Equation (6.8) can be used for compressible flows as well. In the case of $\Omega_\tau = \Omega_\tau(t)$, as is the case in fluid-structure interaction (FSI) problems using the arbitrary Lagrangian-Eulerian method, it can be shown that

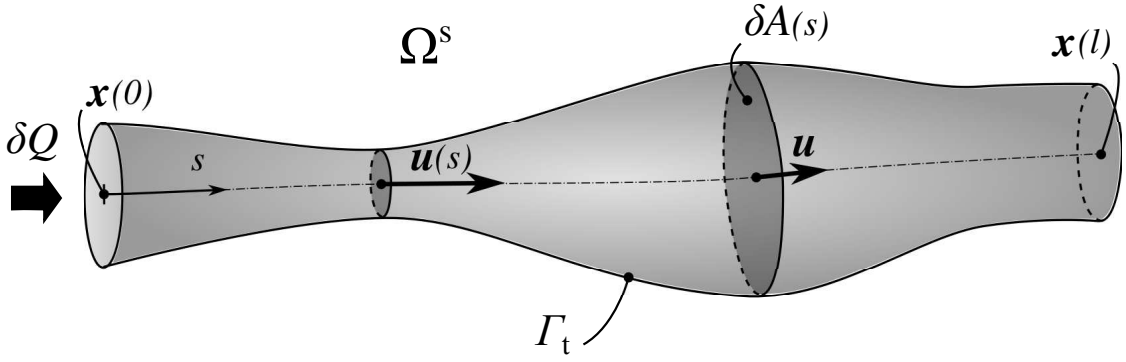

Figure 6.3: Schematic of a single topological manifold, S, which encloses a flow streamline. Velocity at each section, $\boldsymbol{u}(s)$, cross section area, $\delta A(s)$, flow rate, δQ, and its extents, $\boldsymbol{x}(s),\ s \in [0, l]$, are shown. Note there is no transport across Γ_t.

the above result holds if $\boldsymbol{u}$ is replaced with $\boldsymbol{u} - \hat{\boldsymbol{u}}$ and $\frac{\partial \tau}{\partial t}$ is calculated on the referential domain, in which $\hat{\boldsymbol{u}}$ is the referential domain velocity [100]. In this case, V_{Ω_τ} is time dependent in RT_1 calculation (Equation (6.8)) and time average of V_{Ω_τ} is used in RT_2 calculation (Equation (6.16)) [76].

6.1.1 RT_1 and RT_2 relationship

Although the definitions of RT_1 and RT_2 are distinct, they are strongly related. Here we show that RT_2 can be used as a lower bound for RT_1.

lemma 1: Let τ be zero at Γ_i, then:

$$\inf \tau(\boldsymbol{x}, t) \geq 0 \ \forall \ \boldsymbol{x} \in \Omega. \tag{6.17}$$

Proof: Integrating Equation (6.1) in time with $H \geq 0$ directly produces this result.

lemma 2: For a non-diffusive steady flow, in which $\kappa = 0$ and $\boldsymbol{u} = \boldsymbol{u}(\boldsymbol{x})$, in a manifold defined by $S(s) = \{\boldsymbol{x} | \boldsymbol{x}(s) \in \Omega^s \subset \Omega_\tau,\ s \in [0, l],\ \frac{\mathrm{d}\boldsymbol{x}}{\mathrm{ds}} = \frac{\boldsymbol{u}(s)}{\|\boldsymbol{u}\|},\ \boldsymbol{u} \cdot \boldsymbol{n} = 0 \text{ on } \Gamma_\mathrm{t}\}$ the following relation holds: $RT_2 \leq 2RT_1$.

Proof: A schematic of a topological manifold is shown in Figure 6.3. Equation (6.4) in a non-diffusive steady flow is

$$\boldsymbol{u} \cdot \nabla \tau = H. \tag{6.18}$$

Integrating Equation (6.18) on a manifold gives

$$\int_0^s \boldsymbol{u} \cdot \nabla \tau \delta A \mathrm{ds}^* = \int_0^s \delta A \mathrm{ds}^*, \tag{6.19}$$

which after integration by parts and applying the continuity relationship gives

$$\left(\tau(s) - \tau(0)\right) \boldsymbol{u} \delta A = \int_0^s \delta A \mathrm{ds}^* \tag{6.20}$$

and since $\boldsymbol{u}\delta A = \delta Q$ is constant along s,

$$\delta A(s) = \delta Q \frac{\mathrm{d}\tau}{\mathrm{ds}}. \tag{6.21}$$

Simplifying Equation (6.8) for a manifold with the above properties and using a steady flow assumption gives

$$RT_1 = \left[\int_0^l \delta A \mathrm{ds}\right]^{-1} \int_0^l \tau \delta A \mathrm{ds}. \tag{6.22}$$

After evaluating Equations (6.20), (6.21) and (6.22) we have

$$RT_1 = \frac{\delta Q}{\delta Q \left(\tau(l) - \tau(0)\right)} \int_0^l \tau \frac{\mathrm{d}\tau}{\mathrm{ds}} \mathrm{ds}, \tag{6.23}$$

which after integration is

$$RT_1 = \frac{1}{2} \left(\tau(l) + \tau(0)\right). \tag{6.24}$$

Now Equation (6.16) for a steady flow on a manifold is

$$RT_2 = \frac{1}{\delta Q} \int_0^l \delta A \mathrm{ds}, \tag{6.25}$$

which with Equation (6.20) reduces to

$$RT_2 = \tau(l) - \tau(0). \tag{6.26}$$

Since based on lemma 1, $\tau(0) \geq 0$, the proof is complete. Note that if $x(0) \in \Gamma_\mathrm{i}$, $\tau(0) = 0$ and $RT_2 = 2RT_1$.

lemma 3: If for $i = 1, 2$ and $\Omega^i \subset \Omega_\tau$, $\Omega^1 \cap \Omega^2 = \{\}$ the following is true: $RT_2^i \leq 2RT_1^i$, then for $\Omega^t = \Omega^1 \cup \Omega^2$, $RT_2^t \leq 2RT_1^t$ is also true.

Proof: By breaking the integral in Equation (6.8) into two sub domains, it can be shown that

$$RT_1^t = \frac{RT_1^1 V_{\Omega^1} + RT_1^2 V_{\Omega^2}}{V_{\Omega^1} + V_{\Omega^2}}, \tag{6.27}$$

and from Equation (6.16), it can be shown that

$$RT_2^t = \left(V_{\Omega^1} + V_{\Omega^2}\right) \left(\frac{V_{\Omega^1}}{RT_2^1} + \frac{V_{\Omega^2}}{RT_2^2}\right)^{-1}. \tag{6.28}$$

Defining

$$k := \frac{RT_2^1}{RT_2^2}, \tag{6.29}$$

then

$$0 \leq (k-1)^2, \tag{6.30}$$

and since $k \in \mathbb{R}^+$ we have

$$2 \leq k + \frac{1}{k}, \tag{6.31}$$

and hence

$$2 \leq \frac{RT_2^1}{RT_2^2} + \frac{RT_2^2}{RT_2^1}. \tag{6.32}$$

Multiplying Equation (6.32) by $V_{\Omega^1} V_{\Omega^2}$ and adding $V_{\Omega^1}^2 + V_{\Omega^2}^2$ to both sides of the above inequality gives

$$V_{\Omega^1}^2 + 2V_{\Omega^1}V_{\Omega^2} + V_{\Omega^2}^2 \leq V_{\Omega^1}^2 + V_{\Omega^2}^2 + V_{\Omega^1}V_{\Omega^2} \left(\frac{RT_2^1}{RT_2^2} + \frac{RT_2^2}{RT_2^1}\right). \tag{6.33}$$

Rearranging, we have

$$\left(V_{\Omega^1} + V_{\Omega^2}\right)^2 \leq \left(\frac{V_{\Omega^1}}{RT_2^1} + \frac{V_{\Omega^2}}{RT_2^2}\right) \left(V_{\Omega^1} RT_2^1 + V_{\Omega^2} RT_2^2\right), \tag{6.34}$$

and hence from Equation (6.28)

$$\left(V_{\Omega^1} + V_{\Omega^2}\right) RT_2^t \leq \left(V_{\Omega^1} RT_2^1 + V_{\Omega^2} RT_2^2\right) \tag{6.35}$$

and since $RT_2^i \leq 2RT_1^i$

$$V_{\Omega^1} RT_2^1 + V_{\Omega^2} RT_2^2 \leq 2\left(V_{\Omega^1} RT_1^1 + V_{\Omega^2} RT_1^2\right), \tag{6.36}$$

and hence from Equation (6.27)

$$V_{\Omega^1} RT_2^1 + V_{\Omega^2} RT_2^2 \leq 2\left(V_{\Omega^1} + V_{\Omega^2}\right) RT_1^t. \tag{6.37}$$

Comparing Equations (6.35) and (6.37) gives

$$RT_2^t \leq 2RT_1^t. \tag{6.38}$$

Proposition: For a steady non-diffusive flow, $RT_2 \leq 2RT_1$ on Ω_τ.

Proof: Let us divide Ω_τ into n manifolds such that

$$\Omega_\tau = \bigcup_{i=1}^{n} \Omega^i, \tag{6.39}$$

and

$$\Omega^i \cap \Omega^j = \{\},\ i \neq j,\ 1 \leq i, j \leq n. \tag{6.40}$$

Note that, Equation (6.39) does not impose any extra assumptions since there is no upper bound imposed on n and Ω^i can be selected as an infinitesimal volume that satisfies lemma 2. From lemma 2 for each Ω_i,

$$RT_2^i \leq 2RT_1^i,\ \text{on}\ \Omega^{\mathrm{i}},\ 1 \leq \mathrm{i} \leq \mathrm{n}. \tag{6.41}$$

Defining

$$\bar{\Omega}^1 := \Omega^1, \tag{6.42}$$

and

$$\bar{\Omega}^k := \bar{\Omega}^{k-1} \cup \Omega^k,\ 1 < k \leq n, \tag{6.43}$$

and using lemma 3, we have the following

$$RT_2^k \leq 2RT_1^k,\ \text{on}\ \bar{\Omega}^{\mathrm{k}}. \tag{6.44}$$

Since

$$\bar{\Omega}^n = \Omega_\tau, \tag{6.45}$$

we have

$$RT_2 \leq 2RT_1,\ \text{on}\ \Omega_\tau, \tag{6.46}$$

which completes the proof. Physically, the ratio $\frac{RT_2}{RT_1}$ is an indicator of the degree of flow disturbance. In a completely unidirectional flow, which is associated with a single manifold, this ratio is equal to two, where as in a highly disturbed flow with mixing it is closer to zero.

6.1.2 Point-wise RT

A point-wise definition of RT can be extracted from RT_2 by reducing the volume of the region of interest, V_{Ω_τ}, to an infinitesimal value. However, RT_2 goes to zero as V_{Ω_τ} goes to zero, which is expected from a physical point of view. Therefore, to define a point-wise measure of RT that is independent from the volume, we define RT per unit length, $RT_{\mathrm{x}}(\boldsymbol{x})$, i.e. the time required for a fluid particle to travel a unit length from any given point in the direction of flow. One might find this analogous to the normalization of RT or exposure time by the volume in discrete methods [39, 40, 42]. Considering the schematic shown in Figure 6.4 and Equations (6.9), (6.10), (6.16) and setting $\boldsymbol{n} = \frac{\boldsymbol{u}}{\|\boldsymbol{u}\|}$ gives

$$RT_{\mathrm{x}}(\boldsymbol{x}) = \left[\frac{1}{T}\int_{(n-1)T}^{nT} \|\boldsymbol{u}(\boldsymbol{x},t)\|\mathrm{dt}\right]^{-1},\ \boldsymbol{x} \in \Omega - \Gamma_w, \tag{6.47}$$

in which Γ_w is the wall boundary, where $\boldsymbol{u} = 0$ and RT_{x} is not defined. As expected, the value of the point-wise RT reduces to the inverse of the velocity magnitude at that point.

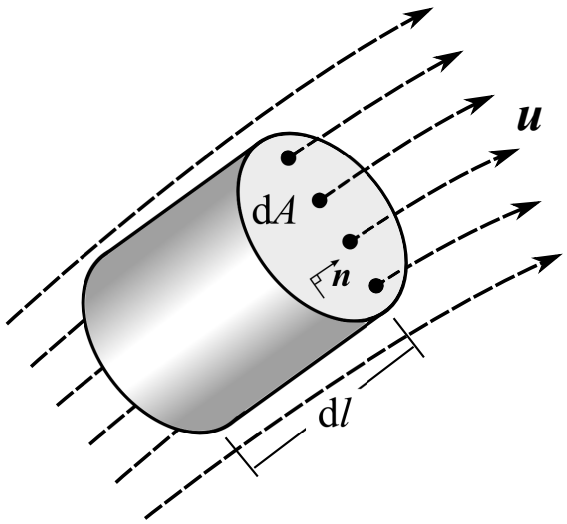

Figure 6.4: Schematic of a finite element considered for point-wise RT calculation. Note that the selected element is aligned with the direction of flow, i.e. $\boldsymbol{n} = \frac{\boldsymbol{u}}{\|\boldsymbol{u}\|}$.

τ absolute value depends on the distance of a parcel of fluid from the inflow of the computational domain. To remove this independence, one can calculate the

gradient of τ. To analyze this vector field in a steady and non-diffusive flow, we rewriting Equation 6.4 as

$$\boldsymbol{u} \cdot \nabla \tau = H. \tag{6.48}$$

Hence, while the gradient of τ in the direction of $\boldsymbol{u}$ is zero outside of the region of interest, is proportional to $\|\boldsymbol{u}\|^{-1}$ inside the region of interest. Therefore, by computing the gradient of τ a vector field is produced that its component in the streamwise direction is zero outside of region of interest and is equal to RT_{x} inside the region of interest. The normal component of $\nabla\tau$ represents the changes in fluid entrapment moving across different layers of the flow. While the streamwise component is large in lower velocity regions, the normal component is dominant in regions of recirculation. In [77], the 2-norm of this vector field is reported, hence combining the contribution of both components into a single scalar field. This allowed for identification of hot spots of high RT gradient that can be compared with regions of developing thrombus.

6.2 Test cases

To demonstrate the application of the proposed RT definitions and determine their relationship to WSS and flow structures, three scenarios are considered in this section: 1) A 2D flow over a cavity 2) flow through an idealized model of a single ventricle heart patient simulated with a multidomain method and 3) flow in a patient specific model of coronary aneurysms caused by Kawasaki disease.

The results that are obtained directly from the velocity field, including WSS, RT_2, RT_{x} are calculated numerically based on previously computed velocity data. To solve Equation (6.5) and obtain RT_1, an in-house FE code is used.

6.2.1 Flow over a cavity

In this case study, we consider a 2D model of a cavity in cross flow. This example is designed to demonstrate the behavior of different measures of RT in a strong recirculating flow.

The computational domain, Ω, is an ensemble of a 2×2 cm cavity attached to a 5×0.5 cm duct (Figure 6.5-a). The fluid viscosity and density are 1.82×10^{-4} g/(s cm) and 1.18×10^{-3} g/cm^3, respectively. At the inlet, a uniform velocity (77.1 cm/s) is prescribed and zero traction is imposed at the outlet. Based on the cavity dimension this produces Re = 1000. A uniform bilinear mesh with a size of 0.5 mm is used that produces 2600 elements and 2751 nodes. Two regions of interest are considered: 1) $\Omega_\tau = \Omega$ and 2) $\Omega_\tau = \Omega_c$ (see Figure 6.5-a). This is to show the sensitivity of RT_1 and RT_2 to the region of interest selection.

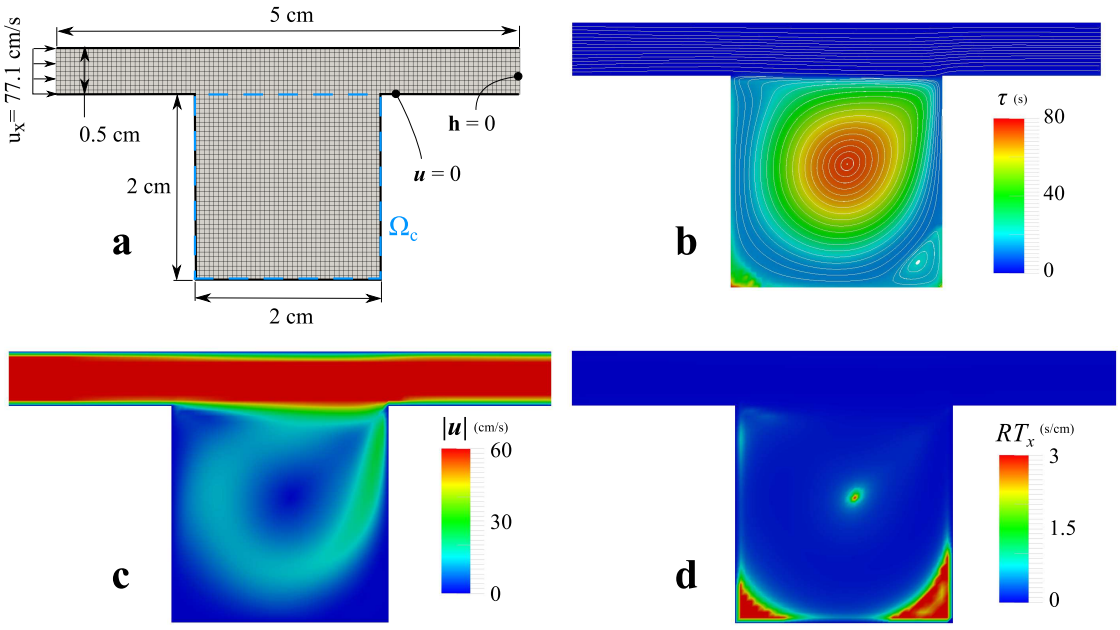

Figure 6.5: Flow over a 2D cavity, a) The mesh and dimensions of the computational domain, b) flow streamlines are plotted on top of τ contours, obtained from solving Equation (6.5), c) velocity magnitude contours, and d) RT_x contours. While τ is very high at the central recirculation regions, RT_x fails to identify this region. The velocity streamlines are roughly perpendicular to $\nabla\tau$ inside the cavity.

Flow is stagnant at the bottom corners and vorticity is high in the middle, trapping the fluid inside the cavity (Figure 6.5). This caused τ to be in the range of 50 s in the center and bottom corners of the cavity, as compared to $\tau \approx 0.05$ s in the duct. This shows that recirculation regions may produce much higher τ compared to regions with uni-directional flow. For this case RT_x, which only

depends on the local velocity value, is only high at the corners and fails to predict high RT for the central region.

RT_1 and RT_2 are calculated for the cavity only (Ω_c) and the entire computational domain (Ω), with results summarized in Table 6.1. RT_2, which is directly proportional to $\bar{Q}$, differs significantly between these two regions of interest. Due to much higher τ inside the cavity, $\int_{\Omega_\tau} \tau \mathrm{d}\Omega$ is almost the same between two regions of interest, causing RT_1 only to scale with the area of the region of interest. As a result, the $\frac{RT_2}{RT_1}$ ratio is increased by a factor of 23, by selecting cavity as the region of interest instead of the entire domain.

Table 6.1: Simulation results for the cavity model. Results are reported for two regions of interest: the cavity only ($\Omega_\tau = \Omega$), and the entire computational domain ($\Omega_\tau = \Omega_c$). Note the sensitivity of RT_2 to the region of interest selection.

Ω_τ	V_{Ω_τ} (cm^2)	$\bar{Q}$ (cm^2/s)	$\int_{\Omega_\tau} \tau \mathrm{d}\Omega$ (cm^{2}s)	RT_1 (s)	RT_2 (s)	$\frac{RT_2}{RT_1}$
Ω	6.5	38.56	135.9	20.90	0.17	0.008
Ω_c	4.0	0.627	135.5	33.87	6.38	0.188

6.2.2 Single ventricle patients

In this case study we explore the RT formulation in an idealized post surgical anatomy that was presented in Section 2.4.4, with one or two systemic-to-pulmonary connections (Figure 6.6). Three basic geometries were constructed to include (Figure 6.6): (A) a distal MBTS and a patent ductus arteriosus (PDA), (B) a proximal MBTS and a PDA, and (C) a proximal MBTS and a central shunt (CS).

While the flow in the shunt is always unidirectional, flow stagnation can occur in the PA segment due to flow competition from the MBTS and the PDA/CS. Depending on the diameter of the PDA/CS, the flow in this region can be stagnant, directed toward the right PA, or directed toward the left PA. Ten geometries were constructed for cases (A) and (B) with PDA diameters of: 0.0 (no PDA), 2.0, 3.5, 4.0, and 5.0 mm. Three geometries were constructed for case (C) with the CS diameters of: 2.0, 3.0, and 4.0 mm. For cases (A) and (B) two values of the PVR were simulated. In all models, the MBTS was slightly curved to make it perpendicular the PA. In total, 23 cases were simulated and compared.

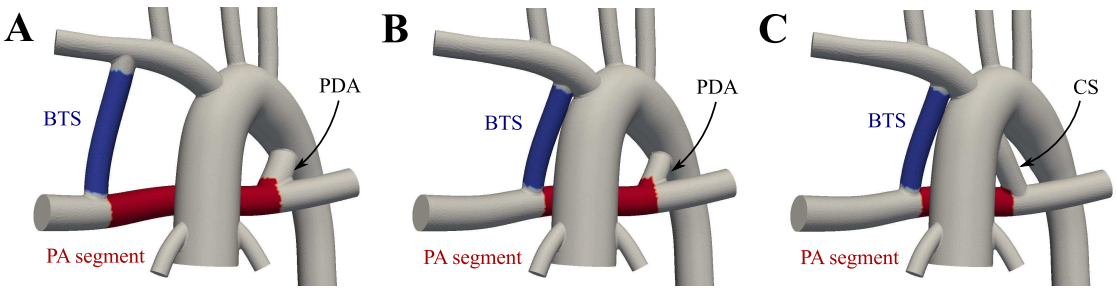

Figure 6.6: Representative anatomies used in this study: (a) distal MBTS and a 4.0 mm PDA, (b) proximal MBTS and a 3.0 mm PDA, and (c) proximal MBTS and a 4.0 mm CS. The PA segment (the red region between CS/PDA and MBTS) and the MBTS (the blue region) are used to compare RT and WSS results.

Flow simulations were performed using a multidomain approach following the framework discussed in Chapter 2 and using the LPN shown in Figure 2.11. In this case all outlets are coupled Neumann boundaries and the inlet, i.e. the AA, is a coupled Dirichlet boundary. Due to the presence of reversed flow at the outlets, backflow stabilization method was adopted in these simulations (Section 3.1.1). The specialized preconditioning method, bi-partitioned algorithm, and sorted data structure were also adopted, achieving significant improvements in computational cost efficiency compared to standard methods (see Chapters 4 and 5). The method described in Appendix D is used for WSS calculation.

Two regions of interest are considered: a segment of the PA between the MBTS and PDA/CS and the MBTS (red and blue regions in Figure 6.6, respectively). The two regions of interest are selected based on the dramatic difference in their hemodynamics and their potential clinical significance. The flow inside the MBTS is unidirectional for the entire cardiac cycle, since blood flows to the lower pressure pulmonary arteries from the higher pressure systemic side. In the PA segment, however, there is flow competition between the MBTS and PDA/CS and the flow direction is highly dependent on the diameter of the PDA/CS. The flow at the core of this region is stagnant for the midrange PDA/CS diameters with highly unsteady recirculation regions close to the MBTS and PDA/CS anastomoses.

The advection-diffusion problem was solved using the same FE method time integration and spatial discretization scheme as the Navier-Stokes solver. In these

simulations T was the length of the cardiac cycle and the time step size was set to 5×10^{-4} s. The normalized difference between the results of the second and subsequent cycles was on the order of 10^{-7}, demonstrating that cyclic convergence was obtained after two cycles.

RT_1 and RT_2 were calculated (Equations (6.8) and (6.16)) for these two regions and WSS was spatially averaged over the walls (Table 6.2).

Table 6.2: Comparison between RT and WSS. *PA-Seg* denotes the region between the PDA and MBTS and BT denotes the region in the MBTS (see red and blue regions in Figure 6.6). D is the diameter of the PDA/CS, with $D = 0$ corresponding to the single MBTS case. *Geom* denotes the choice of geometries shown in Figure 6.6. PVR is the pulmonary vascular bed resistance (N denotes normal PVR and H denotes one fold increase in PVR).

Case	D	Geom/PVR	RT_1 (ms)		RT_2 (ms)		WSS (cgs)	
			PA-Seg	BT	PA-Seg	BT	PA-Seg	BT
01	0.0	A/N	30.4	4.3	48.0	8.4	98.9	267
02	0.0	A/H	32.4	4.5	51.7	8.9	91.9	252
03	0.0	B/N	28.4	4.3	38.0	8.0	93.9	244
04	0.0	B/H	28.3	4.6	39.4	8.4	91.5	232
05	2.0	A/N	56.5	4.7	44.9	9.1	58.9	249
06	2.0	A/H	57.5	5.0	47.6	9.8	58.4	232
07	2.0	B/N	50.6	4.8	30.0	8.9	77.7	219
08	2.0	B/H	51.5	5.1	31.7	9.5	73.8	206
09	3.5	A/N	50.5	6.1	40.7	11.2	78.0	207
10	3.5	A/H	58.0	7.0	44.1	12.8	67.3	181
11	3.5	B/N	28.1	6.2	27.2	11.2	107.3	174
12	3.5	B/H	35.8	7.0	31.5	12.7	90.7	154
13	4.0	A/N	36.3	6.8	39.2	12.2	84.7	190
14	4.0	A/H	44.0	7.8	45.2	13.8	74.2	167
15	4.0	B/N	21.7	6.8	26.8	12.3	119.5	159
16	4.0	B/H	27.0	7.7	32.0	13.9	101.4	140
17	5.0	A/N	23.8	8.5	34.7	14.1	105.3	164
18	5.0	A/H	28.5	9.9	39.7	16.5	90.7	139
19	5.0	B/N	14.9	8.4	22.8	14.8	131.3	134
20	5.0	B/H	17.5	9.9	26.5	17.3	114.0	113
21	2.0	C/H	47.9	5.0	36.3	9.3	79.0	211
22	3.0	C/H	73.7	5.6	38.9	10.2	49.4	190
23	4.0	C/H	58.6	6.4	38.5	11.8	51.5	167

Due to the flow pulsatility, the spatial average of $\tau(\boldsymbol{x}, t)$ becomes nearly

periodic after the first cardiac cycle with a higher value during diastole and a lower value during systole, as expected (Figure 6.7). Due to the unidirectional flow in the MBTS, $\tau(\boldsymbol{x}, t)$ varies almost linearly in the MBTS (Figure 6.8-a), starting from zero at the proximal/systemic end and reaching approximately $2RT_1$ at the distal/pulmonary end, producing a spatial average of RT_1. Since $\tau(\boldsymbol{x}, t)$ at the distal end, i.e. Γ_o, is essentially equal to RT_2, $RT_2 \approx 2RT_1$ in the MBTS, which is consistent with the results in the Table 6.2. However, looking at RT in the PA section, this approximation is no longer true due to the presence of vortices near the PA segment boundaries. This flow produces high $\tau(\boldsymbol{x}, t)$ towards the center despite higher flow rates at the boundaries (Figure 6.8-b), leading to higher RT_1 and lower RT_2. The $\frac{RT_2}{RT_1}$ ratio is close to 2 in the MBTS and close to 1 in the PA section. Consistent with Equation (6.46), the flow in the MBTS can be assumed to be a single manifold, while the flow in the PA section is recirculating and is composed of several manifolds.

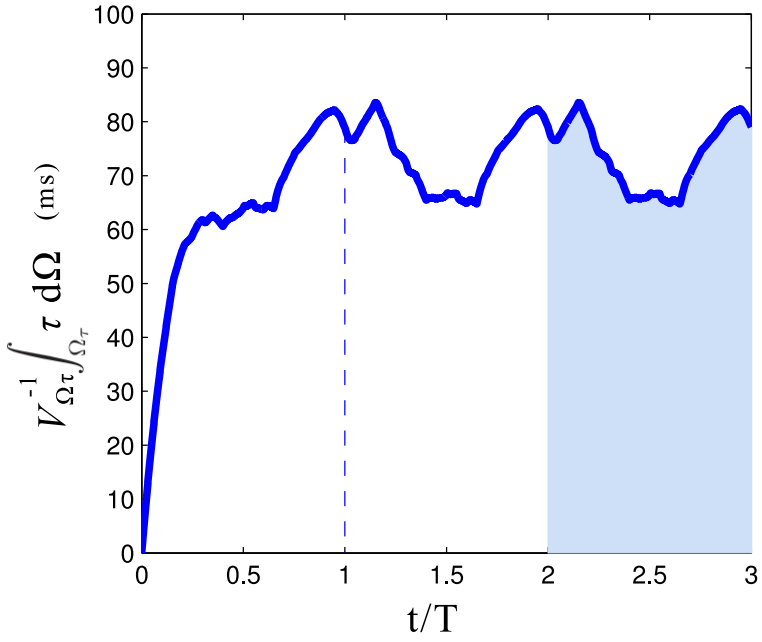

Figure 6.7: Time variation of spatial average τ in the PA section for the case with 3.0 mm CS. The shaded area is equal to RT_1.

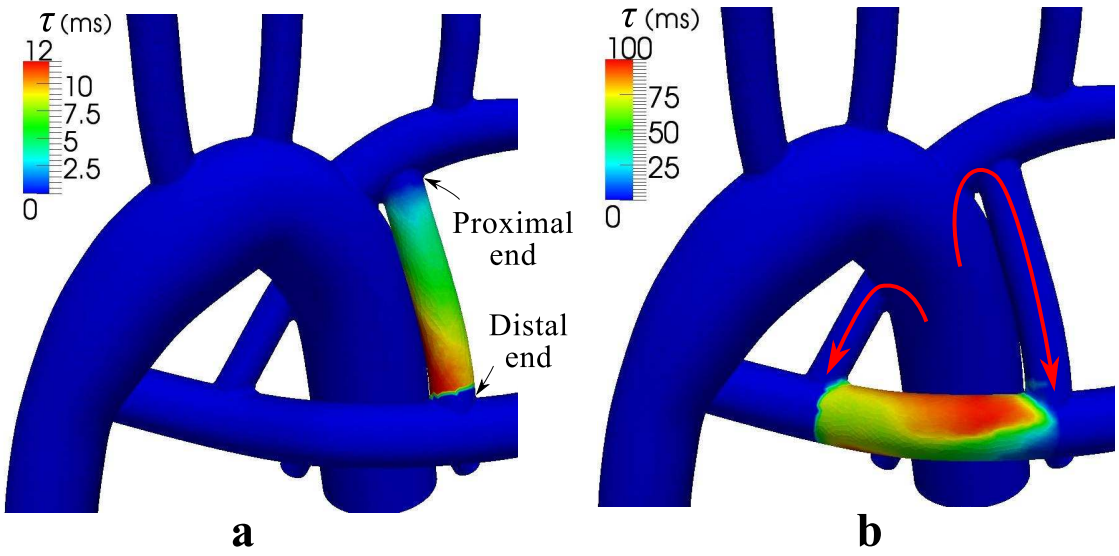

Figure 6.8: (a) Spatial distribution of time averaged τ in the MBTS. Note the linear distribution due to the unidirectional flow. (b) Spatial distribution of time averaged τ in the PA. Note the higher value at the center of the PA that leads to higher RT_1. Due to the high flow rates across the boundaries of the PA-Seg, RT_2 has a lower value in this case. The proximal and distal ends of MBTS and flow direction in the MBTS and PDA are shown.

The results of Table 6.2 are summarized in Figure 6.9. The 3.0 mm CS and 3.5 mm PDA cases had the highest RT in the PA, confirming the presence of a stagnation region between the MBTS and PDA at mid-range diameters. Increasing the PDA diameter beyond 3.5 mm reduces RT in the PA because an imbalance between the PDA/CS and the MBTS flow leads to flow through the PA segment. Since the PA flow rate is lower for the higher PVR cases, RT is higher in the PA and MBTS for these cases.

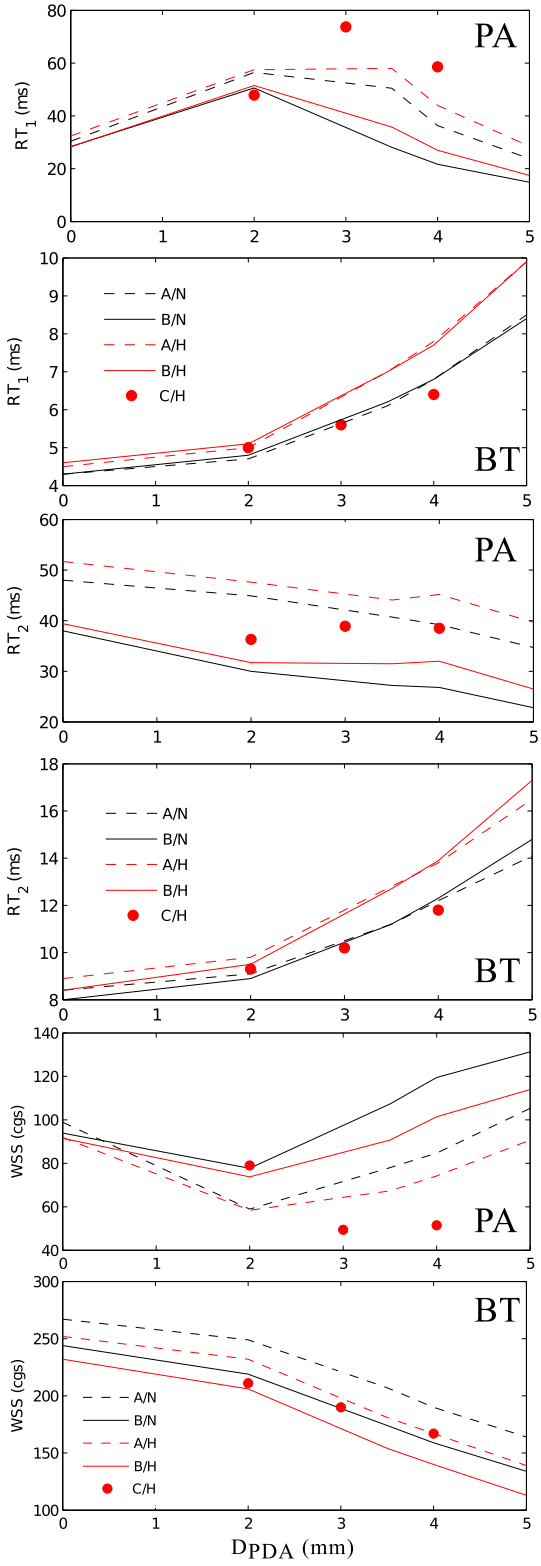

Figure 6.9: RT_1, RT_2, and WSS in the PA segment and in the MBTS as a function of PDA diameter. See Table 6.2 for notation details.

Examining the general trends in Figure 6.9, RT_1 and RT_2 are generally directly related while RT_1 and RT_2 are anti-correlated with WSS. To quantify this relation more directly, we computed the correlation between these three parameters, which is defined as,

$$R(\boldsymbol{x},\boldsymbol{y}) = \left[\sum_i (x^i-\bar{x})^2 \sum_i (y^i-\bar{y})^2\right]^{-\frac{1}{2}} \sum_i (x^i-\bar{x})(y^i-\bar{y}), \tag{6.49}$$

(Figure 6.10). Good correlation was obtained between RT_1 and WSS in both regions of interest, which are associated with different hemodynamics. However, the slope of the correlations in the MBTS and PA segment is not the same. As discussed before, RT_1 and RT_2 are strongly correlated in the MBTS, but poorly correlated in the PA segment.

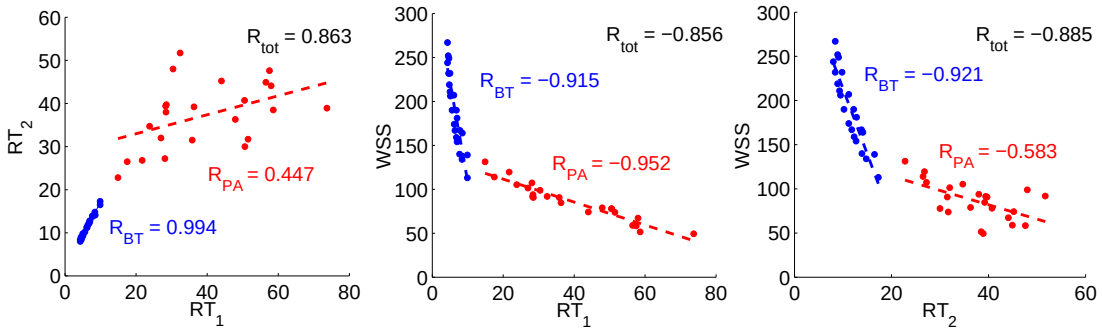

Figure 6.10: Correlation between RT_1, RT_2, and WSS measured in the MBTS (blue) and in the PA-Seg (red). Dashed lines are the best correlated lines. R_{BT} and R_{PA} are the correlation values between parameters in corresponding region and R_{tot} is the correlation between parameters calculated based on all the data points from both regions.

6.2.3 Kawasaki disease

In our third case study, we consider a patient specific model of coronary aneurysms caused by Kawasaki disease. Kawasaki disease is the leading cause of acquired heart disease in children, resulting in coronary artery aneurysms in up to 25% of untreated patients. Patients with aneurysms are at a higher risk of thrombosis formation inside the aneurysms, which can lead to myocardial infarction and sudden death [145, 146]. Regions of low WSS and high particle RTs in the

aneurysm are hypothesized to be an indicator for higher risk of thrombus formation. Clinicians treating Kawasaki disease patients currently use aneurysm diameter as the primary determinant of thrombotic risk, according to AHA guidelines. Aneurysm diameter is typically measured using CT imaging, and patients with diameters >8 mm are treated with anticoagulation therapy. Clinicians are thus often faced with a difficult decision to treat otherwise normal healthy patients with aggressive anticoagulation therapy or to treat with anti-platelet therapy alone and accept the risk of possible myocardial infarction. While aneurysms can be imaged to obtain detailed anatomical information, there are currently no available clinical tools to predict the risk of coronary artery thrombosis or myocardial infarction. Simulations can provide critical hemodynamic information linked to thrombotic risk, including WSS, RT, and oscillatory shear index, which are difficult or impossible to obtain from standard imaging modalities.

Our previous work revealed markedly abnormal hemodynamic conditions compared to normal control, including low WSS and high particle RT, in a case study of a 10 year old male Kawasaki disease patient (Figure 6.11) [41]. Subsequently, hemodynamic simulations in a group of Kawasaki disease patients with aneurysms have demonstrated better correlations between simulated WSS and particle RT and incidence of thrombosis compared to using aneurysm diameter alone [77]. Here, we use the previous results from one patient to compute RT using the proposed method, and compare to prior discrete model calculations.

For RT calculations, the formerly used mesh and reported velocity are used [41]. Model construction, simulation, and adaptive meshing methods are described in our prior work. The maximum diameter of the left anterior descending coronary artery (LAD) and right coronary artery (RCA) were 1.14 and 1.08 cm, respectively. The mesh contained over 3.5 million tetrahedral elements with a 0.2 mm minimum element size. A BC that is specifically designed for the coronary arteries was used and an implicit method was used to couple BCs to the 3D domain [51]. Flow simulation was continued for six cardiac cycles, with a time step size of 1 ms.

Regions of interest are colored red and blue in Figure 6.11. Due to the higher RTs, the advection-diffusion solver required 6 cycles to obtain converged

solution with a time step size of 1 ms.

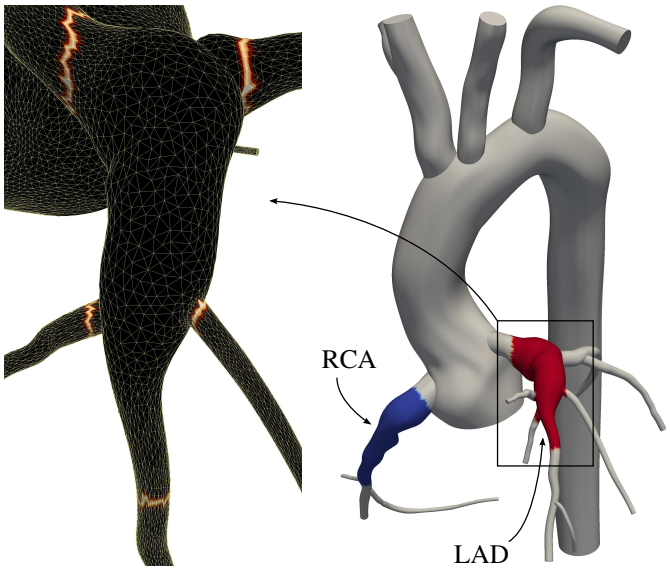

Figure 6.11: The regions of interest, Ω_τ, are indicated by red and blue on the right. The tagged surface for calculating RT_2 in the red region is outlined by a brighter color on the left. $\boldsymbol{u} \cdot \boldsymbol{n}$ is evaluated on these boundaries to calculate RT_2.

High RT is predicted for aneurysmal regions closer to the wall and the middle section of the LAD, where the flow is changing direction (Figure 6.12). Due to the lower velocities and recirculating flow, RT values were higher in this model compared to the second case study (Figure 6.8). Cumulative exposure time (CET), which is calculated with a discrete method, was used previously to quantify RT in the LAD and RCA [41]. CET has units of time per unit volume, hence a quantitative comparison can not be made between CET and RT_{x}. Qualitatively, however, CET and RT_{x} are similarly high in the low velocity regions. CET has an advective effect and predicts higher values in the distal RCA, despite the high velocity in that region (Figure 6.12-(b)). Although 10M particles were released in each cardiac cycle, the CET contours remain pixelated with a large variation between two adjacent elements. To compare simulation costs, the full blood flow simulations took 26 hours on 60 processors, the CET calculation took 2-3 days on a single processor, and the advection-diffusion simulation took 8 hours on a

single processor [41]. This indicates the lower computational cost of the proposed method, though simulation times for both CET and the proposed method could be improved through parallelization.

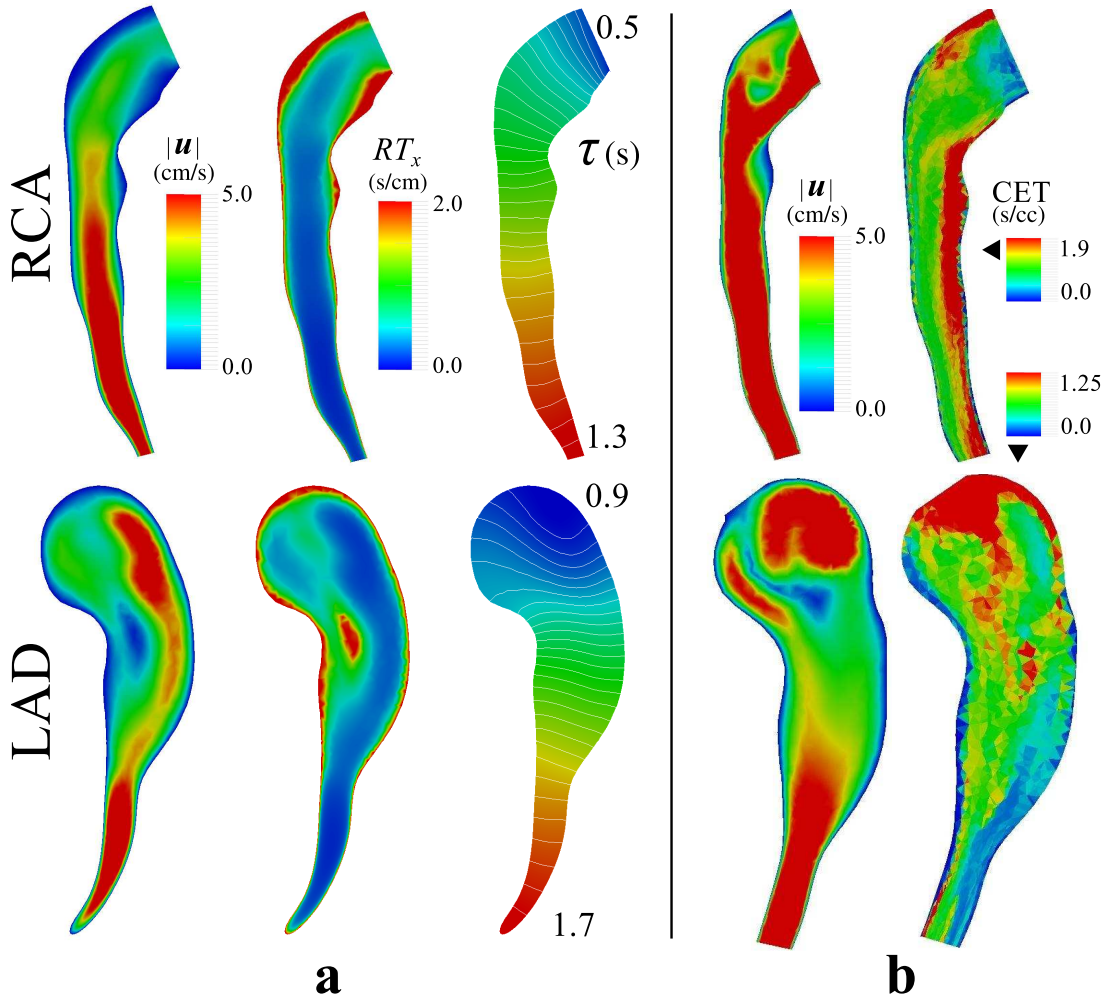

Figure 6.12: (a) Time-averaged velocity, local RT, RT_x, and τ in the LAD and RCA. Regions of high RT_x are associated with regions of low velocity. Note the linear distribution of τ in the downstream branches due to the unidirectional flow. (b) Velocity and CET using a discrete method taken from prior work [41]. Note the continuous distribution of RT measures obtained using the proposed method.

The $\frac{RT_2}{RT_1}$ ratio is larger in the RCA compared to the LAD, indicating less flow disturbance in the RCA (Table 6.3). This can be linked to more uniform variation of τ along the RCA compared to the LAD.

Table 6.3: RT_1 and RT_2 in the LAD and RCA. The regions of interest and the model are shown in Figure 6.11.

Ω_τ	RT_1	RT_2	$\frac{RT_2}{RT_1}$
LAD	1.178	0.988	0.839
RCA	0.817	1.077	1.318

6.3 Discussion

Clot formation is a gradual process, requiring regions of trapped fluid for platelet aggregation to occur. RT is a measure which is sought to identify regions with trapped fluid, thus acting as a surrogate quantitative measure of the likelihood of clot formation. Since there is currently no universal definition of RT, we proposed two intuitive definitions (RT_1 and RT_2) to quantify RT in a given region of interest. Considering τ as the time that particles are inside the region of interest, RT_1 is the average of τ over the region of interest. Physically, this is equivalent to the average in time that particles have been in a region of interest. RT_2 is calculated by averaging τ over the boundaries of the region of interest. This can be interpreted as the average of the time that particles leaving the region of interest, have been in that region. This measure reduces to RT_{x} by reducing the size of region of interest to a point and normalizing it with a characteristic length. In that sense, RT_{x} is a spatial comparative measure of RT at a point, which is directly proportional to the inverse of the velocity norm.

In this study, a non-discrete method was formulated for RT calculations using an Eulerian framework. A time-dependant advection-diffusion equation was solved to compute RT_1 or a control volume technique was used to compute RT_2 based on boundary fluxes on the region of interest. As a result this method accounts for diffusivity and in our experience requires less computational cost and complexity compared to discrete methods. With the present approach, the same numerical framework used in the flow solver can be used to calculate RT. Extending the proposed method to an FSI application with a moving domain will only require including the referential domain velocity in the advective term, hence minimal implementation effort is required. The presented formulation is not based on

the calculation of RT or exposure time in individual elements, hence this method can be applied accurately to an anisotropic mesh with a wide range of element sizes. We note that discrete methods have been used effectively in computing Lagrangian coherent structures (LCS) derived from dynamical systems theory for improved understanding of unsteady flow structures. Previous methods have used LCS in the cardiovascular setting to characterize flow in aneurysms and for assessing thrombotic risk [147, 148].

We have shown that local representation of RT is directly related to the local velocity. RT_2 was shown to be a lower bound for $2RT_1$ in steady non-diffusive flow, however this relation also held for all unsteady cases we considered. Extension of the presented proof to unsteady diffusive flows is left as a subject for future studies. The applicability of this method was shown in a 2D recirculating flow and two representative clinical scenarios, including multiple geometries associated with a first stage single ventricle repair, and a coronary artery aneurysm in a Kawasaki disease patient.

The FE framework used in this work for solving the advection-diffusion equation requires stabilization that is standard to all FE methods for fluid. In practice this translates to the accuracy of the solution, τ, that among other factors depends on the mesh quality, time step size, and Peclet number. In the presented formulation, τ typically lives in the same discrete space as velocity, linking its numerical accuracy to the Navier-Stokes equations solution quality. In other words, by reducing the mesh size and reducing the error of the Navier-Stokes solution (which is the transport of momentum), the error of the advection-diffusion equation solution also reduces (which is the transport of τ).

The main purpose of calculating RT is to identify recirculation regions that trap fluid for extended times. Selecting a region of interest that contains a recirculation region produces locally high τ, leading to high RT_1. The value of RT_2, on the other hand, is determined only by the flow through the boundaries, regardless of the hemodynamic behavior within the domain. This indicates RT_2 is more sensitive to the selected region geometry and may not adequately capture a recirculation region if Ω_τ is not selected properly. Hence, although RT_2 has the

advantage of negligible computational cost, RT_1 was found to be a more physically consistent measure of RT. Likewise, RT_{x}, which is calculated only based on local quantities, fails to capture recirculation regions that depend on the global spatial characteristics of the flow.

In this study we observed good correlation between WSS and RT_1 in the single ventricle example. This is consistent with previous in-vivo and experimental studies, which reported an inverse correlation between WSS and RT [149, 150]. In the MBTS, due to the unidirectional flow, there was a strong correlation between RT_1 and RT_2, hence also between WSS and RT_2. However, in the PA segment, there were many structures in the flow and the flow direction changed with the PDA/CS diameter. Hence the strong correlation between WSS and RT_1 is less obvious. This suggests high RT can also be directly linked to low WSS regions, and hence either of these two parameters may be useful for evaluating a clinical scenario. Since WSS and RT scale differently with vessel diameter, viscosity, and the length of the region of interest, WSS and RT_1 are not correlated in the two different regions of interest considered in the first clinical scenario (R_{tot} is not close to -1 in Figure 6.10). We observed this correlation in a single case study, hence before any generalization this result must be confirmed by further studies in the future.

In the third case study on Kawasaki disease, the proposed measures of RT offer a promising means to obtain surrogates for thrombotic risk that could be used to improve patient selection for anticoagulation therapy. The decision whether to put a patient on anticoagulation medication is a serious one, particularly in children. Our results have demonstrated that the proposed RT methods produce smooth solutions with relatively modest computational effort.

Thrombus formation is a complex process, and recent advances in modeling the chemistry of the coagulation cascade are highly promising [131]. However, there remains a need for surrogates of thrombotic risk that can be obtained directly from the flow field. Because RT_1 measures the time that a fluid particle spends in a given region, it may be a better surrogate for local platelet aggregation time than RT_2, which lacks those local information.

Acknowledgements

The authors wish to thank Ethan Kung, Christopher Long, and Yuri Bazilevs for their useful comments, Dibyendu Sengupta, Jane Burns, and Andrew Kahn for the Kawasaki disease simulations, and Bari Murtuza for his clinical insight.

This chapter, in full, is a reprint of the material as it appears in A non-discrete method for computation of residence time in fluid mechanics simulations in *Physics of Fluids*, 2013, DOI: 10.1063/1.4819142. Authors are M. Esmaily-Moghadam, T-Y. Hsia, and A. Marsden. The dissertation author was the primary investigator and author of this paper.

Chapter 7

Optimization of Shunt Placement

In Chapter 1, we saw that the stage-one or Norwood procedure is performed in children diagnosed with hypoplastic left heart syndrome and other single ventricle conditions [3, 4]. These infants typically undergo a series of three surgical procedures starting immediately after birth with stage-one palliation. In this procedure, performed within the first few days of life, a single functional ventricle is committed to providing systemic perfusion, and the pulmonary blood flow is derived from a shunt (so-called MBTS) between the brachiocephalic artery and the PA (Figure 7.1).

In this circulatory arrangement, instead of being in-series, the systemic and pulmonary blood flow are in parallel. It is of critical importance to maintain a delicate balance in this parallel arrangement to provide sufficient blood supply to both systemic and pulmonary circulation. Either too much or too little pulmonary blood flow can lead to inadequate oxygenation [13, 14, 15]. Pulmonary flow rate is directly linked to the MBTS geometry, which itself has a significant effect on both cardiac output and OD [16]. MBTS diameter, which is typically between 3 to 4 mm, is chosen pre-operatively based on patient condition, weight, and other clinical factors [151].

On the other hand, during cardiac diastole, when the coronary arteries are perfused in normal subjects, in patients with the Norwood circulation, there is a runoff of blood into the pulmonary arterial bed, leading to reduced coronary perfusion [13]. This *steal* of coronary perfusion by the shunt is due to the lower PVR,

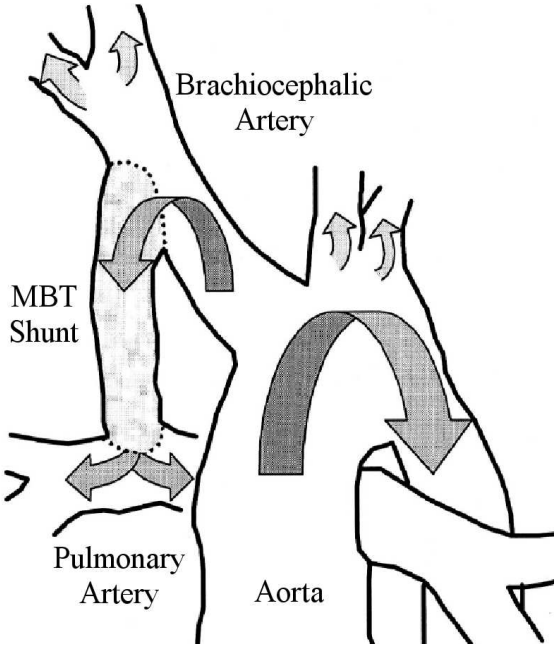

Figure 7.1: Schematic of Modified MBTS anatomy [1].

relative to systemic vascular resistance, and can lead to myocardial ischemia [14]. Thus, maintaining sufficient blood flow to the coronary arteries during diastole, along with balanced flow between systemic and pulmonary beds, are critical to the survival of these patients.

In this chapter, we systematically optimize several shunt geometric parameters for clinically important variables, such as coronary and systemic OD. In doing so, we must choose a suitable optimization method. Several methods have been used in prior work for cardiovascular optimization. Adjoint methods has been used to find the optimal anastomosis configuration in a coronary artery bypass graph [152]. Sensitivity-based (i.e. gradient) optimization has been carried out with steady and unsteady flows to study the effect of fluid constitutive model on the optimal results [153, 154]. Also, numerical optimization has been used to improve efficiency of blood pump design processes [155]. In this study, due to the high computational cost of each multidomain simulation and a lack of objective function gradient information, an effective derivative-free optimization algorithm, called the Surrogate Management Framework (SMF), is used [156, 157, 158]. This

framework has been previously applied to cardiovascular and single ventricle applications [31, 32]. The Norwood circulation represents an ideal substrate for application of these methods, since they are non-intrusive and the problem has a larger set of flexible design parameters. By optimizing for coronary OD, we attempt to mitigate an important potential drawback of the MBTS procedure. An informal survey of multiple clinical experts led us to define the following potential design parameters to investigate in this study: shunt diameter, anastomosis locations of the shunt on both the brachiocephalic and PA, and angles of attachment points. This study thus explored primarily the influence of the shunt diameter, but also the influence of the angle and attachment points, which had not been examined previously. As for the optimization targets, maximizing OD was of highest priority for all experts. Optimizing for cardiac output and pulmonary-to-systemic flow ratio were less important, and there was no real consensus on their target value. Hence, in this study we concentrate on maximizing OD, while reporting other important parameters noted by the clinicians such as cardiac output, pulmonary-to-systemic flow ratio, and pressures of systemic and pulmonary sides.

The chapter is arranged as follows: We briefly review the optimization algorithm and present the selected objective function formulations. Results of the optimization with three objective functions, systemic OD, coronary OD and a combination of the two, are presented. The shunt diameter, anastomosis locations and angles are chosen as design parameters. The optimal geometry results are compared to three standard shunt geometries that are commonly used in clinical practice. The simulation results are verified by comparing them with the reported results in the literature. Finally, we discuss implications of shunt placement for coronary flow and OD, and present a brief sensitivity study.

7.1 Methods

The general optimization framework used in this chapter is shown in Figure 7.2. Starting with a set of shape design parameters, the shunt geometry is analytically specified and automatically inserted into the rest of the model. The

dimensions of the rest of the idealized model are based on angiograms of a group of typical stage one patients during catheterization exam. A multidomain simulation is carried out to obtain the time dependant velocity and pressure inside the 3D model. The objective function is calculated in a post-processing step from the simulation output. Based on the objective function values, the surrogate management framework is used to obtain a new set of design parameters. This process continues until the design converges to an optimal value in the design space. The entire algorithm, including model construction, mesh generation and coupled simulation, is fully automated, which facilitates multiple function evaluations in a reasonable time on a parallel computer.

The FE framework, described in Section 2.1, is used for discretization of Navier-Stokes equations in space and time and obtaining the linear system of equations. As described in Section 3.1.1, we make use of stabilized formulation to prevent divergence due to the the presence of backflow (for example, the AA coupled to the heart model will experience massive inward flow during systole). The LPN used in this work is described in Section 2.4.4 and shown in Figure 2.11 (see Appendix B for LPN values). In these simulations, Neumann BC is imposed at the AA. Also, for the mesh sensitivity study see Section 2.4.4 and for the model construction techniques see Section 2.3.

The time step size for the 3D solver is set to 5×10^{-4} s. The non-linear iterations are continued until the normalized residual is less than 5×10^{-4} or the number of iterations exceeds 8.

7.1.1 Optimization method

The amount of systemic and coronary OD is a significant factor that should be considered for determining the best shunt geometry. As detailed in Appendix C, OD can be calculated using

$$OD(\boldsymbol{d}) = \bar{Q}_{\mathrm{s}}(\boldsymbol{d}) C_{\mathrm{ao}}(\boldsymbol{d}) = \bar{Q}_{\mathrm{s}}(\boldsymbol{d}) C_{\mathrm{p}} - \frac{V_{\mathrm{O}_2} \bar{Q}_{\mathrm{s}}(\boldsymbol{d})}{\bar{Q}_{\mathrm{p}}(\boldsymbol{d})}, \tag{7.1}$$

in which OD, V_{O_2}, Q_{p}, and Q_{s} are the OD to the body, the oxygen consumption by the body, blood flow to the pulmonary and systemic arteries. In Equation

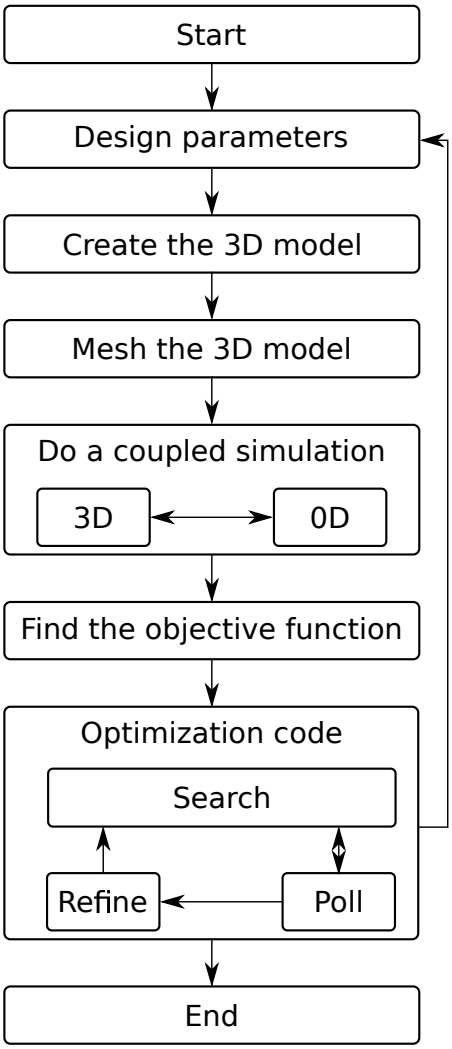

Figure 7.2: Overall framework for optimization.

(7.1), except for V_{O_2} and C_p, all other parameters are assumed to be a function of the design parameters, $\boldsymbol{d} = \{d_1, d_2, ..., d_{n_d}\}$ where n_d is the number of design parameters. Note, the systemic flow rate, Q_s, includes the flow to the coronary arteries.

$\bar{Q}_i$ is the time average flow rate of the surface i in a cardiac cycle, and

$$\bar{Q}_i(\boldsymbol{d}) = \frac{1}{T}\int_{(k-1)T}^{kT} Q_i(\boldsymbol{d}, t)\mathrm{dt}, \tag{7.2}$$

where T is the cardiac cycle period and k is the number of simulated cycles. The above should satisfy,

$$\begin{gathered} 2 \leq k \leq k_{\max}, \\ \left|\frac{CO^k(\boldsymbol{d}) - CO^{k-1}(\boldsymbol{d})}{CO^k(\boldsymbol{d})}\right| \leq \epsilon, \end{gathered} \tag{7.3}$$

where $k_{\max}$ is the upper limit for the number of cardiac cycles to be simulated and CO^k is the cardiac output of cycle k, i.e. $CO^k = \bar{Q}_p + \bar{Q}_s$. The values of $k_{\max}$ and ϵ in Equation (7.3) are set to 5 and 0.1%, respectively. In most of the objective function evaluations, the second constraint in Equation (7.3) is satisfied after 3 to 4 cycles.

Defining the objective function as the ratio of available oxygen to consumed oxygen (or its inverse if J should be minimized), we can write,

$$\frac{1}{J_1(\boldsymbol{d})} = \frac{OD(\boldsymbol{d})}{V_{O_2}} = \left(\frac{C_p}{V_{O_2}} - \frac{1}{\bar{Q}_p(\boldsymbol{d})}\right)\bar{Q}_s(\boldsymbol{d}). \tag{7.4}$$

Similar to Equation (7.4), the objective function for coronary OD (OD_{cor}), J_2, can be obtained from Equation (7.1) by replacing $\bar{Q}_s$ with coronary flow rate, $\bar{Q}_{cor}$,

$$\frac{1}{J_2(\boldsymbol{d})} = \frac{OD_{cor}(\boldsymbol{d})}{V_{O_2}} = \left(\frac{C_p}{V_{O_2}} - \frac{1}{\bar{Q}_p(\boldsymbol{d})}\right)\bar{Q}_{cor}(\boldsymbol{d}). \tag{7.5}$$

Using the following change of variables,

$$\alpha(\boldsymbol{d}) = \frac{\bar{Q}_p(\boldsymbol{d})}{\bar{Q}_s(\boldsymbol{d})}, \tag{7.6}$$

Equation (7.4) can be rewritten as,

$$OD(\boldsymbol{d}) = \frac{C_p CO(\boldsymbol{d})}{1 + \alpha(\boldsymbol{d})} - \frac{V_{O_2}}{\alpha(\boldsymbol{d})}. \tag{7.7}$$

The partial derivative of Equation (7.7) with respect to α is,

$$\frac{\partial OD}{\partial \alpha} = \frac{C_{\mathrm{p}}}{1+\alpha}\frac{\partial CO}{\partial \alpha} - \frac{C_{\mathrm{p}} CO}{(1+\alpha)^2} + \frac{V_{\mathrm{O}_2}}{\alpha^2}. \tag{7.8}$$

Thus, using Equation (7.8) to maximize OD with respect to $\bar{Q}_{\mathrm{p}}/\bar{Q}_{\mathrm{s}}$, while keeping CO fixed, gives,

$$\left.\frac{\bar{Q}_{\mathrm{p}}}{\bar{Q}_{\mathrm{s}}}\right|_{opt} = \frac{\sqrt{V_{\mathrm{O}_2}}}{\sqrt{C_{\mathrm{p}} CO} - \sqrt{V_{\mathrm{O}_2}}}. \tag{7.9}$$

From Equations (7.9) and (7.7),

$$\sqrt{C_{\mathrm{p}} CO} = \sqrt{OD} + \sqrt{V_{\mathrm{O}_2}}. \tag{7.10}$$

Equation (7.10) provides the relationship between CO and OD when the $\bar{Q}_{\mathrm{p}}/\bar{Q}_{\mathrm{s}}$ is optimum. In other words, this equation gives the minimum required theoretical cardiac output for delivering a certain amount of oxygen to the body for the Norwood anatomy. One may rewrite Equation (7.9) based on (7.10) to obtain,

$$\left.\frac{\bar{Q}_{\mathrm{p}}}{\bar{Q}_{\mathrm{s}}}\right|_{opt} = \sqrt{\frac{V_{\mathrm{O}_2}}{OD}}. \tag{7.11}$$

Note that this equation is obtained provided Equation (7.10) holds and CO is fixed. Hence, although cardiac output does not appear in this equation, the optimum $\bar{Q}_{\mathrm{p}}/\bar{Q}_{\mathrm{s}}$ is related to cardiac output via OD. Enforcing the condition $C_{\mathrm{s}} \geq 0$ leads to $OD \geq V_{\mathrm{O}_2}$, hence from Equation (7.11), the optimal $\bar{Q}_{\mathrm{p}}/\bar{Q}_{\mathrm{s}}$ is always less than one.

When choosing an optimization algorithm for this problem, there are several considerations. First, each objective function evaluation in the optimization routine corresponds to k cardiac cycle simulations of the coupled 3D-0D systems, which is very costly (approximately 1 hour on a parallel 56×2.4 GHz processor machine). Second, gradient information for the coupled system is not readily available, and using a finite difference method for obtaining the gradient of the objective function is vulnerable to numerical errors. Finally, it is desirable to choose an algorithm with a known mathematical convergence theory. With all of these considerations, the surrogate management framework (SMF) was chosen for optimization in this problem following our previous work [32, 157, 159].

In the SMF algorithm, a Kriging surrogate function (see for example [157]) is constructed from the known objective function values. This function is updated each time a new point in the parameter space is evaluated by doing a coupled simulation. The SMF algorithm consists of two basic steps: a search and a poll. In the search step, optimization is performed on the surrogate function to identify minimizing points, with minimal computational cost. This step is done to improve the convergence rate of the optimization algorithm toward the optimum point. To mathematically ensure convergence, the poll step is performed, in which the objective function is evaluated on a set of points in positive spanning directions around the current optimum point. A set of positive spanning directions is defined as a set of vectors for which none of the vectors in that set can be constructed by non-negative combination of other vectors from the same set [160, 157].

We define a mesh in the parameter space with equal nodal distances, i.e. homogeneous mesh size, which in this instance includes 11 nodes in each direction. The algorithm starts with a search step, and continues searching as long as improved points are found. An unsuccessful search step, i.e. when a search step fails to improve the objective function, is followed by a poll step, in which a set of neighboring mesh points are evaluated. An unsuccessful poll step is followed by parameter space mesh refinement, and another search step. Thus, the mesh size is reduced when the current optimal point cannot be further improved by moving in the positive spanning directions. Mesh refinement is performed until the user defined refinement criteria (1/32 of the initial mesh size in this work) is achieved and optimization is terminated, as shown in the last block of Figure 7.2.

If the poll step fails to identify an improved point, then the current best point is a mesh local optimizer and the parameter space mesh is refined. As the algorithm progresses, a series of successively finer meshes will be generated, each producing a mesh local optimizer. It is the convergence of the series of mesh local optimizer points that guarantees convergence to a local minimum of the function. Using mesh adaptive direct search, the series of poll steps will generate a dense set of poll directions, and this further strengthens the convergence of the method for the case of constrained optimization. Please see [159, 32, 160, 161] for more

details in this regard.

7.1.2 Parameterization

Starting with a set of design parameters, the solid model is constructed using an automated script. The set of design parameters, which includes the shunt diameter, the shunt anastomosis angles and locations, is shown in Figure 7.3.

The anastomosis angles between the shunt and both the PA and brachiocephalic artery (BA) can be decomposed into four angles, i.e. two angles for each point A and B in Figure 7.3. Let us denote the position and tangent vectors of the centerline of the branch $\mathcal{I}$ with, $\boldsymbol{r}_{\mathcal{I}}(s)$ and $\boldsymbol{t}_{\mathcal{I}}(s)$, where $s \in [0,1]$ is the non-dimensional parameter that moves the point position and tangent vectors along the vessel centerline. Given the position of the points A and B, i.e. $\boldsymbol{r}_{\mathrm{PA}}(s_{\mathrm{A}})$ and $\boldsymbol{r}_{\mathrm{BA}}(s_{\mathrm{B}})$ a local coordinate system with unit vectors $[\boldsymbol{\xi}_1, \boldsymbol{\xi}_2, \boldsymbol{\xi}_3]$ can be specified for these two points,

$$\begin{aligned}
\boldsymbol{\xi}_1 &= \frac{\boldsymbol{r}_{\mathrm{BA}}(s_{\mathrm{B}}) - \boldsymbol{r}_{\mathrm{PA}}(s_{\mathrm{A}})}{\|\boldsymbol{r}_{\mathrm{BA}}(s_{\mathrm{B}}) - \boldsymbol{r}_{\mathrm{PA}}(s_{\mathrm{A}})\|}, \\
\boldsymbol{\xi}_2 &= \frac{\boldsymbol{t}_{\mathrm{PA}}(s_{\mathrm{A}}) \times \boldsymbol{\xi}_1}{\|\boldsymbol{t}_{\mathrm{PA}}(s_{\mathrm{A}}) \times \boldsymbol{\xi}_1\|}, \\
\boldsymbol{\xi}_3 &= \boldsymbol{\xi}_1 \times \boldsymbol{\xi}_2.
\end{aligned} \tag{7.12}$$

In the local coordinate system, the in-plane, θ_{i}, and out-of-plane, θ_{o}, angles for the two points A and B are defined as,

$$\begin{aligned}
\theta_{\mathrm{i,p}} &= \cos^{-1}\left(\frac{\boldsymbol{t}_{\mathrm{s}}(s_p) \cdot \boldsymbol{\xi}_3}{\|\boldsymbol{t}_{\mathrm{s}}(s_p)\|}\right), \ p \in \{\mathrm{A}, \mathrm{B}\}, \\
\theta_{\mathrm{o,p}} &= \cos^{-1}\left(\frac{\boldsymbol{t}_{\mathrm{s}}(s_p) \cdot \boldsymbol{\xi}_2}{\|\boldsymbol{t}_{\mathrm{s}}(s_p)\|}\right), \ p \in \{\mathrm{A}, \mathrm{B}\}.
\end{aligned} \tag{7.13}$$

where $\boldsymbol{t}_{\mathrm{s}} = \frac{\partial \boldsymbol{r}_{\mathrm{s}}}{\partial s}$ is the tangent vector to the shunt centerline, shown by a dashed line in Figure 7.3.

Using Equations (7.12)-(7.13), and given anastomosis angles and locations as the optimization parameters, a 3D spline is analytically specified between points A and B representing the centerline of the shunt. Based on the shunt diameter, which is another optimization parameter, shunt segments are specified and a solid

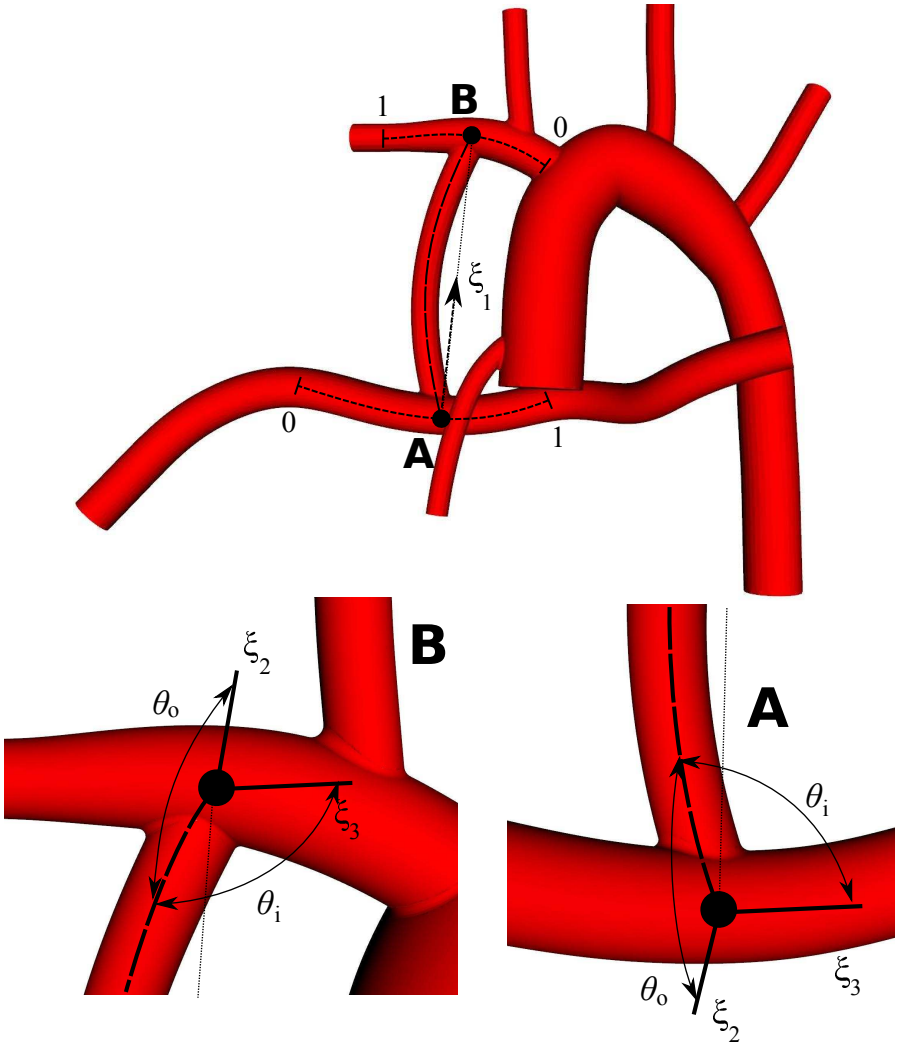

Figure 7.3: Shunt parameterization. Shunt diameter, two anastomoses locations and anastomosis angle are used as the design parameters. Anastomosis angles at each point are decomposed into two in-plane θ_{i}, and out-of-plane θ_{o} angles. The extend of anastomosis points sliding path are shown ($\boldsymbol{r}_{\mathrm{PA}}(s_{\mathrm{A}}),\ s_{\mathrm{A}} \in [0,1]$ for point A and $\boldsymbol{r}_{\mathrm{BA}}(s_{\mathrm{B}}),\ s_{\mathrm{B}} \in [0,1]$ for point B). In this figure, points A and B are at the middle, i.e. $s_{\mathrm{A}} = 0.5$ and $s_{\mathrm{B}} = 0.5$.

Table 7.1: The list of design parameters used in this study with their minimum and maximum bounds.

Name	symbol	min	max
shunt diameter	D_{sh}	2.5	4.0
Out-of-plane angle between shunt-PA	$\cot(\theta_{\text{o,A}})$	-1.0	1.0
PA and shunt anastomosis location	s_{A}	0.0	1.0
PA and shunt anastomosis location	s_{B}	0.0	1.0

representation of the shunt is created by lofting the segments together. The segments of the other branches are then loaded and their corresponding solid vessels are created. A complete solid model is then created by unioning the shunt and the rest of the vessels. Because the brachiocephalic and pulmonary vessel radii exceed that of the shunt, we have not encountered problems with the union operation. However, if the shunt is very skewed, it can intersect with the AA. When this occurs, these models are thrown out (the corresponding point from the parameter space is excluded from the objective function defined space) in the next stage. This process is performed using a customized in-house version of the open source Simvascular software package [70].

As shown in Table 7.1, the set of four design parameters used in this study are: shunt diameter, out-of-plane angle of shunt-PA anastomosis, and two anastomoses locations, i.e. $\boldsymbol{d} = \{D_{\text{sh}}, \cot(\theta_{\text{o,A}}), s_{\text{A}}, s_{\text{B}}\} \in$
$\{[2.5, 4.0], [-1.0, 1.0], [0.0, 1.0], [0.0, 1.0]\}$, $n_d = 4$. Note that $\boldsymbol{r}_{\text{PA}}(s_{\text{A}})$, and $\boldsymbol{r}_{\text{BA}}(s_{\text{B}})$ are specified based on the two latter parameters. The distance between $\boldsymbol{r}_{\text{PA}}(s_{\text{A}} = 0)$ and $\boldsymbol{r}_{\text{PA}}(s_{\text{A}} = 1)$ along the PA is 26 mm, hence the distance of point A from $s_{\text{A}} = 1$ (in Figure 7.3 the point on PA behind the AA) can be approximated by $26 - 26s_{\text{A}}$ in mm. Similarly, the distance between $\boldsymbol{r}_{\text{BA}}(s_{\text{B}} = 0)$ and $\boldsymbol{r}_{\text{BA}}(s_{\text{B}} = 1)$ along the BA is 17 mm, hence the distance of point B from $s_{\text{B}} = 0$ (in Figure 7.3 where BA is attached to the AA) can be approximated by $17s_{\text{B}}$ in mm. Due to surgical constraints and small effect of the other anastomosis angles on the objective function, $\theta_{\text{i,A}}$, $\theta_{\text{i,B}}$, and $\theta_{\text{o,B}}$ are not considered as design parameters and are set to $\pi/2$.

7.2 Results

7.2.1 Systemic OD objective function

The first case we consider is an optimization to find the minimum of J_1 (Equation (7.4)). The results show that the shunt diameter has the most significant effect on the objective function, i.e. the changes in J_1 with the shunt diameter are higher than changes due to the anastomosis angle or locations.

The numerical error in the objective function is proportional to changes in the objective function. So to isolate the effect on the objective function from changes in the shunt diameter versus changes in the anastomosis angle or locations, three separate optimizations are performed. First, we perform optimization with respect to the shunt diameter to estimate the globally optimal shunt diameter. Second, keeping the optimized shunt diameter fixed, we optimize for the anastomosis angle and locations, i.e. $\boldsymbol{d} = \{\cot(\theta_{\mathrm{o,A}}), s_{\mathrm{A}}, s_{\mathrm{B}}\}$. Third, we set the anastomosis angle and locations to the optimized values from the previous step, and perform optimization for the shunt diameter to check that the new optimal shunt diameter is close to the first optimal result.

The history of the objective function versus number of function evaluations is shown in Figure 7.4-(a). In this optimization, the design parameters are anastomosis angle and locations, with shunt diameter fixed to 3.2 mm.

From the objective function history in Figure 7.4-(a), the optimum PA out-of-plane anastomosis angle ($\theta_{\mathrm{o,A}}$) is 76°, the distance between point A and the point behind AA ($s_{\mathrm{A}} = 1$ in Figure 7.3) is 23 mm, and the distance between point B and the aortic arch ($s_{\mathrm{B}} = 0$ in Figure 7.3) is 2 mm. Hence, the optimum shunt to BA anastomosis location is close to the aortic arch. The optimum shunt to PA anastomosis is inclined toward the right PA, which sends more shunt flow to the right PA.

Having the optimum anastomosis angle and locations, the next optimization is done with respect to the shunt diameter. The value of the objective function at a fixed anastomosis angle and locations, $J_1\left|_{\theta_{\mathrm{o,A}}, \boldsymbol{r}_{\mathrm{PA}}(s_{\mathrm{A}}), \boldsymbol{r}_{\mathrm{BA}}(s_{\mathrm{B}})}\right.$, versus shunt diameter is plotted in Figure 7.5. The fixed parameters are equal to the optimal values

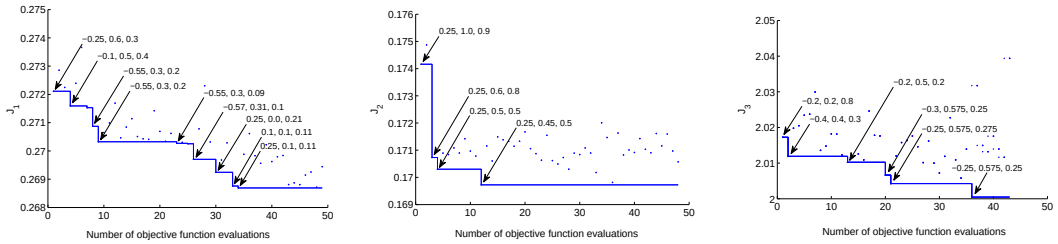

(a) (b) (c)

Figure 7.4: Reduction in objective functions versus the optimization history. The set of parameters shown next to each optimal point are design parameters, $\boldsymbol{d} = \{\cot(\theta_{\mathrm{o,A}}), s_{\mathrm{A}}, s_{\mathrm{B}}\}$. (a) J_1 optimization history. The shunt diameter is fixed to 3.20 mm in this optimization. (b) J_2 optimization history ($0.045J_2$ is plotted here). The shunt diameter is fixed to 3.41 mm in this optimization. (b) J_3 optimization history. The shunt diameter is fixed to 3.36 mm in this optimization.

obtained from the previous optimization.

This final optimum geometry is shown in Figure 7.6-(a). At the optimum point, $D_{\mathrm{sh}} = 3.25$ mm, the ratio of OD to oxygen consumption by the body is $1/J_1 = 3.72$. From Equation (7.10) the minimum required theoretical cardiac output for this amount of OD is 2.04 L/min. This cardiac output, which occurs at $\bar{Q}_{\mathrm{p}}/\bar{Q}_{\mathrm{s}} = 0.519$, is 4.8% less than the CO corresponding to J_1 (from simulation), which occurs at $\bar{Q}_{\mathrm{p}}/\bar{Q}_{\mathrm{s}} = 0.814$. Clearly using a shunt that provides $\bar{Q}_{\mathrm{p}}/\bar{Q}_{\mathrm{s}} = 0.519$ will lead to a CO much less than 2.04 L/min, due to the direct relation between pulmonary resistance and cardiac output [16]. Hence, the optimal $\bar{Q}_{\mathrm{p}}/\bar{Q}_{\mathrm{s}}$ is shifted toward a higher value, which leads to higher OD resulted from a higher CO (Equation (7.7)). This shows the impact of the relation between CO and $\bar{Q}_{\mathrm{p}}/\bar{Q}_{\mathrm{s}}$ on the optimal result. Depending on the physiologic response of the heart to the downstream resistance, deriving Equations (7.9) to (7.11) while neglecting that relation, produces an unrealistic outcome.

In Figure 7.4-(a), J_1 for the worst combination of anastomosis angle and location is 1.8% higher than the best combination, while in Figure 7.5, J_1 for the worst shunt diameter is 6% higher than the optimal diameter. This shows the higher impact of shunt diameter on J_1 compared to the three other design parameters combined. Considering a 10% variation of J_2 in Figure 7.5, this figure

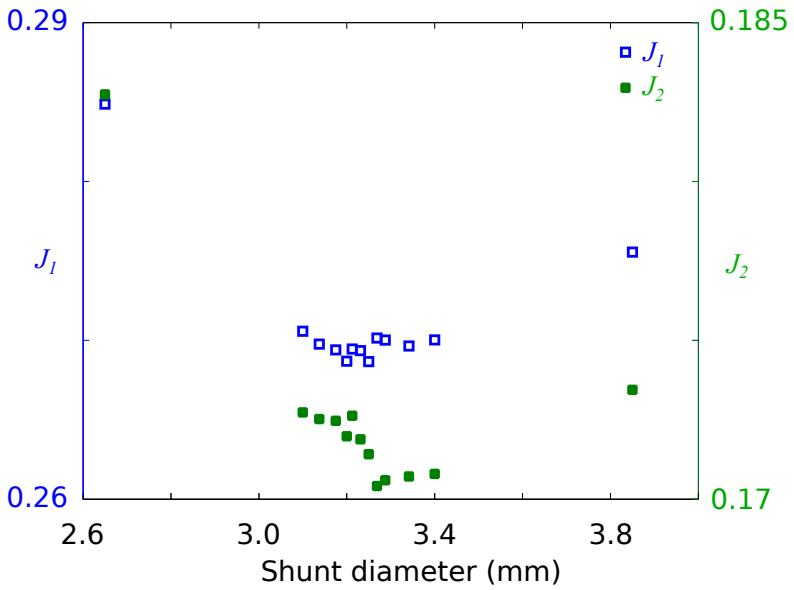

Figure 7.5: Variation of objective function versus the shunt diameter while fixing the other design parameters, i.e. $\{\cot(\theta_{o,A}), s_A, s_B\} = 0.25, 0.1, 0.11$.

implies higher impact of shunt diameter on J_2 (coronary OD) compared to J_1 (systemic OD).

7.2.2 Coronary OD objective function

Following the procedure of the previous section, a shunt diameter of 3.41 mm was found to be optimal for coronary OD. The time history of this optimization is shown in Figure 7.4-(b). The best set of design parameters, i.e. anastomosis angle and locations, are shown in this figure.

As shown in this figure, the optimal set of design parameters is found early during optimization and remaining attempts to decrease J_2 failed. The optimum PA out-of-plane anastomosis angle ($\theta_{o,A}$) is the same as before, i.e. 76°, while the optimum shunt and BA anastomosis location is far from the aortic arch and the optimum shunt and PA attachment point is closer to the middle of the PA. The distance between point A and the point behind AA ($s_A = 1$ in Figure 7.3) is 14 mm and the distance between point B and the aortic arch ($s_B = 0$ in Figure 7.3) is 9 mm. This optimized geometry is shown in Figure 7.6-(b).

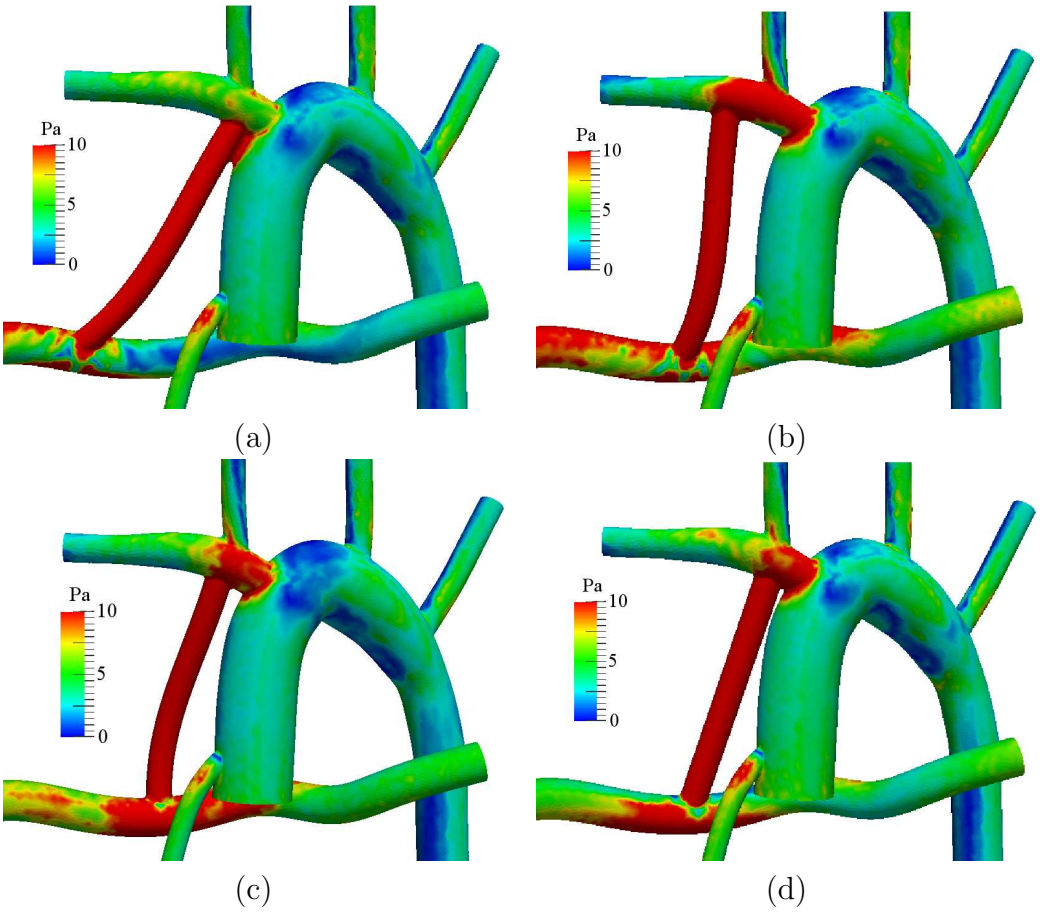

Figure 7.6: The time-averaged WSS over a cardiac cycle for: (a) The optimal geometry for systemic OD, J_1. (b) The optimal geometry for coronary OD, J_2. (c) The optimal geometry for combined systemic and coronary OD, J_3. (d) The standard geometry with a shunt diameter of 3.5 mm (the typical post MBTS surgery geometry). The two optimal geometries are optimized for the D_{sh}, $\cot(\theta_{\text{o,A}})$, $\boldsymbol{r}_{\text{PA}}(s_{\text{A}})$, and $\boldsymbol{r}_{\text{BA}}(s_{\text{B}})$.

7.2.3 Combined objective function

To obtain a design that will balance the two competing objectives discussed above, we now consider a case in which we optimize for a combined objective function. Despite the fact that J_1 and J_2 are normalized values, they have different physical meanings and numerical values, and can not be simply added together without devising a proper method. A popular method is to use a weighted sum of J_1 and J_2 with different weight factors. Here, the minimum values of J_1 and J_2 are used as weighting factors, to obtain similar magnitude contributions from both objective functions in the combined objective function J_3. Hence, the combined objective function is defined by,

$$J_3 = \frac{J_1}{J_{1_{opt}}} + \frac{J_2}{J_{2_{opt}}}, \tag{7.14}$$

where $J_{1_{opt}}$ and $J_{2_{opt}}$ are the optimal values of J_1 and J_2, found from our previous optimizations (i.e. 0.26866 and 3.7717), respectively. Physically, this definition leads to an optimal geometry that equally weights the importance of both systemic and coronary OD.

Analogous to the previous cases, a new optimization has been performed with this new objective function. The objective function history is shown in Figure 7.4-(c). From an initial optimization, the shunt diameter is fixed to 3.36 mm in this optimization. This diameter was found to be the final optimal shunt diameter for J_3. The optimum PA out-of-plane anastomosis angle ($\theta_{\mathrm{o,A}}$) is 104°, the distance between point A and the point behind AA ($s_{\mathrm{A}} = 1$ in Figure 7.3) is 11 mm, and the distance between point B and the aortic arch ($s_{\mathrm{B}} = 0$ in Figure 7.3) is 4 mm. In comparison with the two previous optimal geometries, the optimal shunt diameter and BA anastomosis point for J_3 are between the two former ones. The final optimized geometry is shown in Figure 7.6-(c).

7.2.4 Comparison of Results

To contrast the differences between the pre- and post-optimization results, a set of standard shunt geometries are considered along with the two optimal geometries identified in the previous sections. For the standard geometries a

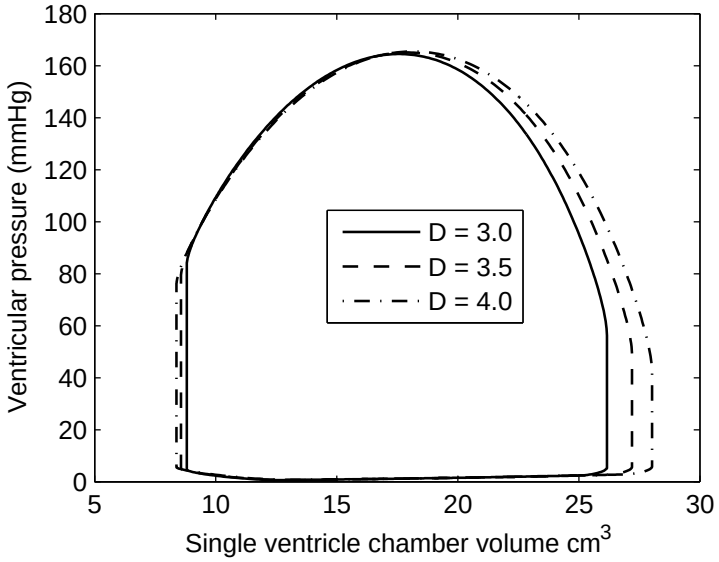

Figure 7.7: The pressure-volume loop of the single ventricle for the standard geometries with 3.0, 3.5, and 4.0 mm shunt.

set of typical design parameters is used for anastomosis angle and locations: an anastomosis angle of $\pi/2$ to produce a straight shunt, a PA anastomosis location in the middle of the PA and a BA anastomosis close to the aortic arch, i.e. $\{\cot(\theta_{\mathrm{o,A}}), s_{\mathrm{A}}, s_{\mathrm{B}}\} = 0.0, 0.5, 0.18$. Three shunt diameters, 3.0, 3.5, and 4.0 mm are selected for the standard geometries. Note that these are currently the only clinically available diameters that shunt grafts are fabricated in. The anatomy with a 3.5 mm shunt is shown in Figure 7.6-(d).

As found in previous work, the shunt resistance affects the total vascular resistance, which in turns affect the cardiac output [16]. To more clearly see this effect, the pressure-volume loop of the single ventricle chamber is shown in Figure 7.7 for the three standard geometries.

A large shunt diameter leads to decreased total vascular resistance, which results in higher cardiac output. This is deduced from Figure 7.7 by comparing the stroke volume, $V_{\max} - V_{\min}$. The peak ventricular pressure of the implemented heart model, on the other hand, does not seem to be a function of vascular resistance. The area inside the pressure-volume loop shows that an increase in the shunt

Table 7.2: Comparison between the three optimized (J_1, J_2, and J_3) and three standard geometries (S_1 to S_3). d_A is the distance between point A and a point on PA behind the AA, i.e. $s_A = 1$ in Figure 7.3. d_B is the distance between point B and the aortic arch, i.e. $s_B = 0$ in Figure 7.3. η is the efficiency defined as the ratio of AA energy flux to the sum of all other branches energy fluxes. $\bar{Q}_{cor}$, $\bar{Q}_s$, $\bar{Q}_p$, and CO are coronary, systemic, pulmonary, and AA (cardiac output) average flow rates, respectively. Sat_s and Sat_{ao} are the percentage oxygen saturations in the systemic veins (weighted average of superior and inferior vena cava) and aorta, respectively. OD and OD_{cor} are the systemic and coronary OD, respectively.

* $Sat_s = 100\frac{C_s}{1.34H_b}$

Parameter	Unit	J_1	J_2	J_3	S_1	S_2	S_3
D_{sh}	mm	3.25	3.41	3.36	3.00	3.50	4.00
d_A	mm	23.0	14.0	11.0	13.0	13.0	13.0
d_B	mm	2.0	9.0	4.0	3.0	3.0	3.0
η	%	47.8	45.1	47.2	49.0	44.4	40.8
$\bar{Q}_{cor}$	mL/min	83.1	81.2	82.7	85.4	79.6	74.1
$\bar{Q}_s$	L/min	1.18	1.12	1.16	1.21	1.11	1.02
$\bar{Q}_p$	L/min	0.96	1.08	1.01	0.88	1.12	1.33
CO	L/min	2.14	2.20	2.17	2.09	2.23	2.35
$\bar{Q}_p/\bar{Q}_s$	-	0.81	0.97	0.87	0.73	1.00	1.30
Sat_s^*	%	53.9	55.5	54.7	52.1	56.2	57.6
Sat_{ao}	%	73.7	76.4	74.8	71.4	77.1	80.1
OD	mL_{O_2}/s	3.25	3.20	3.25	3.23	3.22	3.07
OD_{cor}	mL_{O_2}/s	0.229	0.232	0.232	0.228	0.231	0.223

diameter leads to increased heart load.

The important physiological parameters for the three optimized geometries and the three standard geometries (S_1 to S_3) are presented in Table 7.2.

Table 7.2 shows that, as expected, the optimum geometry when considering systemic OD as the objective function, has the highest OD compared to the other cases, but it has lower coronary OD compared to the J_2 case and the 3.5 mm shunt case. The smaller shunt diameter outperforms the bigger shunt diameters in terms of systemic OD, while in terms of coronary OD the 3.5 mm shunt is better than the 3.0 mm shunt. This is in agreement with the optimization results, where the J_1 optimal shunt diameter is smaller than the J_2 optimal shunt diameter. This smaller shunt increases the average pressure in the aorta, which increases coronary flow rate. Hence, coronary perfusion is slightly higher for J_1 compared to J_2.

However, the total coronary OD, as expected, is higher for J_2 compared to J_1, due to the higher aortic oxygen saturation. It is interesting to see that the third optimization (J_3) has produced a geometry for which the OD to the systemic and coronary arteries is (up to the reported significant digits) the same as the J_1 and J_2 optimal geometries, respectively. For this geometry, the values of $\bar{Q}_{\mathrm{p}}$, $\bar{Q}_{\mathrm{s}}$, and $\bar{Q}_{\mathrm{cor}}$ (hence $\bar{Q}_{\mathrm{p}}/\bar{Q}_{\mathrm{s}}$, Sat_{s}, and Sat_{ao}) are between those of J_1 and J_2. However, the combination of these parameters has produced the same optimal OD as J_1 and the same OD_{cor} as J_2. This results suggest that an optimal geometry for systemic OD can be altered to obtain a higher coronary OD without significantly hindering systemic OD.

Despite the fact that the intrinsic resistance has an inverse relationship with the shunt diameter, the efficiency, which is defined as the ratio of input to output energy flux, has an inverse relationship with the shunt diameter or the shunt flow. This is because highest energy dissipation occurs in the shunt and at the two anastomoses points. This is clearly shown in Figure 7.8. In this figure the sum of dynamic and static pressures in Bernoulli's equation is plotted across a slice in the shunt for the two optimal geometries (J_1 and J_2). At the BA anastomosis, flow must change direction to enter the shunt and accelerate to a much higher velocity, and this is concurrent with a significant reduction of total pressure (approximately 15 mmHg). This is also the case for the impinging jet produced by the high flow velocity coming from the shunt to the PA that reduces the total pressure by 30 mmHg.

Compared to the previous study [25], in which MBTS hemodynamics was studied using a multidomain approach, in this work a new implicit method for coupling the LPN with the 3D domain is developed. The results from these two studies are compared for verification purposes. Previously reported results from [25] are shown in Table 7.3 (R_1 to R_3) along with results from Table 7.2 (S_1 to S_3). Considering the differences between the 3D solvers (FE versus finite volume), LPN, meshes, numerics, and geometries compared to the previously reported cases, differences in results of corresponding anatomies are within acceptable limits. Both sets of cases show similar trends for Q_{s}, Q_{p}, CO, etc. versus the shunt diameter.

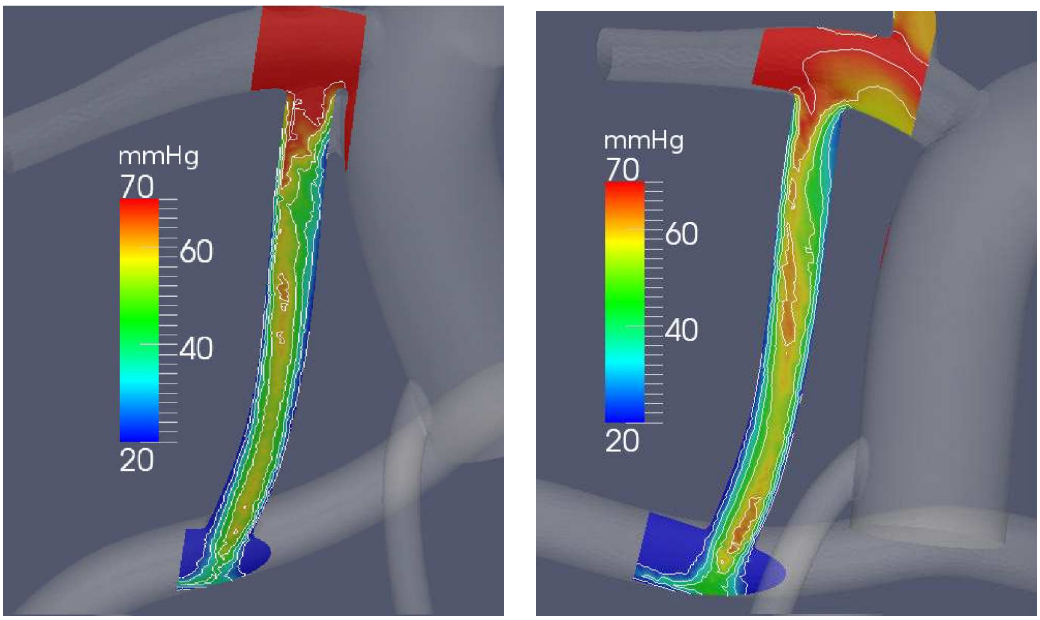

(a) (b)

Figure 7.8: Total pressure (1 mmHg = 133.3 Pa) in the shunt for: (a) the optimum geometry for systemic OD and (b) optimum geometry for coronary OD.

Table 7.3: Comparison between the three standard geometries from the current study (S_1 to S_3) and previously reported values (R_1 to R_3) from [25]. See Table 7.2 for the parameters definitions.

Case	D_{sh}	$\bar{Q}_{cor}$	$\bar{Q}_s$	$\bar{Q}_p$	CO	$\bar{Q}_p/\bar{Q}_s$
S_1	3.00	0.0854	1.21	0.88	2.09	0.726
R_1	3.00	0.082	1.234	0.889	2.123	0.720
S_2	3.50	0.0796	1.11	1.12	2.23	1.004
R_2	3.50	0.076	1.136	1.139	2.275	1.003
S_3	4.00	0.0741	1.02	1.33	2.35	1.302
R_3	4.00	0.071	1.059	1.328	2.387	1.254

Table 7.4: Sensitivity of the optimal results to the design parameters. J_2 is the base geometry and four other geometries (U_1 to U_4) are considered for sensitivity analysis. $\theta_{o,A}$ is out-of-plane angle between the shunt and PA in degrees (see Figure 7.3). See Table 7.2 for the definition of other parameters.

Parameter	Unit	J_2	U_1	U_2	U_3	U_4
D_{sh}	mm	3.41	3.50	3.41	3.41	3.41
d_A	mm	14.0	14.0	12.0	14.0	14.0
d_B	mm	9.0	9.0	9.0	7.0	9.0
$\theta_{o,A}$	$\circ$	76.0	76.0	76.0	76.0	90.0
η	%	45.1	44.6	45.6	46.2	44.6
$\bar{Q}_{cor}$	mL/min	81.2	80.2	81.1	80.9	79.7
$\bar{Q}_s$	L/min	1.12	1.11	1.13	1.13	1.11
$\bar{Q}_p$	L/min	1.08	1.11	1.06	1.05	1.11
CO	L/min	2.20	2.22	2.19	2.19	2.22
$\bar{Q}_p/\bar{Q}_s$	-	0.97	0.99	0.94	0.93	1.00
Sat_s^*	%	55.5	55.9	55.2	55.2	55.9
Sat_{ao}	%	76.4	76.9	75.9	75.8	77.0
OD	mL_{O_2}/s	3.20	3.20	3.20	3.22	3.19
OD_{cor}	mL_{O_2}/s	0.232	0.231	0.231	0.230	0.230

To quantify sensitivity of the optimal results and relative significance of the design parameters, four extra simulations are performed. In each of these, only one of the design parameters is changed by a small increment, to isolate its effect from the others. The optimal geometry for the J_2 case is a baseline for this study. The value of parameters used for each simulation and the results are shown in Table 7.4.

Results of Table 7.4 confirm that the second optimization has converged to a local optimum, because cases U_1 through U_4 have produced lower OD_{cor} compared to the J_2 case. Considering the magnitude of design parameters changes, changes in OD and OD_{cor} are minimal compared to the shunt diameter and the PA-shunt anastomosis location. This can be explained by considering the insignificant 2.5% difference in the shunt diameter, when comparing the U_1 and J_2 cases. Also, moving the shunt-PA anastomosis point along the PA (case U_2 versus J_2) mainly changes the flow distribution to the right PA and left PA, and has a minor effect on the OD. The aortic flow *steal* effect is deducible from U_3 case results, in which the BA-shunt anastomosis point has moved toward the aorta compared to the J_2

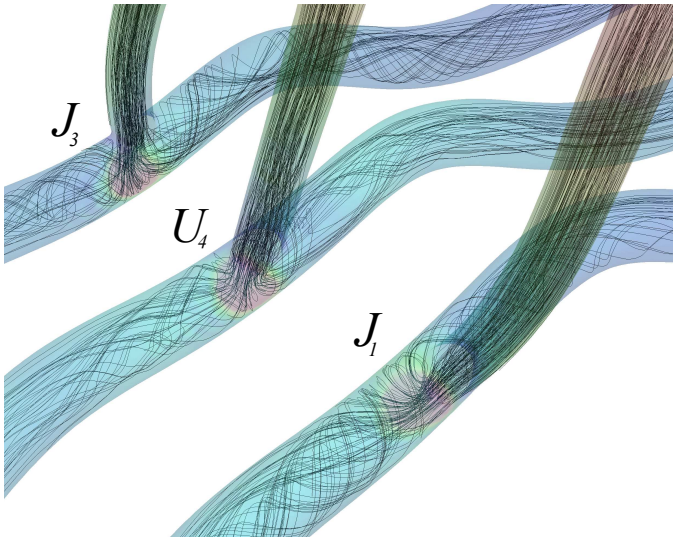

Figure 7.9: The effect of the shunt-PA anastomosis angle on the flow streamlines. For J_1 and J_3 due to the slight out-of-plane angle, there is helical streamlines, while for the U_4 anatomy, the shunt is perpendicular to the PA and there is a rapid change in the flow direction.

geometry. In this case, $\bar{Q}_{\text{cor}}$ is lower and the systemic OD has increased, compared to the J_2 case. Considering the U_4 case and all other optimal geometries (J_1 to J_3), all optimal geometries have a shunt that is connected to the PA with a moderate angle, and U_4, which has a perpendicular shunt to the PA, has the lowest OD and OD_{cor} among all cases in Table 7.4. As shown in Figure 7.9, helical vortices are generated inside the PA for moderate shunt angles (optimal geometries), while there is a sudden 90° change in the direction of flow for a shunt perpendicular to the PA (case U_4). Also, the shunt length is directly related to the anastomosis angle and is shorter for a straight shunt. Hence, the U_4 anatomy with 90° anastomosis angle has a lower pulmonary resistance and higher $\bar{Q}_{\text{p}}$. The results of this case are very similar to the U_1 case, in which shunt diameter is higher than in the J_2 anatomy.

The time-averaged pressure and volume-rendered velocity contours of the two first optimized geometries are shown in Figures 7.10 and 7.11, respectively. The time traces of outlet pressures and flow rates are also plotted for each outlet in mmHg and cm^3/s, respectively. The solid lines in the plots correspond to J_1, i.e.

the optimum case for systemic OD, and the dashed lines in the plots correspond to J_2. The presence of capacitors coupled to the boundaries of the 3D domain, which models distensibility of the vessels, has produced pressure oscillation at the outlets. Comparing the time traces of pressure and flow rate, the highest differences in pressure and flow rate correspond to the right common carotid artery (RCCA) and left PA outlets.

By moving the BA-shunt anastomosis point from the proximal position (J_1) of RCCA to the distal position (J_2), the flow to the RCCA has reduced, specifically at peak flow. This is because in the J_1 anatomy, most of the blood to the shunt is supplied directly from the aorta and there is no significant pressure drop in the proximal part of the BA (where the RCCA is attached to the BA). On the other hand, since the blood to the shunt, which is approximately half of the cardiac output, must pass through the BA for the J_2 anatomy, velocity and dissipation are high, both leading to a lower pressure in the proximal part of the BA for this anatomy. This reduces the blood flow and pressure of the RCCA branch.

Since the shunt diameter is smaller for J_1 compared to J_2, the average shunt flow is lower (see Table 7.2). This lower shunt flow is compensated for in the right PA by changes in attachment angle between the shunt and the PA in J_1 compared to J_2. As a result, both have almost the same average flow rate and pressure. But for the left PA, these two effects, i.e. lower shunt flow rate and angle of attachment between the PA and the shunt, both decrease the flow rate. This significant reduction in blood flow reduces the left PA pressure as well.

7.3 Discussion

Automated shape optimization was performed using a fully coupled multidomain approach. This extended previous work using an LPN for the stage-one simulation performed in [25, 26] by considering additional geometric variables and using a systematic design optimization algorithm. The shunt diameter, anastomosis angle and locations are optimized by allowing for automated parameterization and insertion of different grafts into the model. A derivative-free optimization al-

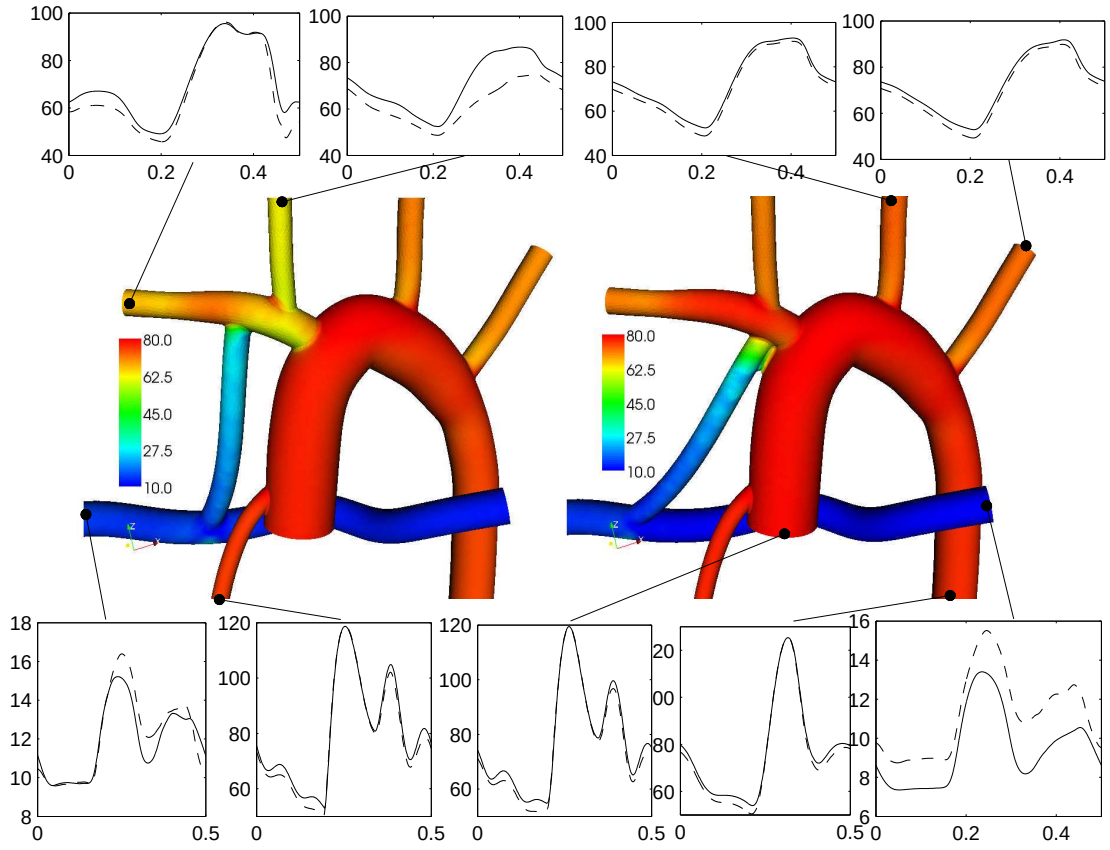

Figure 7.10: Time-averaged pressure contours of the J_2 and J_1 geometries. Pressure time variation of outlets are plotted in mmHg (1 mmHg = 133.3 Pa). The solid line in these plots corresponds to the systemic OD optimum geometry (right) and the dashed line corresponds to the coronary OD optimum geometry (left).

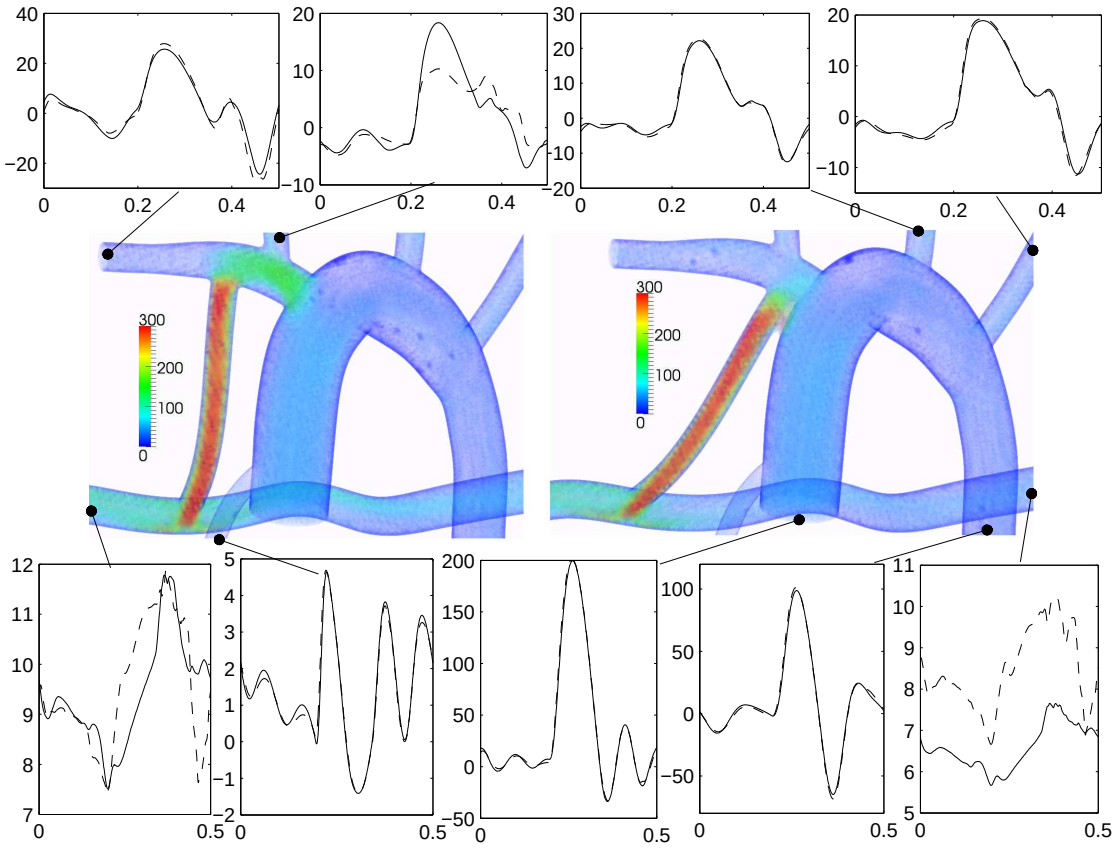

Figure 7.11: Volume rendered time-averaged velocity magnitude of the two optimum geometries. Flow rate variations of each output are plotted in cm^3/s. The solid line in these plots corresponds to the systemic OD optimum geometry (right) and the dashed line corresponds to the coronary OD optimum geometry (left).

gorithm with known convergence theory was coupled to the flow solver to explore the shunt design space.

In Equations (7.4) and (7.5) the value of the objective function depends on the flow rate, and hence on the total cardiac output. Therefore, it is essential to have a multidomain model for MBTS optimization that can predict the behavior of the heart in order to provide a more accurate perspective about the physiological responses of patients to different surgical options. This has been accomplished in this study through the coupling of the 3D domain to the LPN of the heart, thus predicting the variation of cardiac output and producing a more realistic result. Neglecting the relationship between cardiac output and shunt geometry can lead to results that are clinically unexpected. Considering Equation (7.11), which has been found based on a fixed cardiac output assumption, and setting OD to a typical value of $3.5\mathrm{V}_{\mathrm{O}_2} = 3.06\mathrm{mL}_{\mathrm{O}_2}/\mathrm{s}$ produces $\bar{Q}_{\mathrm{p}}/\bar{Q}_{\mathrm{s}} = 0.572$, which is lower than what is produced by typical shunts. By adopting the multidomain approach, comparing the numerical optimization with the theoretical optimum keeping CO fixed, we saw that the dependence of CO on shunt geometry shifts the optimal $\bar{Q}_{\mathrm{p}}/\bar{Q}_{\mathrm{s}}$ to a higher value (i.e. closer to 1.0). This is because the larger shunt allows $\bar{Q}_{\mathrm{p}}$ to approach unity with $\bar{Q}_{\mathrm{s}}$, leading to higher cardiac output and better OD. It is worth mentioning that the same optimization without a multidomain approach, (i.e. with a fixed cardiac output and Windkessel model [29] for the outlets) would produce a shunt diameter of less than 3.0 mm, which is highly inconsistent with the range of shunt diameters commonly in use by the surgical community.

Our results show that a shunt that is attached to the BA close to the aorta functions better at delivering oxygen to the systemic arteries than to the coronary arteries. This can be explained by considering that a shunt close to the aortic arch can exacerbate the siphoning of aortic blood into the pulmonary circulation during diastole, which in turn, diminishes flow into the coronary arteries. On the other hand, the optimal geometry for coronary OD had a BA-shunt anastomosis point further from the aortic arch compared to the BA-RCCA anastomosis. This caused a significant reduction in RCCA flow, which in turn improves coronary perfusion by reducing the diastolic runoff into the shunt from the aorta. Consequently, despite

the fact that the optimal coronary OD geometry has a larger shunt compared to the optimal systemic OD geometry, the coronary perfusion is almost the same (Figure 7.11). The larger shunt in the J_2 anatomy, on the other hand, has increased the pulmonary flow rate, which has increased aortic saturation and coronary OD.

Optimization with a combined objective function, i.e. J_3, showed that it is feasible to find an intermediate geometry that has an OD to systemic arteries very close to J_1 and OD to the coronary arteries very close to J_2, hence achieving the best of both optimal anatomies in a single anatomy. This was possible because the decrease in systemic perfusion was compensated by increase in aortic saturation, when comparing J_3 with J_1; and lower aortic saturation was compensated by higher coronary perfusion, when comparing J_3 with J_2.

All the optimal anatomies have a shunt that is connected with a tilt and slight shift apart from the center line of the PA. Comparing this with a shunt perpendicular to the PA, the flow in the latter geometry has a sharp turn in anastomosis point, while helical streamlines are observed inside the PA for the former optimal geometries.

Since the shunt diameter is only clinically available in discrete sizes, a set of simulations was done with the postoperative anatomy using those available shunt sizes. The results show that pulmonary perfusion, oxygen saturation in the aorta and systemic veins, and cardiac output are directly related to the shunt diameter, while systemic perfusion and efficiency are inversely proportional to the shunt diameter. The relationship between these parameters and the shunt diameter can be explained by the changes in the total pulmonary resistance, i.e. the sum of the pulmonary bed and the shunt resistances. Higher total pulmonary resistance reduces pulmonary flow and allows for a higher portion of cardiac output to be delivered to the systemic and coronary arteries. The decrease of the pulmonary blood flow reduces PA oxygen saturation, since V_{O_2} and C_p are fixed. Since the PA and aorta have the same saturation in the MBTS anatomy, the aortic saturation decreases, which reduces systemic veins saturation in the studied cases. This occurs because the decrease in aortic saturation for a smaller shunt is dominant compared to the increase in systemic flow rate.

In quantifying OD to either the systemic or coronary arteries, the same monotonic relationship to the shunt diameter is no longer valid. Among the three simulated shunt diameters, the 3.0 mm shunt has the highest systemic OD, but this trend is not expected to continue with decreasing shunt diameter. Of the two parameters that contribute to the OD, the systemic blood flow, in contrast to the aortic saturation, decreases with increasing shunt diameter, and the maximum OD occurs in a midrange shunt size. The simulation results of the two optimized and three standard geometries therefore show that a smaller diameter results in better systemic OD.

The results from this work confirm previous findings that shunt diameter has the largest impact on system dynamics in the MBTS anatomy [19]. Most in the surgical community currently make decisions based on shunt size alone, forming a relatively straight connection between the brachiocephalic and the right PA. However, this work highlights the fact that the location of shunt placement and it's anastomosis angles also have impact on clinically important parameters. While still not as important as the shunt size, these additional factors are shown to have potential importance for ensuring adequate coronary flow.

There is an additional rigid wall assumption in this study, however there are several justifications for this assumption. Firstly, the distensibility of the branches is partially accounted for by inserting a capacitor next to the all outlets. Secondly, the aim of this work is optimization, in which we compare among a set of different geometries. Since there is only variation in shunt geometry, which is very stiff, the resulting error should be minimal. Thirdly, doing an FSI simulation requires additional assumptions about the wall properties, thickness, and constitutive equation, thereby introducing additional uncertainty to the simulations. Fourthly, as we will show in the next chapter, distensible wall compared to rigid wall assumption has little effect on the flow distribution and pressure tracings. Since the multidomain simulation results, hence optimization results, solely depends on these two parameters, the effect of a rigid wall assumption on the results is presumed to be minimal.

Due to the physical constraints of commercially available shunt sizes used

in surgery, there is a limitation in implementation of an absolute optimal shunt geometry. However, this study suggests a potential benefit if a greater range of shunt diameters could be manufactured.

The choice of optimal shunt size may also be a function of patient specific parameters such as weight. Additional clinical studies are warranted to collect the appropriate data on geometry and LPN parameters as a function of patient condition.

Like other non-convex optimization methods, the method used in this work only guarantees convergence to a local minimum of the objective function. The only way to guarantee global optimization of a non-convex function is for a method to evaluate every point in the design space, which is infeasible for the current computationally expensive problem.

Acknowledgements

We gratefully acknowledge Dr. Jeffrey A. Feinstein, Dr. Vishal Nigam, and Dr. Adam Dorfman for their valuable assistance regarding objective function and design parameters selection.

This chapter, in full, is a reprint of the material as it appears in Optimization of shunt placement for the Norwood surgery using multi-domain modeling in *Journal of Biomechanical Engineering*, 134(5), 051002, 2012. Authors are M. Esmaily-Moghadam, F. Migliavacca, I. Vignon-Clementel, T-Y. Hsia, and A. Marsden. The dissertation author was the primary investigator and author of this paper.

Chapter 8

Simulations of Multiple Systemic-to-pulmonary connections

Neonates have a natural systemic-to-pulmonary connection through the PDA which normally closes after birth. Shunt placement introduces a new systemic-to-pulmonary connection in stage one surgery, however subsequent graft failure can be caused by thrombus formation, blocking the pulmonary circulation leading to hypoxia and sudden death [14]. Because of these significant risks, some institutions have used multiple shunt insertion to supply the PA from more than one source [44, 45]. In these cases, in addition to inserting a MBTS between the brachiocephalic artery and the right PA, the PDA may be kept open or a CS may be inserted between the PA and the aorta. This practice has been motivated by the perceived need for a spare connection that can prevent total blockage of the pulmonary circulation in the case of shunt blockage due to thrombosis. While this concept appears at the outset to have little downside, we hypothesize that there are are several potentially negative implications of multiple shunts that may lead to undesirable hemodynamics. In this chapter we hypothesize that multiple shunts are unfavorable because 1) flow competition between the two shunts may increase the risk of thrombus formation, and 2) pulmonary over-circulation may reduce OD.

We tested the above hypothesis by comparing two sets of surgical inter-

ventions in simulations: anatomies with single and multiple shunts. In Chapter 7, anatomies with a single MBTS have been studied using multiscale approach. Prior multiscale studies have described the effects of shunt diameter on pulmonary and systemic saturations, pulmonary-to-systemic flow rates, OD, cardiac output, and other clinically relevant parameters, but have not compared surgical approaches with single versus multiple shunts [16, 19, 80, 86, 25]. Here, we compared surgical approaches by generating parameterized 3D models with single and multiple shunts. We systematically varied the PDA diameter to span a wide range of values, resulting in dramatic variation in total pulmonary resistance, leading in turn to global changes in the circulatory system. This situation exemplifies the need for multiscale modeling, which allows one to capture the coupled dynamics of the vascular system in a closed loop as the 3D anatomical model is modified. Following the framework introduced in Chapter 2, a LPN is coupled to a 3D flow solver, generating BCs that capture the physiologic response to anatomical changes. Additionally, to explore the validity of our rigid-wall assumption, a FSI simulation was also performed, representing an advance over prior studies which primarily used open loop configurations and/or rigid wall assumptions.

By automatically parameterizing shunt geometries in the 3D model, we considered a range of PDA and CS diameters, PVR, and MBTS positions. In total, we compared 23 cases by quantifying OD, pulmonary-to-systemic flow ratio, cardiac output, heart load, and oxygen saturation in systemic and pulmonary arteries and veins. Though we did not directly model the complex biochemistry of the thrombus formation process, we compared WSS, WSS gradients (WSSG), oscillatory shear index (OSI), and RT in segments of the PA and MBTS as surrogates for thrombotic risk. Recirculation regions are associated with high RT, which in combination with high shear stress history may increase the risk of thrombus formation [37]. The new non-discrete method that was introduced in Chapter 6 is used for measuring RT. Modeling incorporated realistic patient data and clinically realistic values, and performance of surgical scenarios with single versus multiple shunts was compared using the above metrics of thrombotic risk and physiologic response.

8.1 Methods

The model construction process and simulations methods are fully described in Section 6.2.2. Anatomies with five PDA diameters were considered, 0.0 mm (no PDA), 2.0 mm, 3.5 mm, 4.0 mm, and 5.0 mm. In total, 10 different anatomies were constructed, including these five PDA diameters along with a 3.5 mm proximal or distal MBTS. To compare post-stage one and pre-stage two conditions, 20 simulations were performed, coupling each of the 10 models to an LPN with normal and high PVR. In addition, 3 cases with CS diameters of 2.0, 3.0, and 4.0 mm were studied, using high PVR and a proximal MBTS.

The multidomain formulation (Chapter 2), the backflow stabilization method (Section 3.1.1), bi-partitioned and preconditioning methods (Chapter 6), and sorted data structure (Chapter 5) techniques were employed for multidomain simulations. A rigid wall assumption was used, since, as discussed in Section 8.2, the effect of wall distensibility on the solution was shown to be negligible. The LPN shown in Figure 2.11 was adopted. Connecting a capacitor directly to the AA can cause non-physiological regurgitant flow at the AA inlet. Therefore, our model directly connected the AA to a diode, and the eliminated capacitor was distributed over the rest of the domain to obtain a physiological pressure oscillation between systole and diastole (see Appendix B for the LPN values).

The total excessive blood volume in the LPN was preserved temporally to improve cyclic convergence and accuracy, using

$$\boldsymbol{P}(t) \leftarrow \boldsymbol{P}(t) + \frac{V(0) - V(t)}{\boldsymbol{C} \cdot \boldsymbol{C}} \boldsymbol{C}, \tag{8.1}$$

$$V(t) = \boldsymbol{C} \cdot \boldsymbol{P}(t), \tag{8.2}$$

where $\boldsymbol{P}(t)$, $\boldsymbol{C}$, and $V(t)$ are pressures in the capacitors, capacitance values, and the total blood volume in the LPN, respectively. For the heart chambers, C_{HC} was set to 1 and P_{HC} was set to its volume. Note that the inner product of Equation (8.1) with $\boldsymbol{C}$ produces the initial total blood volume, $V(0)$.

The Eulerian approach developed in Chapter 6 is adopted to obtain a measure of RT, in which the exposure time inside the region of interest is calculated by solving an advection-diffusion equation [127]. Hence, the RT and flow calculations

were performed concurrently by solving an extra scalar equation. Here, the first measure of RT is calculated for all simulations using Equation (6.9).

For fluid flow simulations, non-linear iterations continued until the normalized residual was less than 5×10^{-4} or the number of iterations exceeded 8. Reducing the residual below 5×10^{-4} did not have any significant effect on the results. WSS, WSSG, OSI, and OD are calculated as a post-processing step using the formulation presented in Appendices D and C.

8.2 FSI simulation of the MBTS anatomy

To evaluate the effect of wall distensibility on the results reported in this chapter as well as Chapters 7 and 9 simulations results, flow in a model with a 3.5 mm single proximal MBTS was simulated using both rigid-wall and FSI formulations. For the FSI simulation, the wall was modeled as a nonlinear St. Venant-Kirchhoff elastic solid, allowing for large deformation [162]. To prevent oscillation of the structure and include the effect of surrounding tissues, a damping term was added to the formulation [163]. Different material properties were used for the MBTS and the rest of the vasculature. The MBTS was modeled as a Gore-Tex conduit with density of 3.3 g/cm^3, Young's modulus of 4×10^9 g/(s^{2}cm), and Poisson's ratio of 0.49 [164]. In all other vessels, density, Young's modulus and, Poisson's ratio were 1.06 g/cm^3, 5×10^7 g/(s^{2}cm), and 0.49, respectively [165, 164]. The closed-loop LPN described in Section 2.4.4 was used to prescribe inlet and outlet BCs for the FSI simulation, with identical parameter values. Since blood can accumulate in the 3D geometry due to vessel expansion, the total excessive blood volume was corrected at the beginning of each cardiac cycle, using Equation (8.2).

Variable wall thickness was calculated following the method proposed in [166, 164]. Using this method, the wall thickness at the inlet and outlets was assumed to be 10% of the vessel diameter. To obtain the interior thickness, a Laplace equation was solved with the inlet and outlet thicknesses imposed as Dirichlet BCs. The solution of the Laplace equation, a scalar field, was used to prescribe the local

thickness (Figure 8.1). Using the thickness at each nodal point and the normal vector to the wall, triangular surface elements were extruded to generate wedge elements. In this manner, the fluid and structure meshes match at the interface and the solid domain is three dimensional, with stress and strain varying within the vessel wall. To prevent overlapping wall elements at the corners, thickness was reduced by an order of magnitude and stiffness and density were adjusted accordingly. Note that the model used in this section was modified to accommodate for the wall thickness and is slightly different from the 3.5 mm proximal MBTS model that is used in the following sections.

An arbitrary Lagrangian-Eulerian method was used to formulate the FSI problem [100], employing a quasi-direct FSI solution strategy [167] in which the fluid and structure solutions are computed in a monolithic fashion. Elastic mesh moving was employed with the aid of Jacobian-based stiffening [168, 169]. The computations were performed without re-meshing for ten cycles.

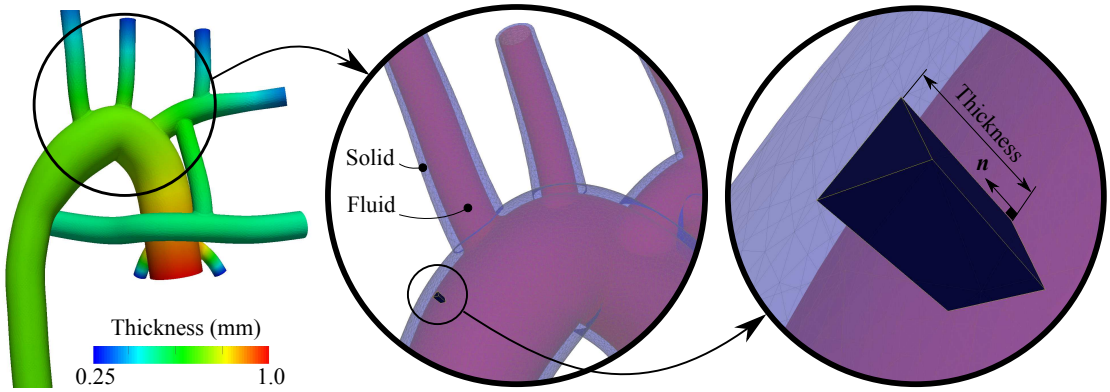

Figure 8.1: Wall thickness is calculated by solving the Laplace equation (left figure). Then the wall of the fluid domain mesh is extruded in the normal direction to generate the solid domain mesh, i.e. vasculature wall (middle and right figures).

Figure 8.2 shows the geometry at peak systole. The MBTS was not deformed due to its stiffer material properties, however, other vessels were deformed to a greater or lesser degree depending on their proximity to the aortic root.

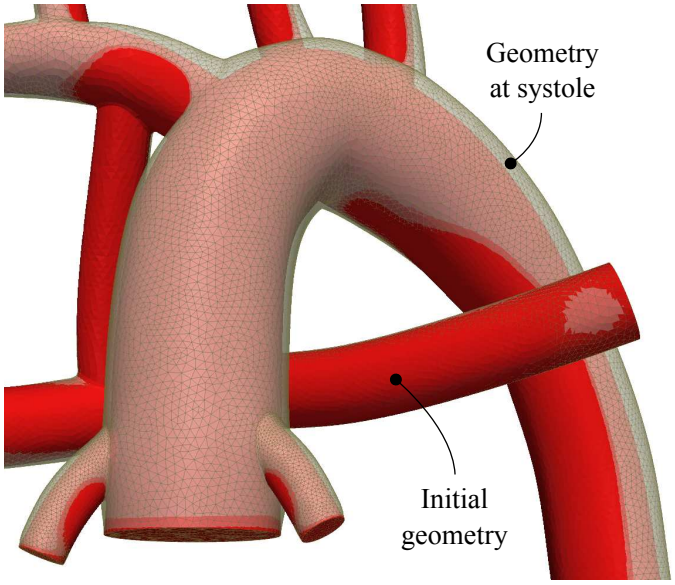

Figure 8.2: Deformation of the vessel walls at the peak systole.

The rigid-wall and FSI simulation results are compared in Table 8.1, with a maximum difference of 3% in pulmonary-to-systemic flow ratio. All differences can be directly linked to the higher cardiac output in the FSI case, producing higher saturations, OD, and pressures. However, due to the PA expansion, RT is increased and WSS is decreased in the FSI case. Because all differences were extremely small, it was determined that rigid-wall simulations were sufficient for the present application and would not affect the final conclusions of the study.

Table 8.1: Comparison between the rigid-wall and FSI simulation results, using the model with single MBTS 8.1.

parameter	Unit	Rigid	FSI	Difference (%)
Cardiac output	L/min	2.634	2.702	2.6
pulmonary-to-systemic flow ratio	-	0.947	0.974	2.9
Aortic saturation	-	79.8	80.6	1.0
OD	mL_{O_2}/s	4.046	4.158	2.8
Coronary OD	mL_{O_2}/s	0.304	0.308	1.3
Aortic pressure	mmHg	98.60	99.07	0.5
Pulmonary pressure	mmHg	12.66	13.00	2.7
RT in the PA	ms	26.5	26.7	0.8
WSS in the PA	$g/(s^2cm)$	81.65	81.44	-0.2

8.3 Results

The single MBTS resulted in the highest systemic and coronary OD, as shown in Table 8.2. Adding an extra shunt caused pulmonary hyperperfusion and systemic hypoperfusion, leading to higher saturations, but lower OD (Figure 8.3). In the worst case, with a distal MBTS and normal PVR, adding a 5.0 mm PDA reduced OD by 10%. As was the case with the proximal MBTS, higher PVR increased the systemic flow rate. Increasing the systemic flow rate generally improved OD, though in an exception, coronary OD was reduced when the MBTS position was moved from distal to proximal. The proximal position leads to blood *steal* from the aorta hindering coronary perfusion during diastole. As a result, the change in the coronary perfusion is dominated by the change in saturation, leading to lower coronary OD [80]. Inclusion of a CS resulted in similar global hemodynamics compared to the case with an equivalent PDA diameter. Hence, the systemic-to-pulmonary resistance is not affected significantly by the anastomosis location of the second shunt, as long as the diameter of the second shunt is kept fixed.

Table 8.2: Comparison between the anatomies. *Case* defines the distal (D) or proximal (P) MBTS (Figure 6.6), high (R) or normal (N) PVR, and central shunt (C) (e.g. *DN* means a distal MBTS with normal PVR and CPR denotes the central shunt simulation with high PVR and proximal MBTS. D is the PDA/CS diameters in mm. MBTS diameter is set 3.5 mm in all simulations. HL is the heart load in Joules per cardiac cycle. $\bar{Q}_{\text{cor}}$, $\bar{Q}_{\text{s}}$, $\bar{Q}_{\text{p}}$, and CO are coronary, systemic, pulmonary, and AA (cardiac output) average flow rates, respectively. $\bar{Q}_{\text{cor}}$ is in mL/min and the rest are in L/min. Sat_s and Sat_{ao} are the oxygen saturations in the systemic veins (weighted average of superior and inferior vena cava) and aorta, respectively. OD is the systemic OD in mL_{O_2}/s. OD_{cor} is the coronary OD in μL_{O_2}/s.

Case	D	HL	Q_{cor}	Q_{s}	Q_{p}	CO	$Q_{\text{p}}/Q_{\text{s}}$	Sat_s	Sat_{ao}	OD	OD_{cor}
DN	0.0	0.89	103.	1.36	1.32	2.68	0.971	63.2	80.4	4.10	310
DR	0.0	0.88	104.	1.39	1.25	2.64	0.905	62.5	79.4	4.12	310
PN	0.0	0.86	104.	1.40	1.27	2.67	0.907	62.9	79.6	4.17	309
PR	0.0	0.85	105.	1.42	1.21	2.63	0.849	62.2	78.6	4.18	309
DN	2.0	0.94	97.0	1.28	1.63	2.92	1.272	65.5	83.7	4.02	304
DR	2.0	0.92	99.2	1.32	1.52	2.84	1.157	65.0	82.7	4.08	307
PN	2.0	0.92	98.5	1.32	1.57	2.90	1.188	65.5	83.2	4.12	307
PR	2.0	0.90	100.	1.35	1.48	2.83	1.092	64.9	82.2	4.16	308
DN	3.5	1.06	87.6	1.15	2.36	3.50	2.052	67.8	88.1	3.79	289
DR	3.5	1.01	90.7	1.21	2.13	3.33	1.767	67.7	87.0	3.93	296
PN	3.5	1.04	88.2	1.18	2.35	3.53	1.989	68.3	88.1	3.89	291
PR	3.5	1.00	92.1	1.24	2.11	3.35	1.706	68.1	87.0	4.03	300
DN	4.0	1.10	85.7	1.12	2.59	3.71	2.303	68.2	89.0	3.74	286
DR	4.0	1.04	89.0	1.18	2.30	3.48	1.955	68.0	87.9	3.88	293
PN	4.0	1.08	86.5	1.15	2.57	3.72	2.234	68.7	88.9	3.83	288
PR	4.0	1.03	90.6	1.23	2.27	3.50	1.854	68.7	87.7	4.03	298
DN	5.0	1.16	82.6	1.09	2.99	4.07	2.747	68.7	90.2	3.67	279
DR	5.0	1.08	87.1	1.17	2.59	3.76	2.216	69.0	89.0	3.90	290
PN	5.0	1.16	83.7	1.13	2.99	4.13	2.639	69.6	90.2	3.83	283
PR	5.0	1.07	87.7	1.19	2.60	3.78	2.190	69.3	89.0	3.95	292
CPR	2.0	0.90	99.5	1.35	1.49	2.83	1.103	65.0	82.3	4.15	307
CPR	3.0	0.96	94.0	1.28	1.85	3.13	1.450	67.1	85.4	4.08	301
CPR	4.0	1.03	90.0	1.24	2.26	3.50	1.827	68.8	87.7	4.06	295

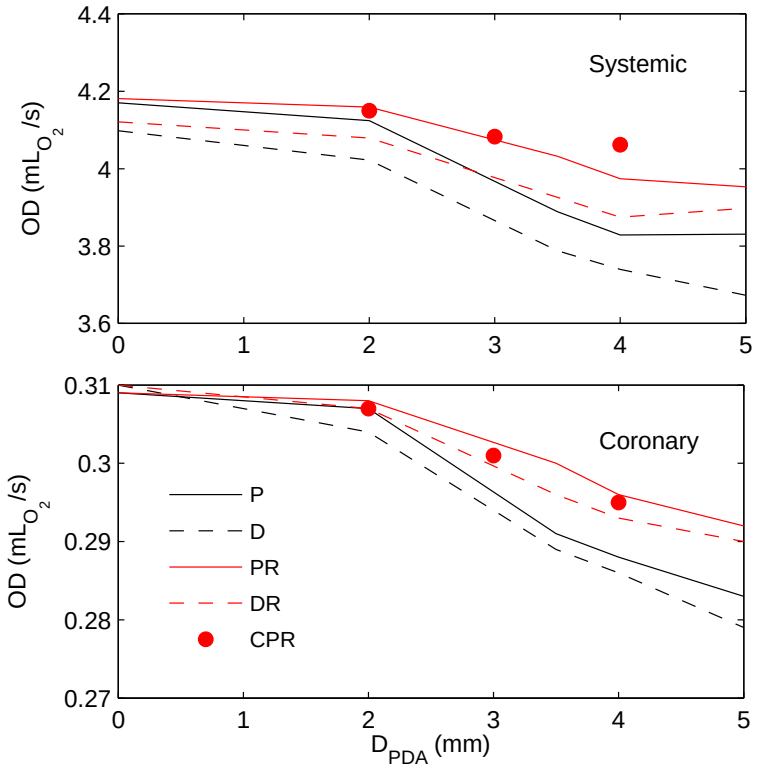

Figure 8.3: Systemic (top plot) and coronary OD (bottom plot) for proximal (solid) and distal (dashed) MBTS and normal PVR (black) and high PVR (red) versus PDA/CS diameter. Note the single MBTS corresponds to $D_{\mathrm{PDA}} = 0$. The results of three simulations with CS are shown with red circles, in which D_{PDA} denotes CS diameter.

The velocity vectors inside the PA are shown for different configurations in Figure 8.4 for normal (top) and high (bottom) values of PVR. The flow distribution was nearly symmetric in the models with a single MBTS. However, the right PA flow rate increased with increasing PDA diameter. Elevated flow stagnation was found in the region between the PDA and MBTS for the 2 mm PDA cases, while the flow was directed toward the right PA for the 4 mm PDA cases.

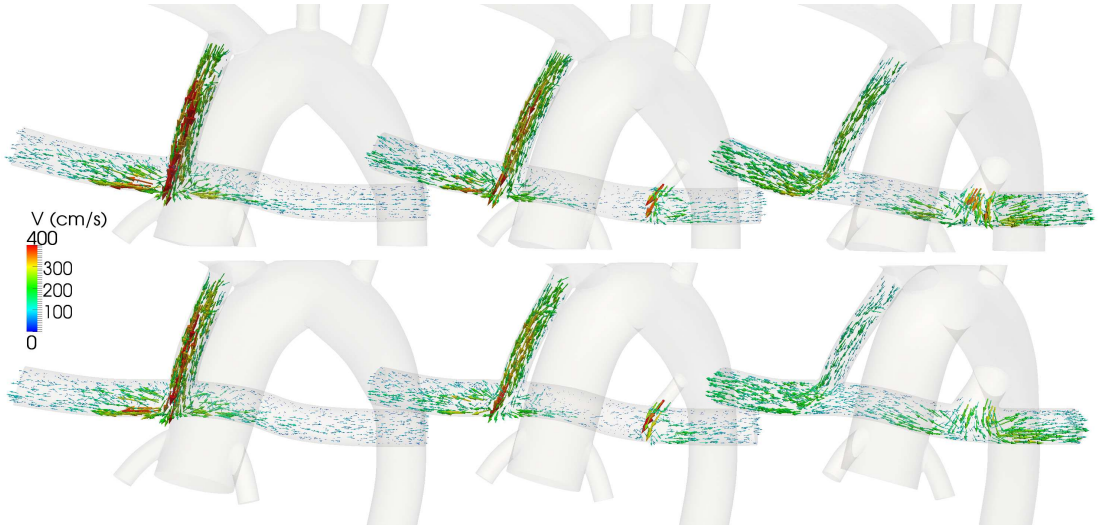

Figure 8.4: Time averaged velocity field in normal PVR (top row) and high PVR (bottom row), and a single proximal MBTS (left column), a proximal MBTS and a 2 mm PDA (middle column), and a proximal MBTS and a 4 mm PDA (right column).

The cycle-averaged pressure contours and corresponding spatially averaged pressure in the PA segment and MBTS are shown in Figure 8.5. Contrary to the PA, the average pressure in the aorta was not significantly affected by changes in PVR. Increasing the PDA/CS diameter increased the PA pressure, due to the higher flow rate to the pulmonary vascular bed, and reduced the AA pressure, due to the reduction in the total resistance. On the other hand, the pressure levels in the PA and AA were unaffected by the locations of the second pulmonary blood source (i.e. PDA versus CS).

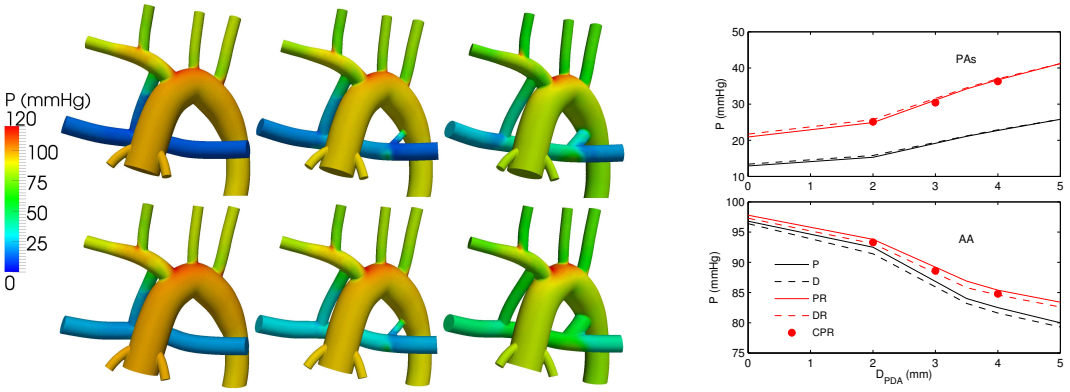

(a) (b)

Figure 8.5: (a) Pressure contours for normal PVR (top row) and high PVR (bottom row), and a single proximal MBTS (left column), a proximal MBTS and a 2 mm PDA (middle column) cases, and a proximal MBTS and a 4 mm PDA (right column). (b) Averaged pressure in the PA outlets (top plot) and in the AA (bottom plot). See Figure 8.3 caption for more details.

The 3D simulations were post-processed using Equations (D.5), (D.8), and (D.9), and the results are shown in Table 8.3. The tabulated pressures were averaged temporally and spatially over the PA and AA outlet and inlet surfaces. RT, WSS, OSI, and WSSG were spatially averaged either over a segment of PA wall (between the MBTS and PDA) or over the MBTS wall (see Figure 6.6).

Table 8.3: Comparison between the pulmonary and aortic pressures (mmHg), RT (ms), WSS (g/(s^{2}cm)), OSI (%), and WSSG (g/(s^{2}cm^2)) of the studied anatomies. PA$_s$ denoted the region between the PDA and MBTS and BT denotes the region in the MBTS (see red and blue regions in Figure 6.6). See Table 8.2 caption for the other notations.

Case	D	P		RT		WSS		OSI		WSSG	
		PA	AA	PA$_s$	BT	PA$_s$	BT	PA$_s$	BT	PA$_s$	BT
DN	0.0	13.4	96.4	30.4	4.3	98.9	267	2.77	1.10	256	491
DR	0.0	21.7	97.3	32.4	4.5	91.9	252	2.17	0.99	235	460
PN	0.0	12.9	96.8	28.4	4.3	93.9	244	2.52	1.50	270	547
PR	0.0	20.9	97.8	28.3	4.6	91.5	232	2.75	1.56	268	525
DN	2.0	15.8	91.4	56.5	4.7	58.9	249	9.39	1.07	248	469
DR	2.0	25.7	93.1	57.5	5.0	58.4	232	8.09	1.06	241	439
PN	2.0	15.3	92.5	50.6	4.8	77.7	219	13.70	1.67	380	503
PR	2.0	24.9	93.8	51.5	5.1	73.8	206	11.66	1.70	339	477
DN	3.5	21.2	83.2	50.5	6.1	78.0	207	6.52	1.38	293	424
DR	3.5	34.5	85.8	58.0	7.0	67.3	181	6.92	1.58	266	377
PN	3.5	21.1	84.0	28.1	6.2	107.3	174	6.60	2.17	433	443
PR	3.5	34.2	86.9	35.8	7.0	90.7	154	10.39	2.31	385	397
DN	4.0	22.9	81.6	36.3	6.8	84.7	190	6.98	1.73	283	408
DR	4.0	37.0	84.6	44.0	7.8	74.2	167	7.64	1.82	255	358
PN	4.0	22.7	82.5	21.7	6.8	119.5	159	10.49	2.47	438	433
PR	4.0	36.7	85.4	27.0	7.7	101.4	140	9.65	2.54	378	381
DN	5.0	25.8	79.3	23.8	8.5	105.3	164	5.80	2.28	308	376
DR	5.0	41.2	82.6	28.5	9.9	90.7	139	6.59	2.41	266	328
PN	5.0	25.8	80.0	14.9	8.4	131.3	134	7.52	3.01	428	391
PR	5.0	41.2	83.4	17.5	9.9	114.0	113	8.56	3.09	366	329
CPR	2.0	25.1	93.3	47.9	5.0	79.0	211	5.91	1.76	256	493
CPR	3.0	30.4	88.6	73.7	5.6	49.4	190	15.78	1.90	242	460
CPR	4.0	36.3	84.8	58.6	6.4	51.5	167	11.56	2.16	224	422

The 3.0 mm CS and 3.5mm PDA cases had the highest RT in the PA (Figure 8.6). RT in the PA for the anatomy with a 3.0 mm CS was 160% higher compared to the anatomy with a single MBTS. For this particular case, WSS was 46% lower and OSI was 473% higher in the PA compared to the single MBTS, indicating disturbed and chaotic flow. This is in agreement with Figure 8.4, which indicates the presence of a stagnation region between the MBTS and PDA at mid range diameters. Increasing the PDA diameter beyond 3.5 mm reduced the RT in the PA, because an imbalance between the PDA/CS and the MBTS flow led to

increased flow through the PA segment. Since the PA flow rate was lower for the higher PVR cases, the RT was higher in the PA and MBTS.

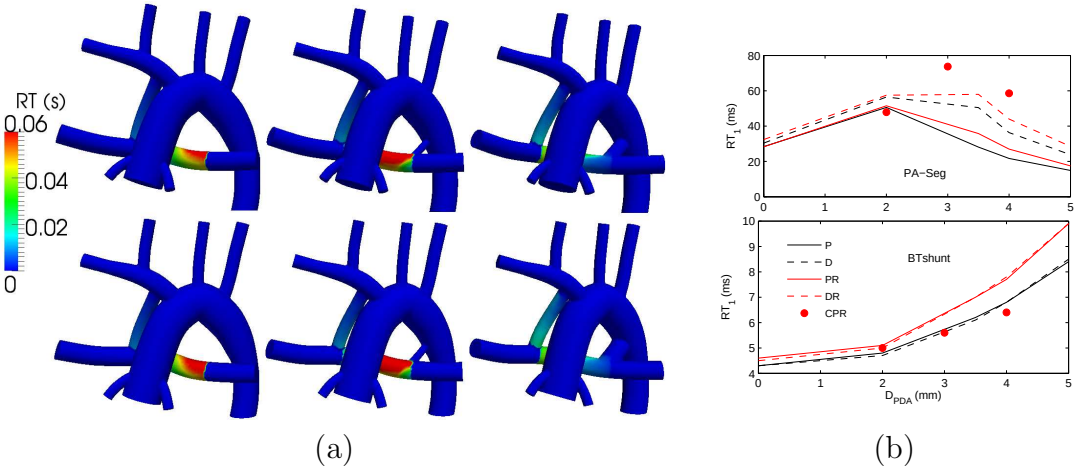

(a) (b)

Figure 8.6: (a) RT contours for normal PVR (top row) and high PVR (bottom row), and a single proximal MBTS (left column), a proximal MBTS and a 2 mm PDA (middle column), and a proximal MBTS and a 4 mm PDA (right column). (b) Spatially averaged RT in the PA segment (top plot) and in the MBTS (bottom plot). See Figure 8.3 caption for more details.

Increasing the PDA/CS diameter decreased the flow rate in the MBTS and consequently WSS in the MBTS (Figure 8.7). Placing the MBTS more proximally and/or increasing PVR also reduced both the MBTS flow rate and WSS. The WSS in the PA segment did not vary monotonically with the PDA/CS size. Depending on the momentum balance between the PDA/CS and MBTS, the flow was stagnant with low WSS (2 mm PDA case), or flow was unidirectional with high WSS (5 mm PDA case). In the PA segment, similar to the MBTS, lower WSS was observed at higher PVR due to the lower PA flow rate. Also, the proximal shunt generally produced higher WSS in the PA compared to the distal shunt.

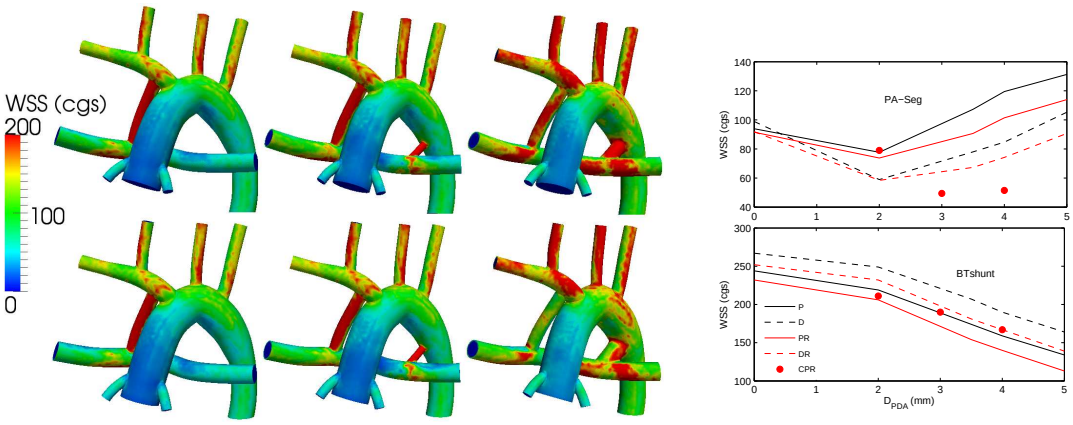

(a) (b)

Figure 8.7: (a) WSS contours for normal PVR (top row) and high PVR (bottom row), and a single proximal MBTS (left column), a proximal MBTS and a 2 mm PDA (middle column), and a proximal MBTS and a 4 mm PDA (right column). (b) Spatially averaged WSS in the PA segment (top plot) and in the MBTS (bottom plot). See Figure 8.3 caption for more details.

Similar to the WSS results, higher PVR and/or larger PDA/CS led to lower WSSG due to the lower MBTS flow rate (Figure 8.8). The flow in the PA decreased as a result of increasing PVR, leading to decreased WSSG. These results suggest that a distal MBTS produces a more uniform flow, hence lower WSSG in the PA segment and MBTS. Differences in WSSG in the PA segment at different PDA/CS sizes depend on the uniformity and magnitude of WSS in the PA segment.

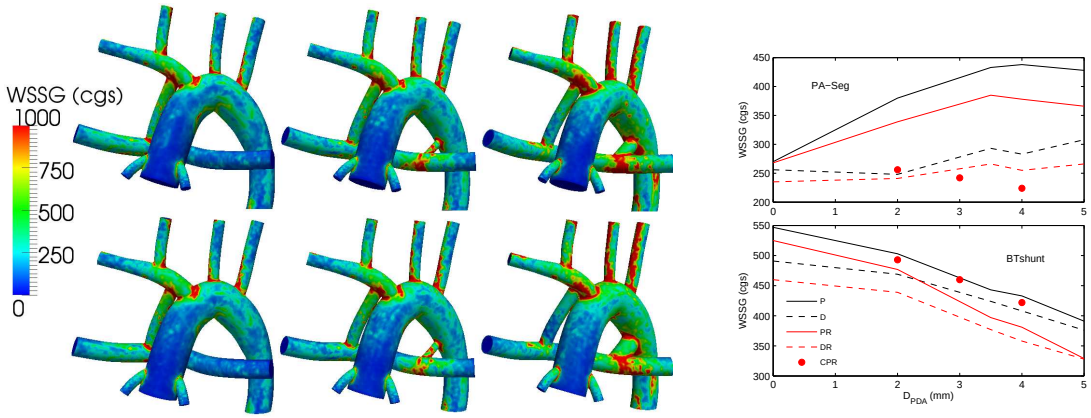

(a) (b)

Figure 8.8: (a) WSSG contours for normal PVR (top row) and high PVR (bottom row), and a single proximal MBTS (left column), a proximal MBTS and a 2 mm PDA (middle column), and a proximal MBTS and a 4 mm PDA (right column). (b) Spatially averaged WSSG in the PA segment (top plot) and in the MBTS (bottom plot). See Figure 8.3 caption for more details.

Low OSI in the MBTS, with a maximum of 3.14%, compared to 15.8% in the PA segment indicates a unidirectional flow in the MBTS (Figure 8.9). OSI in the PA segment correlated with the flow balance between the PDA/CS and MBTS and increased with a dominant PDA/CS or MBTS flow. Similar to WSS, more proximal shunt placement led to a higher OSI.

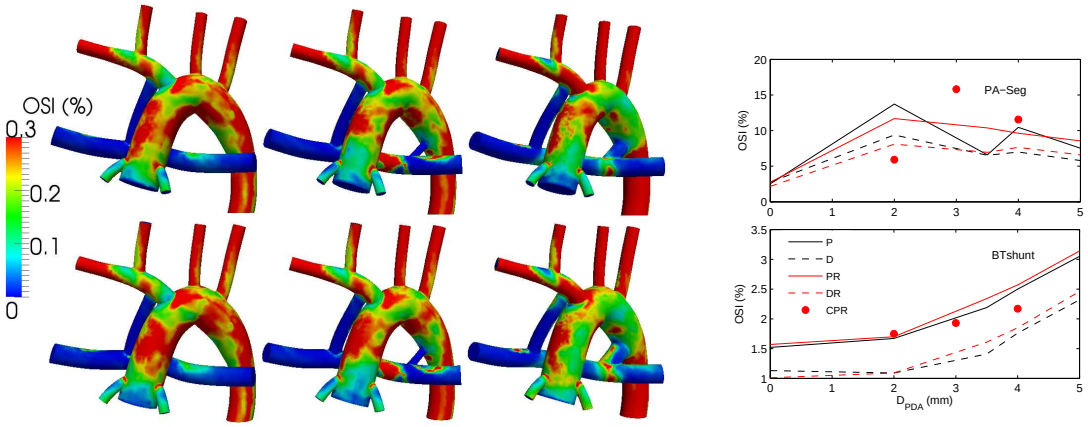

(a) (b)

Figure 8.9: (a) OSI contours for normal PVR (top row) and high PVR (bottom row), and a single proximal MBTS (left column), a proximal MBTS and a 2 mm PDA (middle column), and a proximal MBTS and a 4 mm PDA (right column). (b) Spatially averaged OSI in the PA segment (top plot) and in the MBTS (bottom plot). See Figure 8.3 caption for more details.

8.4 Discussion

A multiscale approach was used to simulate hemodynamics and physiology in models with single versus multiple systemic-to-pulmonary connections. The multiscale approach enabled predictions of global circulatory parameters, such as OD and cardiac workload, that are relevant to clinical decision-making and surgical planning. We simultaneously captured these global changes together with corresponding hemodynamic changes in the 3D domain, including WSS, WSSG, RT, and OSI. Because local hemodynamics are influenced by changes in the 0D domain, employing efficient 3D-0D coupling is essential to obtain a physiologically realistic model, allowing for more accurate predictions. To examine the effect of wall distensibility, a closed-loop FSI simulation was also performed using the same framework. Results confirmed that a rigid-wall assumption was sufficient for this study since the shunt, which primarily effects the hemodynamic outcome of the surgery, behave as a nearly rigid vessel. In summary, the results of this chapter suggest:

1. Pulmonary flow rate is higher with a distal MBTS compared to a proximal MBTS, which can be explained by the sharp turning of flow at the systemic anastomosis point in the proximal MBTS anatomy. This rapid change in flow direction reduces the momentum of flow perfused into the shunt, leading to reduced pulmonary flow. This reduction is consistently observed for the distal MBTS configuration with different PDA diameters in Table 8.2.

2. The distal MBTS configuration produces higher coronary OD at low $Q_{\mathrm{p}}/Q_{\mathrm{s}}$ compared to the proximal configuration, while in all other cases a proximal MBTS produces higher OD. In the presence of a PDA/CS any increase in the pulmonary flow rate decreases OD because of pulmonary over-circulation. In general, OD to the systemic and coronary arteries is reduced by reducing PVR, increasing PDA/CS size, and moving the shunt to a distal position.

3. Results are generally independent of PVR when varying PDA size or shunt positioning. Comparing the simulation results of the normal and high PVR cases, pulmonary flow rates decrease while systemic and coronary flow rates increase. At low pulmonary flow rates, changes in PVR produce insignificant changes in systemic and coronary OD because a large portion of overall pulmonary resistance is created by the shunts, and OD is less sensitive to $Q_{\mathrm{p}}/Q_{\mathrm{s}}$. However, for higher PDA sizes, increasing PVR has a more pronounced effect on pulmonary flow rate, leading to higher OD.

4. The 3.5 mm PDA and 3.0 mm CS in combination with 3.5 mm MBTS are associated with the highest RT. The balance of flow momentum between the MBTS and PDA/CS generates a region between the PDA/CS and MBTS with low velocity, low WSS, high OSI, and high RT. However, as PDA/CS diameter is increased, flow in the PA becomes dominated by flow from the PDA/CS, hence flow stagnation is not observed, RT and OSI are reduced and WSS is increased. In general, the CS produces higher RT in the PA compare to a similar-sized PDA, due to increased stagnant flow in the PA caused by the anastomosis angle between the CS and PA that is opposite to that of the PDA and PA.

Effect of WSS and WSSG on local morphologic changes has been studied in [130, 131, 132]. The use of multiple shunts led to a competitive flow situation inside the PA, producing a region with high RT, especially with lower PDA diameters. WSS was lower in models with large PDAs; nevertheless the WSS values in the shunts are sufficient for triggering platelet activation when compared with reported values of WSS for platelet activation (ranging from 120 to 300 g/(s^2cm) [133, 134, 135]). A combination of a flow stagnation region in the PA with higher WSSG and OSI, accompanied by sufficiently high WSS in the shunts is likely conductive of platelet activation and thrombus formation.

This study identified two concerning findings related to the use of multiple shunts that warrant further clinical study. First, local hemodynamic parameters, which are used here as a surrogate for assessment of thrombotic risk, suggest increased thrombotic risk in anatomies with small PDA/CS diameter. Second, insufficient systemic and coronary OD was observed in anatomies with larger PDA/CS diameter. Together, these findings indicate that the use of multiple shunts is detrimental because it may increase thrombotic risk, while at the same time offering no benefit in terms of OD. Since OD directly relates to pulmonary flow rate, a single shunt with a larger diameter was shown to be a preferable means to provide the same pulmonary flow rate, avoiding issues of flow competition that arise with multiple shunts. The single shunt arrangement was shown in this study to have fewer adverse effects of local hemodynamic parameters, and thus likely reduced thrombotic risk, compared to the multiple shunt arrangement. In addition, the perceived benefit of introducing redundancy by using multiple shunts is compromised for two reasons. First, the individual thrombotic risks in each shunt are highly correlated, because thrombus formation relies on the production and transport of key chemical factors (e.g. thrombin) that accumulate in the blood, thereby increasing the thrombotic risk in the entire circulation and in neighboring shunts. Second, a multiple shunt configuration that is optimized for OD will become suboptimal when one of the shunts is blocked. This cannot be avoided by an initial configuration with multiple larger diameter shunts, as this leads to pulmonary hyperperfusion. For these reasons, our simulation results indicate that the use of

multiple shunts has potential to worsen a patients physiological condition, while increasing their risk of thrombosis. These findings should be corroborated by clinical studies comparing differences in patient outcomes with multiple versus single shunt configurations.

We recognize several limitations of the present study. First, this study examined a limited number of parameters, while in actual clinical scenarios there is significant inter-patient variability and likely a wider range of parameters that could effect hemodynamic conditions. Second, this study examined parameter changes independently, while in actual clinical scenarios hemodynamic parameters are often tightly linked together. For example, hematocrit level is affected by the level of oxygenation but also effects blood viscosity. Hence, in practice, OD, which itself depends on the cardiac output, can also effect cardiac output in a feedback loop. Third, this study used an idealized geometric model. While we do not expect changes in overall trends, it is possible that use of a patient specific model could effect local hemodynamic quantities. Despite these limitations, the simulation framework presented here enabled systematic comparison of different surgical strategies and testing of our hypothesis without confounding variables that would typically appear in a clinical study.

Acknowledgements

The authors wish to thank Giancarlo Pennati, Francesco Migliavacca, and Irene Vignon-Clementel for sharing their expertise in the LPN modeling, and Ethan Kung, Sethuraman Sankaran, and Matthew Bockman for their useful comments.

This chapter, in full, is a reprint of the material as it appears in Simulations reveal adverse hemodynamics in patients with multiple systemic to pulmonary shunts in *Journal of Biomechanical Engineering*. Authors are M. Esmaily-Moghadam, B. Murtuza, T-Y. Hsia, and A. Marsden. The dissertation author was the primary investigator and author of this paper.

Chapter 9

The Assisted Bidirectional Glenn

The first stage of single ventricle repair is usually performed within days of birth and often involves inserting a shunt to connect the systemic and pulmonary circulations in order to create a circulation that enables adequate oxygenation [3, 4]. Such a SPS, which is often a 3 to 3.5 mm modified MBTS connecting the brachiocephalic artery to the PA (Figure 9.1), becomes the sole source of pulmonary blood flow [5, 6]. This physiology is well known to carry the highest mortality and morbidity in the life of a single ventricle patient [7]. There are a number of factors that contribute to the challenges with patient management and the delicate physiology of patients with SPS.

Major drawbacks of the MBTS can be summarized as follows. First, the SPS-dependent circulation must maintain a delicate balance between pulmonary and systemic perfusion. Too much pulmonary blood flow may lead to heart failure and too little may result in unacceptable cyanosis or inadequate oxygenation [13, 14, 15]. Growth and remodeling magnifies this problem, since the SPS does not grow with the rest of the vasculature. Second, thrombosis is a significant risk. As the SPS provides the only source of pulmonary blood flow, there is a risk of sudden death due to clot formation in the SPS and blockage of pulmonary blood flow. Third, high load on the single functional ventricle may lead to higher risk of heart failure. In an SPS-dependent circulation, the single ventricle must operate at systemic pressure level and pump twice as much blood (to both systemic and pulmonary beds) compared to a normal left ventricle. Fourth, OD to end

organs, including brain, liver, and heart, is suboptimal in this circulation. Due to the obligatory mixing of oxygenated and deoxygenated blood in the atrium, the systemic oxygen saturation is reduced compared to a normal infant. Fifth, during cardiac diastole, when the coronary arteries are normally perfused, there is runoff into the pulmonary arterial bed through the SPS, leading to siphoning of coronary perfusion from the myocardium [13]. This *steal* of coronary flow together with lowered systemic saturation can lead to myocardial ischemia [14].

Patients who survive the above issues with the MBTS physiology reach the second stage repair, in which the superior vena-cava (SVC) is connected to the PA in a BGLN or Hemi-Fontan operation (Figure 9.1). The BGLN mitigates most of the aforementioned issues and is associated with much lower mortality compared to the MBTS. As a result, to achieve a more stable and safer physiology it is desirable to perform the BGLN as soon as possible. While the BGLN is a viable stage-two operation, it has been established in early clinical experiences that premature Glenn palliation results in poor clinical outcomes and high mortality rates.

In 50s, Glenn investigated the option of using venous return to augment the pulmonary blood flow in certain congenital anomalies. He performed several experiments on animals to examine long term outcome of this surgery and ensure all SVC flow can bypass the right side of the heart while the SVC elevated pressure is within the tolerance of subjects. Based on those studies, he hypothesized that a 13-17 mmHg pressure is sufficient for pulmonary perfusion but insufficient for producing peripheral edema [170, 171]. He observed 4X drop in PVR three month after the surgery that lead to reduced chance of varicosities and development of collateral venous circulation. His first clinical application on a 7-year-old boy was successful with marked improvement in exercise tolerance, oxygen saturation, and hematocrit levels [8].

Following Glenn's animal study and first clinical trial success in 50s, there was multiple clinical trial of cava-pulmonary anastomosis in 60s, which included patients from few-days-old to over 20-years-old [170, 171]. Post surgical high SVC pressure leading to headache and edema was controlled in these patients using

azygos vein. Azygos vein contribute a significant share of cava blood flow, which after creation of cava-pulmonary shunt would serve as a venous collateral. As a result, SVC pressure was controlled by interrupting or preserving azygos vein in a SVC-RPA anastomosis. To keep SVC pressure low in children under 6 month old, while PVR is reducing, azygos vein was kept patent for a week after surgery. Delayed ligation of azygos vein was achieved by looping a silk suture around the vessel and bring it out through the incision and tying it after a week [172]. A patent azygos in presence of SVC-RPA anastomosis, however, lowered the PA flow and the efficiency of the anastomosis, therefore was only practiced when necessary [173].

Sachs reported 20 cases of end-to-side RPA-SVC anastomosis that was only performed on patients with PA pressure of less that 10 mmHg [172]. They reported 7 death in total. This includes 5 death out of 6 children under one year of age. One remaining patient in this age group reported to be in good condition after 5 years. They experienced 80% of short term survival and 40% long term survival on patients with a SPS [2]. This short-term higher survival rates with SPS also has been reported by others at that time. Although, there were no follow up failure of cava-pulmonary anastomosis, this short-term results was a good reason for choosing SPS for children under one year of age.

A collection of 537 cases in which SVC-RPA shunt was employed clearly shows higher mortality in younger patients (Table 9.1) [174]. In general, if largest group of patients are considered in this study, cava-pulmonary shunt was mostly beneficial in patients with transposition of great vessels with pulmonary stenosis or TGV-PS (16% mortality), then tetralogy of Fallot or TOF (25% mortality), then tricuspid atresia (35% mortality), and then Ebstein's anomaly (53% mortality). In this study, there are indications that in infants with cava-pulmonary connection, pulmonary insufficiency can be a larger thread as compared to high SVC pressure. In the set of patients with TGV-PS, there were 6 patients who had a SPS or PDA along with cava-pulmonary connection. All those patient survived the surgery. In particular, 12 out of 88 TOF patients had arterial shunt in addition to cava-pulmonary connection. Unfortunately the mortality rate for this subset of patients

Table 9.1: The effect of age on mortality following a RPA-SVC connection. Data assembled from [174]. The results highly discourages this surgery for patients under six months old.

Age (months)	Under 1	1-6	6-12	12-24	Over 24
Mortality (%)	86	50	32	23	18
Number of cases	50	121	68	71	227

is not reported, however this anomaly is the only case that had lower mortality for age less than 6 months as compared to age less than 2 years (30% versus 42%). Like other anomalities mortality was much lower (16%) for TOF patients older that 2 years.

The above early clinical studies reported low pulmonary perfusion, low upper-body oxygenation and SVC syndrome in infants with the SVC-RPA connection, which is also of concern in patients with the BGLN. Because of the higher PVR in the neonatal period, the BGLN is typically performed at about 4-6 months of age, after the PVR has dropped. This begs the question if there is a way to help single ventricle patients pass the critical first few months after birth, without exposing them to the higher risk of MBTS physiology. In this study we present a novel surgical approach that we call the Assisted Bidirectional Glenn (ABG), which may provide an answer to this question. The main idea is to assist the venous return and increase the pulmonary perfusion by adding an SPS to the BGLN surgery. Based on the ejector pump concept from fluid mechanics, SVC flow is assisted by the higher energy SPS flow relying on Venturi effect to avoid a large increase in SVC pressure. This results in a radically different surgical approach that could remove the aforementioned MBTS drawbacks, and potentially reduces the number of surgeries from three to two. This novel surgery, which to the best our knowledge never been tried or simulated before, could be performed immediately after birth, and combines the benefits of both the MBTS and BGLN procedures.

In this initial study to evaluate the ABG concept, we adopt a multiscale simulation framework which avoids the ethical issues of clinical and animal studies on a radically new surgical procedure. Multiscale modeling has been used extensively to study the circulation of single ventricle heart patients [25, 21, 80, 175]. This framework poses no danger to patients and allows apple-to-apple comparison

of multiple surgical options while keeping the circulatory parameters unchanged. The adopted framework accounts for the dynamic interplay between the local hemodynamic changes in large vessels in different surgical options and the rest of circulatory system and the heart in a LPN, including blocks for upper and lower body and kidneys. The ABG anatomy is modeled and its performance is compared to the MBTS and BGLN anatomies by examining saturations, flow rates, OD, heart load, and pressure levels. Based on prior clinical studies, we discuss the clinical significance of the results and the possible advantages and drawbacks of the ABG, as well as future directions.

9.1 Proposed surgery: ABG

In the ABG (Figure 9.1), the SVC is connected to the PA as in the BGLN procedure and, additionally, a shunt is inserted between the systemic circulation and the SVC. In essence, ABG is a hybrid of the BGLN and the MBTS, in which the pulmonary perfusion is partly supplied through the SVC and partly through the SPS. Draining the SVC into the PA reduces mixing of oxygenated and deoxygenated blood in the atrium. This concept allows for the same level of pulmonary flow rate as in the MBTS to be obtained with a lower level of SPS flow. As a result, we hypothesize that oxygen saturation and OD will be improved while cardiac output and heart load are reduced.

From a fluid mechanics perspective, flow in the systemic circulation has high energy content because of its high pressure. In the MBTS, this energy is dissipated through the SPS and its pressure is reduced to the level of the pulmonary circulation to avoid pulmonary hyperperfusion. In the ABG, however, we propose that this energy can be harvested to pump SVC flow using the concept of an ejector pump. As shown in Figure 9.2, a flow with high energy content (aortic flow) can be used to pump ('assist') a low energy content flow (SVC flow) and elevate the pressure at the outlet (PA flow). This elevated pressure is used to supply sufficient blood to the PA, while keeping SVC pressure low. Therefore, compared to the BGLN, we hypothesize that pulmonary perfusion could be enhanced and

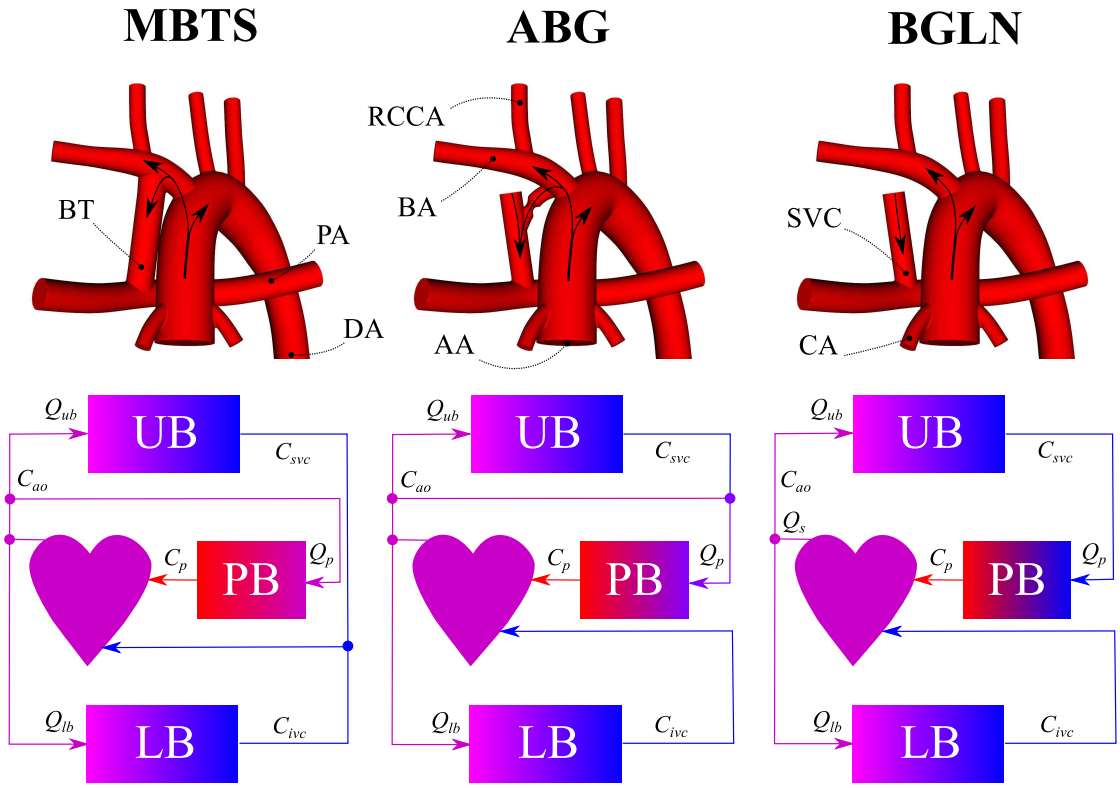

Figure 9.1: The idealized models of the MBTS, ABG, and BGLN are shown at the top row. In these anatomies, aortic arch including AA and descending aorta (DA), coronary arteries (CA), PA, SVC, Blalock-Taussig shunt (BT), and upper branches including brachiocephalic artery (BA) and right common carotid artery (RCCA) are shown. The circulation schematics are shown at the bottom row. Q_p, Q_s, Q_{lb}, and Q_{ub} denote pulmonary, systemic, lower body, and upper body flow rates. C_s, C_p, C_{ao} denote systemic vein, pulmonary vein, and aortic oxygen concentrations. The color used in the circulation schematics represent the level of oxygen concentration.

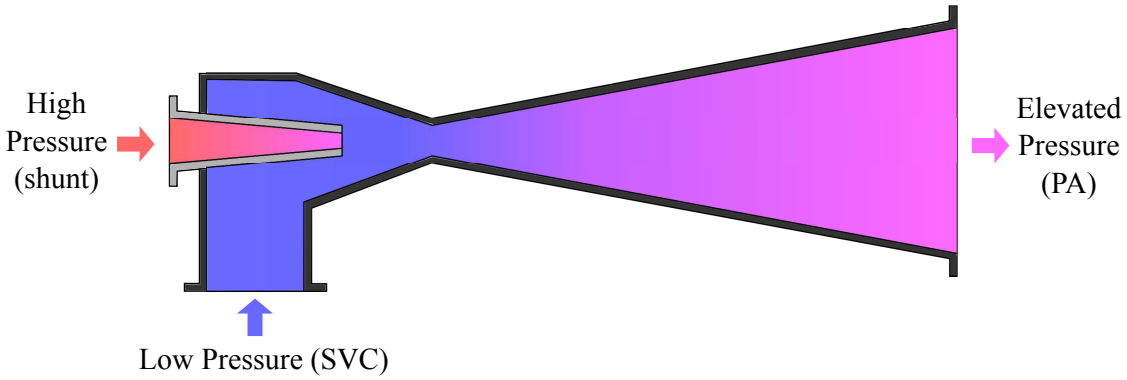

Figure 9.2: A schematic of an industrial ejector pump. This device transfers the energy of flow with higher pressure to the flow with lower pressure, hence elevating the pressure at the outlet. Based on the same concept, flow through the SVC can be assisted by flow through the shunt to obtain a higher pressure at the PA without increasing SVC pressure.

subsequent respiratory complications in subjects with high PVR such as lack of pulmonary circulation growth, hypercapnia, and increased physiologic lung dead space could be potentially avoided.

Designing an ejector pump relies on reducing the pressure of the high-energy-content flow to the same level as the low-energy-content flow, while maintaining the desired flow rates. This is accomplished by using a nozzle that increases the velocity and decreases the pressure of the high-energy-content flow using the Venturi effect. In the actual surgery, there are several potential means to accomplish this. In this study, we explore the use of a shunt with a clip, since this can be implemented using current techniques. The kinetic energy of the high velocity flow is converted to pressure (potential energy) in the diffuser section of the ejector pump. Ideally, the SVC vessel may be used for this purpose, however to construct an anastomosis between the SPS and SVC that is surgically feasible, a simplified geometry is considered in this study.

9.1.1 Multidomain simulations

The multiscale framework presented in Chapter 2 is adopted in this study to couple local hemodynamics to a closed loop model of the circulatory physiology.

In this framework, the computational domain is decomposed into: 1) a 3D model of the large vessels where the Navier-Stokes equations are solved and 2) a 0D LPN representing the behavior of the heart and closed loop circulation .

The adopted LPN is based on the prior studies of the MBTS circulation in Chapters 7 and 8. Separate blocks model the upper body, lower body, pulmonary bed, coronary circulation, and the heart. These blocks are partitioned into arterial bed, capillary bed, and venous bed sections. Component values are obtained from a prior study that incorporated clinical catheterization and angiographic data from 28 Norwood patients [16]. Upper body venous return is directly connected to the SVC in the ABG and BGLN LPNs (Figure 9.3). To avoid regurgitant flow a coupled Dirichlet boundary is imposed at the AA. The total excess blood volume in the LPN is preserved temporally to improve cyclic convergence and accuracy, using Equation 8.2. To mimic the auto-regulation mechanism, the total excess blood volume is adjusted among different simulations to keep aortic pressures fixed.

The 3D idealized geometric models are constructed based on the former study of MBTS (Figure 9.1). Models includes the SPS, the SVC, the aortic arch, four upper branches, two coronary arteries, and the PAs. A 3.5 mm shunt is used in the MBTS geometry. The SVC diameter is assumed to be 4.5 mm. Two SPS-SVC anastomosis are considered for the ABG model: an straight shunt (denoted by ABG_S) and a clipped shunt (denoted by ABG) (Figure 9.3). Note that the ABG with a clipped shunt is the model we refer to as ABG in the following sections. The LPN obtained from Section Section 2.4.4 is used to simulate pre-stage two condition (representing few month old patients). To model pre-stage one condition (newborn patients), three times higher PVR (21 Wood units or mmHg·min/L) is considered. In total eight simulations are performed with the important results reported in the next section.

For the 3D domain, we assume an incompressible Newtonian fluid and rigid walls. The time step size of the 3D solver is set to 0.5 ms. The OD is calculated based on the flow rates and average oxygen consumption (see Appendix C). For more details on the numerical methods, model construction process, and mesh convergence study see Chapters 2-5.

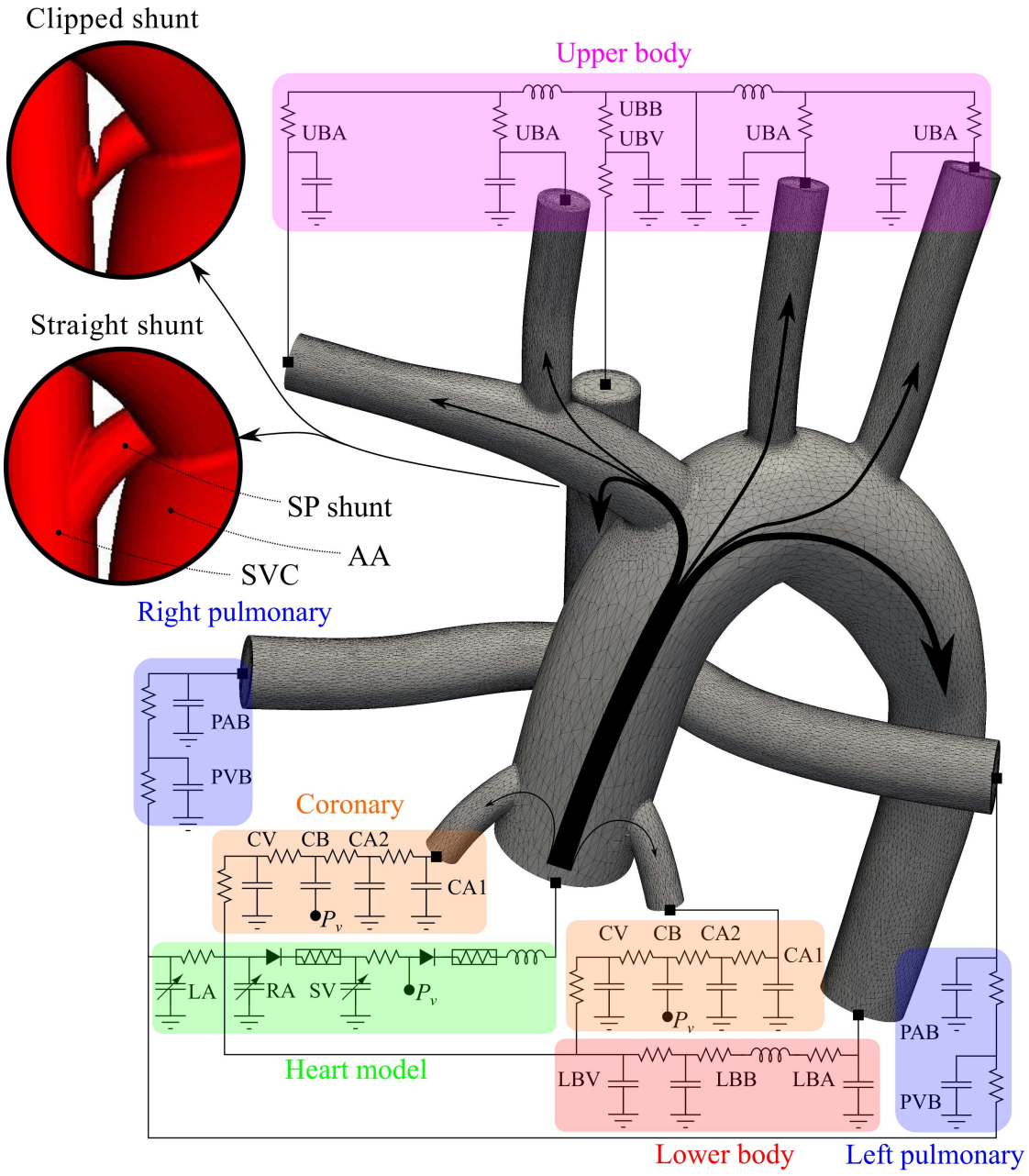

Figure 9.3: LPN coupled to the ABG anatomy. See Figure 2.11 for abbreviation. Two geometries, clipped and straight, are shown for the SPS. Pulmonary flow is supplied through the SVC and the SPS, which is anastomosed to the BA and the SVC.

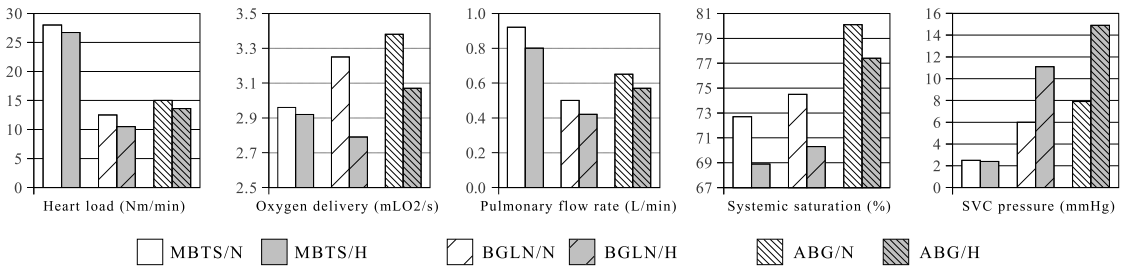

Figure 9.4: MBTS, BGLN, ABG heart load, OD, pulmonary flow rate, systemic oxygen saturation, and SVC pressure at normal (white) and high (gray) PVR.

9.2 Results

Comparing the results of ABG_S and ABG from Table 9.2 shows that using an straight SPS sends too much blood to the pulmonary circulation, producing a high SVC pressure, low upper body perfusion, low OD, and high heart load. By constraining the SPS, less flow is drawn from the systemic circulation and OD and heart load are improved. This also produces a jet along the SVC flow direction and slightly assists drainage of upper body circulation into the pulmonary arteries by lowering SVC pressure.

The ABG cardiac output and heart load are comparable to BGLN and are significantly lower than MBTS (Figure 9.4). The ABG has the highest OD among all cases regardless of PVR, while BGLN delivers more oxygen than MBTS only at normal PVR. Pulmonary flow rate (Q_p) in BGLN is twice lower than MBTS and ABG Q_p is the median of BGLN and MBTS. The ABG has the highest systemic oxygen saturation compared to MBTS and BGLN, with BGLN saturation being slightly higher than MBTS. The SVC pressure is approximately 2 mmHg in MBTS and it varies between 6-11 mmHg in BGLN and 8-15 mmHg in ABG, depending on the PVR.

The nozzle effect of clipped SPS is shown in Figure 9.5. The systemic pressure, either at systole or diastole, is reduced to the level of SVC pressure at the clipped section of SPS. A low pressure zone is observed inside the SVC at the entrainment region. The reduced pressure is transformed to the kinetic energy, as there is a high velocity flow being ejected into the SVC from the SPS. The

Table 9.2: Simulations results of different surgical options at normal (N = 2.3 woods) and high (H = 6.9 woods) PVR. BTS, GLN, ABG_s, ABG denote MBTS, bidirectional Glenn, ABG with a straight shunt, and ABG with a clipped shunt procedures, respectively. OD, OD_{cor}, and OD_{ub} are the systemic, coronary, and upper body OD in mL_{O_2}/s, respectively. HL is approximately load on the single ventricle. $\bar{Q}_{\text{cor}}$, $\bar{Q}_{\text{lb}}$, $\bar{Q}_{\text{ub}}$ $\bar{Q}_{\text{s}}$, $\bar{Q}_{\text{p}}$, and CO are coronary, lower body, upper body, systemic, pulmonary, and AA (cardiac output) average flow rates, respectively. $\bar{P}_{\text{ao}}$, $\bar{P}_{\text{svc}}$, and $\bar{P}_{\text{pa}}$ are aortic, SVC and PA average pressure, respectively. Sat_{svc}, Sat_{ao}, and Sat_{ivc} are the percentage oxygen saturations in the SVC, aorta, and IVC, respectively.

	Unit	BTS	GLN	ABG_s	ABG	BTS	GLN	ABG_s	ABG
PVR	-	N	N	N	N	H	H	H	H
OD	mL_{O_2}/s	2.96	3.25	3.32	3.38	2.92	2.79	2.87	3.07
OD_{cor}	mL_{O_2}/s	0.22	0.24	0.27	0.26	0.22	0.22	0.26	0.25
OD_{ub}	mL_{O_2}/s	1.30	1.39	1.28	1.41	1.28	1.11	0.92	1.16
HL	N·m/min	28.0	12.5	20.9	15.0	26.7	10.5	16.6	13.6
CO	L/min	2.01	1.17	1.63	1.31	1.93	1.06	1.43	1.23
$\bar{Q}_{\text{p}}/\bar{Q}_{\text{s}}$	-	0.85	0.43	0.98	0.58	0.71	0.40	0.90	0.54
$\bar{Q}_{\text{s}}$	L/min	1.09	1.17	1.03	1.13	1.13	1.06	0.92	1.06
$\bar{Q}_{\text{p}}$	L/min	0.92	0.50	1.01	0.65	0.80	0.42	0.82	0.57
$\bar{Q}_{\text{lb}}$	L/min	0.61	0.67	0.63	0.66	0.63	0.64	0.62	0.66
$\bar{Q}_{\text{ub}}$	L/min	0.48	0.50	0.39	0.47	0.50	0.42	0.29	0.40
$\bar{Q}_{\text{cor}}$	mL/min	8.16	8.71	8.43	8.65	8.42	8.29	8.20	8.64
$\bar{P}_{\text{ao}}$	mmHg	52.1	54.6	55.0	55.2	53.7	51.8	52.9	54.9
$\bar{P}_{\text{svc}}$	mmHg	2.5	6.0	12.3	7.9	2.4	11.1	21.5	14.9
$\bar{P}_{\text{pa}}$	mmHg	8.1	4.7	9.0	6.2	17.9	10.1	19.1	13.5
Sat_{ao}	%	72.7	74.5	86.4	80.1	68.9	70.3	83.8	77.4
Sat_{svc}	%	48.2	51.1	56.9	55.2	45.5	42.5	44.1	48.2
Sat_{ivc}	%	53.7	57.1	68.0	62.4	50.5	52.0	65.0	59.8

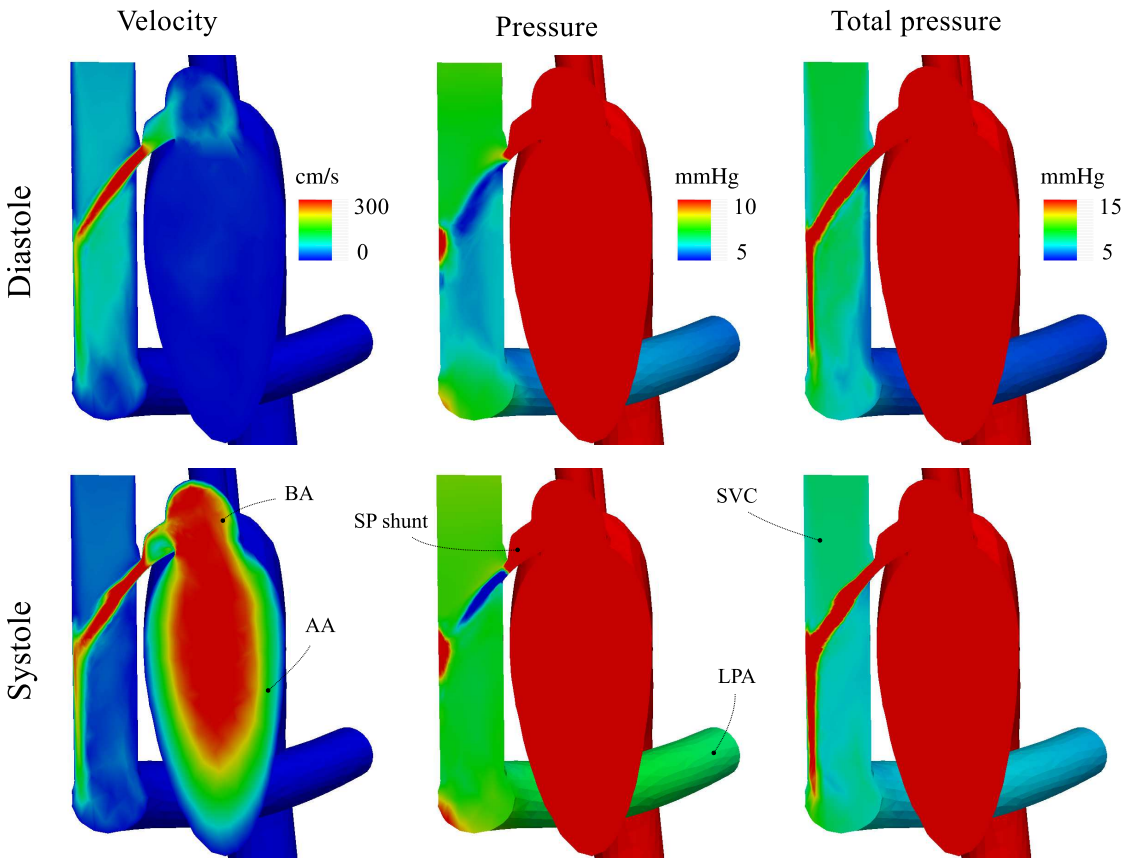

Figure 9.5: Pressure, velocity, and total pressure at a slice of SVC and SPS. These are based on ABG simulation results with normal PVR at diastole and systole.

total pressure of this flow, which is calculated based on Bernoulli's equation, is preserved before its impingement to the SVC intima. At the impingement, there is a stagnation region with high pressure and high velocity gradient that dissipate the energy of the jet. This reduces the available energy and pumping capacity and leads to a higher SVC pressure. By using a more acute anastomosis angle, entrainment region can be extended and more energy can be transformed to the SVC flow. Also, energy can be transformed in a shorted distance by increasing the contact area between the jet flow and the surrounding flow. This can be accomplished by using a nozzle with a higher aspect ratio or constricting the SVC at the downstream of the anastomosis. Also, pressure can be recovered more efficiently by having a diffuser-shaped SVC, similar to an industrial ejector pump (Figure 9.2).

9.3 Discussion

There are a number of serious deficiencies associated with the MBTS physiology that keep mortality rates as high as 21% and make the MBTS much higher risk than the subsequent BGLN and Fontan procedures. This underscores the need for an alternative to the MBTS.

Based on the presented results, the ABG offers following possible advantages. First, the entire upper body venous return is directed to the PAs and the SPS flow rate is reduced compared to the MBTS circulation. This leads to early volume unloading of the single ventricle and improves its mechanical efficiency. Second, the deoxygenated blood from the upper body will no longer mix with the oxygenated blood in the right atrium. This leads to higher systemic saturation compared to the MBTS. Systemic saturation is also higher than the BGLN due to higher pulmonary flow rate. Third, lower SPS flow rate is associated with higher diastolic pressure in the aorta. Due to the higher diastolic pressure and systemic saturation, the ABG produces the highest coronary OD as well. Fourth, the ABG could be converted to the BGLN by occluding the SPS via a catheter at a later time. This would obviate the need for the second stage open-chest surgery. Fifth, having two sources of pulmonary flow in the ABG reduces the risk of total blockage of pulmonary circulation by thrombus formation. The SPS is highly susceptible to thrombus formation due to high levels of WSS and pressure drop. The SVC, however, is generally a patent connection based on autopsy reports of patients with RPA-SVC anastomosis. Therefore, blockage of the SPS in the ABG will merely cause a transition to the BGLN circulation, while blockage of the SPS in the MBTS generally results in sudden death.

Even considering all the above mentioned benefits, there remains an open question as to whether the ABG is a viable approach for patients under six months of age. Considering the historical clinical experience demonstrating high mortality associated with the BGLN in this age group, one naturally must ask whether the ABG would result in similar clinical outcomes. This question can be studied from several perspectives. First, the aforementioned clinical reports in 1960s implemented a traditional SVC-RPA anastomosis that differed from the ABG and

the BGLN in terms of SVC pressure, upper body flow rate, and lung perfusion [174, 172, 176]. Draining SVC flow into a single lung lobe compared to both lobes could generate much higher SVC pressure and lower upper-body and lung perfusion. Second, there are multiple potential causes of high mortality in newborns with cavopulmonary connection and the ABG shares only some of those drawbacks with the BGLN. Three main possible causes for high mortality in newborns with cavopulmonary connection are: a) low OD, b) low pulmonary flow rate and respiratory complications, and c) high SVC pressure.

Simulation results show that OD in the BGLN is lowest in the neonatal stage and exceeds the OD of the MBTS as PVR drops. Considering the mortality rate and OD of the BGLN and MBTS shows they have inverse trends at different age groups. Insufficient OD, specifically to the upper body, in the BGLN at high PVR is caused by impaired upper body flow rate and hypoxemia. In the ABG, however, the low upper-body flow rate is accompanied by high systemic saturation. As a result, the ABG produces OD rates that are as high or higher than the MBTS and BGLN.

Low pulmonary flow rate and respiratory complication can also be considered as a main cause of death in newborn with cavopulmonary connections. In a study in early 70s, Hunt reported 46 patients with RPA-SVC anastomosis whom 18 of them were under 6 months of age [176]. There were 10 death in infants under 6 months of age, half due to the respiratory complication. They also reported lower tolerance to exercise in patients with caval anastomosis as compared to those with SPS. This is explained by the independence of SVC blood flow rate and exercise level [176]. Having a SPS provides a variable blood flow rate with exercise that may obviate this complication.

Also, the respiratory failure forms the majority of infants (53 patients out of 129) with post-surgical complication in another study [177]. The respiratory failure is characterized by excessive work of breathing and fatigue, hypercapnia, hypoxemia, high physiologic dead space-tidal volume and a PA pressure larger that 0.75% of aortic pressure. Hypercapnia, which leads to pulmonary vasoconstriction and hypertension, is due to elevated $PaCO_2$ and low PaO_2 in the pulmonary arter-

ies. Also it has been argued that patients with impaired pulmonary blood flow also have decreased lung capacitance, significant ventilation-perfusion inequalities, and increased physiologic dead space [177]. Therefore, the risk of respiratory failure may be reduced by the oxygen saturation improvement and the pulmonary blood flow increase in the ABG as compared to the BGLN.

There are also other instances in literature that supports this hypothesis. Brouchow reported a clinical trial of cava-pulmonary anastomosis to a 4-day-old patient with tetralogy of Fallot and pulmonary atresia [178]. He reported that the patient *did fairly well for 4 months, when increasing signs of SVC syndrome and increasing cyanosis and hematocrit slowly developed*. Patient died due to the cardiac arrest at the age of sixteen month during second surgery, which was an attempt to increase pulmonary blood flow. They reported a widely open SVC-PA and closed PDA at autopsy. They postulated that the closure of the PDA after 4 months reduced pulmonary blood flow, leading to hypoxemia, polycythemia, and increased blood viscosity. As a result of increased PVR, the flow through anastomosis reduced and signs of sever SVC syndrome appeared leading to a non-functional connection [178]. Based on their argument, this is the low pulmonary blood flow that initiated a chain reaction of low oxygenation, higher hematocrit level, higher blood viscosity, increased PVR, and even lower pulmonary blood flow. This chain can be avoided all together by having sufficient pulmonary blood flow to begin with.

Simulation results show that SVC pressure can be as high as 15 mmHg in the ABG at high PVR, while it is less than 3 and 12 mmHg in the MBTS and BGLN, respectively. High SVC pressure is an important parameter that is hypothesized to cause cerebral hemorrhage and peripheral edema. To mitigate SVC pressure increase in the ABG, we used high velocity SPS flow to pump SVC flow to the PA. The two SPS geometries, considered in this study, are basic designs intended for technical feasibility, but not yet fully optimized from the point of view of fluid mechanics. For maximal recovery, it is essential to reduce viscous dissipation by using a minimal length for the shunt, a diffuser-shaped SVC, and a proper anastomosis angle and cross section. A wide range of SPS designs could be

considered in the future that may lead to lower SVC pressure.

Using a straight shunt in the ABG_S removes the jet effect and can be considered to be a variation of BGLN with accessory pulmonary flow, which has been studied extensively in clinical [179, 180, 181, 182] as well as computational and in vitro settings [182]. These studies in general show, consistent with the present study, higher saturation levels, higher pulmonary flow rate, higher SVC pressure, and higher cardiac load in the presence of accessory flow. Assuming the added shunt in the ABG_S is comparable to the BGLN with accessory flow, we showed that clipping the shunt in the ABG offers an advantage by lowering SVC pressure and heart load. The reported mortality and morbidity rates in patients with accessory flow differs among institutions. Van de Wal et al. reported no influence on the survival rate in a study of 205 patients with an average age of 5.6 years, McElihinney et al. reported higher, yet statistically insignificant, mortality in a study of 160 patients with an average age of 7.8 months, and Mainwaring et al. reported higher mortality in study of 149 patients with an average age of 10 months [179, 180, 181]. Earlier completion of Fontan was reported in patients with accessory flow and it is argued that if hepatic-factor is important for the prevention of pulmonary arteriovenous malformation, having accessory pulsatile flow might represent an advantage [179]. Also it has been suggested accessory flow may improve exercise tolerance by providing a variable pulmonary flow [176].

Acknowledgements

This chapter, in full, is a reprint of the material as it appears in The Assisted Bidirectional Glenn: simulations of a novel surgical approach for first stage single ventricle heart patients in *The Journal of Thoracic and Cardiovascular Surgery*. Authors are M. Esmaily-Moghadam, T-Y. Hsia, and A. Marsden. The dissertation author was the primary investigator and author of this paper.

Chapter 10

Conclusion and Future Directions

10.1 Concluding remarks

We presented a framework for coupling an arbitrary, user-defined LPN to a discretized 3D FE domain, which exhibits the stability of monolithic approaches, while maintaining the flexibility and modularity of a partitioned approach. Two types of coupled boundaries, i.e. 'Neumann' and 'Dirichlet' BCs, were discussed. The instability associated with backflow for the Neumann boundaries was addressed by adding an additional stabilization term to the formulation. In this formulation, at each nonlinear iteration of the Navier-Stokes solver, flow rates of Neumann boundaries and pressures of Dirichlet boundaries are sent from the 3D to 0D domain, where ODE's are numerically integrated, and pressure or flow rate are passed back to the 3D domain. By using a finite difference technique to evaluate the 0D domain contribution to the tangent matrix of the 3D domain, a strongly coupled implicit formulation is proposed to improve the stability and convergence properties when using coupled Neumann boundaries. Good convergence properties were shown when accounting only for the effect of each Neumann surface on its own traction in the tangent matrix. Validating this framework against a Windkessel analytical solution demonstrated its accuracy; and strong stability properties were demonstrated through two case studies with closed-loop LPN.

We performed a quantitative comparison of three outlet treatment methods used to address the problem of numerical divergence due to backflow. Using

identical numerics, models, and meshes, we compared the methods of outlet stabilization, normal velocity constraint, and Lagrange profile constraints. We have shown that the normal constraint can be safely used in the case of slight flow reversal, producing a stable result with little impact on the flow physics. However, this requires the constrained direction vector to be close to the direction of reversed flow and that only the part of the outlet with flow reversal be constrained. Our results showed that the Lagrange method, while often successful in stabilizing the solution, suffered from high impact on the pressure field solution, high computational cost, and increased difficulty in both implementation and ease-of-use. While results with highly tuned outlet flows matched very well with the stabilized method results, a lack of tuning can produce drastically different results that are not confined to the vicinity of the outlet. The stabilization method was shown to have the highest robustness, and the least impact on the flow field, with no extra computational cost, and high ease of implementation and use. In addition, the stability of this method is improved to include a wider range of time steps by adding only a fraction of the convection term in our formulation. This implementation also reduced the impact of this method on the pressure field. In overall, the addition of an outlet stabilization term provides an accurate, robust, and easy-to-use method that reliably prevents backflow divergence in numerical simulations of blood flow.

Bi-partitioned iterative algorithm was introduced for solving system of linear equations that are obtained from the FE discretization of Navier-Stokes equations. By dividing the solution space into two, i.e. velocity and pressure, a richer space is obtained, guaranteeing improved convergence. The system of linear equations are solved block-by-block using a Schur compliment that is fully integrated into the bi-partitioned algorithm. Also, a PC is introduced for problems containing coupled Neumann BC, as those encountered in multidomain simulations. By deriving an analytical form for the proposed PC, implementation effort and evaluation cost are minimized. We showed this PC closely approximates a block of the LHS matrix, hence it can be efficiently used in the Schur compliment and bi-partitioned algorithm. Through several examples we showed effectiveness of the bi-partitioned algorithm combined with the PC, reducing the cost of solving system of linear

equations more than an order of magnitude in certain cases.

A method for iterative linear equation solvers was presented that allows a systematic conversion of sequential algebraic operations, such as vector inner product and matrix-vector product, to their parallel counterparts. Improved parallel performance is obtained by introducing a mapping that separates the shared entries from its unshared entries. This allows one to combine non-blocking communications with massive computations in matrix-vector products, and to avoid performing repeated computations on the shared entries in a vector inner products. The initialization and use of the new data structures have minimal time and memory requirements. The proposed method was tested on a varying number of processors using three computational models of different size and complexity, and showed superior performance to a well-known and commonly used iterative linear algebra library.

A non-discrete method was introduced for calculating RT in a given region of interest. The proposed method lacks drawbacks associated with Lagrangian discrete methods, such as dependence of the results to the temporal and spatial seeding points and mesh dependency. RT can be calculated based on the time a parcel of fluid spends in a region of interest (RT_1) or the time fluid exiting the boundary has spent in the region of interest (RT_2). Results show that RT_2 is more sensitive to the region of interest selection and this definition can lead to misleadingly low values if a segment of the region of interest lies in a high velocity region. The results show that WSS and RT_1 values are inversely correlated in different flow conditions. It was shown that in a steady flow RT_2 provides a lower bound for $2RT_1$.

The coupled LPN was used to predict the downstream and upstream behavior of an idealized postoperative MBTS model. By implementing the coupled model into a fully automated optimization algorithm, the optimum shunt geometry, considering systemic and coronary OD as the objective function, was found. Consistent with the clinicians consensus, the shunt diameter was the parameter that had the most influence on the results, but we showed that attachment geometry of the shunt also has an impact. The results showed that a shunt with

larger diameter and with a more distal anastomosis provides better coronary OD; and the systemic OD is maximized with a shunt that is a smaller and connected closer to the aorta. This was due to the fact that the coronary perfusion is almost the same for the small proximal shunt and large distal shunt, while the oxygen saturation is higher for the large shunt. This led to higher coronary OD for the distal shunt. The former optimal systemic and coronary OD can be achieved in a single anatomy if midrange values of shunt diameter and anastomosis point are chosen compared to the two former optimal geometries.

Multidomain framework was employed to evaluate the circulatory arrangement of stage-one patients with multiple systemic-to-pulmonary connections and compare it with single MBTS. Simulation were designed to study the effect of PVR, the MBTS positioning, the diameter of PDA, and existence of PDA or CS on a set of parameters. The results showed that using multiple connections, moving the MBTS to a distal position, increasing the diameter of PDA/CS, and lowering PVR lead to pulmonary hyperfusion and OD reduction and lead to increased RT and OSI and decreased WSS and WSSG in the MBTS. The flow condition inside the PA highly depends on momentum of the MBTS and PDA/CS competing flows. A unidirectional flow is observed in presence of a large PDA/CS or in anatomies with only a single MBTS. A competing disturbed flow is observed in cases which the MBTS and PDA/CS have similar sizes. We observed lower WSS and higher RT, OSI, and WSSG in the PA in presence of competing flow and absence of unidirectional flow. These results discouraged use of multiple systemic-to-pulmonary connections, as it can either lower OD or increase RT in the PA, which is a surrogate for thrombotic risk assessment.

Considering the critical condition of stage-one patients and limited improvement obtained from optimization of current surgical procedure, we proposed a new surgery by combining stage-one and two surgeries. The key idea in this surgery is to assist venous return by the high energy systemic flow, hence reducing venous return pressure while augmenting pulmonary perfusion and OD. The reason for high mortality among patients who receive cavopulmonary connection in the neonatal period is not fully understood. If low pulmonary perfusion and low oxygenation

are the leading causes, the ABG could have potential as a viable alternative to the MBTS, as it could reduce the heart load and cardiac output significantly, provide higher levels of oxygenation, add redundancy to sources of pulmonary blood flow and reduce risk of mortality caused by blockage of SPS, and potentially reduce the total number of palliative surgeries to two. High SVC pressure remains as a concern in the ABG and future studies are required to address this potential drawback.

10.2 Future directions

Multiscale behavior is observed in many physical and biological systems. Numerical modeling of multiscale systems is still a challenging problem, as issues of numerical stability, modularity, accuracy, and uncertainty need to be addressed. The multiscale framework that was developed here treats high order (e.g. 3D) and low order models as two separate domains, each solved independently using different numerical schemes and coupled through a predetermined interface. Although separating the domains offers the advantage of modularity, it also produces instabilities and certain limitations associated with the interface between domains. Integration of two domains into one, while respecting the scales of each domain, could remove those drawbacks. This requires translating the lower order model formulation into the higher order model formulation and using a unified numerical scheme for both domains. More specifically, FE principals can be used to formulate the lower order model and potentially implement an efficient space-time formulation for both domains.

A deterministic multiscale modeling approach relies on achieving an accurate representation of the lower order model based on physically acquirable data. Given the physical measurements, currently there is no systematic approach to obtain a unique lower order model. The current process is generally very time consuming, involves trial and error, and most importantly depends on user decisions. This produces results that are study-specific and imposes limits on comparing results of separate studies that aim at an identical problem. Performing

a statistical analysis on such a study requires an automated tuning process that is user-independent. Therefore, a deterministic framework can be developed that systematically produces a multiscale model based on given physical measurements.

The automatic tuning process, on the other hand, generally requires running multiple expensive simulations. The number of simulations grows rapidly as the number of components in the lower order model increases. Cost-wise, it is generally impractical to perform all of these simulations using the expensive high order model. Hence, a surrogate for the high order model can be developed that is cheap to evaluate and closely represents the actual model. To design this surrogate, the governing physics of the high order model must be considered and components that represents those physical principles must be chosen closely.

Considering the idealized LPN used in the study of stage-one surgery, uncertainty analysis should be used in future work to quantify the sensitivity of the results to variation in patient specific parameters. The adopted model for the coronary artery did not take into account changes in elastance of the heart due to reduced coronary flow. While the reduction in coronary flow is small in this study, these effects should be investigated in future work. To design more comprehensive future studies, a broader range of patients should be considered, and results should be correlated with patient outcome statistics.

The ABG is an example of the application of multiscale modeling to test radically different surgical concepts that would otherwise be ethically or technically infeasible. In the future, existing idealized models can be expanded to patient specific models to test ABG under more realistic physiologic and geometrical conditions. Optimization and uncertainty quantification tools will allow for refinement of the SPS design and accuracy assessment. A more extensive LPN may be needed to accurately capture the physiological response of the circulatory system to the large variations imposed by drastically different surgeries. Based on these results, in-vitro animal and clinical studies can be designed in future work. Adding a shunt to a failing BGLN, as an alternative to take-down of the BGLN, seems the best substrate for initial clinical trial of the ABG.

To reduce the SVC pressure in the ABG, it is possible to implant a mechan-

ical device that replaces the connection of the SPS and SVC, thereby improving efficiency of the connection as compared to a traditional surgical connection. The idea is to fabricate a device with two inlets, i.e. a high and a low pressure inlet, and one outlet, which are connected to the SPS, the SVC, and the PA, respectively, similar to an industrial ejector pumps (Figure 10.1). The geometry of this device can be optimized such that pressure is recovered more efficiently in the nozzle. In comparison with common ventricular assist devices, the proposed device contains no moving parts, no active mechanisms, and the entire device can be implanted inside the patient. Hence, it lowers thrombotic risk, reduces patient management complications, simplifies the design and testing of the device, and removes the requirement of being in proximity of a source of energy at all time.

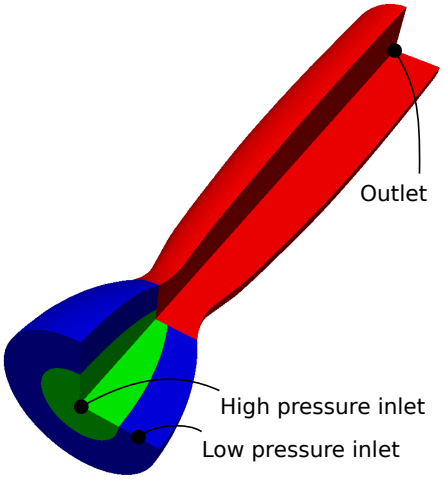

Figure 10.1: Isogeometric analysis of the implanted ejector pump in the ABG. Three patches are employed to construct the high pressure inlet, connected to the systemic circulation, low pressure inlet, connected to the SVC, and outlet nozzle, connected to the PA.

Appendix A

Coupled Neumann Boundary Stability Analysis

Here, we provide a possible explanation for the numerically observed divergence of a simulation when a Neumann boundary is coupled to an inductor. In this case, the coupled surface pressure at each Newton iteration must be updated based on the flow rate,

$$\mathcal{P}^{(k),n+1} = \mathcal{P}_\mathrm{d} + L\frac{\Delta Q^{(k-1)}}{\Delta t}, \tag{A.1}$$

where $\mathcal{P}^{(k),n+1}$ and $\mathcal{P}_\mathrm{d}$ are the predicted pressure of the coupled surface for iteration k and distal point pressure (see Figure 2.5). For infinitesimal changes, the following linear relationship is assumed between pressure and flow rate, which models the 3D domain behavior,

$$\Delta Q^{(k-1)} = -\lambda \Delta \mathcal{P}^{(k-1)}. \tag{A.2}$$

where, physically, λ is proportional to the reciprocal of vascular resistance. From Equation (A.1) and (A.2),

$$\mathcal{P}^{(k),n+1} = \mathcal{P}_\mathrm{d} - \frac{L\lambda}{\Delta t}\left(\mathcal{P}^{(k-1),n+1} - \mathcal{P}^{n}\right). \tag{A.3}$$

This equation is unstable for $|L\lambda/\Delta t| > 1$. In practice, since $\lambda \neq 0$, the pressure of the coupled surface will oscillate and rapidly diverge for small time step sizes. Similarly for a Dirichlet boundary coupled to a capacitor, it can be shown that $Q^{(k),n+1}$ will be an unstable function of $Q^{(k-1),n+1}$.

Appendix B

Single Ventricle LPN Values

The values of the LPN (Figure 2.11) elements are shown in Table B.1. Outside the heart model, all the resistances, capacitors, and inductances have linear behavior. To model turbulence associated with the heart valves, two resistances are included in the LPN, and the pressure drop through them is proportional to the square of their flow rates. Heart chamber pressures are considered to be composed of active and passive parts. The atrial pressure is modeled using,

$$P_{\mathrm{a}} = A_{\mathrm{a}} E_{\mathrm{a}} (V_{\mathrm{a}} - V_{\mathrm{a_u}}) + P_{\mathrm{a_0}} (e^{K_{\mathrm{a}}(V_{\mathrm{a}} - V_{\mathrm{a_u}})} - 1). \tag{B.1}$$

A_{a} is modeled with a sinusoidal function which is non-zero during atrium contraction and E_{a}, $P_{\mathrm{a_0}}$, K_{a}, and $V_{\mathrm{a_u}}$ are the constants of this model. The same model is used for the ventricle, except the active pressure, i.e. the first term in Equation (B.1), is replaced with a parabolic function,

$$P_{\mathrm{v}} = A_{\mathrm{v}} [E_{\mathrm{v_1}} (V_{\mathrm{v}} - V_{\mathrm{v_u}}) + E_{\mathrm{v_2}} (V_{\mathrm{v}} - V_{\mathrm{v_u}})^2] + P_{\mathrm{v_0}} (e^{K_{\mathrm{v}}(V_{\mathrm{v}} - V_{\mathrm{v_u}})} - 1). \tag{B.2}$$

All the constants of the heart model along with the rest of LPN are shown in Table B.1 and B.2.

Table B.1: Figure 2.11 circulatory parameters values.

Block	Parameter	Value	Unit
UBA	R	2.809×10^{1}	mmHg s/ml
	C	4.430×10^{-2}	ml/mmHg
	L	2.138×10^{-2}	mmHg s^2/ml
UBB	R	6.451×10^{-1}	mmHg s/ml
	C	1.552×10^{-1}	ml/mmHg
UBV	R	1.653×10^{-1}	mmHg s/ml
	C	2.039	ml/mmHg
PAB	R	8.338×10^{-1}	mmHg s/ml
	C	2.039×10^{-2}	ml/mmHg
PVB	R	2.194×10^{-2}	mmHg s/ml
	C	4.438×10^{-1}	ml/mmHg
LBA	R	7.022	mmHg s/ml
	C	7.758×10^{-2}	ml/mmHg
	L	1.069×10^{-2}	mmHg s^2/ml
LBB	R	6.451×10^{-1}	mmHg s/ml
	C	7.758×10^{-2}	ml/mmHg
LBV	R	1.653×10^{-1}	mmHg s/ml
	C	2.039	ml/mmHg
CA1	R	1.067×10^{1}	mmHg s/ml
	C	1.944×10^{-3}	ml/mmHg
CA2	R	1.067×10^{1}	mmHg s/ml
	C	5.183×10^{-3}	ml/mmHg
CB	R	2.135×10^{1}	mmHg s/ml
	C	7.774×10^{-3}	ml/mmHg
CV	R	1.067×10^{1}	mmHg s/ml
	C	5.000×10^{-3}	ml/mmHg

Table B.2: Figure 2.11 heart parameters values. $\hat{R}_{\text{tric}}$ and $\hat{R}_{\text{ao}}$ are non-linear resistances modeling the tricuspid and aortic valves, respectively. R_{asd} is atrial septal defect resistance (resistance between left and right atria). Depending on the type of BC imposed on AA, C_{ao} (for Neumann BC, Chapters 2 and 7) or L_{ao} is used (for Dirichlet BC, Chapters 8 and 9), Continued.

Block	Parameter	Value	Unit
LA/RA	R_{asd}	1.000×10^{-3}	mmHg s/ml
	E_{a}	7.350	mmHg/ml
	V_{a_u}	1.000	ml
	P_{a_0}	1.700×10^{-1}	mmHg
	K_{a}	4.840×10^{-1}	1/ml
SV	$\hat{R}_{\text{tric}}$	4.000×10^{-5}	mmHg s^2/ml^2
	E_{v_1}	1.850×10^{1}	mmHg/ml
	E_{v_2}	-4.200×10^{-2}	mmHg/ml^2
	V_{v_u}	4.000	ml
	P_{v_0}	9.000×10^{-1}	mmHg
	K_{v}	6.200×10^{-2}	1/ml
AA	$\hat{R}_{\text{ao}}$	4.000×10^{-4}	mmHg s^2/ml^2
	R_{sv}	9.000×10^{-2}	mmHg s/ml
	C_{ao}	4.156×10^{-2}	ml/mmHg
	L_{ao}	1.155×10^{-2}	mmHg s^2/ml

Appendix C

Calculation of Oxygen Delivery

Let V_{O_2}, $V_{O_2}^{lb}$, and $V_{O_2}^{ub}$, be the total, lower body, and upper body oxygen consumption, and C_{p}, C_{ao}, C_{ivc}, and C_{svc} be the oxygen concentration in pulmonary vein, aorta, IVC and SVC, respectively. We define,

$$r = \frac{V_{O_2\,\mathrm{lb}}}{V_{O_2}}, \tag{C.1}$$

hence,

$$V_{O_2\,\mathrm{ub}} = (1 - r)V_{O_2}. \tag{C.2}$$

By definition the oxygen delivery is,

$$OD = C_{\mathrm{ao}}Q_{\mathrm{s}}. \tag{C.3}$$

From the conservation of oxygen [183],

$$V_{O_2\,\mathrm{ub}} = Q_{\mathrm{ub}}\left(C_{\mathrm{ao}} - C_{\mathrm{svc}}\right), \tag{C.4}$$

that is true for all the studied anatomies. From Equations (C.2) and (C.4),

$$C_{\mathrm{svc}} = C_{\mathrm{ao}} - (1 - r)\frac{V_{O_2}}{Q_{\mathrm{ub}}}, \tag{C.5}$$

Considering a saturation of 98% for pulmonary veins and based on typical clinical data obtained from catheterization exams [16], the C_{p} and V_{O_2} are set to 0.22 mL_{O_2}/mL and 0.874 mL_{O_2}/s, respectively. We assume half of the total oxygen is consumed by the upper body, i.e. $r = 0.5$.

C.1 MBTS

Considering the conservation of oxygen in MBTS anatomy,

$$V_{O_2} = Q_p \left(C_p - C_{ao}\right), \tag{C.6}$$

From Equations (C.3) and (C.6),

$$OD = Q_s C_p - \frac{Q_s}{Q_p} V_{O_2}, \tag{C.7}$$

C.2 Glenn

Considering the conservation of oxygen in BGLN anatomy,

$$V_{O_2} = Q_p \left(C_p - C_{svc}\right). \tag{C.8}$$

In the BGLN anatomy, Q_p is equal to Q_{ub}, hence from Equations (C.5) and (C.8),

$$C_{ao} = C_p - r\frac{V_{O_2}}{Q_p}. \tag{C.9}$$

From Equations (C.3) and (C.9),

$$OD = Q_s C_p - r\frac{Q_s}{Q_p} V_{O_2}. \tag{C.10}$$

C.3 ABG

Considering the conservation of oxygen in ABG anatomy,

$$V_{O_2} = \left(Q_p - Q_{ub}\right)\left(C_p - C_{ao}\right) + Q_{ub}\left(C_p - C_{svc}\right). \tag{C.11}$$

Substituting for C_{svc} from Equation (C.5),

$$C_{ao} = C_p - r\frac{V_{O_2}}{Q_p}. \tag{C.12}$$

Using Equations (C.3) and (C.12),

$$OD = Q_s C_p - r\frac{Q_s}{Q_p} V_{O_2}, \tag{C.13}$$

that is identical to BGLN result.

Oxygen delivery of MBTS, BGLN, and ABG only depends on Q_{p} and Q_{s} (beside constant variables C_{p}, $V_{\mathrm{O_2}}$, and r). Systemic flow rate is sum of upper and lower body flow rates, i.e. $Q_{\mathrm{s}} = Q_{\mathrm{ub}} + Q_{\mathrm{lb}}$, which can be calculated after simulations. Since the second term in right hand side of Equations (C.10) and (C.13) are multiplied by r (that is less than one) as comparing to Equation (C.7), at the same systemic and pulmonary flow rates, MBTS has always lower oxygen delivery compared to the ABG and BGLN.

Note that to obtain oxygen delivery to a particular part of the body, flow rate to that part is multiplied by C_{ao} instead of Q_{s}. For example coronary oxygen delivery for ABG is,

$$OD_{\mathrm{cor}} = Q_{\mathrm{cor}} C_{\mathrm{p}} - r \frac{Q_{\mathrm{cor}}}{Q_{\mathrm{p}}} V_{\mathrm{O_2}}, \tag{C.14}$$

Appendix D

Calculation of Hemodynamic Indices

D.1 WSS

WSS is calculated directly from velocity, using

$$\boldsymbol{\sigma}(\boldsymbol{x},t) = \mu(\nabla \boldsymbol{u} + \nabla \boldsymbol{u}^T), \quad \boldsymbol{x} \in \Omega, \tag{D.1}$$

$$\boldsymbol{\tau}_{\mathrm{e}}(\boldsymbol{x},t) = \boldsymbol{\sigma}\boldsymbol{n} - (\boldsymbol{n}^T\boldsymbol{\sigma}\boldsymbol{n})\boldsymbol{n}, \quad \boldsymbol{x} \in \Gamma, \tag{D.2}$$

where μ, $\boldsymbol{\sigma}(\boldsymbol{x},t)$, $\boldsymbol{n}(\boldsymbol{x})$, and $\boldsymbol{\tau}_{\mathrm{e}}(\boldsymbol{x},t)$ are fluid viscosity, stress tensor, outward normal vector to wall, and tangential traction vector exerted on the wall at each element. The following function maps the traction to the nodes

$$\boldsymbol{\tau}(\boldsymbol{x},t) = \mathcal{F}(\boldsymbol{\tau}_{\mathrm{e}}), \quad \boldsymbol{x} \in \Gamma, \tag{D.3}$$

where $\mathcal{F}(\boldsymbol{s}(\boldsymbol{x},t)) \in \mathbb{R}^m$, $\boldsymbol{s}(\boldsymbol{x},t) \in \mathbb{R}^m$, is found such that for any test function $\boldsymbol{w}(\boldsymbol{x},t) \in \mathbb{R}^m$ the following holds:

$$\int_\Gamma \boldsymbol{w} \cdot \mathcal{F} \, \mathrm{d}\Gamma = \int_\Gamma \boldsymbol{w} \cdot \boldsymbol{s} \, \mathrm{d}\Gamma. \tag{D.4}$$

Equation (D.4) is a least squares problem which produces a linear system of equations with a mass matrix on the left hand side. Calculating traction directly

from velocity, as described above, requires less mesh refinement to produce mesh-independent results compared to using the traction obtained from the residual vector of the discretized Navier-Stokes equations, as described in [184].

Time averaged WSS($\boldsymbol{x}$) is defined from the traction obtained from Equation (D.3) using

$$\mathrm{WSS}(\boldsymbol{x}) = \frac{1}{\mathrm{T}} \int_{\mathrm{t_0}}^{\mathrm{t_0+T}} \|\boldsymbol{\tau}\| \ \mathrm{dt}, \quad \boldsymbol{x} \in \Gamma. \tag{D.5}$$

D.2 WSSG

The unit vectors tangential, $\boldsymbol{s}_1$, and orthogonal, $\boldsymbol{s}_2$, to the time averaged WSS vector defined at each element, are

$$\begin{aligned} \boldsymbol{s}_1 &= \frac{\int_{t_0}^{t_0+T} \boldsymbol{\tau}_\mathrm{e} \ \mathrm{dt}}{\left\| \int_{t_0}^{t_0+T} \boldsymbol{\tau}_\mathrm{e} \ \mathrm{dt} \right\|}, \\ \boldsymbol{s}_2 &= \boldsymbol{s}_1 \times \boldsymbol{n}. \end{aligned} \tag{D.6}$$

The approach for finding the WSS gradient is similar to that of WSS. However, for bilinear shape functions, the second derivative of velocity is zero inside the elements. Therefore the traction components obtained from Equation (D.2) are decomposed into tangential and orthogonal directions, and then mapped to the nodes using

$$\begin{aligned} \tau_{\mathrm{s_1}}(\boldsymbol{x}, t) &= \mathcal{F}(\boldsymbol{\tau}_\mathrm{e} \cdot \boldsymbol{s}_1), \quad \boldsymbol{x} \in \Gamma, \\ \tau_{\mathrm{s_2}}(\boldsymbol{x}, t) &= \mathcal{F}(\boldsymbol{\tau}_\mathrm{e} \cdot \boldsymbol{s}_2), \quad \boldsymbol{x} \in \Gamma. \end{aligned} \tag{D.7}$$

The time averaged WSSG($\boldsymbol{x}$) is then calculated as

$$\mathrm{WSSG}(\boldsymbol{x}) = \frac{1}{\mathrm{T}} \mathcal{F} \left(\int_{\mathrm{t_0}}^{\mathrm{t_0+T}} \sqrt{\left(\boldsymbol{s}_1 \cdot \nabla \tau_{\mathrm{s_1}}\right)^2 + \left(\boldsymbol{s}_2 \cdot \nabla \tau_{\mathrm{s_2}}\right)^2} \ \mathrm{dt} \right), \quad \boldsymbol{x} \in \Gamma. \tag{D.8}$$

D.3 OSI

OSI($\boldsymbol{x}$) is directly calculated from the nodal traction [185, 186] as

$$\mathrm{OSI}(\boldsymbol{x}) = \frac{1}{2} \left(1 - \frac{\left\| \int_{\mathrm{t_0}}^{\mathrm{t_0+T}} \boldsymbol{\tau} \ \mathrm{dt} \right\|}{\int_{\mathrm{t_0}}^{\mathrm{t_0+T}} \|\boldsymbol{\tau}\| \ \mathrm{dt}} \right), \quad \boldsymbol{x} \in \Gamma. \tag{D.9}$$

Bibliography

[1] F. Migliavacca, G. Pennati, E. D. Martino, G. Dubini, R. Pietrabissa, Pressure drops in a distensible model of end-to-side anastomosis in systemic-to-pulmonary shunts, Computer Methods in Biomechanics and Biomedical Engineering 5 (3) (2002) 243–248.

[2] A. Blalock, H. B. Taussig, The surgical treatment of malformations of the heart, Journal of the American Medical Association 128 (3) (1945) 189–202.

[3] M. Canfield, M. Honein, N. Yuskiv, J. Xing, C. Mai, J. Collins, O. Devine, J. Petrini, T. Ramadhani, C. Hobbs, R. Kirby, National estimates and race/ethnic-specific variation of selected birth defects in the united states, 1999-2001, Birth Defects Research Part A: Clinical and Molecular Teratology 76 (11) (2006) 747–756.

[4] J. Tikkanen, O. Heinonen, Risk factors for hypoplastic left heart syndrome, Teratology 50 (2) (1994) 112–117.

[5] W. Norwood, J. Kirklin, S. Sanders, Hypoplastic left heart syndrome: Experience with palliative surgery, The American Journal of Cardiology 45 (1) (1980) 87–91.

[6] W. Norwood, P. Lang, A. Castaneda, D. Campbell, Experience with operations for hypoplastic left heart syndrome, The Journal of Thoracic and Cardiovascular Surgery 82 (1981) 511–519.

[7] D. Tamisier, P. Vouhe, F. Vernant, F. Leca, C. Massot, J. Neveux, Modified blalock-taussig shunts: Results in infants less than 3 months of age, Ann Thorac Surg 49 (1990) 797–801.

[8] W. W. Glenn, Circulatory bypass of the right side of the heart: shunt between superior vena cava and distal right pulmonary arteryreport of clinical application, New England Journal of Medicine 259 (3) (1958) 117–120.

[9] F. Fontan, E. Baudet, Surgical repair of tricuspid atresia, Thorax 26 (3) (1971) 240–248.

[10] W. Norwood, M. Jacobs, J. Murphy, Fontan procedure for hypoplastic left heart syndrome, Ann Thorac Surg 54 (1992) 1025–1030.

[11] G. B. Shachar, B. P. Fuhrman, Y. Wang, R. Lucas, J. E. Lock, Rest and exercise hemodynamics after the fontan procedure., Circulation 65 (6) (1982) 1043–1048.

[12] J. W. Gaynor, W. T. Mahle, M. I. Cohen, R. F. Ittenbach, W. M. DeCampli, J. M. Steven, S. C. Nicolson, T. L. Spray, Risk factors for mortality after the norwood procedure, European journal of cardio-thoracic surgery 22 (1) (2002) 82–89.

[13] R. Wong, V. Baum, S. Sangwan, Truncus arteriosus: Recognition and therapy of intraoperative cardiac ischemia, Anesthesiology 74 (2) (1991) 378–380.

[14] U. Bartram, J. Grnenfelder, R. V. Praagh, Causes of death after the modified Norwood procedure: A study of 122 postmortem cases, The Annals of Thoracic Surgery 64 (6) (1997) 1795–1802.

[15] J. Tweddell, N. Ghanayem, K. Mussatto, M. Mitchell, L. Lamers, N. Musa, S. Berger, S. B. Litwin, G. Hoffman, Mixed venous oxygen saturation monitoring after stage 1 palliation for hypoplastic left heart syndrome, The Annals of Thoracic Surgery 84 (4) (2007) 1301–1311.

[16] F. Migliavacca, G. Pennati, G. Dubini, R. Fumero, R. Pietrabissa, G. Urcelay, E. Bove, T. Hsia, M. de Leval, Modeling of the Norwood circulation: effects of shunt size, vascular resistances, and heart rate, American Journal of Physiology-Heart and Circulatory Physiology 280 (2001) H2076–H2086.

[17] C. Taylor, C. Figueroa, Patient-specific modeling of cardiovascular mechanics, Annual Review of Biomedical Engineering 11 (2009) 109–134.

[18] C. Taylor, D. Steinman, Image-based modeling of blood flow and vessel wall dynamics: applications, methods and future directions, Ann Biomed Eng 38 (2010) 1188–1203.

[19] G. Pennati, F. Migliavacca, G. Dubini, E. Bove, Modeling of systemic-to-pulmonary shunts in newborns with a univentricular circulation: State of the art and future directions, Progress in Pediatric Cardiology 30 (1-2) (2010) 23–29.

[20] I. Vignon-Clementel, A. Marsden, J. Feinstein, A primer on computational simulation in congenital heart disease for the clinician, Progress in Pediatric Cardiology 30 (2010) 3–13.

[21] F. Migliavacca, G. Dubini, G. Pennati, R. Pietrabissa, R. Fumero, T. Hsia, M. de Leval, Computational model of the fluid dynamics in systemic-to-pulmonary shunts, Journal of Biomechanics 33 (5) (2000) 549–557.

[22] J. Waniewski, W. Kurowska, J. Mizerski, A. Trykozko, K. Nowiski, G. Brzeziska-Rajszys, A. Kociesza, The effects of graft geometry on the patency of a systemic-to-pulmonary shunt: A computational fluid dynamics study, Artificial Organs 29 (2005) 642–650.

[23] G. Pennati, G. B. Fiore, F. Migliavacca, K. Lagan, R. Fumero, G. Dubini, In vitro steady-flow analysis of systemic-to-pulmonary shunt haemodynamics, Journal of Biomechanics 34 (1) (2001) 23–30.

[24] G. Pennati, F. Migliavacca, F. Gervaso, G. Dubini, Assessment by computational and in vitro studies of the blood flow rate through modified Blalock-Taussig shunts, Cardiology in the Young 14 (2004) 24–29.

[25] K. Lagana, R. Balossino, F. Migliavacca, G. Pennati, E. Bove, M. de Leval, G. Dubini, Multiscale modeling of the cardiovascular system: application to the study of pulmonary and coronary perfusions in the univentricular circulation, Journal of Biomechanics 38 (5) (2005) 1129–1141.

[26] F. Migliavacca, R. Balossino, G. Pennati, G. Dubini, T. Hsia, M. de Leval, E. Bove, Multiscale modelling in biofluiddynamics: Application to reconstructive paediatric cardiac surgery, Journal of Biomechanics 39 (6) (2006) 1010–1020.

[27] H. Kim, C. Figueroa, T. Hughes, K. Jansen, C. Taylor, Augmented lagrangian method for constraining the shape of velocity profiles at outlet boundaries for three-dimensional finite element simulations of blood flow, Computer Methods in Applied Mechanics and Engineering 198 (45-46) (2009) 3551–3566.

[28] C. Taylor, C. Cheng, L. Espinosa, B. Tang, D. Parker, R. Herfkens, In vivo quantification of blood flow and wall shear stress in the human abdominal aorta during lower limb exercise, Annals of Biomedical Engineering 30 (2002) 402–408.

[29] I. Vignon-Clementel, C. Figueroa, K. Jansen, C. Taylor, Outflow boundary conditions for three-dimensional simulations of non-periodic blood flow and pressure fields in deformable arteries, Computer Methods in Biomechanics and Biomedical Engineering 13 (5) (2010) 625–640.

[30] Y. Bazilevs, J. Gohean, T. Hughes, R. Moser, Y. Zhang, Patient-specific isogeometric fluid-structure interaction analysis of thoracic aortic blood flow

due to implantation of the Jarvik 2000 left ventricular assist device, Computer Methods in Applied Mechanics and Engineering 198 (45-46) (2009) 3534–3550.

[31] W. Yang, A. Jeffrey, A. Marsden, Constrained optimization of an idealized Y-shaped baffle for the Fontan surgery at rest and exercise, Computer Methods in Applied Mechanics and Engineering 199 (33-36) (2010) 2135–2149.

[32] A. Marsden, J. Feinstein, C. Taylor, A computational framework for derivative-free optimization of cardiovascular geometries, Computer Methods in Applied Mechanics and Engineering 197 (21-24) (2008) 1890–1905.

[33] M. Esmaily-Moghadam, I. Vignon-Clementel, R. Figliola, A. Marsden, A modular numerical method for implicit 0D/3D coupling in cardiovascular finite element simulations, Journal of Computational Physics 224 (2013) 63–79.

[34] D. J. Kuck, E. S. Davidson, D. H. Lawrie, A. H. Sameh, Parallel supercomputing today and the cedar approach, Science 231 (4741) (1986) 967–974.

[35] E. Polizzi, A. H. Sameh, A parallel hybrid banded system solver: the SPIKE algorithm, Parallel computing 32 (2) (2006) 177–194.

[36] A. H. Sameh, D. J. Kuck, On stable parallel linear system solvers, Journal of the ACM (JACM) 25 (1) (1978) 81–91.

[37] D. Bluestein, L. Niu, R. Schoephoerster, M. Dewanjee, Fluid mechanics of arterial stenosis: Relationship to the development of mural thrombus, Annals of Biomedical Engineering 25 (1997) 344–356.

[38] A. Reininger, C. Reininger, U. Heinzmann, L. Wurzinger, Residence time in niches of stagnant flow determines fibrin clot formation in an arterial branching model–detailed flow analysis and experimental results, Thrombosis and Haemostasis 74 (1995) 916–922.

[39] M. Kunov, D. Steinman, C. Ethier, Particle volumetric residence time calculations in arterial geometries, J Biomech Eng. 118 (1996) 158–164.

[40] G. Suh, A. Les, A. Tenforde, S. Shadden, R. Spilker, J. Yeung, C. Cheng, R. Herfkens, R. Dalman, C. Taylor, Quantification of particle residence time in abdominal aortic aneurysms using magnetic resonance imaging and computational fluid dynamics, Annals of Biomedical Engineering 39 (2011) 864–883.

[41] D. Sengupta, A. Kahn, J. Burns, S. Sankaran, S. Shadden, A. Marsden, Image-based modeling of hemodynamics in coronary artery aneurysms

caused by Kawasaki disease, Biomechanics and Modeling in Mechanobiology 11 (2012) 915–932.

[42] A. Lonyai, A. Dubin, J. Feinstein, C. Taylor, S. Shadden, New insights into pacemaker lead-induced venous occlusion: Simulation-based investigation of alterations in venous biomechanics, Cardiovascular Engineering 10 (2010) 84–90.

[43] T. Gundert, S. Shadden, A. Williams, B.-K. Koo, J. Feinstein, J. LaDisa, A rapid and computationally inexpensive method to virtually implant current and next-generation stents into subject-specific computational fluid dynamics models, Annals of Biomedical Engineering 39 (2011) 1423–1437.

[44] A. Corno, E. Mazzera, B. Marino, F. Parisi, C. Marcelletti, Simultaneous patency of ductus arteriosus and surgical shunt in pulmonary atresia with intact ventricular septum: A cause of acute myocardial failure?, Scandinavian Cardiovascular Journal 20 (2) (1986) 123–127.

[45] M. Zahorec, Z. Hrubsova, P. Skrak, R. Poruban, M. Nosal, L. Kovacikova, A comparison of Blalock-Taussig shunts with and without closure of the ductus arteriosus in neonates with pulmonary atresia, The Annals of thoracic surgery 92 (2) (2011) 653–658.

[46] N. Westerhof, F. Bosman, C. D. Vries, A. Noordergraaf, Analog studies of the human systemic arterial tree, Journal of Biomechanics 2 (2) (1969) 121–143.

[47] L. Formaggia, J. Gerbeau, F. Nobile, A. Quarteroni, Numerical treatment of defective boundary conditions for the Navier-Stokes equations, SIAM Journal on Numerical Analysis 40 (2002) 376–401.

[48] A. Quarteroni, A. Veneziani, Analysis of a geometrical multiscale model based on the coupling of ODEs and PDEs for blood flow simulations, Multiscale Model Simul. 1 (2) (2003) 173–195.

[49] I. Vignon-Clementel, C. Figueroa, K. Jansen, C. Taylor, Outflow boundary conditions for three-dimensional finite element modeling of blood flow and pressure in arteries, Computer Methods in Applied Mechanics and Engineering 195 (29-32) (2006) 3776–3796.

[50] H. Kim, I. Vignon-Clementel, C. Figueroa, J. Ladisa, K. Jansen, J. Feinstein, C. Taylor, On coupling a lumped parameter heart model and a three-dimensional finite element aorta model, Annu. Rev. Biomed. Eng. 37 (2009) 2153–2169.

[51] H. Kim, I. Vignon-Clementel, J. Coogan, C. Figueroa, K. Jansen, C. Taylor, Patient-specific modeling of blood flow and pressure in human coronary arteries, Annals of Biomedical Engineering 38 (2010) 3195–3209.

[52] C. Bertoglio, A. Caiazzo, M. Fenandez, Fractional-step schemes for the coupling of distributed and lumped models in hemodynamics, Research Report RR-7937, INRIA (Apr. 2012).
URL http://hal.inria.fr/hal-00690493

[53] S. Urquiza, P. Blanco, M. Venere, R. Feijoo, Multidimensional modelling for the carotid artery blood flow, Computer Methods in Applied Mechanics and Engineering 195 (33-36) (2006) 4002–4017.

[54] P. Blanco, R. Feijoo, S. Urquiza, A unified variational approach for coupling 3D-1D models and its blood flow applications, Computer Methods in Applied Mechanics and Engineering 196 (41-44) (2007) 4391–4410.

[55] A. Quarteroni, S. Ragni, A. Veneziani, Coupling between lumped and distributed models for blood flow problems, Computing and Visualization in Science 4 (2001) 111–124.

[56] J. Leiva, P. Blanco, G. Buscaglia, Iterative strong coupling of dimensionally-heterogeneous models, Int J Num Meth Engng 81 (12) (2010) 1558–1580.

[57] A. Malossi, P. Blanco, S. Deparis, A. Quarteroni, Algorithms for the partitioned solution of weakly coupled fluid models for cardiovascular flows, Int. J. Numer. Meth. Biomed. Engng. 27 (12) (2011) 2035–2057.

[58] D. Johnson, P. Naik, A. Beris, Efficient implementation of the proper outlet flow conditions in blood flow simulations through asymmetric arterial bifurcations, International Journal for Numerical Methods in Fluids 66 (11) (2011) 1383–1408.

[59] M. Esmaily-Moghadam, Y. Bazilevs, T. Hsia, I. Vignon-Clementel, A. Marsden, A comparison of outlet boundary treatments for prevention of backflow divergence with relevance to blood flow simulations, Computational Mechanics 48 (3) (2011) 277–291.

[60] A. Zupani Valant, L. iberna, Y. Papaharilaou, A. Anayiotos, G. Georgiou, The influence of temperature on rheological properties of blood mixtures with different volume expandersimplications in numerical arterial hemodynamics simulations, Rheologica Acta 50 (4) (2011) 389–402.

[61] I. Babuska, Error-bounds for finite element method, Numerische Mathematik 16 (4) (1971) 322–333.

[62] F. Brezzi, On the existence, uniqueness and approximation of saddle-point problems arising from lagrangian multipliers, ESAIM: Mathematical Modelling and Numerical Analysis-Modélisation Mathématique et Analyse Numérique 8 (R2) (1974) 129–151.

[63] C. Whiting, K. Jansen, A stabilized finite element method for the incompressible Navier-Stokes equations using a hierarchical basis, International Journal for Numerical Methods in Fluids 35 (1) (2001) 93–116.

[64] L. Franca, S. Frey, Stabilized finite element methods: II. the incompressible Navier-Stokes equations, Computer Methods in Applied Mechanics and Engineering 99 (2-3) (1992) 209–233.

[65] A. Brooks, T. Hughes, Streamline upwind/Petrov-Galerkin formulations for convection dominated flows with particular emphasis on the incompressible Navier-Stokes equations, Computer Methods in Applied Mechanics and Engineering 32 (1-3) (1982) 199–259.

[66] Y. Bazilevs, V. Calo, J. Cottrell, T. Hughes, A. Reali, G. Scovazzi, Variational multiscale residual-based turbulence modeling for large eddy simulation of incompressible flows, Computer Methods in Applied Mechanics and Engineering 197 (1-4) (2007) 173–201.

[67] K. Jansen, C. Whiting, G. Hulbert, A generalized-[alpha] method for integrating the filtered Navier-Stokes equations with a stabilized finite element method, Computer Methods in Applied Mechanics and Engineering 190 (3-4) (2000) 305–319.

[68] P. Kundu, I. Cohen, Fluid Mechanics, 4th Edition, Academic press, 2008.

[69] D. de Zelicourt, L. Ge, C. Wang, F. Sotiropoulos, A. Gilmanov, A. Yoganathan, Flow simulations in arbitrarily complex cardiovascular anatomies-an unstructured cartesian grid approach, Computers and Fluids 38 (9) (2009) 1749–1762.

[70] J. Schmidt, S. Delp, M. Sherman, C. Taylor, V. Pande, R. Altman, The simbios national center: Systems biology in motion, Proceedings of the IEEE, special issue on Computational System Biology 96 (8) (2008) 1266–1280.

[71] K. Jansen, Parallel hierarchic adaptive stabilized transient analysis (phasta).

[72] E. Kung, A. Les, C. Figueroa, F. Medina, K. Arcaute, R. Wicker, M. McConnell, C. Taylor, In vitro validation of finite element analysis of blood flow in deformable models, Annals of Biomedical Engineering 39 (2011) 1947–1960.

[73] Multi-physics finite element solver (mupfes) (May 2014).
URL https://sites.google.com/site/memt63/MUPFES

[74] D. A. Steinman, Y. Hoi, P. Fahy, L. Morris, M. T. Walsh, N. Aristokleous, A. S. Anayiotos, Y. Papaharilaou, A. Arzani, S. C. Shadden, P. Berg,

G. Janiga, J. Bols, P. Segers, N. Bressloff, M. Cibis, F. Gijsen, S. Cito, J. Pallares, L. Browne, J. Costelloe, A. Lynch, J. Degroote, J. Vierendeels, W. Fu, A. Qiao, S. Hodis, D. Kallmes, H. Kalsi, Q. Long, V. Kheyfets, E. Finol, K. Kono, A. Malek, A. Lauric, P. Menon, K. Pekkan, M. Esmaily-Moghadam, A. Marsden, M. Oshima, K. Katagiri, V. Peiffer, Y. Mohamied, S. Sherwin, J. Schaller, L. Goubergrits, G. Usera, M. Mendina, K. Valen-Sendstad, D. Habets, J. Xiang, H. Meng, Y. Yu, G. Karniadakis, N. Shaffer, F. Loth, Variability of computational fluid dynamics solutions for pressure and flow in a giant aneurysm: the ASME 2012 summer bioengineering conference CFD challenge, Journal of biomechanical engineering 135 (2) (2013) 021016.

[75] J. Lee, M. Esmaily-Moghadam, E. Kung, H. Cao, T. Beebe, Y. Miller, B. L. Roman, C.-L. Lien, N. C. Chi, A. L. Marsden, K. H. Tzung, Moving domain computational fluid dynamics to interface with an embryonic model of cardiac morphogenesis, PloS one 8 (8) (2013) e72924.

[76] C. Long, M. Esmaily-Moghadam, A. Marsden, Y. Bazilevs, Computation of residence time in the simulation of pulsatile ventricular assist devices, Computational Mechanics (2013) 1–9doi:10.1007/s00466-013-0931-y.

[77] D. Sengupta, A. Kahn, E. Kung, M. Esmaily-Moghadam, O. Shirinsky, G. Lyskina, J. Burns, A. Marsden, Thrombotic risk stratification using computational modeling in patients with coronary artery aneurysms following Kawasaki disease, Biomechanics and Modeling in Mechanobiology (2014) 1–16doi:10.1007/s10237-014-0570-z.

[78] S. Sankaran, M. Esmaily-Moghadam, A. Kahn, E. Tseng, J. Guccione, A. Marsden, Patient-specific multiscale modeling of blood flow for coronary artery bypass graft surgery, Annals of Biomedical Engineering 40 (2012) 2228–2242.

[79] A. Baretta, C. Corsini, W. Yang, I. Vignon-Clementel, A. Marsden, J. Feinstein, T. Hsia, G. Dubini, F. Migliavacca, G. Pennati, MOCHA, Virtual surgeries in patients with congenital heart disease: a multi-scale modelling test case, Philos Transact A Math Phys Eng Sci 369 (1954) (2011) 4316–4330.

[80] M. Esmaily-Moghadam, F. Migliavacca, I. Vignon-Clementel, T. Hsia, A. Marsden, Optimization of shunt placement for the Norwood surgery using multi-domain modeling, Journal of Biomechanical Engineering 134 (5) (2012) 051002.

[81] M. Olufsen, H. Tran, J. Ottesen, R. Program, L. Lipsitz, V. Novak, Modeling baroreflex regulation of heart rate during orthostatic stress, Am J Physiol Regul Integr Comp Physiol. 291 (5) (2006) R1355–R1368.

[82] S. Pope, L. Ellwein, C. Zapata, V. Novak, M. Kelley, M. Olufsen, Estimation and identification of parameters in a lumped cerebrovascular model, Mathematical Biosciences Engineering 6 (1) (2009) 93–115.

[83] G. Troianowski, C. Taylor, J. Feinstein, I. Vignon-Clementel, Three-dimensional simulations in glenn patients: clinically based boundary conditions, hemodynamic results and sensitivity to input data, Journal of Biomechanical Engineering 133 (11) (2011) 111006.

[84] G. Pennati, C. Corsini, D. Cosentino, T. Hsia, V. Luisi, G. Dubini, F. Migliavacca, Boundary conditions of patient-specific fluid dynamics modelling of cavopulmonary connections: possible adaptation of pulmonary resistances results in a critical issue for a virtual surgical planning, Interface Focus 1 (2011) 297–307.

[85] C. Bertoglio, P. Moireau, J. Gerbeau, Sequential parameter estimation for fluidstructure problems: Application to hemodynamics, Int. J. Num. Meth. Biomed. Engn. 28 (4) (2012) 434–455.

[86] E. Bove, F. Migliavacca, M. de Leval, R. Balossino, G. Pennati, T. Lloyd, S. Khambadkone, T. Hsia, G. Dubini, Use of mathematic modeling to compare and predict hemodynamic effects of the modified Blalock-Taussig and right ventricle-pulmonary artery shunts for hypoplastic left heart syndrome, The Journal of Thoracic and Cardiovascular Surgery 136 (2) (2008) 312–320.e2.

[87] K. Lagana, G. Dubini, F. Migliavacca, R. Pietrabissa, G. Pennati, A. Veneziani, A. Quarteroni, Multiscale modelling as a tool to prescribe realistic boundary conditions for the study of surgical procedures, Biorheology 39 (2002) 359–364.

[88] J. Heywood, R. Rannacher, S. Turek, Artificial boundaries and flux and pressure conditions for the incompressible Navier-Stokes equations, International Journal for Numerical Methods in Fluids 22 (5) (1996) 325–352.

[89] L. Formaggia, A. Veneziani, C. Vergara, A new approach to numerical solution of defective boundary valve problems in incompressible fluid dynamics, SIAM Journal on Numerical Analysis 46 (6) (2008) 2769–2794.

[90] A. Marsden, I. Vignon-Clementel, F. Chan, J. Feinstein, C. Taylor, Effects of exercise and respiration on hemodynamic efficiency in CFD simulations of the total cavopulmonary connection, Annals of Biomedical Engineering 35 (2007) 250–263.

[91] K. Pekkan, L. Dasi, P. Nourparvar, S. Yerneni, K. Tobita, M. Fogel, B. Keller, A. Yoganathan, In vitro hemodynamic investigation of the embryonic aortic arch at late gestation, Journal of Biomechanics 41 (8) (2008) 1697 – 1706.

[92] K. Pekkan, O. Dur, K. Sundareswaran, K. Kanter, M. Fogel, A. Yoganathan, A. Undar, Neonatal aortic arch hemodynamics and perfusion during cardiopulmonary bypass, Journal of Biomechanical Engineering 130 (6) (2008) 061012.

[93] T. Tezduyar, S. Ramakrishnan, S. Sathe, Stabilized formulations for incompressible flows with thermal coupling, International Journal for Numerical Methods in Fluids 57 (2008) 1189–1209.

[94] T. Tezduyar, K. Takizawa, C. Moorman, S. Wright, J. Christopher, Space-time finite element computation of complex fluid-structure interactions, International Journal for Numerical Methods in Fluids 64 (2010) 1201–1218.

[95] I. Borazjani, L. Ge, F. Sotiropoulos, High-resolution fluidstructure interaction simulations of flow through a bi-leaflet mechanical heart valve in an anatomic aorta, Annals of Biomedical Engineering 38 (2010) 326–344.

[96] I. Vignon-Clementel, A coupled multidomain method for computational modeling of blood flow, Ph.D. thesis, Stanford (2006).

[97] P. Gresho, R. Sani, Incompressible Flow and the Finite Element Method, Vol. 2, Wiley, 2000.

[98] O. Sahni, J. Muller, K. Jansen, M. Shephard, C. Taylor, Efficient anisotropic adaptive discretization of the cardiovascular system, Computer Methods in Applied Mechanics and Engineering 195 (41-43) (2006) 5634 – 5655.

[99] Y. Bazilevs, V. Calo, Y. Zhang, T. Hughes, Isogeometric fluidstructure interaction analysis with applications to arterial blood flow, Computational Mechanics 38 (2006) 310–322.

[100] Y. Bazilevs, V. Calo, T. Hughes, Y. Zhang, Isogeometric fluid-structure interaction: theory, algorithms, and computations, Computational Mechanics 43 (2008) 3–37.

[101] K. Takizawa, C. Moorman, S. Wright, J. Purdue, T. McPhail, P. Chen, J. Warren, T. Tezduyar, Patient-specific arterial fluid-structure interaction modeling of cerebral aneurysms, International Journal for Numerical Methods in Fluids 65 (2011) 308–323.

[102] T. Tezduyar, K. Takizawa, T. Brummer, P. Chen, Space-time fluid-structure interaction modeling of patient-specific cerebral aneurysms, International Journal for Numerical Methods in Biomedical Engineering-doi:10.1002/cnm.1433.

[103] A. Kuprat, S. Kabilan, J. Carson, R. Corley, D. Einstein, A bidirectional coupling procedure applied to multiscale respiratory modeling, Journal of Computational Physics (2012) –doi:10.1016/j.jcp.2012.10.021.

[104] T. Tezduyar, J. Liou, Grouped element-by-element iteration schemes for incompressible flow computations, Computer Physics Communications 53 (1) (1989) 441–453.

[105] T. Tezduyar, M. Behr, S. Aliabadi, S. Mittal, S. Ray, A new mixed preconditioning method for finite element computations, Computer Methods in Applied Mechanics and Engineering 99 (1) (1992) 27–42.

[106] N. Nigro, M. Storti, S. Idelsohn, T. Tezduyar, Physics based GMRES preconditioner for compressible and incompressible Navier-Stokes equations, Computer Methods in Applied Mechanics and Engineering 154 (3) (1998) 203–228.

[107] T. E. Tezduyar, S. Sathe, Enhanced-approximation linear solution technique (EALST), Computer Methods in Applied Mechanics and Engineering 193 (21) (2004) 2033–2049.

[108] T. E. Tezduyar, S. Sathe, Enhanced-discretization successive update method (EDSUM), International Journal for Numerical Methods in Fluids 47 (6-7) (2005) 633–654.

[109] T. E. Tezduyar, A. Sameh, Parallel finite element computations in fluid mechanics, Computer Methods in Applied Mechanics and Engineering 195 (13) (2006) 1872–1884.

[110] T. Washio, T. Hisada, H. Watanabe, T. Tezduyar, A robust preconditioner for fluid–structure interaction problems, Computer Methods in Applied Mechanics and Engineering 194 (39) (2005) 4027–4047.

[111] T. E. Tezduyar, S. Sathe, Modelling of fluid-structure interactions with the space-time finite elements: solution techniques, International Journal for Numerical Methods in Fluids 54 (6-8) (2007) 855–900.

[112] M. Manguoglu, A. H. Sameh, F. Saied, T. E. Tezduyar, S. Sathe, Preconditioning techniques for nonsymmetric linear systems in the computation of incompressible flows, Journal of Applied Mechanics 76 (2) (2009) 021204.

[113] M. Manguoglu, K. Takizawa, A. H. Sameh, T. E. Tezduyar, A parallel sparse algorithm targeting arterial fluid mechanics computations, Computational Mechanics 48 (3) (2011) 377–384.

[114] M. Manguoglu, A. H. Sameh, T. E. Tezduyar, S. Sathe, A nested iterative scheme for computation of incompressible flows in long domains, Computational Mechanics 43 (1) (2008) 73–80.

[115] M. Manguoglu, K. Takizawa, A. H. Sameh, T. E. Tezduyar, Solution of linear systems in arterial fluid mechanics computations with boundary layer mesh refinement, Computational Mechanics 46 (1) (2010) 83–89.

[116] M. Manguoglu, K. Takizawa, A. H. Sameh, T. E. Tezduyar, Nested and parallel sparse algorithms for arterial fluid mechanics computations with boundary layer mesh refinement, International Journal for Numerical Methods in Fluids 65 (1-3) (2011) 135–149.

[117] Y. Saad, Iterative methods for sparse linear systems, SIAM, 2003.

[118] G. Carey, B.-N. Jiang, Nonlinear preconditioned conjugate gradient and least-squares finite elements, Computer Methods in Applied Mechanics and Engineering 62 (2) (1987) 145–154.

[119] P. Fischer, Projection techniques for iterative solution of Ax=b with successive right-hand sides, Computer Methods in Applied Mechanics and Engineering 163 (1) (1998) 193–204.

[120] Y. Saad, M. Schultz, GMRES: a generalized minimal residual algorithm for solving nonsymmetric linear systems, Tech. Rep. YALEU/DCS/RR-254, Department of Computer Science, Yale University (1983).

[121] F. Shakib, T. Hughes, Z. Johan, A multi-element group preconditioned GMRES algorithm for nonsymmetric systems arising in finite element analysis, Computer Methods in Applied Mechanics and Engineering 75 (1-3) (1989) 415–456.

[122] J. Sherman, W. Morrison, Adjustment of an inverse matrix corresponding to a change in one element of a given matrix, The Annals of Mathematical Statistics 21 (1) (1950) 124–127.

[123] S. Balay, J. Brown, K. Buschelman, V. Eijkhout, W. Gropp, D. Kaushik, M. Knepley, L. C. McInnes, B. Smith, H. Zhang, PETSc Users Manual Revision 3.4 (2013).

[124] M. Esmaily-Moghadam, Y. Bazilevs, A. Marsden, Low entropy data mapping for sparse iterative linear solvers, in: Proceedings of the Conference on Extreme Science and Engineering Discovery Environment: Gateway to Discovery, ACM, 2013, p. 2.

[125] M. R. Hestenes, E. Stiefel, Methods of conjugate gradients for solving linear systems, Journal of Research of the National Bureau of Standards 49 (1952) 409–436.

[126] M. Esmaily-Moghadam, Y. Bazilevs, A. L. Marsden, A new preconditioning technique for implicitly coupled multidomain simulations with applications to hemodynamics, Computational Mechanics 52 (5) (2013) 1141–1152.

[127] M. Esmaily-Moghadam, T.-Y. Hsia, A. Marsden, A non-discrete method for computation of residence time in fluid mechanics simulations, Physics of FluidsDoi:10.1063/1.4819142.

[128] kraken cray xt5 system specifications (oct 2013).
URL http://www.nics.tennessee.edu/computing-resources/kraken

[129] G. Karypis, V. Kumar, MeTis: Unstructured Graph Partitioning and Sparse Matrix Ordering System, Version 4.0, http://www.cs.umn.edu/ metis (2009).

[130] L. Rouleau, M. Farcas, J. Tardif, R. Mongrain, R. Leask, Endothelial cell morphologic response to asymmetric stenosis hemodynamics: Effects of spatial wall shear stress gradients, Journal of Biomechanical Engineering 132 (8) (2010) 081013.

[131] Z. Xu, N. Chen, M. Kamocka, E. Rosen, M. Alber, A multiscale model of thrombus development, Journal of The Royal Society Interface 5 (24) (2008) 705–722.

[132] H. Meng, Z. Wang, Y. Hoi, L. Gao, E. Metaxa, D. Swartz, J. Kolega, Complex hemodynamics at the apex of an arterial bifurcation induces vascular remodeling resembling cerebral aneurysm initiation, Stroke 38 (6) (2007) 1924–1931.

[133] V. Turitto, C. Hall, Mechanical factors affecting hemostasis and thrombosis, Thrombosis Research 92 (6, Supplement 2) (1998) S25–S31.

[134] P. Holme, U. Orvim, M. Hamers, N. Solum, F. Brosstad, R. Barstad, K. Sakariassen, Shear-induced platelet activation and platelet microparticle formation at blood flow conditions as in arteries with a severe stenosis, Arteriosclerosis, Thrombosis, and Vascular Biology 17 (4) (1997) 646–653.

[135] W. Yin, S. Shanmugavelayudam, D. Rubenstein, The effect of physiologically relevant dynamic shear stress on platelet and endothelial cell activation, Thrombosis Research 127 (3) (2011) 235–241.

[136] J. Jozsa, T. Kramer, Modelling residence time as advectiondiffusion with zero-order reaction kinetics, in: Proceedings of the Hydrodynamics 2000

Conference, International Association of Hydraulic Engineering and Research, 2000, pp. 23–27.

[137] J. Ortega, J. Hartman, J. Rodriguez, D. Maitland, Virtual treatment of basilar aneurysms using shape memory polymer foam, Annals of biomedical engineering 41 (4) (2013) 725–743.

[138] V. Rayz, L. Boussel, L. Ge, J. Leach, A. Martin, M. Lawton, C. McCulloch, D. Saloner, Flow residence time and regions of intraluminal thrombus deposition in intracranial aneurysms, Annals of Biomedical Engineering 38 (10) (2010) 3058–3069.

[139] A. Narracott, S. Smith, P. Lawford, H. Liu, R. Himeno, I. Wilkinson, P. Griffiths, R. Hose, Development and validation of models for the investigation of blood clotting in idealized stenoses and cerebral aneurysms, Journal of Artificial Organs 8 (2005) 56–62.

[140] T. Hughes, M. Mallet, M. Akira, A new finite element formulation for computational fluid dynamics: II. beyond SUPG, Computer Methods in Applied Mechanics and Engineering 54 (3) (1986) 341–355.

[141] T. Hughes, The finite element method: linear static and dynamic finite element analysis, Dover Publications, 2000.

[142] Y. Bazilevs, V. Calo, T. Tezduyar, T. Hughes, Yzβ discontinuity capturing for advection-dominated processes with application to arterial drug delivery, International Journal for Numerical Methods in Fluids 54 (6-8) (2007) 593–608.

[143] R. Steen, E. Evers, B. V. Hattum, W. Cofino, U. Brinkman, Net fluxes of pesticides from the scheldt estuary into the north sea: a model approach, Environmental Pollution 116 (1) (2002) 75–84.

[144] E. Delhez, A. Heemink, E. Deleersnijder, Residence time in a semi-enclosed domain from the solution of an adjoint problem, Estuarine, Coastal and Shelf Science 61 (4) (2004) 691–702.

[145] J. Newburger, M. Takahashi, M. Gerber, M. Gewitz, L. Tani, J. Burns, S. Shulman, A. Bolger, P. Ferrieri, R. Baltimore, W. Wilson, L. Baddour, M. Levison, T. Pallasch, D. Falace, K. Taubert, Diagnosis, treatment, and long-term management of Kawasaki disease, Circulation 110 (17) (2004) 2747–2771.

[146] J. Gordon, A. Kahn, J. Burns, When children with Kawasaki disease grow up: myocardial and vascular complications in adulthood, Journal of the American College of Cardiology 54 (21) (2009) 1911–1920.

[147] S. C. Shadden, F. Lekien, J. E. Marsden, Definition and properties of Lagrangian coherent structures from finite-time Lyapunov exponents in two-dimensional aperiodic flows, Physica D: Nonlinear Phenomena 212 (3) (2005) 271–304.

[148] F. Lekien, S. C. Shadden, J. E. Marsden, Lagrangian coherent structures in n-dimensional systems, Journal of Mathematical Physics 48 (2007) 065404.

[149] H. A. Himburg, D. M. Grzybowski, A. L. Hazel, J. A. LaMack, X.-M. Li, M. H. Friedman, Spatial comparison between wall shear stress measures and porcine arterial endothelial permeability, American Journal of Physiology-Heart and Circulatory Physiology 286 (5) (2004) H1916–H1922.

[150] D. Kersh, A. Liberzon, Relations of pulsatility index and particle residence time to the wall-shear-stress properties in pulsating flows with reverse flow phase, arXiv preprint arXiv:1303.3727 - (2013) –.

[151] D. Ashburn, B. McCrindle, C. Tchervenkov, M. Jacobs, G. Lofland, E. Bove, T. Spray, W. Williams, E. Blackstone, Outcomes after the Norwood operation in neonates with critical aortic stenosis or aortic valve atresia, The Journal of Thoracic and Cardiovascular Surgery 125 (5) (2003) 1070–1082.

[152] A. Quarteroni, G. Rozza, Optimal control and shape optimization of aorto-coronaric bypass anastomoses, Mathematical models and methods in applied sciences 12 (2003) 1801–1824.

[153] F. Abraham, M. Behr, M. Heinkenschloss, Shape optimization in steady blood flow: A numerical study of non-Newtonian effects, Computer Methods in Biomechanics and Biomedical Engineering 8 (2) (2005) 127–137.

[154] F. Abraham, M. Behr, M. Heinkenschloss, Shape optimization in unsteady blood flow: A numerical study of non-Newtonian effects, Computer Methods in Biomechanics and Biomedical Engineering 8 (3) (2005) 201–212.

[155] W. Burgreen, F. Antaki, Z. Wu, A. Holmes, Computational fluid dynamics as a development tool for rotary blood pumps, Artificial Organs 25 (5) (2001) 336–340.

[156] M. Abramson, C. Audet, J. Chrissis, J. Walston, Mesh adaptive direct search algorithms for mixed variable optimization, Optimization Letters 3 (1) (2009) 35–47.

[157] A. Marsden, M. Wang, J. Dennis, P. Moin, Optimal aeroacoustic shape design using the surrogate management framework, Optimization and Engineering 5 (2004) 235–262.

[158] A. Marsden, M. Wang, J. Dennis, P. Moin, suppression of vortex-shedding noise via derivative-free shape optimization, Physics of Fluids 16 (10) (2004) L83–L86.

[159] A. Booker, J. Dennis, P. Frank, D. Serafini, V. Torczon, M. Trosset, A rigorous framework for optimization of expensive functions by surrogates, Structural and Multidisciplinary Optimization 17 (1999) 1–13.

[160] C. Audet, J. Dennis, Mesh adaptive direct search algorithms for constrained optimization, Society for Industrial and Applied Mathematics Journal on Optimization 17 (2006) 188–217.

[161] M. Abramson, C. Audet, J. Dennis, S. Digabel, OrthoMADS: A deterministic MADS instance with orthogonal directions, Society for Industrial and Applied Mathematics Journal on Optimization 20 (2009) 948–966.

[162] G. A. Holzapfel, Nonlinear solid mechanics: a continuum approach for engineering, John Wiley & Sons Ltd., 2000.

[163] T. E. Tezduyar, S. Sathe, M. Schwaab, B. S. Conklin, Arterial fluid mechanics modeling with the stabilized space–time fluid–structure interaction technique, International Journal for Numerical Methods in Fluids 57 (5) (2008) 601–629.

[164] C. Long, M. Hsu, Y. Bazilevs, J. Feinstein, A. Marsden, Fluid-structure interaction simulations of the Fontan procedure using variable wall properties, Int. J. Numer. Meth. Biomed. Engng. 28 (2012) 513–527.

[165] J. S. Coogan, J. D. Humphrey, C. A. Figueroa, Computational simulations of hemodynamic changes within thoracic, coronary, and cerebral arteries following early wall remodeling in response to distal aortic coarctation, Biomechanics and modeling in mechanobiology 12 (1) (2013) 79–93.

[166] Y. Bazilevs, M. Hsu, D. Benson, S. Sankaran, A. Marsden, Computational fluidstructure interaction: methods and application to a total cavopulmonary connection, Computational Mechanics 45 (2009) 77–89.

[167] T. E. Tezduyar, S. Sathe, R. Keedy, K. Stein, Space-time finite element techniques for computation of fluid-structure interactions, Computer Methods in Applied Mechanics and Engineering 195 (17) (2006) 2002–2027.

[168] T. Tezduyar, S. Aliabadi, M. Behr, A. Johnson, S. Mittal, Parallel finite-element computation of 3d flows, Computer 26 (10) (1993) 27–36.

[169] K. Stein, T. Tezduyar, R. Benney, Mesh moving techniques for fluid-structure interactions with large displacements, Journal of Applied Mechanics 70 (2003) 58–63.

[170] W. Glenn, J. Patino, Circulatory by-pass of the right heart. i. preliminary observations on the direct delivery of vena caval blood into the pulmonary arterial circulation. azygos vein-pulmonary artery shunt, The Yale journal of biology and medicine 27 (1954) 147–151.

[171] S. B. Nuland, W. Glenn, P. Guilfoil, Circulatory bypass of the right heart. III. some observations on long-term survivors., Surgery 43 (2) (1958) 184.

[172] B. F. Sachs, R. G. Pontius, J. R. Zuberbuhler, The clinical use of the superior vena cava-pulmonary artery shunt: A report of 20 cases, Journal of pediatric surgery 3 (3) (1968) 364–375.

[173] F. Robicsek, P. W. Sanger, F. H. Taylor, A. Najib, The azygos steal syndrome in cava-pulmonary anastomosis, Annals of Surgery 158 (6) (1963) 1007.

[174] W. Glenn, M. Browne, R. Whittemore, Circulatory bypass of the right side of the heart: cava-pulmonary artery shuntindications and results (report of a collected series of 537 cases), The Heart and Circulation in the Newborn and Infant. Grune & Stratton, New York.

[175] M. Esmaily-Moghadam, B. Murtuza, T. Hsia, A. Marsden, Simulations reveal adverse hemodynamics in patients with multiple systemic to pulmonary shunts, Journal of Biomechanical Engineering(Under review).

[176] D. Hunt, W. S. Edwards, P. B. Deverall, L. Bargeron, Superior vena cava to right pulmonary artery anastomosis results in 46 infants and children, Thorax 25 (5) (1970) 550–555.

[177] J. Downes, H. Nicodemus, W. Pierce, J. Waldhausen, E. A. Moffitt, Acute respiratory failure in infants following cardiovascular surgery, Survey of Anesthesiology 15 (2) (1971) 157–158.

[178] I. B. Boruchow, T. D. Bariley, L. P. Elliott, G. L. Schiebler, Late superior vena cava syndrome after superior vena cava–right pulmonary artery anastomosis: Report of four cases, New England Journal of Medicine 281 (12) (1969) 646–650.

[179] H. J. van de Wal, R. Ouknine, D. Tamisier, M. Levy, P. R. Vouhe, F. Leca, Bidirectional cavopulmonary shunt: is accessory pulsatile flow, good or bad?, European journal of cardio-thoracic surgery 16 (2) (1999) 104–110.

[180] D. B. McElhinney, S. M. Marianeschi, V. M. Reddy, Additional pulmonary blood flow with the bidirectional Glenn anastomosis: does it make a difference?, The Annals of thoracic surgery 66 (2) (1998) 668–672.

[181] R. D. Mainwaring, J. J. Lamberti, K. Uzark, R. L. Spicer, M. W. Cocalis, J. W. Moore, Effect of accessory pulmonary blood flow on survival after the bidirectional Glenn procedure, Circulation 100 (suppl 2) (1999) II–151.

[182] F. Gervaso, S. Kull, G. Pennati, F. Migliavacca, G. Dubini, V. S. Luisi, The effect of the position of an additional systemic-to-pulmonary shunt on the fluid dynamics of the bidirectional cavo-pulmonary anastomosis, Cardiol Young 14 (3) (2004) 38–43.

[183] O. Barnea, W. Santamore, A. Rossi, E. Salloum, S. Chien, E. Austin, Estimation of oxygen delivery in newborns with a univentricular circulation, Circulation 98 (14) (1998) 1407–1413.

[184] C. Figueroa, A coupled-momentum method to model blood flow and vessel deformation in human arteries: applications in disease research and simulation-based medical planning, Ph.D. thesis, Stanford (2006).

[185] X. He, D. Ku, Pulsatile flow in the human left coronary artery bifurcation: Average conditions, Journal of Biomechanical Engineering 118 (1) (1996) 74–82.

[186] C. Taylor, T. Hughes, C. Zarins, Effect of exercise on hemodynamic conditions in the abdominal aorta, Journal of Vascular Surgery 29 (6) (1999) 1077 – 1089.